Journal of the Serbian Chemical Society

*e*version
lectronic

VOLUME 80

No 4

BELGRADE 2015

Available on line at

СХД
1897

www.shd.org.rs/JSCS/

CONTENTS

Available on line at www.shd.org.rs/JSCS/

SHORT COMMUNICATION

Novel one-pot process for the synthesis of ethyl 2-imino-4--methyl-2,3-dihydrothiazole-5-carboxylates

HAMID BEYZAEI*, REZA ARYAN and HADI MOGHADAS

Department of Chemistry, Faculty of Science, University of Zabol, Zabol 9861335856, Iran

Abstract: A facile one-pot, two-step process for the synthesis of ethyl 2-imino--4-methyl-2,3-dihydrothiazole-5-carboxylates *via* the cyclocondensation of ethyl 3-oxo-2-thiocyanatobutanoate with a variety of hydrazine and hydrazide derivatives was developed. Ethyl 3-oxo-2-thiocyanatobutanoate itself was synthesized as an intermediate from the reaction of ethyl 2-chloroacetoacetate with potassium thiocyanate (KSCN). The molecular structures of these newly synthesized compounds were elucidated based on elemental analysis and spectral data.

Keywords: three-component reaction; thiocyanation; thiazole derivatives; cyclocondensation; hydrazines; hydrazides.

INTRODUCTION

Thiazoles are of eminent importance because of their potential as bioactive compounds[1,2] and versatile building blocks for natural products and pharmaceuticals.[3,4] Thiazole heterocycles are important subunits in many complex natural compounds and drugs, *e.g.*, vitamin B_1, epothilones, thiostrepton, nizatidine (ulcer therapeutic), ritonavir (a potent inhibitor of HIV protease, Fig. 1) and thiamine pyrophosphate (TPP, a coenzyme that is part of the Krebs cycle in the process of cellular respiration).[3–6] A tetrahydrothiazole also appears in the skeleton of penicillin, which is one of the first and most important broad spectrum antibiotics. Thiazole derivatives display a wide range of biological activities, such as cardiotonic, fungicidal, sedative, anesthetic, bactericidal and anti--inflammatory.[7–12] Furthermore, there are many other applications of thiazole derivatives, for example in liquid crystals or cosmetics (sunscreens).[13,14]

The synthesis of thiazole derivatives is important because of their wide range of pharmaceutical and biological properties. Many methods have been developed

---

* Corresponding author. E-mail: hbeyzaei@yahoo.com

453

for the construction of thiazole ring systems. One classical and widely used method is the condensation of *α*-haloketones with thioamide derivatives, which is known as the Hantzsch reaction.[15–17] Another efficient method is the introduction of substituents onto a thiazole core structure through Stille coupling, which involves the use of organostannane intermediates.[18] In recent years, a new and frequently encountered method for thiazole synthesis is the conversion of thiazoline derivatives through the use of dehydrogenating reagents, such as sulfur, KMnO$_4$, Cu(I)/Cu(II)/peroxide oxidation, MnO$_2$, NaH/DBU, etc.[19–26]
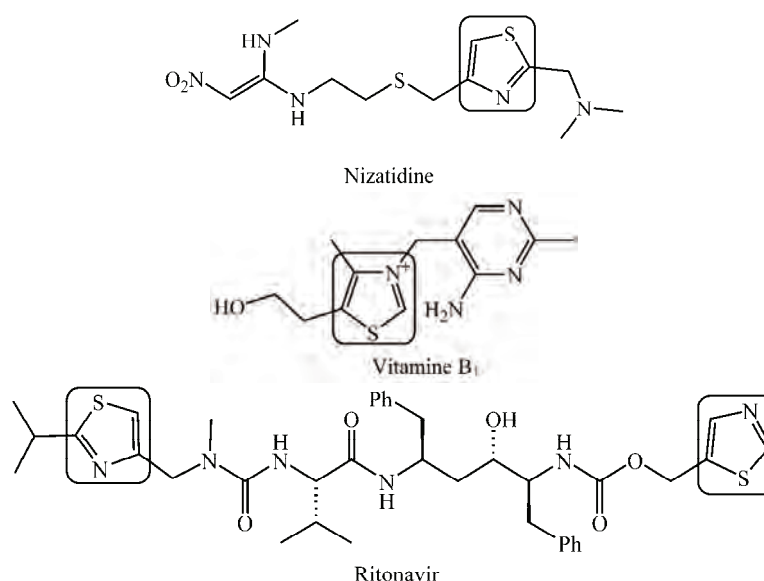
Fig. 1. Thiazoles as part of some natural compounds and drugs.

These findings prompted the present synthesis of new ethyl 2-imino-4--methyl-2,3-dihydrothiazole-5-carboxylates. These synthesized compounds were characterized by NMR and IR spectral data, and elemental analysis data.

EXPERIMENTAL

All chemicals and solvents were purchased from Merck and TCI Chemical Companies and were used without purification. All yields refer to isolated products and are expressed in %. Melting points were recorded on a Kruss type KSP1N melting point meter and are uncorrected. The IR spectra of the products in the range 400–4,000 cm^{-1} were recorded on a Bruker Tensor-27 FT-IR spectrometer and only noteworthy absorptions are listed. The ^{1}H- and ^{13}C-NMR spectra of DMSO-d_6 solutions were recorded on a Bruker FT-NMR Ultra Shield-400 spectrometer with residual protons of the solvent as internal standard (2.50 ppm for ^{1}H and 39.48 ppm for ^{13}C). Elemental analyses were performed for C, H, N and S on a Thermo Finnigan Flash EA microanalyzer. Monitoring of the progress of the reactions and the

purity of the products were affected by TLC on alufoil plates pre-coated with silica gel (60, Merck); the eluent was $CHCl_3:CH_3OH$, 9:1 and visualization was with I_2 vapor.

Physical, analytical and spectral data of the synthesized compounds are given in Supplementary material to this paper.

General procedure for the synthesis of ethyl 2-imino-4-methyl-2,3-dihydrothiazole-5-carboxylates (4a–f)

A suspension of ethyl 2-chloroacetoacetate (**1**, 1.65 g, 10 mmol) and potassium thiocyanate (KSCN) (0.97 g, 10 mmol) in acetonitrile (10 mL) was stirred at room temperature for 2 h. Then, hydrazine or hydrazide derivatives **3a**–**f** were added dropwise to the reaction mixture and the mixture was stirred for a further 1 h at the same temperature before it was heated under reflux for 2.5–5 h (2.5 h for **4a** and **b**; 4 h for **4c** and 5h for **4d**–**f**). The reaction mixture was cooled to room temperature, the precipitate was filtered off, and washed with water (10 mL) and ethanol (10 mL), dried in air, and recrystallized from methanol, to give the pure products **4a**–**f** as white, yellow or red crystals.

RESULTS AND DISCUSSION
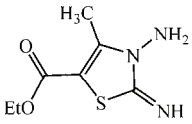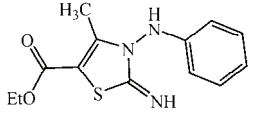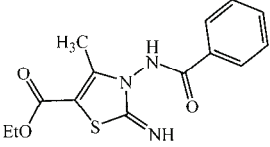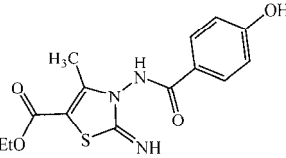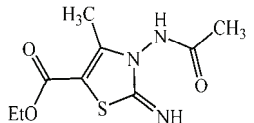
Ethyl 2-imino-4-methyl-2,3-dihydrothiazole-5-carboxylates **4a**–**f** were prepared in a simple and facile one-pot, two-step procedure. First, ethyl 2-chloroacetoacetate (**1**) was reacted with potassium thiocyanate (KSCN) in acetonitrile as a solvent at room temperature for 2 h to give ethyl 3-oxo-2-thiocyanatobutanoate (**2**) as an intermediate. Then, treatment of this compound with various hydrazine or hydrazide derivatives (**3a**–**f**) under reflux for 2.5–5 h gave new thiazoles **4a**–**f** in 48–83 % yields after recrystallization from methanol (Scheme 1). The structures of all products are presented in Table I.

R = H; C_6H_5; 2,4-$[NO_2]_2$-C_6H_3; C_6H_5CO; 4-OH-C_6H_4CO; CH_3CO
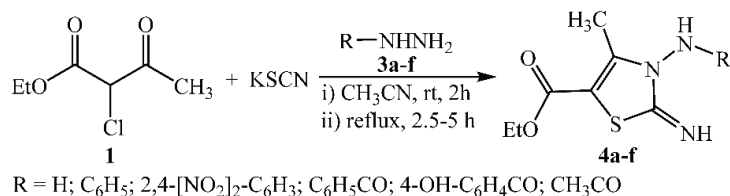
Scheme 1. Total synthesis of thiazole derivatives **4a**–**f**.

A plausible mechanism is depicted in Scheme 2 for the formation of these compounds. As shown, first, ethyl 3-oxo-2-thiocyanatobutanoate (**2**) as an intermediate was probably produced from the substitution reaction between ethyl 2-chloroacetoacetate (**1**) and potassium thiocyanate (KSCN). Then, condensation of compound **2** with hydrazine and hydrazide derivatives **3a**–**f** generated intermediates **3′a**–**f** or **3″a**–**f**. Finally, ethyl 2-imino-4-methyl-2,3-dihydrothiazole-5-carboxylates **4a**–**f** were afforded from intramolecular addition reactions of intermediates **3″a**–**f** by attack of the NH group to the carbon atom of the C≡N bond. Note that in this multistep synthesis, none of the likely key intermediates was isolated.

TABLE I. Synthesis of thiazole derivatives **4a**–**f**

No.	Product	R	Reagent **3a**–**f**	Yield, %	M.p., °C
4a		H	Hydrazine	50	285–286
4b		C_6H_5	Phenylhydrazine	55	280–281 (Decomp.)
4c		2,4-[NO₂]₂-C₆H₃	2,4-Dinitrophe-nylhydrazine	83	218–219 (Decomp.)
4d		C_6H_5CO	Benzhydrazide	68	200–201
4e		4-OH-C₆H₄CO	4-Hydroxybenz-hydrazide	48	185–186
4f		CH_3CO	Acetohydrazide	60	179–180

The structural assignments of compounds **4a**–**f** were based on their anal-ytical and spectral data. The ^{1}H-NMR spectra of compounds **4a**–**f** showed triplet and quartet signals due to methyl and methylene protons included in the ethoxy group within δ 1.23–1.30 and 4.15–4.27 ppm ($J \approx 7.1$ Hz), signals due to the methyl and –NH– groups of the thiazole ring within δ 1.91–2.55 and 10.02–11.44
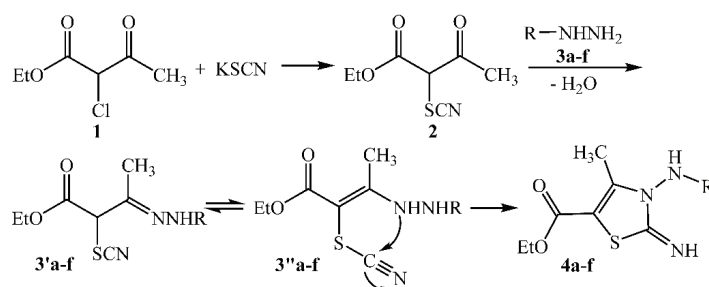
Scheme 2. The proposed mechanism of formation of products **4a**–**f**.

ppm, respectively, and signals within δ 7.81–11.00 ppm belonging to the –NNH– groups of compounds **4b**–**f**. The ^{13}C-NMR spectra of the products exhibited signals within δ 14.00–14.44, 59.67–62.81 and 162.44–169.91 ppm attributed to methyl, methylene and carbonyl carbons, respectively, included in the –CO$_2$Et group, signals within δ 11.31–22.41, 106.08–107.95, 161.35–163.03 and 157.06––161.58 ppm, attributed to the –C=C**C**H$_3$, –**C**=CCH$_3$, –C=**C**CH$_3$ and –C=NH carbons, respectively, signals within δ 165.11–167.73 ppm belonging to the carbonyl carbons adjacent to the –NH– groups of compounds **4d**–**f**. The FT-IR spectra of **4a**–**f** in KBr disks showed absorption bands within ν 3305–3467 cm^{-1} corresponding to –NH– groups, 1647–1715 cm^{-1} belonging to carbonyl groups, 1601–1666 cm^{-1} belonging to imine groups and 1406–1611 cm^{-1} attributed to the –C=C– bonds. All this evidence plus microanalytical data strongly supports the formation of all products.
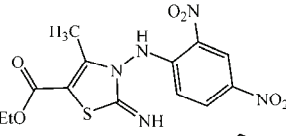
CONCLUSIONS

In summary, several new ethyl 2-imino-4-methyl-2,3-dihydrothiazole-5-carboxylates were synthesized in a one-pot, two-step process from the cyclocondensation of ethyl 3-oxo-2-thiocyanatobutanoate as an intermediate with various hydrazines and hydrazides, which constitute potential precursors for the synthesis of various biological and pharmaceutical compounds.

SUPPLEMENTARY MATERIAL

Physical, analytical and spectral data of the synthesized compounds are available electronically from http://www.shd.org.rs/JSCS/, or from the corresponding author on request.

ИЗВОД
НОВ ПОСТУПАК СИНТЕЗЕ ЕТИЛ-2-ИМИНО-4-МЕТИЛ-2,3-ДИХИДРОТИАЗОЛ-5-
-КАРБОКСИЛАТА У ЈЕДНОМ РЕАКЦИОНОМ КОРАКУ

HAMID BEYZAEI, REZA ARYAN и HADI MOGHADAS

Department of Chemistry, Faculty of Science, University of Zabol, Zabol 9861335856, Iran

Развијен је нов поступак синтезе етил-2-имино-4-метил-2,3-дихидротиазол-5-кар-боксилата, у једном реакционом кораку циклокондензације етил-3-оксо-2-тиоцијанато-бутаноата и хидразина или хидразинских деривата. Полазно једињење етил-3-оксо-2--тиоцијанатобутаноат синтетисан је из етил-2-хлорацетата и калијум-тиоцијаната (KSCN). Структура добијених једињења одређена је на основу резултата спектроскопске и елементалне анализе.

(Примљено 21. октобра, ревидирано 13. децембра, прихваћено 17. децембра 2014)

REFERENCES

1. J. A. Joule, K. Mills, *Heterocyclic Chemistry*, 4th ed., Blackwell Science., Oxford, 2000, p. 402

2. a) A. S. Kalgutkar, B. C. Crews, L. J. Marnett, *Biochemistry* **35** (1996) 9076; b) I. Hutchinson, M. F. G. Stevens, A. Westwell, *Tetrahedron Lett.* **41** (2000) 425; c) T. L. Gilchrist, *J. Chem. Soc., Perkin Trans. 1* (2001) 2491

3. R. J. Mullins, A. M. Azman, in *Heterocyclic Chemistry - A Guide for the Synthetic Chemist*, J. J. Li, G. W. Gribble, Eds., Tetrahedron Organic Chemistry Series, Vol. 26, Elsevier, Oxford, 2007, p. 345

4. M. M. Campbell, in *Comprehensive Organic Chemistry*, Vol. 4, Sir D. Barton, W. D. Ollis, Eds., Pergamon Press, London, 1979, p. 961

5. A. Dondini, *Org. Biomol. Chem.* **8** (2010) 3366

6. a) K. A. Trumm, H. J. Sattler, S. Postius, I. Szelenyi, W. Schunack, *Arzneim. Forsch./Drug Res.* **35** (1985) 573; b) D. J. Kempf, H. L. Sham, K. C. Marsh, C. A. Flentge, D. Betebenner, B. E. Green, E. McDonald, S. Vasavanonda, A. Saldivar, N. E. Wideburg, W. M. Kati, L. Ruiz, C. Zhao, L. Fino, J. Patterson, A. Molla, J. J. Plattner, D. W. Norbeck, *J. Med. Chem.* **41** (1998) 602

7. K. A. Suri, O. P. Suri, C. K. Atal, *Indian Drugs* **23** (1980) 207

8. H. Tripati, S. N. Mahapatra, *J. Indian Chem. Soc.* **52** (1975) 766

9. Y. Sawa, T. Ishida, *J. Pharm. Soc. Jpn.* **76** (1956) 337

10. A. Geronikaki, G. Theophilidis, *Eur. J. Med. Chem.* **27** (1992) 709

11. R. G. N. Mean, C. R. O. Mocoelo, *Afinidad* **50** (1993) 319

12. T. Giridhar, R. B. Reddy, B. Prasanna, G. V. P. Chandra Mouli, *Indian J. Chem., B* **40** (2001) 1279

13. a) K. Dölling, H. Zaschke, H. Schubert, *J. Prakt. Chem. (Leipzig)* **321** (1979) 643; b) A. A. Kiryanov, P. Sampson, A. J. Seed, *J. Org. Chem.* **66** (2001) 7925; c) A. Mori, A. Sekiguchi, K. Masui, T. Shimada, K. Horie, K. Osakada, M. Kawamoto, T. Ikeda, *J. Am. Chem. Soc.* **125** (2003) 1700

14. T. Bach, S. Heuser, *Tetrahedron Lett.* **41** (2000) 1707

15. K. M. Aitken, R. A. Aitken, *Tetrahedron* **64** (2008) 4384

16. T. M. Potewar, S. A. Ingale, K. V. Srinivasan, *Tetrahedron* **63** (2007) 11066

17. M. Narender, M. S. Reddy, R. Sridhar, Y. V. D. Nageswar, K. R. Rao, *Tetrahedron Lett.* **46** (2005) 5953

18. J. Hämmerle, M. Spina, M. Schnürch, M. D. Mihovilovic, P. Stanetty, *Synthesis* **19** (2008) 3099

19. A. Friedrich, T. Max, G. Karl, *Justus Liebigs Ann. Chem.* **639** (1961) 133

20. R. A. Aitken, D. P. Armstrong, R. H. B. Galt, S. T. E. Mesher, *J. Chem. Soc. Perkin Trans. 1* (1997) 935

21. A. I. Meyers, F. X. Tavares, *J. Org. Chem.* **61** (1996) 8207

22. X. Fernandez, E. Duňach, *Tetrahedron: Asymmetry* **12** (2001) 1279

23. X. Fernandez, R. Fellous, L. Lizzani-Cuvelier, M. Loiseau, E. Duňach, *Tetrahedron Lett.* **42** (2001) 1519

24. S. L. You, J. W. Kelly, *Tetrahedron* **61** (2005) 241

25. S. L. You, J. W. Kelly, *Chem. Eur. J.* **10** (2004) 71

26. G. L. Mislin, A. Burger, M. A. Abdallah, *Tetrahedron* **60** (2004) 12139.

Novel one-pot process for the synthesis of ethyl 2-imino-4--methyl-2,3-dihydrothiazole-5-carboxylates

HAMID BEYZAEI*, REZA ARYAN and HADI MOGHADAS

Department of Chemistry, Faculty of Science, University of Zabol, Zabol 9861335856, Iran

PHYSICAL, ANALYTICAL AND SPECTRAL DATA OF THE SYNTHESIZED COMPOUNDS

Ethyl 3-amino-2-imino-4-methyl-2,3-dihydrothiazole-5-carboxylate (4a). Yield: 50 %; white crystals; m.p.: 285–286 °C; Anal. Calcd. for $C_7H_{11}N_3O_2S$: C, 41.78; H, 5.51; N, 20.88; S, 15.93 %. Found: C, 41.82; H, 5.56; N, 20.86, S, 15.85 %; IR (KBr, cm^{-1}): 1585 (C=C stretching of thiazole ring), 1623 (C=N stretching of imine group), 1693 (C=O stretching of CO_2Et group), 3467, 3434 (NH stretching of imine and primary amine groups); ^{1}H-NMR (400 MHz, DMSO-d_6, δ / ppm): 1.24 (3H, *t*, *J* = 7.1 Hz, CH$_3$), 2.07 (3H, *s*, =CCH$_3$), 4.16 (2H, *q*, *J* = 7.1 Hz, OCH$_2$), 7.91 (2H, *s*, NH$_2$, D$_2$O exchangeable), 10.16 (1H, *s*, NH, D$_2$O exchangeable); ^{13}C-NMR (100 MHz, DMSO-d_6, δ / ppm): 169.91 (C=O), 161.32 (=**C**CH$_3$), 159.99 (C=NH), 106.65 (**C**=CCH$_3$), 59.73 (OCH$_2$), 19.91 (C=C**C**H$_3$), 14.44 (CH$_2$**C**H$_3$).

Ethyl 2-imino-4-methyl-3-(phenylamino)-2,3-dihydrothiazole-5-carboxylate (4b). Yield: 55 %; white crystals; Decomp. 280–281 °C; Anal. Calcd. for $C_{13}H_{15}N_3O_2S$: C, 56.30; H, 5.45; N, 15.15; S, 11.56 %. Found: C, 56.24; H, 5.52; N, 15.18, S, 11.48 %; IR (KBr, cm^{-1}): 1406, 1545 (C=C stretching of aromatic ring), 1611 (C=C– stretching of thiazole ring), 1666 (C=N stretching of imine group), 1709 (C=O stretching of CO_2Et group), 3349 (NH stretching of imine and secondary amine); ^{1}H-NMR (400 MHz, DMSO-d_6, δ / ppm): 1.30 (3H, *t*, *J* = 7.1 Hz, CH$_3$), 2.09 (3H, *s*, =CCH$_3$), 4.27 (2H, *q*, *J* = 7.1 Hz, OCH$_2$), 7.43, 7.72 (3H, *m*, 2H, *d*, *J* = 10.1 Hz, aromatic), 7.81 (1H, *s*, N**H**Ph, D$_2$O exchangeable), 10.06 (1H, *s*, C=NH, D$_2$O exchangeable); ^{13}C-NMR (100 MHz, DMSO-d_6, δ / ppm): 162.44 (C=O), 161.44 (=**C**CH$_3$), 157.06 (C=NH), 145.85, 130.72, 123.05, 115.79 (aromatic), 106.93 (**C**=CCH$_3$), 60.96 (OCH$_2$), 17.31 (=C**C**H$_3$), 14.13 (CH$_2$**C**H$_3$).

---

* Corresponding author. E-mail: hbeyzaei@yahoo.com

Ethyl 3-((2,4-dinitrophenyl)amino)-2-imino-4-methyl-2,3-dihydrothiazole-5-carboxylate (4c). Yield: 83 %; red crystals; Decomp. 218–219 °C; Anal. Calcd. for $C_{13}H_{13}N_5O_6S$: C, 42.51; H, 3.57; N, 19.07; S, 8.73 %. Found: C, 42.55; H, 3.53; N, 19.14, S, 8.67 %; IR (KBr, cm^{-1}): 1338, 1427 (N–O stretching of NO$_2$ group), 1498, 1594 (C=C stretching of aromatic and thiazole rings), 1613 (C=N stretching of imine group), 1715 (C=O stretching of CO$_2$Et group), 3089, 3305 (NH stretching of imine and secondary amine); ^{1}H-NMR (400 MHz, DMSO-d_6, δ / ppm): 1.26 (3H, *t*, *J* = 7.1 Hz, CH$_3$), 2.55 (3H, *s*, =CCH$_3$), 4.26 (2H, *q*, *J* = 7.1 Hz, OCH$_2$), 8.30, 8.33, 9.03 (1H, *d*, *J* = 2.6 Hz, 1H, *d*, *J* = 2.6 Hz, 1H, *d*, *J* = 9.3 Hz, aromatic), 8.95 (1H, *s*, N**H**Ph, D$_2$O exchangeable), 11.44 (1H, *s*, C=NH, D$_2$O exchangeable); ^{13}C-NMR (100 MHz, DMSO-d_6, δ / ppm): 168.65 (C=O), 161.83 (C=**C**CH$_3$), 159.11 (C=NH), 148.99, 143.07, 138.47, 130.25, 122.79, 116.27 (aromatic), 107.95 (**C**=CCH$_3$), 62.81 (OCH$_2$), 14.00 (CH$_2$**C**H$_3$), 11.31 (=CC**H$_3$**).

Ethyl 3-benzamido-2-imino-4-methyl-2,3-dihydrothiazole-5-carboxylate (4d). Yield: 68 %; white crystals; m.p.: 200–201 °C; Anal. Calcd. for $C_{14}H_{15}N_3O_3S$: C, 55.07; H, 4.95; N, 13.76; S, 10.50 %. Found: C, 55.00; H, 5.01; N, 13.79, S, 10.45 %; IR (KBr, cm^{-1}): 1463, 1509 (C=C stretching of aromatic and thiazole rings), 1601 (C=N stretching of imine group), 1647 (C=O stretching of CONH group), 1669 (C=O stretching of CO$_2$Et group), 3442 (NH stretching of imine and amide); ^{1}H-NMR (400 MHz, DMSO-d_6, δ / ppm): 1.23 (3H, *t*, *J* = 7.0 Hz, CH$_3$), 2.12 (3H, *s*, =CCH$_3$), 4.15 (2H, *q*, *J* = 7.0 Hz, OCH$_2$), 7.53–7.98 (5H, *m*, aromatic), 10.72 (1H, *s*, C=NH, D$_2$O exchangeable), 11.00 (1H, *s*, CONH, D$_2$O exchangeable); ^{13}C-NMR (100 MHz, DMSO-d_6, δ / ppm): 168.47 (CO$_2$Et), 165.11 (CONH), 161.35 (=**C**CH$_3$), 159.72 (C=NH), 132.14, 131.92, 128.53, 127.60 (aromatic), 106.08 (**C**=CCH$_3$), 59.67 (OCH$_2$), 16.96 (=C**C**H$_3$), 14.44 (CH$_2$**C**H$_3$).

Ethyl 3-(4-hydroxybenzamido)-2-imino-4-methyl-2,3-dihydrothiazole-5-carboxylate (4e). Yield: 48 %; yellow crystals; m.p.: 185–186 °C; Anal. Calcd. for $C_{14}H_{15}N_3O_4S$: C, 52.33 %; H, 4.71; N, 13.08; S, 9.98 %. Found: C, 52.39; H, 4.66; N, 13.15, S, 9.90 %; IR (KBr, cm^{-1}): 1472, 1506 (C=C– stretching of aromatic and thiazole rings), 1609 (C=N stretching of imine group), 1674 (C=O stretching of CONH group), 1702 (C=O stretching of CO$_2$Et group), 3419 (NH stretching of imine and amide); ^{1}H-NMR (400 MHz, DMSO-d_6, δ / ppm): 1.24 (3H, *t*, *J* = 7.0 Hz, CH$_3$), 2.16 (3H, *s*, =CCH$_3$), 4.17 (2H, *q*, *J* = 7.0 Hz, OCH$_2$), 6.93, 7.80 (2H, *d*, *J* = 8.2 Hz, 2H, *d*, *J* = 8.2 Hz, aromatic), 8.15 (1H, *s*, OH, D$_2$O exchangeable), 10.13 (1H, *s*, C=NH, D$_2$O exchangeable), 10.59 (1H, *s*, CONH, D$_2$O exchangeable); ^{13}C-NMR (100 MHz, DMSO-d_6, δ / ppm): 169.85 (CO$_2$Et), 167.73 (CONH), 163.03 (=**C**CH$_3$), 161.58 (C=NH), 159.73, 132.32, 129.41, 114.93 (aromatic), 106.63 (**C**=CCH$_3$), 60.40 (OCH$_2$), 22.41 (=C**C**H$_3$), 14.35 (CH$_2$**C**H$_3$).

*Ethyl 3-acetamido-2-imino-4-methyl-2,3-dihydrothiazole-5-carboxylate (**4f**).* Yield: 60 %; white crystals; m.p.: 179–180 °C; Anal. Calcd. for $C_9H_{13}N_3O_3S$: C, 44.43; H, 5.39; N, 17.27; S, 13.18 %. Found: C, 44.39; H, 5.37; N, 17.33, S, 13.14 %; IR (KBr, cm^{-1}): 1590 (C=C stretching of aromatic and thiazole rings), 1616 (C=N stretching of imine group), 1673 (C=O stretching of CONH group), 1703 (C=O stretching of CO_2Et group), 3253, 3382 (NH stretching of imine and amide); ^{1}H-NMR (400 MHz, DMSO-d_6, δ / ppm): 1.23 (3H, t, J = 7.1 Hz, CH_3), 1.91 (3H, s, =CCH_3), 2.43 (3H, s, $COCH_3$), 4.16 (2H, q, J = 7.1 Hz, OCH_2), 10.02 (1H, s, C=NH, D_2O exchangeable), 10.39 (1H, s, CONH, D_2O exchangeable); ^{13}C-NMR (100 MHz, DMSO-d_6, δ / ppm): 168.99 (CO_2Et), 167.72 (CONH), 161.79 (=**C**CH_3), 161.49 (C=NH), 106.86 (**C**=CCH_3), 60.03 (OCH_2), 20.45 (=C**C**H$_3$), 17.29 (CO**C**H$_3$), 14.24 (CH$_2$**C**H$_3$).

Journal of the Serbian Chemical Society

SHORT COMMUNICATION

N-Methylimidazole-mediated synthesis of aryl alkyl ethers under microwave irradiation and solvent free conditions

HOORIEH DJAHANIANI[1]*, LAILA AGHADADASHI-ABHARI[2] and BITA MOHTAT[3]

[1]*Department of Chemistry, Islamic Azad University, East Tehran Branch, Tehran, Iran,*
[2]*Department of Chemistry, East Tehran Branch, Payame Noor University, Tehran, Iran*
and [3]*Department of Chemistry, Islamic Azad University, Karaj Branch, Karaj, Iran*

Abstract: A microwave-assisted three-component reaction was established for the synthesis of aryl alkyl ethers. The reaction was performed under solvent--free conditions in the presence of *N*-methylimidazole and dialkyl acetylene-dicarboxylate to furnish a novel approach to *O*-alkylation of phenol derivatives in high yield.

Keywords: microwave-assisted; three-component reaction; *N*-methylimidazole; *O*-alkylation; dialkyl acetylenedicarboxylate.

INTRODUCTION

Aryl ethers are used as raw materials for the manufacture of a variety of durable surface coatings, paints, varnishes, printing inks, wire enamels, surface-active agents, rubber chemicals, antioxidants, fungicides, heat carriers, foaming agents, synthetic resins and perfumes.[1–4] These compounds can be prepared by different approaches.

It was found that alkylation of phenol could be performed with homogenous catalytic systems, such as imidazolium salts ionic liquids,[5] use of bases such as NaOH and K_2CO_3 in the presence of dimethyl sulfate (DMSA) catalyzed by solid base zeolites,[6] Cs-loaded zeolites,[7] dimethyl carbonate under solid/liquid phase transfer systems[8] and KNO_3/NaY.[9] Though high catalytic performances were achieved in homogenous systems, the drawbacks were poor catalyst recovery and product separation. Hence, some heterogeneous catalysts for the selective synthesis of aryl alkyl ether were investigated.[10] Basic zeolites, alumina or alumina–silica were usually used as catalysts for the vapor phase alkylation of

---

phenol,[11] but considerable amounts of by-products (*C*-alkylation) were always present.

Thus, the development of an efficient, safe, and environmentally friendly method for *O*-alkylation constitutes an important challenge; moreover, synthesis without solvents under microwave irradiation offers several advantages. The absence of solvent may reduce the risk of hazardous explosions when the reaction occurs in a closed vessel in an oven.[12,13] The addition of phenol derivatives to *tert*-butyl propiolate in the presence of triphenylphosphine, which led to alkyl aryloxypropenoates, in CH_2Cl_2 at room temperature was previously described.[3] In connection with ongoing work on the development of new synthetic methods to heterocyclic compounds using phenol derivatives,[14,15] herein, a method to realize *O*-alkylation of some OH acids by nucleophilic substitution reactions (Scheme 1) is reported.

Ar—OH + [CO_2R / CO_2R] (2) + [imidazole N-Me] (3) $\xrightarrow{\text{MW, Solvent free} \atop 100\ ^{\circ}\text{C, 4-7 min}}$ Ar—OR (4)

(1)

1	Ar
a	4-hydroxycoumarin
b	7-hydroxycoumarin
c	4-hydroxyquinoline
d	6-hydroxyquinoline
e	8-hydroxyquinoline
f	2-naphthol

2	R
a	Me
b	Et
c	^{t}Bu

4	Ar	R	Yield %
a=c	4-hydroxycoumarin	Me	95
b	4-hydroxycoumarin	Et	90
d=f	7-hydroxycoumarin	Me	98
e	7-hydroxycoumarin	Et	95
g	4-hydroxyquinoline	Me	85
h	6-hydroxyquinoline	Me	85
i=j	8-hydroxyquinoline	Me	95
k	2-naphthol	Me	90

Scheme 1. Typical procedure for the preparation of compounds **4a**–**k**.
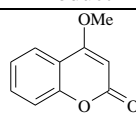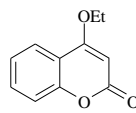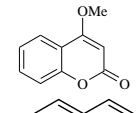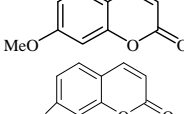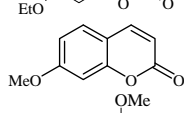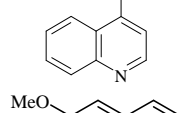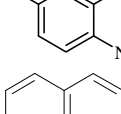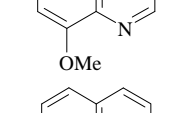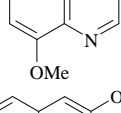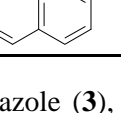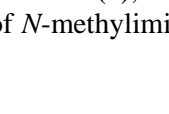
RESULTS AND DISCUSSION

Our studies were initiated by the reaction of 4-hydroxycoumarin (**1a**) with dimethyl acetylenedicarboxylate (DMAD) (**2a**) or diethyl acetylenedicarboxylate (DEAD) (**2b**) in the presence of *N*-methylimidazole (**3**) without solvent under microwave irradiation (green chemistry), which afforded the 4-alkoxy coumarins **4a** and **b**, respectively, in high yields after 4–7 min.

Surprisingly, when this reaction was performed with di-*tert*-butyl acetylene-dicarboxylate (DTAD, **2c**), TLC and the ^{1}H-NMR spectrum of the product showed that the obtained product was 4-methoxycoumarin (**4a**). Then the substrate scope of this reaction was investigated by using hydroxyquinoline deri-

vatives and naphthols under the same conditions. As expected, using DMAD and DEAD, the products were methoxy and ethoxy derivatives, respectively. When the reaction occurred with DTAD, the isolated products were methoxy derivatives. The structures, yields and melting points of the products are summarized in Table I.

TABLE I. *O*-Alkylation of hydroxycoumarins, hydroxyquinolines and 2-naphthol

Entry	Ar	R	Product	Time, min	Yield, %
1	4-Hydroxycoumarin	Me		6	95
2	4-Hydroxycoumarin	Et		7	90
3	4-Hydroxycoumarin	*t*-Bu		5	80
4	7-Hydroxycoumarin	Me		4	98
5	7-Hydroxycoumarin	Et		4	95
6	7-Hydroxycoumarin	*t*-Bu		5	70
7	4-Hydroxyquinoline	Me		7	85
8	6-Hydroxyquinoline	Me		6	85
9	8-Hydroxyquinoline	Me		7	95
10	8-Hydroxyquinoline	*t*-Bu		7	85
11	2-Naphthol	Me		7	90

To illustrate the role of *N*-methylimidazole (**3**), the reaction of 2-naphthol with DMAD was studied in the absence of *N*-methylimidazole. The formation of

the *O*-methylated product was not observed in the absence of *N*-methylimidazole. The TLC and ^{1}H-NMR spectra of the reaction mixture confirmed only 2-naphthol.

It is reasonable to assume that the products **4a**, **b**, **d**, **e**, **g–i** and **k** result from initial addition of *N*-methylimidazole to the dialkyl acetylenedicarboxylates **2a** and **b** and subsequent protonation of the zwitterions **5** by OH acids.[16] Then the reactions proceed *via* a protonated intermediate that activates the electrophile for attack by the conjugate base of phenol onto the carbon atom group of the acetylenic ester, which provides the stable products (Scheme 2). The fact that DMAD and DEAD reacted showed that the displacement step could have S_N2 character.[17]
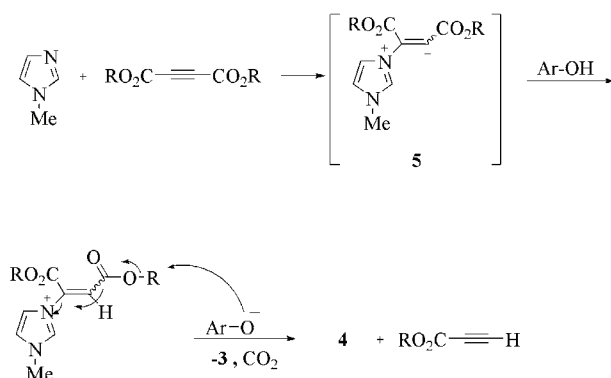
Scheme 2. A possible mechanism for the preparation of **4a**, **b**, **d**, **e**, **g–i** and **k**.

Formation of the product **4c**, **4f** and **4j** using DTAD suggests that steric effects are important and hence, the conjugate base of phenol attacks into the methyl group of *N*-methylimidazole instead of the alkyl group of the acetylenic ester, which again suggests that the displacement step could have S_N2 character (Scheme 3).
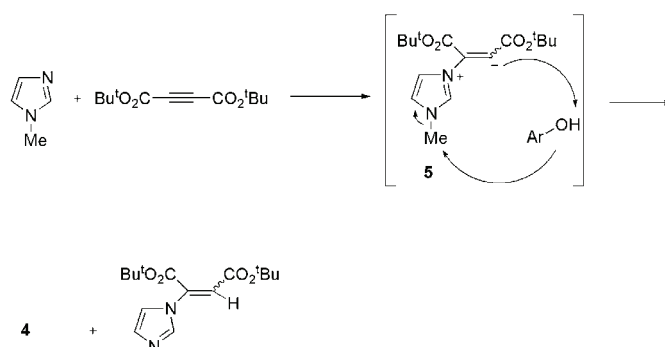
Scheme 3. A possible mechanism for reactions of DTAD.

EXPERIMENTAL

Microwave irradiation was performed with a Milestone ETHOS 1600 microwave oven. The chemicals were purchased from Fluka and used without further purification. The melting points were measured on an Electrothermal 9100 apparatus. The IR spectra were recorded on a Shimadzu IR-460 spectrometer. The ^{1}H- and ^{13}C-NMR spectra were obtained on a Bruker Avance DRX-400 spectrometer using CDCl$_3$ as the applied solvent and TMS as an internal standard.

Physical, analytical and spectral data for the compounds **4a**–**k** are given in the Supplementary material to this paper.

*Typical procedure for the synthesis of alkoxycoumarin (**4**)*

In a 10-mL reaction vial, a mixture of *N*-methylimidazole (**3**, 0.26 g, 2.0 mmol) and dimethyl acetylenedicarboxylate (**2a**, 0.24 mL, 2.0 mmol) under solvent-free condition was stirred for 1 min. Subsequently, 4-hydroxycoumarin (**1a**, 0.32 g, 2.0 mmol) was added to the reaction mixture, and the reaction vial was capped and pre-stirred for 20 s. The mixture was subjected to microwave irradiation at a power of 600 W for 6 min at 100 °C. Upon completion, monitored by TLC, the reaction mixture was cooled to room temperature. The resulting precipitate was separated by filtration and recrystallized from diethyl ether (Et$_2$O) to afford the pure compound **4a**.

CONCLUSIONS

In the present investigation, a simple and economical one-step procedure for ethers of coumarin, quinoline and naphthol under microwave irradiation was developed. This method offers marked improvements concerning high isolated yields of the products, avoidance of hazardous organic solvents and toxic catalysts and a simple protocol of the alkylation of different phenols.

SUPPLEMENTARY MATERIAL

Physical, analytical and spectral data for the compounds **4a**–**k** are available electronically from http://www.shd.org.rs/JSCS/, or from the corresponding author on request.

И З В О Д

СИНТЕЗА АЛКИЛ-АРИЛ-ЕТАРА У ПРИСУСТВУ *N*-МЕТИЛИМИДАЗОЛА ПОД УТИЦАЈЕМ МИКРОТАЛАСА И У ОДСУСТВУ РАСТВАРАЧА

HOORIEH DJAHANIANI[1], LAILA AGHADADASHI-ABHARI[2] и BITA MOHTAT[3]

[1]Chemistry Department, Islamic Azad University, East Tehran Branch, Tehran, Iran, [2]Chemistry Department, East Tehran Branch, Payame Noor University, Tehran, Iran u [3]Chemistry Department, Islamic Azad University, Karaj Branch, Karaj, Iran

Развијен је поступак за трокомпонентну реакцију за синтезу арил-алкил-етара под утицајем микроталаса. Реакције су вршене у присуству *N*-метилимидазола и диалкил ацетилендикарбоксилата без растварача. Овим поступком је остварена синтеза *O*-алкилованих фенола у високом приносу.

REFERENCES

1. C. Cazorla, E. Pfordt, M. Duclos, E. Metay, M. Lemaire, *Green Chem.* **13** (2011) 2482

2. J. Gui, H. Ban, X. Cong, X. Zhang, Z. Hu, Z. Sun, *J. Mol. Catal. A: Chem.* **225** (2005) 27
3. I. Yavari, S. Souri, M. Sirouspour, H. Djahaniani, F. Nasiri, *Synthesis* **11** (2005) 1761
4. W. C. Choi, J. S. Kim, T. H. Lee, S. I. Woo, *Catal. Today* **63** (2000) 229
5. F. Mohanazadeh, M. Aghvami, *Monatsh. Chem.* **138** (2007) 47
6. S. W. Lee, D. H. Kim, K. S. Kim, T. J. Lee, J. C. Kim, *Hwahak Konghak (Korea)* **35** (1997) 621 (in Korean)
7. S. C. Lee, S. W. Lee, K. S. Kim, T. J. Lee, D. H. Kim, J. C. Kim, *Catal. Today* **44** (1998) 253
8. S. Ouk, S. Thiebaud, E. Borredon, P. Legars, L. Lecomte, *Tetrahedron Lett.* **43** (2002) 2661
9. B. Xue, K. Jia, J. Xu, N. Liu, P. Liu, C. Xu, Y. Li, *React. Kinet., Mech. Catal.* **107** (2012) 435
10. L. Ronchin, A. Vavasori, L. Toniolo, *J. Mol. Catal. A: Chem.* **355** (2012) 134
11. R. Bal, K. Chaudhari, S. Sivasanker, *Catal. Lett.* **70** (2000) 75
12. A. B. Tapase, V. S. Suryawanshi, N. D. Shinde, B. D. Shinde, *Bull. Environ. Pharmacol. Life Sci.* **1** (2012) 30
13. D. H. More, D. G. Hundiwale, U. R. Kapadi, P. P. Mahulikar, *J. Sci. Ind. Res.* **65** (2006) 817
14. B. Mohtat, H. Djahaniani, R. Khorrami, S. Mashayekhi, I. Yavari, *Synth. Commun.* **41** (2011) 784
15. B. Mohtat, S. Rezazadeh, M. Matinfar, V. Arabzadeh, H. Djahaniani, Z. Hossaini, *Lett. Org. Chem.* **9** (2012) 150
16. R. Ghahremanzadeh, S. Ahadi, M. Sayyafi, A. Bazgir, *Tetrahedron Lett.* **49** (2008) 4479
17. G. Lamoureux, C. Agüero, *Arkivoc* **i** (2009) 251

SUPPLEMENTARY MATERIAL TO

N-Methylimidazole-mediated synthesis of aryl alkyl ethers under microwave irradiation and solvent free conditions

HOORIEH DJAHANIANI[1]*, LAILA AGHADADASHI-ABHARI[2] and BITA MOHTAT[3]

[1]Chemistry Department, Islamic Azad University, East Tehran Branch, Tehran, Iran,
[2]Chemistry Department, East Tehran Branch, Payame Noor University, Tehran, Iran and
[3]Chemistry Department, Islamic Azad University, Karaj Branch, Karaj, Iran

PHYSICAL, ANALYTICAL AND SPECTRAL DATA FOR THE COMPOUNDS **4a**–**k**

*4-Methoxy-2*H-*chromen-2-one (4-methoxycoumarin, **4a**)*. [20280-81-3] Yield: 0.33 g (95 %); pale yellow crystals; m.p.: 121–123 °C [lit.: 123–125 °C[1]]; IR (KBr, cm^{-1}): 1705 (–C=O stretching of –COOR group), 1238 and 1030 (–C–O stretching of –C–O group); ^{1}H-NMR (400 MHz, CDCl$_3$, δ / ppm): 4.02 (3H, *s*, CH$_3$), 5.72 (1H, *s*, vinyl), 7.28–7.35 (2H, *m*, aromatic), 7.57 (1H, *dt*, *J* = 7.2 Hz, *J* = 1.6 Hz, aromatic), 7.84 (1H, *dd*, *J* =6.4 Hz, *J* =1.6 Hz, aromatic); ^{13}C-NMR (100.6 MHz, CDCl$_3$, δ / ppm): 56.4 (OCH$_3$), 90.1 (CH=), 115.6 (CH=), 116.8 (CH=), 123.0 (CH=), 123.9 (CH=), 132.4 (C), 153.3 (C–O), 162.9 (C=O), 166.5 (C–O).

*4-Ethoxy-2*H-*chromen-2-one (4-ethoxycoumarin, **4b**)*. Yield: 0.34 g (90 %); yellow crystals; m.p.: 135–137 °C; IR (KBr, cm^{-1}): 1721 (–C=O stretching of –COOR group), 1238 and 1027 (–C–O stretching of –C–O group); ^{1}H-NMR (400 MHz, CDCl$_3$, δ / ppm): 1.57 (3H, *t*, *J* = 7.2 Hz, CH$_3$), 4.23 (2H, *q*, *J* = 7.2 Hz, OCH$_2$), 5.69 (1H, *s*, vinyl), 7.29–7.35 (2H, *m*, aromatic), 7.57 (1H, *dt*, *J* = = 7.2 Hz, *J* = 1.6 Hz, aromatic), 7.86 (1H, *dd*, *J* = 6.4 Hz, *J* = 1.6 Hz, aromatic); ^{13}C-NMR (100.6 MHz, CDCl$_3$, δ / ppm): 14.1 (CH$_3$), 65.2 (OCH$_2$), 90.4 (CH=), 115.8 (CH=), 116.9 (CH=), 123.1 (CH=), 123.8 (CH=), 132.3 (C), 153.4 (C–O), 163.1 (C = O), 165.7 (C–O).

*7-Methoxy-2*H-*chromen-2-one (7-methoxycoumarin,**4d**)*. [531-59-9] Yield: 0.34 g (98 %), pale yellow crystals; m.p.: 119–121 [lit. 117–121 °C[1]]; IR (KBr, cm^{-1}): 1702 (–C=O stretching of –COOR group), 1230 (–C–O stretching of –C–O group); ^{1}H-NMR (400 MHz, CDCl$_3$, δ / ppm): 3.91 (3H, *s*, OCH$_3$), 6.29 (1H, *d*, *J* = 9.5 Hz, aromatic), 6.85–6.89 (1H, *m*, aromatic), 7.40 (1H, *d*, *J* = 8.5 Hz,

---

*Corresponding author. E-mail: jahanbani.ho@gmail.com

aromatic), 7.67 (1H, *d*, *J* = 9.5 Hz, aromatic); ^{13}C-NMR (100.6 MHz, CDCl$_3$, δ / ppm): 55.8 (OCH$_3$), 101.0 (CH=), 112.6 (C), 112.7 (CH=), 113.2 (CH=), 128.8 (CH=), 143.8 (CH=), 156.0 (C–O), 161.3 (C=O), 163.0 (C–O).

*7-Ethoxy-2*H*-chromen-2-one (7-ethoxycoumarin, 4e)*. [31005-02-4] Yield: 0.36 g (95 %); golden yellow crystals; m.p.: 84–86 °C [lit. 89–90 °C[1]]. IR (KBr, cm^{-1}): 1734 (–C=O stretching of –COOR group), 1231 and 1044 (–C–O, stretching of –C–O group); ^{1}H-NMR (400 MHz, CDCl$_3$, δ / ppm): 1.46 (3H, *t*, *J* = 6.8 Hz, CH$_3$), 4.08 (2H, *q*, *J* = 6.8 Hz, OCH$_2$), 6.24 (1H, *d*, *J* = 9.2 Hz, aromatic), 6.79–6.85 (2H, *m*, aromatic), 7.37 (1H, *d*, *J* = 8.8 Hz, aromatic), 7.64 (1H, *d*, *J* = 9.6 Hz, aromatic); ^{13}C-NMR (100.6 MHz, CDCl$_3$, δ / ppm): 14.6 (CH$_3$), 64.2 (OCH$_2$), 101.3 (CH=), 112.4 (C), 112.9 (CH=), 112.9 (CH=), 128.7 (CH=), 143.5 (CH=), 155.9 (C–O), 161.3 (C=O), 162.2 (C–O).

4-Methoxyquinoline (4g). [607-31-8] Yield: 0.27 g (85 %); dark yellow oil; IR (KBr, cm^{-1}): 1273 and 1073 (–C–O, stretching of –C–O group), 1618–1506 (C=C, stretching of –C=C aromatic group); ^{1}H-NMR (400 MHz, CDCl$_3$, δ / ppm): 4.09 (3H, *s*, OCH$_3$), 6.79 (1H, *d*, *J* = 5.6 Hz, aromatic), 7.55 (1H, *dt*, *J* = 6.8 Hz, *J* = 0.8 Hz, aromatic), 7.74 (1H, *dd*, *J* = 7.2 Hz, *J* = 1.6 Hz, aromatic). 8.1 (1H, *d*, *J* = 8.4 Hz, aromatic), 8.24 (1H, *dd*, *J* = 8.4 Hz, *J* = 1.2 Hz, aromatic), 8.80 (1H, *d*, *J* = 5.2 Hz, aromatic); ^{13}C-NMR (100.6 MHz, CDCl$_3$, δ / ppm): 55.8 (OCH$_3$), 100.1 (CH=), 121.4 (CH=), 121.9 (CH=), 125.9 (CH=), 128.4 (C), 130.1 (CH=), 148.5 (C), 151.0 (CN), 162.7 (C–O).

6-Methoxyquinoline (4h). [5263-87-6] Yield: 0.27 g (85 %); brown oil; m.p.: [lit. 18–20 °C[1]]; IR (KBr, cm^{-1}): 1247 and 1037 (–C–O, stretching of –C–O group), 1600–1500 (C=C, stretching of –C=C aromatic group); ^{1}H-NMR (400 MHz, CDCl$_3$, δ / ppm): 3.92 (3H, *s*, OCH$_3$), 7.12 (1H, *d*, *J* = 2.8 Hz, aromatic), 7.41–7.44 (2H, *m*, aromatic), 8.08–8.15 (2H, *m*, aromatic), 8.8 (1H, *d*, *J* = 3.2 Hz, aromatic); ^{13}C-NMR (100.6 MHz, CDCl$_3$, δ / ppm): 55.6 (OCH$_3$), 105.1 (CH=), 121.4 (CH=), 121.7 (CH=), 122.8 (CH=), 129.5 (C), 130.3 (CH=), 135.5 (CH=), 147.3 (C–N), 158.0 (C–O).

8-Methoxyquinoline (4i). [938-33-0] Yield: 0.3 g (95 %); dark brown oil; IR (KBr, cm^{-1}): 1258 and 1076 (–C–O, stretching of –C–O group), 1600–1500 (C=C, stretching of –C=C aromatic group); ^{1}H-NMR (400 MHz, CDCl$_3$, δ / ppm): 4.1 (3H, *s*, OCH$_3$), 7.04 (1H, *d*, *J* = 7.6 Hz, aromatic), 7.30–7.46 (3H, *m*, aromatic), 8.11 (1H, *dd*, *J* = 8.3 Hz, *J* = 1.6 Hz, aromatic), 8.92 (1H, *dd*, *J* = 4.2 Hz, *J* = 1.6 Hz, aromatic); ^{13}C-NMR (100.6 MHz, CDCl$_3$, δ / ppm): 56.1 (OCH$_3$), 108.0 (CH=), 119.9 (CH=), 122.1 (CH=), 127.1 (C), 129.7 (CH=), 136.4 (CH=), 140.4 (C), 149.5 (N–C), 155.7 (C–O).

2-Methoxynaphthalene (4k). [93-04-9] Yield: 0.28 g (90 %); gray solid; m.p.: 70–72 °C [lit. 70–73 °C[1]]; IR (KBr, cm^{-1}): 1256 and 1027 (–C–O, stretching of –C–O group), 1593–1506 (C=C, stretching of –C=C aromatic group); ^{1}H-NMR (400 MHz, CDCl$_3$, δ / ppm): 3.96 (3H, *s*, OCH$_3$), 7.17 (1H, *s*,

aromatic), 7.19 (1H, *d*, *J* = 2.4 Hz, aromatic), 7.38–7.47 (2H, *m*, aromatic), 7.76––7.81 (3H, *m*, aromatic); ^{13}C-NMR (100.6 MHz, CDCl$_3$, δ / ppm): 55.3 (OCH$_3$), 105.7 (CH=), 118.7 (CH=), 123.6 (CH=), 126.4 (CH=), 126.7 (CH=), 127.7 (CH=), 129.0 (C), 129.4 (CH=), 134.5 (C), 157.6 (C–O).

REFERENCES

1. LookChem®, Look for Chemicals, www.lookchem.com and www.chemicalbook.com (accessed in Apr, 2015).

Chemical constituents of the essential oils of *Tephrosia purpurea* and *Ipomoea carnea* and their repellent activity against *Odoiporus longicollis*

KITHERIAN SAHAYARAJ[1]*, POOLPANDI KOMBIAH[1], ANAND K. DIKSHIT[2]** and J. MARTIN RATHI[3]***

[1]*Crop Protection Research Centre, St. Xavier's College (Autonomous), Palayamkottai – 627 002, Tamil Nadu, India,* [2]*Division of Agrochemicals, Indian Agricultural Research Institute, New Delhi - 110 012, India and* [3]*Department of Chemistry, St. Mary's College, Thoothukudi – 628 002, Tamil Nadu, India*

Abstract: The chemical constituents of the essential oils (EOs) obtained from stem and root of *Tephrosia purpurea* (L.) Pers. and *Ipomoea carnea* Jacq. were investigated by gas chromatography–mass spectrometry (GC–MS). The total contents of lipid and oil were higher in the stem than in the root of *T. purpurea* and *I. carnea.* The essential oils extracted from the stem and root of *T. purpurea* and *I. carnea* contained 9 and 8 compounds, respectively. Hexadecanoic acid was found to be the principal constituent of stem (69.61 %) and root (46.97 %) of *T. purpurea* and of the stem (70.61 %) and root (88.89 %) of *I. carnea*. The findings of the present study suggest that the EOs of *T. purpurea* and *I. carnea* could be a source of hexadecanoic acid that could be used for industrial purposes. The essential oils of *T. purpurea* and *I. carnea* showed stronger repellent activity for males (–0.73 and –0.70 for *T. purpurea* and *I. carnea* stem EO, respectively) than for females (–0.63 and –0.59 for *T. purpurea* and *I. carnea* stem EO, respectively) of the banana pseudostem weevil *Odoiporus longicollis.* The results indicated that the active compounds of essential oils from stems of *T. purpurea* and *I. carnea* could be explored as natural repellents for the control of *Odoiporus longicollis.*

Keywords: *Tephrosia purpurea*; *Ipomoea carnea*; essential oils; hexadecanoic acid; repellent activity.

INTRODUCTION

Essential oils are complex mixtures of volatile compounds characterized by a strong odor, and are utilized in pest control measures. *Tephrosia purpurea* (Linn.) Pers (Fabaceae) is a copiously branched, herbaceous, perennial and medi-

---

465

cinally important plant.[1] It possesses antitumor[2] antiplasmodial[3] and anti-diabetic[4,5] activities. *T. purpurea* extracts showed insecticidal activity against houseflies, mosquitoes, rice weevil and flour beetle[6] *Myzus persicae* adults, third instar larvae of *Pluttella xylostella*[7] and adults of *Dysdercus cingulatus* (Fab.).[8] Phytochemical investigations of *T. purpurea* indicated the presence of terpurinflavone,[3] semiglabrin, pongamol, lanceolatins A and B, rutin, lupeol, and *β*-sitosterol. Flavonoids including (+)-tephrorin A and B, (+)-tephrosone; 7,4′--dihydroxy-3′,5′-dimethoxyisoflavone (isoflavone) and a chalcone, (+)-tephropurpurin,[9] tephroglabrin, tepurindiol,[10] apollinine, tephropurpulin A[11] and isoglabratephrin[12] were reported to be present.

Ipomoea carnea Jacq. (Convolvulaceae) is a common weed as well as a toxic plant found abundantly in India, Brazil, USA, *etc*.[13] Different extracts of *I. carnea* possess antibacterial, antifungal, anti-oxidant, anticancer, anticonvulsant, immunomodulatory, hepatoprotective, anti-inflammatory, anxiolytic, sedative, wound healing[14,15] and skin disease healing activities.[16] This weed also has depressant,[17] HIV type 1 reverse transcriptase inhibitory[18] and antidiabetic activities.[19] The toxic principles of this plant include calystegines B2, C1, swainsonine[20] 2-epi-lentiginosine, calystegines B1, B2, B3, C1, and *N*-methyl-*trans*-4--hydroxy-L-proline,[21] whereas non-toxic principles, such as chitinase, were recorded.[13,22] Various solvent extracts of *Ipomoea carnea* had ovicidal activity against the gelechiid *Phthorimaea operculella*[23] and insecticidal activity on *Achaea janata*.[24]

Odoiporus longicollis (Oliv.) (Insecta: Coleoptera: Curculionidae) or banana stem weevil (BSW) is one of the most widely spread and serious monophagous pests of banana. It has been estimated that the BSW causes 10–90 % yield losses depending on the infestation stage and management efficiency. Control of the BSW relies heavily on the use of synthetic insecticides, which has led to several adverse effects on the environment, induced insect resistance and toxicity to non-target species.[25] Hence, botanical insecticides, such as neem azal,[25] azadirachtin[26] and Gin–Dulaw–Luya[27] (a combination of ginger, turmeric and gin) were tested for their efficacy against this weevil to develop an alternative control method that is safe for the environment and highly efficient for the management of *O. longicollis.*

The essential oils of these plants, with ovicidal, larvicidal, repellent, deterrent, antifeedant and toxic effects against a wide range of insects have the potential for use in crop protection.[28–31] There are no reports on the chemical constituents and repellent properties of *T. purpurea* and *I. carnea* essential oils. This paper presents the first report on the essential oils of these plants and their chemical composition as well as repellent activity against *O. longicollis* adults.

MATERIALS AND METHODS

Plant materials

Root and stem of *T. purpurea* and *I. carnea* were collected from in and around Palayamkottai (8.7166° N and 77.7333° E). The plant materials were identified by the Department of Plant Biology and Plant Biotechnology, St. Xavier's College (Autonomous), Palayamkottai. Voucher specimens were deposited with the Crop Protection Research Centre, St. Xavier's College, Palayamkottai (herbarium specimen number: CPRC TP-006 and CPRC TP-007 for *T. purpurea* and *I. carnea* respectively). Immediately after collection, the stem and root portions were separated and air-dried for two weeks under laboratory conditions at 28±2 °C and 60±10 % RH at an 8L:16D photoperiod. The dried materials were partially ground using a domestic blender (Preethi model 7540; Preethi Kitchen Appliances Pvt. Ltd., Chennai) and transferred into each of four plastic jars of 1 L capacity, and stored at room temperature for further studies.

Extraction of essential oil

The essential oils were obtained by steam distillation from the air-dried stem and root samples (100 g each) of *T. purpurea* and *I. carnea* using a Clevenger apparatus for 6 h. The volatile distillate was collected. The distillate was saturated with sodium chloride solution and added to 0.5–1.0 mL diethyl ether. Then, the ether layer and aqueous layer were separated and the organic layer was dried over anhydrous sodium sulfate to remove the moisture and the ether was distilled off over a water bath maintained at 50 °C. The remainder, *i.e.*, oils, were dried over anhydrous sodium sulfate, weighed and stored at 5 °C for further analysis.

Gas Chromatography–Mass Spectrometry (GC–MS) analyses

Essential oils of *T. purpurea* and *I. carnea* were subjected to gas chromatography (Hewlett-Packard gas chromatography model 5890) equipped with megabore column (10 m×0.53 mm i.d., fused silica) packed with OV-1 and a nitrogen phosphorous detector (NPD). The temperature program used for the analysis was as follows: initial temperature at 80 °C, held for 2 min, increased to 120 °C at 28 °C min^{-1}, held isothermal at 120 °C for 1 min, increase to 200 °C at 58 °C min^{-1}, and held isothermal at 200 °C for 2 min; injection temperature, 220 °C; detector temperature, 250 °C; and nitrogen (1.0 mL min^{-1}) was the carrier gas. The samples (0.1 % in absolute ethanol) were injected into the GC by split mode with a split ratio of 1/20. Methyl salicylate was used as an internal standard. The percentages of the constituents were calculated by electronic integration of FID peak areas without response factor correction. GC–MS analyses were performed using JEOL JMS-D300 mass spectrophotometer at 70 eV using electron impact ionization with the source at ambient temperature. The conditions were same as those described above. Injector temperature, 250 °C; split flow, 50 mL min^{-1}; carrier gas, He (1.0 mL min^{-1}). Diluted sample (1.0 mL, 1:10 in Et$_2$O) was injected manually. MS: at 70 eV; mass range 35–425 amu; ion source temperature, 200 °C; interface temperature, 250 °C. The chemical constituents were identified based on the comparison of their mass spectral pattern and retention indices with those obtained from the Wiley 138.L, NBS 75K.L, and SDBS libraries, as well as those published by Adams.[32] The retention indices (*RI*) were calculated according to the literature.[33]

Estimation of percentage of essential oil

Five gram coarsely powdered *T. purpurea* and *I. carnea* stem and root were extracted with petroleum ether in a Soxhlet apparatus for about 1 h. The thimble containing unextracted

portion was taken out, dried and weighed. The percentage of oil present in the material was calculated.[34]

Extraction and estimation of total lipids

One gram of partially powdered plant material was mixed with 10 mL mixture of diethyl ether and ethanol (3:1) in a mortar and centrifuged at 2000 rpm for 10 min. The supernatant was transferred into a separating funnel and 2 mL of 0.05 M potassium chloride solution added. The mixture was allowed to stand until two layers separated. The lipids were present in organic layer. The salt prevented any emulsion formation.[34]

Insect rearing

O. longicollis adults (Fig. 1) were obtained from a colony maintained in the Crop Protection Research Centre, St. Xavier's College (Autonomous), Palayamkottai, Tamil Nadu, India. The insects were reared on fresh banana pseudostem. Cultures were maintained in the dark at 28±1 °C and 70±5 % relative humidity.

Fig. 1. Banana pseudostem weevil *Odoiporus longicollis* adult.

Repellent activity bioassay

Bioassays were conducted according to the method of Sahayaraj and Kombiah.[35] A Whatman number 1 paper strip of 1.5 cm×1.5 cm was selected for the determination of the repellent activity. A Y-shaped olfactometer[35] was used to conduct two-choice bioassays. A piece of paper soaked in 1 mL of essential oil was placed in the experimental arm, whereas the control arm contained a piece of paper soaked in the same amount of solvent, diethyl ether and ethanol in 3:1 ratio (negative control) only. Three one-week old adult male beetles were introduced into the non-reacting base arm of the olfactometer. The numbers of insects in each arm were counted after 30, 60, 90, 120, 150 and 180 min. The insects chose either the test chamber or control chamber or neither. Insects that moved towards the solvent showed attractant phenomena while those moving towards the EOs showed a repellency effect. If the insect chose neither of the chambers, then it was considered that the insect made no choice. The experiment was replicated six times with different insects of the same age group. A similar protocol was followed for one-week old adult female beetles.

Statistical analysis

The weevils preferred either fresh EOs, solvent or neither. Weevil choosing the EOs was considered as attractant. If the weevil chose neither of the chambers then it was considered that weevil made no choice. From the recorded observations, the Access Proportion Index (*API*) was calculated using the formula:[35]

$$API = NS–NC/NS+NC$$

where NS = number of insects choosing the sample (EO) side and NC = number of insects choosing the control (solvent) side.

The approaching behavior of the insect between EOs and solvent was subjected to the χ^2 test and the significance was expressed at 5 % level using MS-Excel 2007. The same package was used to analyze the approaching data of male and female beetles.

RESULTS AND DISCUSSION

Total lipid and oil contents

More total lipid (4.8 mL g^{-1} dry weight stem) and content of oil (12.53 mL g^{-1} dry weight stem) was found in the stem of *T. purpurea* than in root (4.0 mL g^{-1} dry weight root and 8.0 % for total lipid and oil, respectively). Similarly, a higher oil (13.75 % oil) and total lipid content (4.5 mL g^{-1} dry weight stem) was observed in the stem of *I. carnea* than in the root (4.0 ml g^{-1} dry weight root and 5.75 % of total lipid and oil, respectively). However, *I. carnea* yielded only 0.15 to 0.2 % of oil by the steam distillation method.[36] In general, the total lipid content as well as biosynthesis of essential oil was higher in the stem than in the root of flowering plants, depending on the metabolic state and preset developmental differentiation program of the synthesizing tissue.[37]

Chemical composition of essential oil

The steam-distillation of *T. purpurea* and *I. carnea* stem and root yielded yellowish and slightly viscous essential oils. The EOs of *T. purpurea* and *I. carnea* showed distinct unpleasant odors. This might be due to the presence of caryophyllene, geraniol, linalool, eugenol,[38] linalool, methyl chavicol, 1,8-cineole, α-pinene, β-pinene, myrcene, ocimene, terpinolene, camphor, terpinen-4-ol, α-terpineol, eugenol and sesquiterpenes.[39]

In all, 9 and 10 compounds were identified by gas chromatography and mass spectrometry data in the essential oils of stem and root of *T. purpurea* and *I. carnea*, respectively (Tables I and II). Of these, three volatile compounds were

TABLE I. Chemical constituents of the essential oils from *T. purpurea* stem and root analyzed by GC–MS; *RT*: retention time relative to *n*-alkanes (C_6–C_{24}) on an RTX-5 MS column

Plant part	Compound name	Molecular formula	*RT* / min	Content, %
Stem	β-Caryophyllene oxide	$C_{15}H_{24}O$	21.69	3.53
	Bulnesol	$C_{15}H_{26}O$	22.10	3.30
	Tetradecanoic acid	$C_{14}H_{28}O_2$	22.32	2.48
	Caryophyllene oxide	$C_{15}H_{24}O$	22.69	10.03
	Hexadecanoic acid	$C_{16}H_{32}O_2$	25.62	69.61
	Linoleic Acid	$C_{18}H_{32}O_2$	27.29	11.05
Root	Isolongifolan-8-ol	$C_{15}H_{24}$	20.45	5.74
	Epiglobulol	$C_{15}H_{26}O$	20.98	12.66
	Azulene	$C_{10}H_8$	22.10	10.28
	Bulnesol	$C_{15}H_{26}O$	22.85	16.82
	Hexadecanoic acid	$C_{16}H_{32}O_2$	25.63	46.97
	Linoleic acid	$C_{18}H_{32}O_2$	27.29	7.52

common in both the stem and root of the plants. However, *Tephrosia egregia* Sandw. stem oil consisted of 10 volatile compounds.[40] The essential oils mainly contained hexadecanoic acid with *α*-pinene, *γ*-terpinene, *β*-pinene, isoamyl bromide, *p*-cymene, limonene and geraniol being minor components.

TABLE II. Chemical constituents of the essential oils from *I. carnea* stem and root analyzed by GC–MS; *RT*: retention time relative to *n*-alkanes (C_6–C_{24}) on an RTX-5 MS column

Plant part	Compound name	Molecular formula	*RT* / min	Content, %
Stem	2-(12-Pentadecynyloxy)tetrahydro-2*H*-pyran	$C_{20}H_{36}O_2$	23.82	2.84
	1-Octadecanol	$C_{18}H_{32}O$	26.82	3.22
	Hexadecanoic acid	$C_{16}H_{32}O_2$	25.64	70.61
	Epiglobulol	$C_{15}H_{26}O$	22.52	4.35
	Squalene	$C_{30}H_{50}$	28.16	3.00
	1-Octadecanol	$C_{18}H_{38}O$	27.29	15.99
Root	2-Ethyl-1,3-dimethylbenzene	$C_{10}H_{14}$	10.11	1.52
	2-(12-Pentadecynyloxy)tetrahydro-2*H*-pyran	$C_{20}H_{36}O_2$	23.82	1.70
	3-Furanyl[2-hydroxy-4-methyl-2--(2-methylpropyl)cyclopentyl]-methanone	$C_{15}H_{22}O_3$	24.47	1.68
	2,2-Dideuterooctadecanal	$C_{18}H_{36}O$	24.80	2.46
	Hexadecanoic acid	$C_{16}H_{32}O_2$	25.64	88.89
	Linoleic acid	$C_{18}H_{32}O_2$	27.28	3.76

To the best of our knowledge, this is the first report regarding the presence of the chemical constituents in the oils of stem and root of *T. purpurea* and *I. carnea.* Six compounds each were identified in stem and root of *T. purpurea.* Hexadecanoic acid was the main compound of the stem (69.61 %) and root (46.97 %) of *T. purpurea.* Other common components in the oil of *T. purpurea* were linoleic acid, bulnesol and epiglobulol. Similarly, in *I. carnea*, the fatty acid (hexadecanoic acid) was found to be the principal and common constituent of the root (88.89 %) and stem (70.61 %) oils. Other minor chemical components in the oil of *I. carnea* were epiglobulol, 1-octadecanol, squalene and 2-(12-pentadecynyloxy)-tetrahydro-2*H*-pyran in the stem and linoleic acid, 2,2-dideuterooctadecanal, 2-(12-pentadecynyloxy)-tetrahydro-2*H*-pyran, 3-furanyl[2-hydroxy-4--methyl-2-(2-methylpropyl)-cyclopentyl]methanone and 2-ethyl-1,3-dimethylbenzene in the root. Chemo-profiling of these oils showed differences in the composition among the studied species although volatile constituents were previously reported in other species of the *Tephrosia* genus.[40,41] Caryophyllene oxide was the major component (63.9 %) of leaves of *T. cinerea* Pers,[41] whereas the major components of the stem oil of *T. egregia* Sandw. were geijerene and pregeijerene.[40] *T. vogelii* Hook f. seed consisted more hexadecanoic acid (pal-

mitic acid, 18.70 %) along with tetradecanoic acid, pentadecanoic acid, heptade-canoic acid, stearic acid, oleic acid, linoleic acid, linolenic acid, eicosanoic acid, heneicosanoic acid, docosanoic acid, tricosanoic acid and tetracosanoic acid.[42]

Repellent activity

T. purpurea stem oil showed pronounced repellency (overall mean *API =* = –0.73) (*df*[1], *p* = 3.94, *p* < 0.005) of *O. longicollis* adults followed by *I. carnea* stem oil (overall mean *API* = –0.70) (*df*[1], *p* = 3.86, *p* < 0.05, Table III). Invariably, the tested oils deterred the male adults of *O. longicollis* more than the female adults (*t* = 1.743; *p* < 0.05). Similarly, both neem oil and pongamia oil showed strong repellent effects on *O. longicollis*.[43] The results showed that repellent activity of the oil might be due to the presence of hexadecanoic acid or the mixture of this with the other chemical constituents of the EOs that are toxic to the insect and are present in the oil. The principal compound, hexadecanoic acid possesses a variety of biological activities including insecticidal activity.[44–46]

TABLE III. Repellent activity of *T. purpurea* and *I. carnea* oils on pseudostem weevil *Odoiporus longicollis*; *t* test performed between male and female of the same category; the same letter means insignificant at the 5 % level

Plant	Part Used	Insect sex	Time after the introduction of insect, min						Mean repellence
			30	60	90	120	150	180	
T. purpurea	Stem	Male	–0.64[b]	–0.69[b]	–0.75[b]	–0.79[b]	–0.80[b]	–0.86[b]	–0.73[b]
		Female	–0.52[a]	–0.63[a]	–0.67[a]	–0.67[a]	–0.70[a]	–0.72[a]	–0.63[a]
	Root	Male	–0.16[b]	–0.33[b]	–0.50[a]	–0.62[b]	–0.63[b]	–1.0[b]	–0.33[b]
		Female	–0.09[a]	–0.15[a]	–0.20[a]	–0.27[a]	–0.57[a]	–0.76[a]	–0.38[a]
I. carnea	Stem	Male	–0.33[b]	–0.55[b]	–0.67[b]	–0.78[b]	–0.81[b]	–1.0[b]	–0.70[b]
		Female	–0.14[a]	–0.37[a]	–0.55[a]	–0.75[a]	–0.80[a]	–0.89[a]	–0.59[a]
	Root	Male	–0.28[b]	–0.40[b]	–0.53[b]	–0.77[a]	–0.91[b]	–1.0[b]	–0.69[b]
		Female	–0.25[a]	–0.30[a]	–0.33[a]	–0.74[a]	–0.80[a]	–0.82[a]	–0.56[a]

To the best of our knowledge, this is the first report on the repellent action of the essential oils from the root and stem of these plants against any pests, particularly *O. longicollis*. Furthermore, this fatty acid should be separated during bio-oil production and utilized as a source of an effective insect repellent compound. The essential oils of the stem (70 %) and root (89 %) of *T. purpurea* and *I. carnea* contained high levels of hexadecanoic acid, which could be utilized as an insect repellent. The development and utilization of this natural pesticide would also help to decrease the negative impact of synthetic chemicals, such as residues, resistance and environmental pollution.

И З В О Д

ХЕМИЈСКИ САСТАВ ЕТАРСКИХ УЉА *Tephrosia purpurea* И *Ipomoea carnea* И ЊИХОВА РЕПЕЛЕНТНА АКТИВНОСТ СПРАМ ЖИШКА *Odoiporus longicollis*

KITHERIAN SAHAYARAJ[1], POOLPANDI KOMBIAH[1], ANAND K. DIKSHIT[2] и J. MARTIN RATHI[3]

[1]*Crop Protection Research Centre, St. Xavier's College (autonomous), Palayamkottai – 627 002, Tamil Nadu, India,* [2]*Division of Agrochemicals, Indian Agricultural Research Institute, New Delhi - 110 012, India u* [3]*Department of Chemistry, St. Mary's College, Thoothukudi – 628 002, Tamil Nadu, India*

Хемијски састав етарских уља добијених из стабла и корена биљака *Tephrosia purpurea* (Linn.) Pers. и *Ipomoea carnea* Jacq. је анализиран гасно–масеном спектрометријом (GC–MS). Укупни удео липида и уља је био висок у свим узорцима. Етарско уље из стабла и корена *T. purpurea* је садржало 9 састојака, а из *I. carnea* 8. Хексадеканска киселина је била главни састојак у свим узорцима: у стаблу и корену *T. purpurea* је чинила 69,61 и 46,97 %, а код *T. purpurea* 70,61, односно 88,89 %. Налази ове студије указују да би се етарска уља *T. purpurea* и *I. carnea* могла користити као извор хексадеканске киселине за индустријске сврхе. Етарска уља су испољила јачу репелентну активност спрам мужјака (−0,73 и −0,70, уља из стабала *T. purpurea* и *I. carnea*) него женки (−0,63 и −0,59) жишка банане, *Odoiporus longicollis.* Резултати су показали да активни састојци етарских уља стабла *T. purpurea* и *I. carnea* могу наћи примену као природни репеленти за контролу жишка *O. longicollis.*

REFERENCES

1. A. Khatri, A. Garg, S. Shyam, S, Agarwal, *J. Ethnopharmacol*. **122** (2009) 1
2. L. C. Chang, D. Chavez, L. L. Song, N. R. Farnsworth, J. M. Pezzuto, A. D. Kinghorn, *Org. Lett*. **2** (2000) 515
3. W. P. Juma, H. M. Akala, F. L. Eyase, L. M. Muiva, M. Heydenreich, F. A. Okalebo, P. M. Gitu, M. G. Peter, D. S. Walsh, M. Imbuga, *Phytochem. Lett*. **4** (2011) 176
4. L. E. A. Hassan, M. B. K. Ahamed, A. S. A. Majid, M. A. Iqbal, F. S. R. Al Suede, R. A. Haque, A. M. S. A. Majid, *PloS One* **9** (2014) e90806
5. P. Vijayakumar, V. Thirumurugan, K. Bharathi, S. Surya, M. Kavitha, G. Muruganandam, M. Sethuraman, *Int. J. Pharm. Sci. Rev. Res.* **24** (2014) 46
6. B. N. Saxena, D. N. Dubey, A. L. Nair, *Defence Sci. J.* **24** (1994) 43
7. Y. Z. Li, G. H. Li, X. Y. Wei, Z. H. Liu, H. H. Xu, *Acta Entomol. Sin.* **54** (2011) 1368
8. K. Sahayaraj, J. Shoba, *Asian J. Biochem.* **7** (2012) 112
9. P. Satadru, B. Kr-Dey, N. K. Singh, *Chin. J. Nat. Med.* **12** (2014) 1
10. A. Pelter, R. S. Ward, E. V. Rao, N. R. J. Raju, *J. Chem. Soc., Perkin Trans.* **9** (1981) 2491
11. A. K. Khalafallah, S. A. Suleiman, A. H. Yousef, N. A. A. El-Kanzi, A. E. H. H. Mohamed, *Chin. Chem. Lett*. **20** (2009) 1465
12. M. E. F. Hegazy, M. H. Abd El-Razek, F. Nagashima, Y. Asakawa, P. W. Pare, *Phytochemistry* **70** (2009) 1474
13. A. K. Patel, V. K. Singh, R. P. Yadav, A. J. G. Moir, V. Medicherla, A. Jagannatham, *Phytochemistry* **70** (2009) 1210
14. E. Khatiwora, V. B. Adsul, M. M. Kulkarni, N. R. Deshpande, R. V. Kashalkar, *Int. J ChemTech Res*. **2** (2010) 1698
15. N. Fatima, M. M. Rahman, M. Khan, J. Fu, *J. Complement. Integr. Med.* **11** (2014) 55
16. R. Jain, N. Jain, S. Jain, *S. Asian J. Pharm. Clin. Res.* **2** (2009) 64

17. S. K. Bhattacharya, A. Ray, B. Dasgupta, *Indian J. Pharmacol.* **7** (1975) 31
18. W. Woradulayapinij, N. Soonthornchareonnon, C. J. Wiwat, *Ethnopharmacology* **101** (2005) 84
19. T. Y. Khan, R. Raina, P. K. Verma, M. Sultana, M. K. Jyoti, *J. Exp. Integr. Med.* **4** (2014) 137
20. K. I. M. De Balogh Katinka, A. P. Dimande, J. J. Van der Lugt, R. J. Molyneux, T. W. Naude, W. G. Welman, *J. Vet. Diagn. Invest.* **11** (1999) 266
21. M. Haraguchi, S. L. Gorniak, K. Ikeda, Y. Minami, A. Kato, A. A. Watson, *J. Agric. Food Chem.* **51** (2003) 4995
22. A. K. Patel, V. K. Singh, R. P. Yadav, A. J. G. Moir, M. V. Jagannadham, *Process. Biochem.* **45** (2010) 675
23. S. S. Shelke, L. D. Jakhav, G. N. Salunkhe, *Biovigyanam* **13** (1987) 40
24. K. Sahayaraj, P. Selvaraj, G. Raju, *J. Appl. Zool. Res.* **14** (2003) 48
25. P. Sivasubramanian, Z. Kavitharaghavan, S. Jaya Prabhavathi, K. Samiayyan, *Karnataka J. Agric. Sci.* **22** (2010) 561
26. S. Irulandi, A. Aiyanathan, K. Eraivan, B. Bhuvaneswari, S. Srivara, *J. Biopestic.* **5** (2012) 68
27. C. H. Aguilar, F. Lasalita-Zapico, J. Namocatcat, A. Fortich, R. M. Bojadores, *Int. Proc. Chem. Biol. Environ. Eng.* **63** (2014) 22
28. C. Regnault-Roger, *Integrated Pest Manag. Rev.* **2** (1997) 25
29. M. B. Isman, *Crop Prot.* **19** (2000) 603
30. C. Regnault-Roger, in *Natural Products*, K. G. Ramawat, J. M. Mérillon, Eds., Springer, Berlin, 2013, p. 4087
31. G. C. Shah, G. Pawar, N. Singh, *Res. J. Agric. Environ. Manag.* **3** (2014) 076
32. R. P. Adams, *Identification of essential oils components by gas chromatography/mass spectrometry*, Allured Publisher, Academic Press, San Diego, CA, 1995
33. H. Van den Dool, P. D. Kratz. *J. Chromatogr., A* **11** (1963) 463
34. A. Buzarbarua, *A text book of practical plant chemistry*, S. Chand & Co. Ltd., New Delhi, 2009, p. 76
35. K. Sahayaraj, P. Kombiah, *J. Biopest.* **2** (2009)173
36. T. G. Thomas, S. Rao, S. Lal, *Jpn. J. Infect. Dis.* **57** (2004) 176
37. N. S. Sangwan, A. H. A. Farooqi, F. Shabih, R. S. Sangwan, *Plant Growth Regul.* **34** (2001) 3
38. G. T. Eyres, P. J. Marriott, J. P. Dufour, *J. Agric. Food Chem.* **55** (2007) 6252
39. J. E. Simon, D. Reiss-Bubenheim. *Herb Spice Med. Plant Dig.* **6** (1987) 1
40. A. M. Arriaga, F. E. Magalhães, E. M. Feitosa, G. T. Malcher, M. Andrade-Neto, R. F. Nascimento, *J. Essential Oil Res.* **17** (2005) 451
41. A. M. C. Arriaga, G. T. Malcher, J. O. Lima, F. E. Magalhães, T. M. Gomes, M. Da Conceição, G. M. P. Santiago, *J. Essent. Oil Res.* **20** (2008) 450
42. X. Yu, Z. Yan, X. Li, X. Huang, X. Zeng, *Acta Sci. Nat. Univ. Sunyatseni* **1** (2009) 11 (in Chinese, ISSN 0529-6579)
43. B. Bhagawati, M. K. Deka, P. Patgiri, *Ann. Plant Prot. Sci.* **17** (2009) 366
44. R. S. Satyan, S. Malarvannan, P. Eganathan, S. Rajalakshmi, A. Parida, *J. Econ. Entomol.* **102** (2009) 1197
45. P. Prveen Kumar, S. Kumaravel, C. Lalitha. *Afr. J. Biochem. Res.* **4** (2010) 191
46. S. Liu, L. A. Caceres, K. Schiek, C. Booker, B. M. McGarvey, K. Yeung, I. M. Scott, *J. Agric. Food Chem.* **62** (2014) 3610.

Allelopathic effects and insecticidal activity of aqueous extracts of *Satureja montana* L.

JOVANA ŠUĆUR[1]*, ALEKSANDRA POPOVIĆ[1], MILOŠ PETROVIĆ[1], GORAN ANAČKOV[2], VOJISLAVA BURSIĆ[1], BILJANA KIPROVSKI[1] and DEJAN PRVULOVIĆ[1]

[1]*Faculty of Agriculture, University of Novi Sad, Trg Dositeja Obradovića 8, 21000 Novi Sad, Serbia and* [2]*Faculty of Science, University of Novi Sad, Trg Dositeja Obradovića 3, 21000 Novi Sad, Serbia*

Abstract: Extensive use of synthetic insecticides, herbicides and other pesticides has negative effects on the environment and on human and animal health. Therefore, scientists are turning towards natural pesticides, such as active components of plant extracts. The effect of two concentrations (0.1 and 0.2 %) of a *Satureja montana* L. aqueous extract on the lipid peroxidation process, as well as on the activity of the antioxidant enzymes superoxide dismutase (SOD), guaiacol peroxidase (GPX), pyrogallol peroxidase (PPX) and catalase (CAT) in the leaves and roots of pepper and black nightshade seedlings were examined 24, 72 and 120 h after treatment. The results showed that the higher concentration of *S. montana* aqueous extract induced lipid peroxidation in black nightshade roots. Furthermore, significant increases of pyrogallol and guaiacol peroxidase were detected in black nightshade leaves treated with 0.2 % of the *S. montana* aqueous extract. The second aim was to evaluate effectiveness of the aqueous extract as a contact toxicant against whitefly. It was observed that the 0.2% aqueous extract exhibited a toxic effect with 68.33 % mortality after 96 h.

Keywords: allelochemicals; antioxidants; biopesticides.

INTRODUCTION

The synthetic agrochemicals, such as herbicides, may cause imbalance of soil microorganisms and nutrient deficiency, resulting in decreases in crop productivity. The application of allelochemicals into natural and agricultural practice may reduce the use of herbicides, insecticides, and other pesticides, thereby reducing environmental pollution and diminishing auto-toxicity hazards. Allelochemicals are secondary metabolites of plants and may be present in all plant organs, including leaves, flowers, fruits, roots, rhizomes, stems and seeds.[1,2]

475

Allelochemicals extracted from the roots or shoots of plants were shown to directly inhibit or stimulate growth and development of other plants.[3] Some plant extracts imparted insecticidal effects on adult insects by killing them or inducing complete inhibition of the feeding activity of the insect pests.[4]

One of the effects of allelochemicals on target plants, and one of the important mechanism by which plants are damaged, is the excess production of reactive oxygen species (ROS), such as superoxide anions ($O_2^-\cdot$), and the more reactive hydroxyl ($^\bullet OH$) or hydroperoxyl ($HO_2^\bullet$) radicals.[5,6] These plant–plant allelopathic interactions generates a cascade of signaling events, including Ca^{2+} influx and proton efflux that activates the nicotinamide adenine dinucleotide phosphate (NADPH)-oxidase complex (generating $O_2^{-\bullet}$), and pH-sensible cell wall peroxidases (producing H_2O_2), which initiate an oxidative burst.[7] Enhancement of ROS production during an oxidative burst is one of the earliest reactions elicited in response to various abiotic and biotic stimuli. These molecules are very toxic to cells and their excessive production is accompanied by the activation of the cellular antioxidant system.[6,8,9] Thus, H_2O_2 can act as an intercellular messenger to induce some enzymes, such as superoxide dismutase (SOD), glutathione peroxidase (GSHPx), catalase (CAT), etc.[10] These enzymes play important roles in protecting a cell against the potentially deleterious effects of reactive oxygen species.[11] Within a cell, the superoxide dismutases (SODs) constitute the first line of defense against ROS.[12] Superoxide dismutases (SODs) are metal-containing enzymes that catalyze the dismutation of superoxide free radical anions, converting them to H_2O_2.[13–15] Plants contain several types of enzymes that are able to metabolize hydrogen peroxide. These include catalases and peroxidases. Catalases are highly expressed enzymes, particularly in certain plant cell types, and are thus an integral part of the plant oxidative system.[16] Catalases are peroxisomal enzymes that, in contrast to peroxidases, do not require a reducing substrate for their activity.[5] Catalases are also distinguished from many other peroxide-metabolizing enzymes by their high specificity for H_2O_2, but weak activity against organic peroxides.[16] The cellular level of H_2O_2 could be sufficiently toxic to inhibit the activity of the enzymes, leaving the plant vulnerable to oxidative damage.[10] Some allelochemicals rapidly depolarize the cell membrane, increasing the permeability of the membrane, inducing lipid peroxidation and causing a generalized cellular disruption that ultimately leads to cell death.[17–19]

Satureja montana L., commonly called winter or mountain savory, belongs to the Lamiaceae family and is native to the Mediterranean regions.[20–22] This aromatic herb, found in nature and also cultivated, is a well known medicinal plant that contains various biologically active constituents, such as, essential oil, triterpenes and flavonoids.[22,23] It has been used in traditional medicine for various diseases, such as: asthma and peptic ulcer, as a diarrheic, antipyretic, anti-inflammatory, antibacterial and antiviral medicine and for its insecticidal acti-

vities.[21] An aqueous extract of winter savory had a high antioxidant capacity.[24] Furthermore, aqueous extracts of *Satureja* species had inhibitory effects on the growth of the root, stem, leaf, shoot, germination rate and germination percentage of seeded weeds, *Chenopodium album* and *Portulaca oleracea*.[25]

Due to an increase in the number of herbicide-resistant weeds and environmental concerns in the use of synthetic herbicides, there have been considerable efforts in designing alternative weed management strategies. Extensive use of synthetic insecticides usually has negative effects on the environment and on human and animal health and resistance develops among insects. Therefore, scientists are turning towards natural insect suppressants.[4]

The aim of this study was to examine the effects of aqueous extract of *S. montana* L. on pepper and black nightshade antioxidant activity and to explore the potential of this species in weed control. The second aim was to evaluate the effectiveness of *S. montana* aqueous extract as a contact toxicant against greenhouse whitefly.

EXPERIMENTAL

Plant material and preparation of the aqueous extract

The wild, aromatic plant, *S. montana* was collected at localities near the Adriatic coast in Montenegro, in June, 2012. Voucher specimens of the collected plant were confirmed and deposited at the Herbarium of The Department of Biology and Ecology, Faculty of Science, University of Novi Sad.

The air-dried plant material was ground into powder. The powdery material (10 g) was extracted with 100 mL distilled water. After 24 h, the extract was filtered through filter paper and kept at 4 °C until application.

Determination of total phenolic and flavonoid contents in S. montana *aqueous extract*

The total phenolic content of *S. montana* aqueous extract was determined according to the Folin–Ciocalteu method.[26] Extract (0.02 mL) was mixed with 3.36 mL of deionized water, 0.4 mL of 20 % sodium carbonate and 0.2 mL of 33 % Folin–Ciocalteu reagent. After incubation at room temperature for 30 min, the absorbance of the reaction mixture was measured at 720 nm. The data are expressed as mg gallic acid equivalents g^{-1} dry weight (mg GA equivalents g^{-1} d.w.).

The total flavonoids were estimated according to the method described by Markham.[27] Extract (0.4 mL) was mixed with 1 mL of deionized water and 2.5 mL of 2 % aluminum chloride hexahydrate solution. After incubation at room temperature for 15 min, the absorbance of the reaction mixture was measured at 430 nm. The data are expressed as mg rutin equivalents g^{-1} dry weight (mg rutin equivalents g^{-1} d.w.).

Determination of phenolic compounds in S. montana *aqueous extract*

Chemicals and apparatus. All solvents used were of chromatography grade and were obtained from J. T. Baker (Deventer, The Netherlands). Ferulic acid (99.0 %), *trans*-cinnamic acid (99.0 %), gallic acid (99.9 %), caffeic acid (98.0 %), 2-hydroxycinamic acid (97.0 %), *p*-coumaric acid (98.0 %), chlorogenic acid (95.0 %), quercetin (98.0 %) and kaempferol (97.0 %), all Sigma–Aldrich, were used as analytical standards. The stock standard solutions were prepared by dissolving the required analytical standard in methanol, while the working

solution, *i.e.*, the mixture of the studied phenol compounds, was obtained by mixing and diluting the stock standards with mobile phase, resulting in a final mass concentration of 100 µg mL^{-1}. The composite mixtures of all phenol compounds at appropriate concentrations were used to spike samples in the data validation settings. Acetic acid was of *p.a.* grade (Carl Roth).

HPLC analysis. The chromatographic separation for phenolic compounds was achieved using an Agilent 1100 (Agilent Technologies, USA) HPLC system with a binary pump and diode array detector - DAD. The phenolic acids were separated on a ZORBAX SB-Aq (5 µm particle size: 4.6 mm×250 mm, Agilent) column. The aqueous extract was filtered through 0.45-µm syringe filters and directly injected through a 30 µL fixed loop onto the column.

The mobile phase was acetonitrile with 2.0 % acetic acid (solvent A) and Milli-Q water with 2.0 % acetic acid (solvent B) in gradient mode, at a flow rate of 1.0 mL min^{-1}. The gradient was as follows: 92 % A at 0 min, 80 % A at 18 min, 60 % A at 25 min, 55 % A at 30 min, 35 % A at 40 min and 20 % A at 42 min. Stop time was 2.5 min.

Validation parameters. The repeatability of the method was determined by analyzing a sample of the same mass concentration level (10.0 µg mL^{-1}) in six replicates and shown through the relative standard deviation (*RSD*). The detection limit (*LOD*) was defined as the amount of phenolic compounds that produces a signal three times the noise signal. The limit of quantification (*LOQ*) is the amount of phenolic compounds that produces a signal ten times the noise signal. The *LOD*s were determined by adding 100 µL of the standard mixture of the phenol compounds to a concentration of 1.0 µg mL^{-1} into 0.5 g of the sample in six replicates and the *LOD*s were calculated.

Seedling growth

The pepper (*Capsicum annuum* L.) cultivars Anita and black nightshade (*Solanum nigrum* L.) seeds were grown in a controlled climate chamber at 28 °C, 60 % relative humidity, a photoperiod of 18 h, and a light intensity of 175 µmol m^{-2} s^{-1} in plastic pots containing sterile sand. After 30 days, the seedlings were transplanted into plastic pots containing 700 mL of Hoagland solution prepared according to Hoagland and Arnon,[28] and 7 and 14 mL of *S. montana* aqueous extract, while the pots of the control contained the same volume of Hoagland solution. Seedlings were harvested for further biochemical analyzes 24, 72 and 120 h after the treatments.

Enzyme extraction

Fresh leaves and roots (2 g each) were homogenized in 10 mL of phosphate buffer (0.1 M, pH 7.0). The homogenates were centrifuged for 20 min at 10,000×*g* and filtered. The supernatants were used to test enzyme activity and to determine intensity of lipid peroxidation.

Membrane lipid peroxidation

Lipid peroxidation was measured at 532 nm using the thiobarbituric acid (TBA) test. The enzyme extract (0.5 mL) was incubated with 2 mL of 20 % trichloroacetic acid (TCA) containing 0.5 % thiobarbituric acid for 40 min at 95 °C. The reaction was stopped by cooling on ice for 10 min and the product was centrifuged at 10,000×*g* for 15 min. The total amount of TBA-reactive substances is given as nmol malondialdehyde (MDA) equivalents mg^{-1} protein.[29]

Assay of catalase activity

The catalase (CAT) (EC 1.11.1.6) activity was determined according to Sathya and Bjorn.[30] The decomposition of H$_2$O$_2$ was followed as a decrease in absorbance at 240 nm. The

enzyme extract (0.02 mL extract of leaves or 0.1 mL extract of roots, separately) was added to the assay mixture containing 1 mL for leaves and 1.5 mL for roots of 50 mM potassium phosphate buffer (pH 7.0) and 10 mM H_2O_2. The activity of the enzyme is expressed as U per 1 g of protein (U g^{-1} protein).

Assay of superoxide dismutase activity

Superoxide dismutase (SOD) (EC 1.15.1.1) activity was assayed according to a slightly modified method of Mandal *et al.*[29] by measuring its ability to inhibit photochemical reduction of nitro blue tetrazolium (NBT) chloride. The reaction mixture contained 50 mM phosphate buffer (pH 7.8), 13 mM L-methionine, 75 µM NBT, 0.1 mM EDTA, 2 µM riboflavin and 0.02 mL of the enzyme extract. It was kept under a fluorescent lamp for 30 min, and then the absorbance was read at 560 nm. One unit of the SOD activity is defined as the amount of enzyme required to inhibit the reduction of NBT by 50 %. The activity of the enzyme is expressed as U per 1 mg of protein (U mg^{-1} protein).

Assay of peroxidase activity

Peroxidase (EC 1.11.1.7) activity was measured using guaiacol (guaiacol peroxidase; GPX) and pyrogallol (pyrogallol peroxidase; PPX) as substrates according to Morkunas and Gmerek.[31] The peroxidase activity (GPX and PPX) is expressed as U per 1 mg of protein (U mg^{-1} protein).

Pyrogallol peroxidase activity. This method is based on the measurement of the content of purpurogallin – a product of pyrogallol oxidation. The enzyme extract (0.02 mL) was added to the assay mixture containing 3 mL of 180 mM pyrogallol and 0.02 mL of 2 mM H_2O_2. The absorbance was recorded at 430 nm.

Guaiacol peroxidase activity. This method consists of an assay of tetraguaiacol – a colored product of guaiacol oxidation in the investigated sample. The enzyme extract (0.04 mL) was added to the assay mixture containing 3 mL of 20 µM guaiacol and 0.02 mL of 3 mM H_2O_2. The absorbance was recorded at 436 nm.

Insects

The experiment on the adult of whitefly, *Trialeurodes vaporariorum* (Westwood, 1856) (Hemiptera: Aleyrodidae), collected in a greenhouse, was performed at the Faculty of Agriculture, University of Novi Sad.

Toxicity test

The bioassays were realized using groups of 20 adult insects *T. vaporariorum*, kept in transparent laboratory dishes (25 cm×12 cm), fed on the pepper nursery plants containing a known concentration (0.1 and 0.2 %) of aqueous extract. The aqueous extracts were applied together with adjuvant (Trend) for better adhesion to the leaf surface. Pepper plants with water adjuvant and 20 insects for each dish were used as the controls. The experiment was set up in three replicates and a control. The no-choice method, in which control and treated plants were placed individually in each dish, was adopted in this experiment. The mortality was checked after 24, 48 and 96 h.

Statistical analysis

Values of the biochemical parameters were expressed as means ± standard error (*SE*) of determinations made in triplicates and tested by ANOVA followed by comparison of the means by the Duncan multiple range test ($P < 0.05$). Data were analyzed using Statistica for Windows, version 11.0.

<center>RESULTS AND DISCUSSION</center>

Chemical composition

The total amount of phenols in *S. montana* aqueous extract was 53.96±3.9 mg GA equivalents g^{-1} dry weight. Flavonoids were found in an amount of 0.36±0.01 mg rutin equivalents g^{-1} d.w. According to Tahirović *et al.*[32], the total amount of phenols in *S. montana* herbal tea infusion was 78.5±23.49 mg GA 100 mL^{-1}. On the other hand, Chrpová *et al.*[24], found a lower amount of phenols (27.1 mg GA g^{-1}). The different amounts of the active substances found confirms that the chemical composition of the plants depends on the season in which they were collected, on the geographical area and other factors, such as environmental temperatures prevailing during plant growth.[33,34]

The main constituent of phenol components was caffeic acid (78.17 µg g^{-1}). The second largest component was gallic acid (15.36 µg g^{-1}). Quercetin, *p*-coumaric acid, chlorogenic acid and ferulic acid were represented at concentration of 2.36, 1.59, 1.36 and 0.50 µg g^{-1}, respectively. The HPLC-DAD chromatogram of standard solutions of the phenolic compounds prepared in mobile phase is shown in Fig. S-1 of the Supplementary material to this paper. Some of the validation parameters are given in Table S-I of the Supplementary material. The obtained *LOD* values for all the investigated phenolic compounds were 0.01 µg mL^{-1}, with *LOQ* values of 0.03 µg mL^{-1}.

The chemical composition study of *S. montana* aqueous extract enabled its properties to be understood, pending clarification of this work by a structure–activity relationship study.

Effect of extracts on MDA content and antioxidant enzyme activity in pepper and black nightshade seedlings

The response of plants to damaging adverse circumstances is closely related to their enzyme activity.[35] The obtained results showed a significant increase of peroxidases activities in the roots of black nightshade treated with 0.2 % *S. montana* aqueous extract 24 h after the treatment (Table S-II of the Supplementary material). The higher concentration had the same effect on the activity of CAT after 72 h. In the leaves of black nightshade, the activities of SOD and CAT were significantly increased by the lower concentration (0.1 %) of *S. montana* aqueous extract, while significant increases of the peroxidases activities were observed in plants treated with the higher concentration (0.2 %) 72 and 120 h after the treatment (Table S-III of the Supplementary material). The increases in the activities of SOD, CAT and peroxidases probably occur in response to stress.[35] Significant increases in lipid peroxidation were previously observed in various plant species under oxidative stress.[36] The malondialdehyde (MDA) content, an end-product of the lipid peroxidation process, is used as an oxidant biomarker. It was suggested that different concentrations of allelochemicals induce the production of

MDA; however, due to their antagonistic and synergistic effect, the MDA content is not always in reciprocity with the concentration of these substances.[36,37] In the roots of black nightshade, significant increases in the MDA content were recorded 72 and 120 h after the treatment (Table S-II). Two tested extract concentrations affected lipid peroxidation in the roots of black nightshade in the same way, but the higher level of MDA was observed in the roots treated with the higher concentration (0.2 %). The MDA content increased with the duration of the experiment. An increase in the MDA content indicates a high concentration of ROS that was beyond the threshold of scavenging by the antioxidant enzymes.[35] In spite of the increased activity of the enzymes, there were no significant changes in the LP intensity in the leaves of black nightshade between the plants from the control group and the treatments. This could indicate that the allelopathy-provoked stress was not strong enough and scavenging effects of SOD, CAT and the peroxidases could still prevent an oxidative burst and the induction of LP. The higher production of MDA in the roots of black nightshade compared with the MDA content in leaves showed that the roots were more affected by the allelochemicals than leaves. This may be attributed to the permeability of allelochemicals to root tissues arising from direct contact with the phytotoxic compounds present in the extract.[35] This finding is in agreement with the results of a previous study in which it was found that roots are more sensitive to allelopathic substances than shoots.[38]

In the roots and in the leaves of the pepper, there were no significant increases in the activities of CAT and peroxidases (Tables S-IV and S-V of the Supplementary material). An increase in the activity of SOD was detected after 120 h in plants treated with both concentrations of *S. montana* aqueous extract. In the leaves of pepper, no significant difference was recorded in the LP intensity. A significant increase in LP intensity was recorded 120 h after the treatment only in roots of pepper plants treated with the lower concentration (0.1 %).

The allelopathic effects of *Thymus kotschyanus* were studied on the growth of *Bromus tomentellus* and *Trifolium repens* seedling.[3] The phytotoxic effects of the extracts were found to be different between the two species under study, which points to different sensitivity of species when facing allelochemicals. Research on allelopathy of some plants of the Lamiaceae family on weeds showed that a water extract promoted growth of the test plants at low concentration, but inhibited them at high, and inhibition became stronger with increasing concentration.[39]

Toxicity test

Plant extracts are currently being studied as an ecologically friendly alternative to manage plant pests. Natural products have low mammalian toxicity as well as high target specificity and biodegradability, and contain many active ing-

redients, thus possessing biopesticide activity against multiple pests and pathogens.[40] In the present work, the aqueous extract of *S. montana* was evaluated on greenhouse whitefly. The mortality rate of greenhouse whiteflies after 96 h was above 50 % (Table I). The higher-concentrated *S. montana* aqueous extract (0.2 %) was more effective with a mortality of 68.33 %. The main constituent of the extract was caffeic acid, which was proved to have insecticidal activity.[41,42] According to some authors,[41] the presence of caffeic acid in *Impatiens parviflora* might be the reason for the insecticidal activity of this plant and the mortality of green peach aphid. Caffeic acid is one of the many phenolics considered as important parts of the defense mechanism of plants against microbial infection, insects and other predators.[42] The results of other authors indicate a potential use of aqueous plant extracts in pest management of greenhouse whiteflies.[43]

TABLE I. Mortality (%) of *Trialeurodes vaporariorum* adult fed for 4 days with formulations containing a known concentration (0.1 and 0.2 %) of *Satureja montana* aqueous extracts; a–d: values without the same superscripts within each column differ significantly ($P < 0.001$)

Formulation	Time, h		
	24	48	96
Control	8.33[c]	10.00[c]	16.66[bc]
0.1 %	1.6[d]	8.33[b]	41.66[a,b]
0.2 %	3.33[d]	41.66[a]	68.33[a]

CONCLUSIONS

Extracts from different plant species and their active components are natural sources of biopesticides. This study contributes to an assessment of the potential use of medicinal plants as insecticides. The *S. montana* aqueous extracts were evaluated for their effect on greenhouse whitefly, an important insect pest of many plants, including pepper. It was observed that the aqueous extract with a concentration of 0.2 % showed a toxic effect with a high mortality rate 68.33 % after 96 h. The obtained results showed that use of natural substances could be an alternative method of insect control. This was supported by the results on the antioxidant properties of pepper seedlings. The extract did not exhibit any phytotoxic effect on the pepper or black nightshade seedlings. Therefore, it could be concluded that this plant should be explored in the development of bioinsecticides.

SUPPLEMENTARY MATERIAL

HPLC-DAD analysis and effects of the aqueous extracts of *Satureja montana* on the anti-oxidant enzymes and lipid peroxidation are available electronically from http:////www.shd.org.rs/JSCS/, or from the corresponding author on request.

ИЗВОД

АЛЕЛОПАТСКИ УТИЦАЈ И ИНСЕКТИЦИДНА АКТИВНОСТ ВОДЕНОГ ЕКСТРАКТА БИЉКЕ *Satureja montana* L.

ЈОВАНА ШУЋУР[1], АЛЕКСАНДРА ПОПОВИЋ[1], МИЛОШ ПЕТРОВИЋ[1], ГОРАН АНАЧКОВ[2], ВОЈИСЛАВА БУРСИЋ[1], БИЉАНА КИПРОВСКИ[1] и ДЕЈАН ПРВУЛОВИЋ[1]

[1]*Пољопривредни факултет, Универзитет у Новом Саду, Трг Доситеја Обрадовића 8, 21000 Нови Сад и* [2]*Природно–математички факултет, Универзитет у Новом Саду, Трг Доситеја Обрадовића 3, 21000 Нови Сад*

Широка употреба синтетичких инсектицида, хербицида и других пестицида има негативан утицај на околину, као и на здравље људи и животиња. Стога научници све више посвећују пажњу природним пестицидима, тј. активним компонентама биљних екстраката. У овом раду је испитан утицај две концентрације (0,1 и 0,2 %) воденог екстракта биљке *Satureja montana* L. на процес липидне пероксидације, и на активност антиоксидантних ензима у листу и корену паприке и црне помоћнице 24, 72 и 120 h након третмана. Добијени резултати су показали да 0,2 % концентрација воденог екстракта *S. montana* повећава интензитет липидне пероксидације у корену црне помоћнице. Поред тога, статистички значајно повећање активности пирогалол- и гвајакол-пероксидазе уочен је у листовима црне помоћнице након третмана са 0,2% воденим екстрактом *S. montana*. Други циљ рада био је испитивање токсичности воденог екстраката према лептирастој ваши. Водени екстракт концентрације 0,2 % проузроковао је смртност од 68,33 %.

(Примљено 2. јула, ревидирано 15. октобра, прихваћено 28. октобра 2014)

REFERENCES

1. M. Akbarzadeh, I. Bajalan, E. Qalayi, *Int. J. Agron. Plant Prod.* **4** (2013) 1285
2. A. B. Gatti, A. G. Ferreira, M. Arduin, S. C. G. A. Perez, *Acta Bot. Bras.* **24** (2010) 454
3. H. Safari, A. Tavili, M. Saberi, *Front. Agric. China* **4** (2010) 475
4. M. Farooq, K. Jabran, Z. A. Cheema, A. Wahid, K. H. M. Siddique, *Pest Manag. Sci.* **67** (2011) 493
5. D. Inzé, M. V. Montagu, *Curr. Opin. Biotechnol.* **6** (1995) 153
6. A. Gniazdowska, R. Bogatek, *Acta Physiol. Plant.* **27** (2005) 395
7. W. D. Dos Santos, M. M. L. Ferrarese, O. Ferrarese-Filho, *Funct. Plant Sci. Biotechnol.* **2** (2008) 47
8. K. E. Hammond-Kosack, J. D. G. Jones, *Plant Cell* **8** (1996) 1773
9. M. B. De Albuquerque, R. C. Dos Santos, L. M. Lima, P. A. Melo Filho, R. J. M. C. Nogueira, C. A. G. Da Câmara, A. R. Ramos, *Agron. Sustainable Dev.* **31** (2011) 379
10. C. Mandal, N. Ghosh, M. K. Adak, N. Dey, *Theor. Exp. Plant Physiol.* **25** (2013) 203
11. H. Kuthan, H. J. Haussmann, J. Werringloer, *Biochem. J.* **237** (1986) 175
12. R. G. Alscher, N. Erturk, L. S. Heath, *J. Exp. Bot.* **53** (2002) 1331
13. J. M. McCord, I. Fridovich, *J. Biol. Chem.* **244** (1969) 6049
14. A. F. Miller, *Curr. Opin. Chem. Biol.* **8** (2004) 162
15. A. S. Gupta, R. P. Webb, A. S. Holaday, R. D. Allen, *Plant Physiol.* **103** (1993) 1067
16. A. Mhamdi, G. Queval, S. Chaouch, S. Vanderauwera, F. Van Breusegem, G. Noctor, *J. Exp. Bot.* **61** (2010) 4197
17. S. R. Devi, M. N. V. Prasad, *Biol. Plantarum* **38** (1996) 387
18. R. S. Zeng, S. M. Luo, Y. H. Shi, M. B. Shi, C. Y. Tu, *Agron. J.* **93** (2001) 72
19. J. Q. Yu, S. F. Ye, M. F. Zhang, W. H. Hu, *Biochem. Syst. Ecol.* **31** (2003) 129

20. C. Serrano, O. Matos, B. Teixeira, C. Ramos, N. Neng, J. Nogueira, M. L. Nunes, A. Marques, *J. Sci. Food Agric.* **91** (2011) 1554

21. D. Djenane, J. Yangüela, L. Montañés, M. Djerbal, P. Roncalés, *Food Control* **22** (2011) 1046

22. F. V. M. Silva, A. Martins, J. Salta, N. R. Neng, J. M. F. Nogueira, D. Mira, N. Gaspar, J. Justino, C. Grosso, J. S. Urieta, A. M. S. Palavra, A. P. Rauter, *J. Agric. Food Chem.* **57** (2009) 11557

23. H. D. Hassanein, A. H. Said-al, M. M. Abdelmohsen, *Int. J. Pharm. Pharm. Sci.* **6** (2014) 578

24. D. Chrpová, L. Kouřimská, M. H. Gordon, V. Heřmanová, I. Roubíchková, J. Pánek, *Czech J. Food Sci.* **28** (2010) 317

25. B. A. Gholami, M. Faravani, M. T. Kashki, *J. Appl. Environ. Biol. Sci.* **1** (2011) 283

26. A. Hagerman, I. Harvey-Mueller, H. P. S. Makkar, *Quantification of Tannins in Tree Foliage – a Laboratory Manual*, FAO/IAEA, Vienna, 2000, p. 4

27. K. R. Markham, in *Methods in Plant Biochemistry 1,* P. M. Dey, J. B. Harborne, Eds., Academic Press, London, 1989, p. 197

28. D. R. Hoagland, D. I. Arnon, *Circ.-Calif. Agr. Exp. Stn.* **347** (1950) 1

29. S. Mandal, A. Mitra, N. Mallick*, Physiol. Mol. Plant Pathol.* **72** (2008) 56

30. E. Sathya, M. Bjorn*, Plant Stress Tolerance*, Humana Press, Oklahoma City, OK, 2010, p. 273

31. I. Morkunas, J. Gmerek*, J. Plant Physiol.* **164** (2007) 185

32. I. Tahirović, M. Kožljak, J. Toromanović, A. Čopra-Janićijević, A. Klepo, A. Topčagić, H. Demirović, *Bull. Chem. Technol. Bosnia Herzegovina* **42** (2014) 51

33. M. S. Gião, C. I. Pereira, M. E. Pintado, F. X. Malcata, *LWT Food Sci. Technol.* **50** (2013) 320

34. K. Ramanauskienė, A. Savickas, A. Inkėnienė, K. Vitkevičius, G. Kasparavičienė, V. Briedis, A. Amšiejus, *Medicina (Kaunas)* **45** (2009) 712

35. T. O. Sunmonu, J. Van Staden, *S. Afr. J. Bot.* **90** (2014) 101

36. J. Ding, Y. Sun, C. L. Xiao, K. Shi, Y. H. Zhou, J. Q. Yu, *J. Exp. Bot.* **58** (2007) 3765

37. G. R. Haddadchi, Z. Gerivani, *Int. J. Plant Prod.* **3** (2009) 63

38. F. Omezzine, M. Bouaziz, M. S. J. Simmonds, R. Haouala, *Food Chem.* **148** (2014) 188

39. Y. Zhang, Master Thesis, Globe Thesis, China, 2000, www.globe-thesis.com/?t=2143360245465855 (accessed in Apr, 2015)

40. D. M. C. Nguyen, D. J. Seo, H. B. Lee, I. S. Kim, K. Y. Kim, R. D. Park, W. J. Jung, *Microb. Pathog.* **56** (2013) 8

41. R. Pavela, N. Vrchotová, B. Šerá, *J. Biopest.* **2** (2009) 48

42. F. Harrison, J. K. Peterson, M. E. Snook, R. Bohac, D. M. Jackson, *J. Agric. Food Chem.* **51** (2003) 2943

43. M. Dehghani, K. Ahmadi, *Bulg. J. Agric. Sci.* **19** (2013) 691.

SUPPLEMENTARY MATERIAL TO

Allelopathic effects and insecticidal activity of aqueous extracts of *Satureja montana* L.

JOVANA ŠUĆUR[1]*, ALEKSANDRA POPOVIĆ[1], MILOŠ PETROVIĆ[1], GORAN ANAČKOV[2], VOJISLAVA BURSIĆ[1], BILJANA KIPROVSKI[1] and DEJAN PRVULOVIĆ[1]

[1]Faculty of Agriculture, University of Novi Sad, Trg Dositeja Obradovića 8, 21000 Novi Sad, Serbia and [2]Faculty of Science, University of Novi Sad, Trg Dositeja Obradovića 3, 21000 Novi Sad, Serbia

RESULTS OF THE HPLC-DAD ANALYSIS OF THE INVESTIGATED PHENOLIC COMPOUNDS
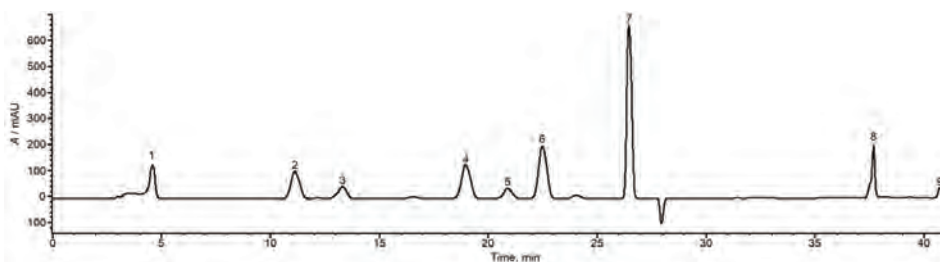
Fig. 1. HPLC-DAD chromatogram of phenolic compounds, 1 – gallic acid; 2 – chlorogenic acid; 3 – caffeic acid; 4 – *p*-coumaric acid; 5 – ferulic acid; 6 – 2-hydroxy cinnamic acid; 7 – *trans*-cinnamic acid; 8 – kaempferol; 9 – quercetin.

* Corresponding author. E-mail: jovanasucur@yahoo.com

S125

TABLE S-I. Retention time, linearity (R^2) and repeatability (*RSD*) for the investigated phenolic compounds

Phenolic acid	Retention time, min	R^2	*RSD* / %
Gallic acid	4.58	0.9998	6.76
Ferulic acid	22.48	0.9966	2.42
2-Hydroxy cinnamic acid	24.00	0.9967	9.61
trans-Cinnamic acid	26.43	0.9949	5.09
Caffeic acid	13.29	0.9984	9.48
p-Coumaric acid	18.94	0.9985	2.74
Chlorogenic acid	11.21	0.9996	4.18
Kaempferol	37.67	0.9996	11.93
Quercetin	40.75	0.9992	7.25

EFFECT OF THE AQUEOUS EXTRACTS OF *Satureja montana* ON THE ANTI-OXIDANT ENZYMES AND LIPID PEROXIDATION IN THE ROOTS AND LEAVES OF BLACK NIGHTSHADE AND PEPPER SEEDLINGS

TABLE S-II. Effect of two concentrations of *S. montana* aqueous extracts on the activities of CAT, SOD, GPX and PPX and on the MDA content in the roots of black nightshade seedlings; the data are mean values $\pm$ *SE*; a–f values without the same superscripts within each column differ significantly ($P < 0.05$); CAT, catalase; SOD, superoxide dismutase; GPX, guaiacol peroxidase; PPX, pyrogallol peroxidase; LP, lipid peroxidation

Time, h	24	72	120
CAT / U g^{-1} protein			
Control	3.61 ± 0.07^a	20.06 ± 0.59^c	$9.36 \pm 0.33^{a,b}$
0.1 %	6.50 ± 0.06^a	13.13 ± 1.39^b	11.15 ± 1.77^b
0.2 %	13.04 ± 0.93^b	35.55 ± 2.79^d	12.67 ± 0.47^b
SOD / U mg^{-1} protein			
Control	33.82 ± 0.08^a	25.90 ± 1.91^b	11.37 ± 0.68^f
0.1 %	75.65 ± 0.44^d	26.04 ± 0.15^b	27.09 ± 1.53^b
0.2 %	59.80 ± 0.48^c	25.60 ± 3.06^b	19.36 ± 0.25^e
GPX / U mg^{-1} protein			
Control	$1478 \pm 60^{a,b}$	$1474 \pm 80^{a,b}$	2077 ± 76^d
0.1 %	$1545 \pm 113^{a,b}$	$1363 \pm 77^{a,b}$	1811 ± 68^c
0.2 %	2742 ± 122^e	$1601 \pm 83^{a,c}$	1218 ± 71^a
PPX / U mg^{-1} protein			
Control	$1305 \pm 24^{a,b}$	1348 ± 21^a	$1273 \pm 54^{a,b}$
0.1 %	$1020 \pm 47^{b,c}$	1143 ± 60^b	$1225 \pm 39^{a,b}$
0.2 %	1729 ± 99^d	1690 ± 76^d	947 ± 22^c
LP (MDA content / nmol mg^{-1} protein)			
Control	2.38 ± 0.08^a	3.37 ± 0.07^c	1.88 ± 0.05^b
0.1 %	3.46 ± 0.06^c	3.41 ± 0.04^c	3.54 ± 0.11^c
0.2 %	3.33 ± 0.03^c	4.57 ± 0.10^d	3.45 ± 0.08^c

TABLE S-III. Effect of two concentrations of *S. montana* aqueous extracts on the activities of CAT; SOD, GPX and PPX and on the MDA content in the leaves of black nightshade seedlings; the data are mean values ± standard error; a–g values without the same superscripts within each column differ significantly ($P < 0.05$); CAT, catalase; SOD, superoxide dismutase; GPX, guaiacol peroxidase; PPX, pyrogallol peroxidase; LP, lipid peroxidation

Time, h	24	72	120
CAT / U g^{-1} protein			
Control	10.34 ± 0.11^a	25.83 ± 1.76^d	15.28 ± 0.15^b
0.1 %	46.29 ± 0.21^f	32.13 ± 1.42^e	20.67 ± 0.55^c
0.2 %	31.41 ± 0.97^e	26.15 ± 2.49^d	11.81 ± 0.77^a
SOD / U mg^{-1} protein			
Control	16.50 ± 0.04^a	16.28 ± 0.19^a	9.88 ± 0.11^e
0.1 %	21.72 ± 0.22^d	23.15 ± 0.06^g	19.49 ± 0.14^b
0.2 %	22.69 ± 0.13^f	21.96 ± 0.15^d	13.80 ± 0.05^c
GPX / U mg^{-1} protein			
Control	99.26 ± 6.03^a	94.99 ± 7.02^a	85.71 ± 5.18^a
0.1 %	127.18 ± 7.73^b	98.31 ± 6.16^a	$104.41 \pm 5.47^{a,b}$
0.2 %	99.10 ± 5.14^a	134.73 ± 15.72^b	136.44 ± 10.84^b
PPX / U mg^{-1} protein			
Control	145.90 ± 3.99^a	151.05 ± 3.54^a	112.65 ± 3.88^b
0.1 %	$137.38 \pm 5.31^{a,b}$	152.53 ± 7.59^a	94.00 ± 1.45^c
0.2 %	147.96 ± 4.70^a	209.90 ± 13.76^d	120.86 ± 3.31^b
LP (MDA content / nmol mg^{-1} protein)			
Control	1.68 ± 0.04^a	2.15 ± 0.05^c	1.96 ± 0.08^b
0.1 %	2.38 ± 0.03^d	2.39 ± 0.03^d	2.67 ± 0.05^e
0.2 %	1.91 ± 0.02^b	2.64 ± 0.05^e	2.17 ± 0.03^c

TABLE S-IV. Effect of two concentrations of *S. montana* aqueous extracts on the activities of CAT, SOD, GPX and PPX and on the MDA content in the roots of pepper seedlings; the data are mean values ± standard error; a–g values without the same superscripts within each column differ significantly ($P < 0.05$); CAT, catalase; SOD, superoxide dismutase; GPX, guaiacol peroxidase; PPX, pyrogallol peroxidase; LP, lipid peroxidation

Time, h	24	72	120
CAT / U g^{-1} protein			
Control	22.93 ± 0.67^a	20.40 ± 0.73^b	10.56 ± 0.22^f
0.1 %	$12.41 \pm 0.40^{e,f}$	$11.55 \pm 0.39^{e,f}$	33.37 ± 1.03^c
0.2 %	14.87 ± 0.80^d	13.01 ± 0.35^e	11.05 ± 0.54^f
SOD / U mg^{-1} protein			
Control	7.27 ± 0.15^a	7.99 ± 0.07^a	9.34 ± 0.21^b
0.1 %	9.85 ± 0.20^b	2.10 ± 0.06^c	21.41 ± 0.72^f
0.2 %	0.88 ± 0.03^d	11.87 ± 0.54^e	25.28 ± 0.49^g
GPX / U mg^{-1} protein			
Control	2.66 ± 0.22^a	$3.59 \pm 0.15^{b,c}$	3.32 ± 0.17^b
0.1 %	2.26 ± 0.05^a	$3.44 \pm 0.08^{b,c}$	2.68 ± 0.13^a
0.2 %	2.30 ± 0.20^a	5.03 ± 0.10^d	3.84 ± 0.17^c

ŠUĆUR *et al.*

TABLE S-IV. Continued

Time, h	24	72	120
PPX / U mg^{-1} protein			
Control	2.62 ± 0.03^a	2.41 ± 0.12^b	1.88 ± 0.07^d
0.1 %	$1.48 \pm 0.04^{e,f}$	2.10 ± 0.06^c	1.59 ± 0.07^e
0.2 %	1.35 ± 0.02^f	2.24 ± 0.06^c	2.40 ± 0.09^b
LP (MDA content / nmol mg^{-1} protein)			
Control	2.23 ± 0.17^a	2.98 ± 0.06^b	$2.85 \pm 0.24^{b,c}$
0.1 %	$2.29 \pm 0.15^{a,c}$	2.92 ± 0.08^b	5.37 ± 0.44^d
0.2 %	$2.61 \pm 0.08^{a,b}$	2.92 ± 0.06^b	$2.55 \pm 0.11^{a,b}$

TABLE S-V. Effect of two concentrations of *S. montana* aqueous extracts on the activities of CAT; SOD, GPX and PPX and on the MDA content in the leaves of pepper seedlings; The data are mean values ± standard error; a–g values without the same superscripts within each column differ significantly ($P < 0.05$); CAT, catalase; SOD, superoxide dismutase; GPX, guaiacol peroxidase; PPX, pyrogallol peroxidase; LP, lipid peroxidation

Time, h	24	72	120
CAT / U g^{-1} protein			
Control	18.32 ± 0.48^a	16.84 ± 0.53^a	17.88 ± 0.77^a
0.1 %	34.27 ± 0.37^e	23.64 ± 0.78^b	31.43 ± 0.58^d
0.2 %	31.77 ± 1.48^d	35.76 ± 0.50^e	27.06 ± 0.33^c
SOD / U mg^{-1} protein			
Control	11.23 ± 0.06^a	7.42 ± 0.04^f	5.96 ± 0.28^g
0.1 %	8.70 ± 0.14^e	4.77 ± 0.12^h	14.41 ± 0.34^d
0.2 %	10.38 ± 0.08^b	6.36 ± 0.06^g	12.86 ± 0.11^c
GPX / U mg^{-1} protein			
Control	0.55 ± 0.01^a	0.48 ± 0.01^b	0.55 ± 0.02^a
0.1 %	0.30 ± 0.02^d	$0.35 \pm 0.02^{c,d}$	0.60 ± 0.02^a
0.2 %	0.38 ± 0.04^c	0.46 ± 0.01^b	0.56 ± 0.02^a
PPX / U mg^{-1} protein			
Control	0.59 ± 0.01^a	0.71 ± 0.02^c	0.77 ± 0.01^d
0.1 %	0.53 ± 0.01^e	$0.67 \pm 0.02^{b,c}$	$0.74 \pm 0.01^{c,d}$
0.2 %	0.59 ± 0.01^a	0.66 ± 0.03^b	$0.61 \pm 0.02^{a,b}$
LP (MDA content / nmol mg^{-1} protein)			
Control	2.76 ± 0.14^a	2.86 ± 0.06^a	3.29 ± 0.07^c
0.1 %	2.38 ± 0.05^b	2.81 ± 0.07^a	2.83 ± 0.05^a
0.2 %	2.48 ± 0.11^b	2.95 ± 0.04^a	2.72 ± 0.05^a

Journal of the Serbian Chemical Society

Physicochemical characterization of zofenopril inclusion complex with 2-hydroxypropyl-*β*-cyclodextrin

LUCREŢIA UDRESCU[1,2]*, LAURA SBÂRCEA[1]**, ADRIANA FULIAŞ[1],
IONUŢ LEDEŢI[1], TITUS VLASE[3], PAUL BARVINSCHI[4] and LUDOVIC KURUNCZI[1,2]

[1]*Faculty of Pharmacy, University of Medicine and Pharmacy, 300041 Timişoara, Romania,*
[2]*Institute of Chemistry Timişoara of the Romanian Academy, 300223 Timişoara, Romania,*
[3]*Research Center for Thermal Analysis in Environmental Problems, West University of
Timişoara, 300115 Timişoara, Romania and* [4]*Faculty of Physics, West University of
Timişoara, 300223 Timişoara, Romania*

Abstract: Zofenopril calcium (ZOF) is one of the newest angiotensin-converting enzyme (ACE) inhibitors, highly lipophilic and with low water solubility. This research investigates the interaction between ZOF and a chemically modified derivative of *β*-cyclodextrin, 2-hydroxypropyl-*β*-cyclodextrin (HPBCD), in order to prove the formation of an inclusion complex with an enhanced water solubility profile of ZOF. In this research, for the first time, the physicochemical characterization and the solubility profile of an inclusion complex between ZOF and HPBCD are reported. Different spectroscopic techniques (UV absorption spectrometry, powder X-ray diffraction, attenuated total reflectance Fourier transform IR spectroscopy) were applied in order to prove the formation of the ZOF/HPBCD inclusion complex, both in water and in the solid state, backed by thermal analysis (TGA/DTG/HF). The obtained results confirmed that the physicochemical properties of the ZOF/HPBCD binary system, prepared using the kneading method, are different in comparison to both with the parent substances and the corresponding physical mixture, thus suggesting that an inclusion complex was formed. After the formation of the inclusion complex with HPBCD, the solubility test indicated that the water solubility of ZOF was increased 5-fold.

Key words: Job's plot; ATR-FTIR; PXRD; thermal analysis; solubility.

INTRODUCTION

Zofenopril calcium (ZOF), chemically named calcium (2*S*,4*S*)-1-[(2*S*)-3-(benzoylsulfanyl)-2-methylpropanoyl]-4-(phenylsulfanyl)pyrrolidine-2-carboxylate, is a sulfhydryl-containing ACE inhibitor (Fig. 1A). It is a selective cardiac ACE

485

inhibitor, being an effective antihypertensive agent and a valuable therapeutic option in congestive heart failure and in acute myocardial infarction.[1–3]
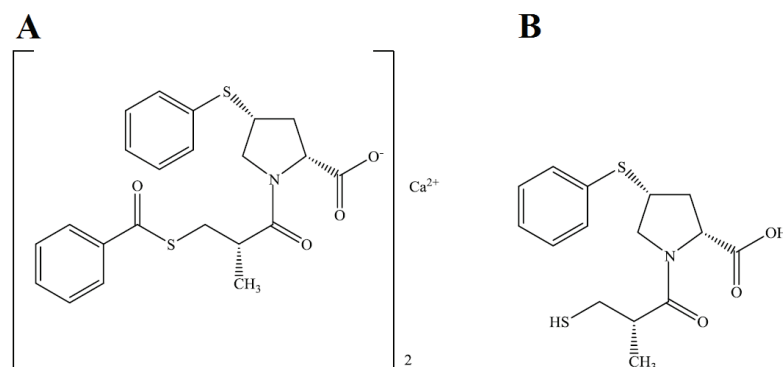
Fig. 1. The chemical structures of: A) zofenopril calcium and B) its active form, zofenoprilat.

ZOF is an ester prodrug of the active acid form, namely zofenoprilat (Fig. 1B), which contains a sulfhydryl group.[4] This potent ACE inhibitor also possesses remarkable antioxidant and cardioprotective properties.[5,6] The major inconvenience is the low water solubility of the calcium salt of zofenopril (0.3 mg ml^{-1} reported by Subissi *et al.*[1]), this form being utilized in the oral dosage forms. On the other hand, zofenopril calcium exhibits the tendency of forming numerous polymorph forms,[7] resulting in its decreasing water solubility.

According to the biopharmaceutics classification system (BCS), a drug that has low water solubility and high permeability is assigned to Class II. Therefore, the formulation effects and the biological parameters can hamper the dissolution profile, this type of drugs presenting variable absorption.[8] Based on the low water solubility and its good permeability, ZOF is categorized as Class II under the BCS framework. The polymorphism is a critical aspect for BCS Class II compounds.[9] Considering these outlooks, the employment of inclusion complexation using cyclodextrin becomes a useful approach.[10]

The cyclodetrins are a class of cyclic oligosaccharides made up of six, seven or eight α-D-glucopyranose units, named α-, β-, and γ-cyclodextrin, respectively. Their particular cavity structure is of biomedical and pharmaceutical interest, because they are able to form inclusion complexes with drugs (or lipophilic moieties) with improved solubility, stability or other physicochemical properties.[11,12] The rendered amorphous solid state following the complexation with cyclodextrins[11,13] has a potential benefit for oral tablets containing ZOF, because of the increased water solubility and the opportunity of transferring ZOF from Class II into Class I of BCS (*i.e.*, into a highly soluble and highly permeable drug).[8]

Hitherto, there have been a few studies on ZOF inclusion complexes with native β-cyclodextrin,[14] but no scientific report on ZOF inclusion complex with

HPBCD. In this study, the formation of the inclusion complexes between ZOF and HPBCD because of ZOF molecular encapsulation within cyclodextrin cavity was investigated. Thus, spectroscopic techniques and TGA/DTG/HF thermal analysis were applied as the most facile and reliable methods for the study of the host–guest interaction (*e.g.,* HPBCD and ZOF).

EXPERIMENTAL

Materials

Zofenopril calcium was a gift sample from Berlin-Chemie Menarini (Berlin, Germany). 2-Hydroxypropyl-*β*-cyclodextrin (average formula weight 1309.3, *DS* = 3) was purchased from Cyclolab R&D Ltd. (Budapest, Hungary). The substances were used as received. All other chemicals and reagents were of analytical grade. All experiments were performed using ultrapure water.

Stoichiometry determination using the Job's plot and Benesi–Hildebrand method

The spectrophotometric measurements were performed using a Spectronic Unicam – UV 300 UV-Visible double beam spectrophotometer with 1 cm matched quartz cells.

The stoichiometry of the inclusion complex was determined by application of the Job's method of continuous variation.[15,16] Thus, equimolar 4×10^{-4} M solutions of ZOF and HPBCD were mixed in volumetric flasks to a standard volume of 10 ml (1:9; 2:8, *etc*.), varying the mole ratio while the total concentration of the species was kept constant. An analogous set of ZOF solutions was prepared using ultrapure water as references. After stirring for 24 h at the room temperature, the absorbance for all solutions was measured. The differences between the absorbance values in the presence (A) and in the absence (A_0) of HPBCD were calculated as $\Delta A = A - A_0$. The ΔA (ZOF) values were plotted against the mole fractions, R, where $R = [ZOF]/([ZOF] + [HPBCD])$.

The Benesi–Hildebrand method was performed by measuring the ZOF absorbance values under complexation-free conditions and in the presence of increasing concentrations of HPBCD. Hence, the concentration of ZOF was kept constant at 0.02 mM and the HPBCD concentration was varied from 0 to 4.5 mM. All the absorption spectra were collected in the UV spectral range of 220–320 nm using 1 cm quartz cells.

Binary systems preparation

The accurate weight of HPBCD for a 1:1 mole ratio ZOF:HPBCD was triturated with an appropriate quantity of water at ambient temperature for 10 min, up to homogenization. Then ZOF was slowly added to the paste. While grinding, a small quantity of water was blended with the mixture in order to assist the dissolution of the drug. The paste was kneaded for 1 h. During this process, an appropriate quantity of water was added in order to maintain a suitable paste consistency. The paste rendered by this process was dried in the oven at 40 °C for 24 h. Then, the dried kneaded product, named ZOF/HPBCD KP, was pulverized and passed through a 75-μm size sieve.

The aforementioned kneaded product was compared with the corresponding physical mixture. Hence, the stoichiometric quantities of ZOF and HPBCD corresponding to a 1:1 mole ratio were gently mixed in a mortar at ambient temperature for 10 min, in order to obtain a homogenous blend. Thereby, a 1:1 mole ratio physical mixture consisting of ZOF and HPBCD at the same ratio as for the inclusion complex was obtained (ZOF/HPBCD PM).

ATR-FTIR analysis

The FTIR spectra were recorded using a Bruker Vertex 70 spectrometer equipped with a platinum ATR unit, type Bruker Diamond A225/Q. Each spectrum represents 64 co-added scans, achieved at a resolution of 2 cm^{-1}, in the 4000–400 cm^{-1} wavenumber range.

PXRD analysis

X-Ray diffraction studies of the pure substances (ZOF and HPBCD) and of their binary systems (the corresponding PM and KP) were performed using a Bruker D8 Advance powder X-ray diffractometer, in the range of 5–45° angular domain (2θ), with CuK radiation generated at 40 mA, 40 kV and a Ni filter.

Thermal analysis

The pure substances and the binary systems were characterized by performing thermal analysis. A Perkin-Elmer Diamond simultaneous TGA/DTA instrument was used. The samples were placed in aluminum crucibles. The DTA curves (in μV) were changed with the heat flow (HF) curves (in mW) in order to determine the heat effects. The thermal behavior of the substances were studied under an air atmosphere, at a flow rate of 100 mL min^{-1}, under non-isothermal conditions by increasing the ambient temperature up to 350 °C at a constant heating rate of 10 °C min^{-1}.

Standard curve for ZOF and the solubility profile of the kneaded product

A set of ZOF aqueous solutions was prepared with concentrations ranging between 9–70 μg ml^{-1}. The absorbance was recorded at 248 nm at 25 °C in order to represent absorbance (*A*) as a function of concentration (*c* / μg ml^{-1}) to obtain the standard curve for ZOF.

The water solubility of ZOF within its inclusion complex was determined as follows: an excess amount of kneaded product was placed in 2 mL of distilled water, to obtain a saturated solution. The mixture was shaken for 24 h at 25 °C. The insoluble substance was removed by filtration using a 0.45-μm cellulose acetate filter. The clear supernatant was properly diluted and its absorbance was measured at 248 nm at 25 °C. The residue dosing was calculated by means of the standard ZOF curve.

RESULTS AND DISCUSSION

Stoichiometry determination

According to the Job's method,[15] if a physical parameter directly related to the concentration (*i.e.*, absorbance) of the complex can be measured for a series of samples with continuously varying mole fraction of its components, then the maximum concentration of the complex will be obtained when the mole ratio *R* corresponds to the complexation stoichiometry. The maximum variation in absorbance ΔA was consequently observed for the mole ratio *R* = 0.5 (Fig. 2A), thus indicating that the ZOF/HPBCD stoichiometry is 1:1.

Additional investigations using the Benesi–Hildebrand method were performed, in order to verify the stoichiometry. A good linear relationship by double-reciprocal plotting of $1/\Delta A$ *vs*. 1/[HPBCD] (R^2 = 0.9996) was accomplished (as presented in Fig. 2B) using the Benesi–Hildebrand Equation:[17,18]

$$\frac{1}{\Delta A} = \frac{1}{[\text{ZOF}][\text{HPBCD}]\Delta\varepsilon K_s} + \frac{1}{\Delta\varepsilon[\text{ZOF}]} \tag{1}$$

The results highlighted the 1:1 stoichiometry of the ZOF/HPBCD binary system under these experimental conditions.
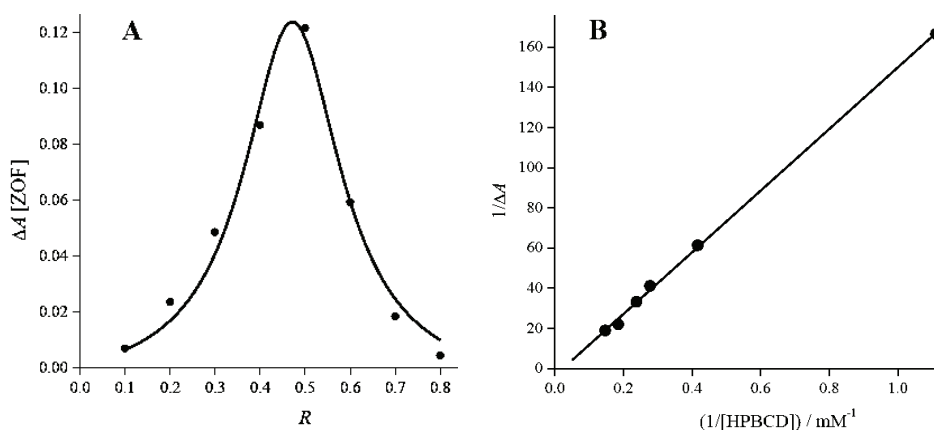
Fig. 2. A) Job's plot for different mole ratios of ZOF and HPBCD from absorbance measurements and B) Benesi–Hildebrand linear plot for $1/\Delta A$ vs. $1/[\text{HPBCD}]$.

ATR-FTIR analysis

FTIR spectroscopy is an important method regarding an evaluation of the interactions between the components of a mixture. The changes in the position or intensity, as well as the disappearance or appearance of absorption bands are irrefutable proofs for an interaction between a host-cyclodextrin and a drug--guest. The major benefits of the ATR-FTIR technique in comparison with the KBr pellets technique are the small amount of the samples, the rapidity and accuracy, and the lack of the extra interactions induced by the mechanical press, as occurs in the formulation of a KBr pellet.

The ATR-FTIR spectra of the pure ZOF and HPBCD, along with their physical mixture and kneaded product are presented in Fig. 3. The characteristic absorbance peaks of ZOF and HPBCD, as well as the changes which appear after the physical mixing and the kneading process, are summarized in Table I.

The ATR-FTIR spectrum of pure ZOF, as shown in Fig. 3A, is characterized by the presence of peaks for the proline group (at 1470 cm^{-1}),[19] the carboxyl groups (the anti-symmetric and symmetric stretching C=O vibrations at 1659 and 1612 cm^{-1}, respectively) and the aromatic ring (the C_{ar}–H stretching vibration arises at 3061 cm^{-1}, the skeletal vibration of the aromatic ring appears at 1582 cm^{-1}, and the C_{ar}–H and C_{ar}–C_{ar} bending vibrations appear at 772 and 746 cm^{-1}, respectively).[20]

A

B
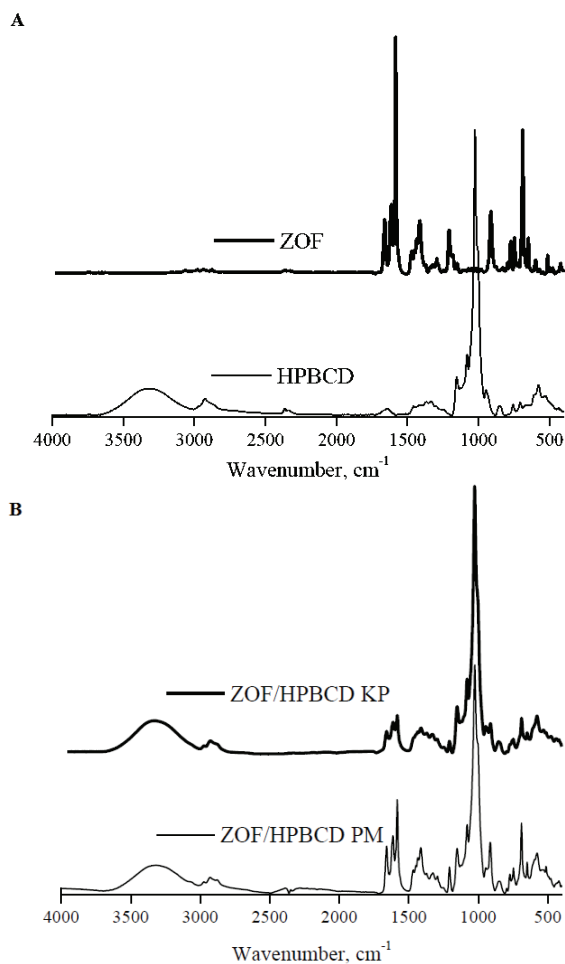
Fig. 3. ATR-FTIR spectra of: A) ZOF and HPBCD and B) their binary systems in the 4000–400 cm^{-1} spectral range.

TABLE I. Wavenumbers, cm^{-1}, and peak assignments from the ATR-FTIR spectra of ZOF, HPBCD, ZOF/HPBCD PM and ZOF/HPBCD KP

ZOF	HPBCD	ZOF/HPBCD PM	ZOF/HPBCD KP
	3325, ν(O–H)	3319	3321
3061, ν(C$_{ar}$–H)			
2978, ν(C–H) from CH$_2$ + CH$_3$		2974	2970
2936, ν(C–H) from CH$_2$ + CH$_3$	2924, ν(C–H) from CH$_2$	2928	2926
1659, ν_{asym}(C=O) from carboxylate		1659	1659
1612, ν_{sym}(C=O) from carboxylate		1614	1614

TABLE I. Continued

ZOF	HPBCD	ZOF/HPBCD PM	ZOF/HPBCD KP
1582, skeletal vibration aromatic ring		1584	1584
1470, proline group vibration		1468	
	1456, δ(C–H) from CH$_2$ + CH$_3$	1448	1448
1435, 1412, δ(C–H) from CH$_2$ and CH$_3$			
	1364, δ(C–H) from CH$_3$	1371	1371
	1331, coupled δ(O–C–H), δ(C–O–H), δ(H–C–H) 1152, δ(C–O–C)	1327	1329
	1024, ν(C–C–O) from C–OH	1024	1026
	947, skeletal vibration involving α-1,4 linkage	945	945
	851, δ(C–C–H), (C–O), (C–C) from anomeric vibration	854	854
772, δ(C$_{ar}$–H) from the phenyl ring		772	770
746, δ(C$_{ar}$–C$_{ar}$) from the phenyl ring		746	748
513, γ(aromatic ring)		513	511

The O–H stretching vibrations from HPBCD (see Fig. 3A) exhibit a broad band with a maximum value at 3325 cm^{-1}, and characteristic peaks that correspond to C–H, C–O–H, O–C–H, and C–O–C bending vibrations in the 1000––1500 cm^{-1} spectral range. These data are in agreement with previously reported results.[18,21,22]

The IR spectrum of the inclusion complex prepared by kneading, shown in Fig. 3B, revealed some differences in comparison with the corresponding physical mixture and the parent substances. Almost all the characteristic peaks of ZOF are intact in the physical mixture spectrum, but they are shifted (or absent) in the ZOF/HPBCD KP spectrum, thus indicating inclusion interaction between the two components. On analyzing the spectral data, it was found that the ZOF C$_{ar}$–H stretching vibration is present neither in ZOF/HPBCD PM, nor in the ZOF/HPBCD KP, which indicate that one from the two ZOF aromatic rings is entrapped within the HPBCD cavity. The C=O stretching vibrations and aromatic ring skeletal vibration of ZOF are still present in the spectra of the binary systems, albeit shifted and attenuated in ZOF/HPBCD KP, as a consequence of the drug–cyclodextrin interaction when the kneading method was employed. Simultaneously, the proline group vibration, which was identified at 1470 cm^{-1} in the

ZOF spectrum, was shifted to 1468 cm^{-1} in the ZOF/HPBCD PM spectrum, and was no longer present in the ZOF/HPBCD KP spectrum, thus suggesting that an inclusion complex was formed and the 4-(phenylsulfanyl)pyrrolidine was enclosed in the cavity of the cyclodextrin.

PXRD analysis

PXRD is a fast analytical method that is applied for an assessment of the crystalline nature of a sample. This technique allowed the observation of sharp peaks attenuation of the crystalline substance (*i.e.*, ZOF) due to the interaction by inclusion with the amorphous cyclodextrin (HPBCD).

The PXRD patterns of the native ZOF and HPBCD and of their physical mixture and kneaded product are depicted in Fig. 4.
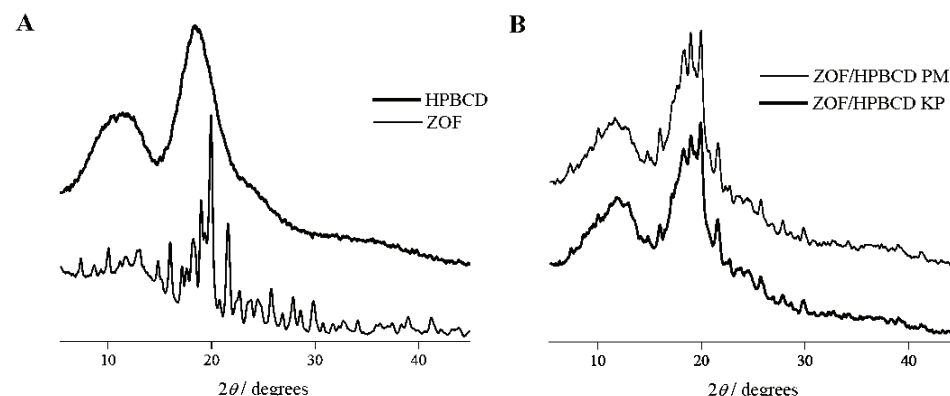
Fig. 4. PXRD patterns of: A) the native substances and B) their binary systems.

The PXRD spectrum of ZOF, presented in Fig 4A, emphasizes its highly crystalline nature by its characteristic diffraction peaks at 2θ 9.72, 13.74, 14.48, 16.00, 17.70, 18.42, 18.52, 19.00, 19.98, 20.56, 22.34 and 24.60°.[22] The XRD pattern of HPBCD (Fig. 4A) had two broad peaks and many diffuse peaks of low intensity, reflecting the amorphous nature of this cyclodextrin. The XRD spectrum of ZOF/HPBCD PM (Fig. 4B) almost overlapped with the individual patterns. In contrast, the XRD pattern of the kneaded product (Fig. 4B) revealed that the crystallinity of ZOF was drastically reduced, as inferred by the mitigated intensities of the characteristic sharp peaks (*i.e.*, at 2θ 16.00, 17.70, 19.00, 19.98 and 21.93°). This was the result of modifications in the environment of ZOF and HPBCD when inclusion complexation occurred.[18]

Thermal analysis

Thermal analysis techniques led to valuable outcomes regarding the formation of cyclodextrin inclusion complexes. The thermal behavior of the studied products under non-isothermal conditions is presented in Fig. 5.
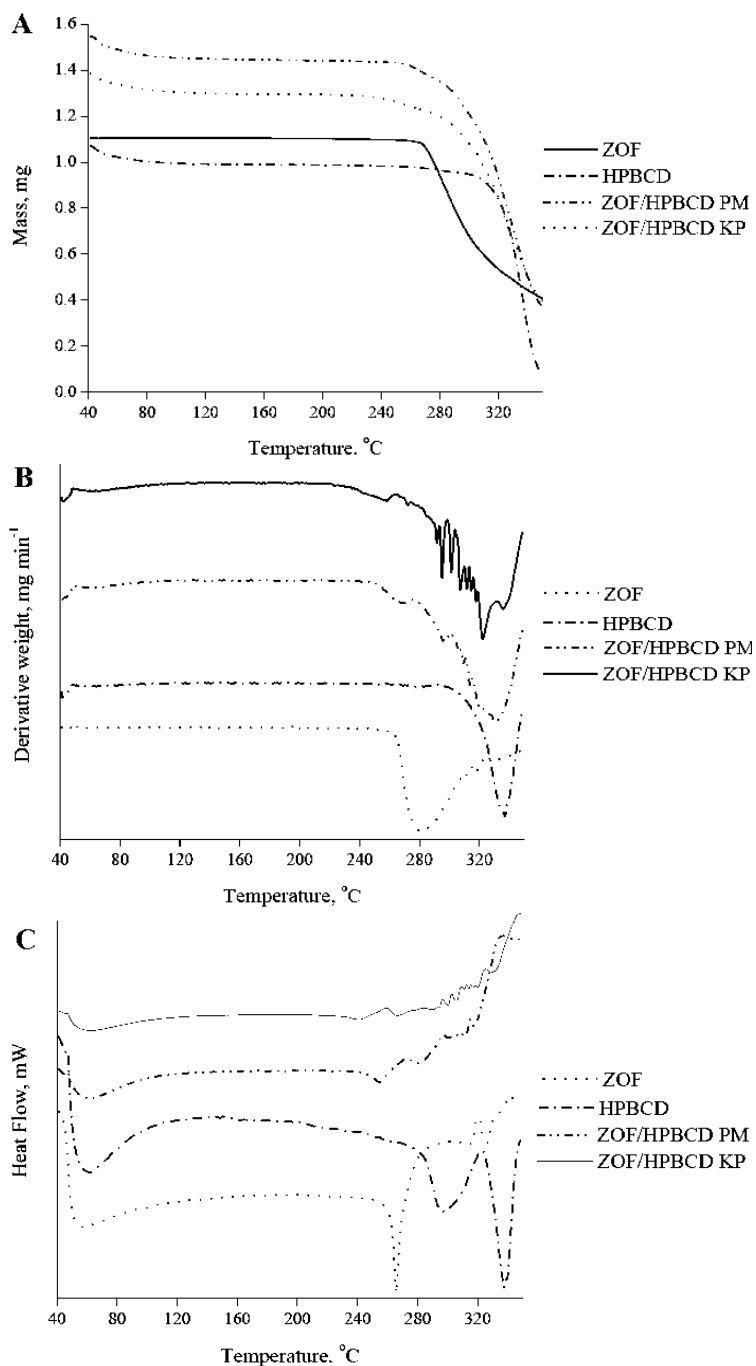
Fig. 5. A) Thermogravimetric, B) derivative thermogravimetric and C) heat flow curves of ZOF, HPBCD, ZOF/HPBCD PM and ZOF/HPBCD KP.

The TG diagrams obtained for native compounds, as well as for their binary systems, are presented in Fig. 5A. ZOF exhibited thermal stability up to 250 °C, followed by decomposition processes. The pure HPBCD and the studied binary systems exhibit a small mass loss corresponding to their dehydration, which occurred between 50 and 130 °C. The water loss of HPBCD, as well as of the binary systems, was also revealed by small and broad endothermic peaks, as indicated by the DTG curves in Fig. 5B.

The melting peak of ZOF appeared at 265 °C,[23] as given by the HF diagram (Fig. 5C). The endothermic process was followed by thermal degradation – a process that was confirmed by the TG curve (Fig. 5A). The broad endothermic HF peak also indicated HPBCD dehydration within the same temperature interval; the melting point of HPBCD had a higher value than that of ZOF (336 °C), proven by both the HF and DTG curves, which is consistent with the previously reported value.[24] The HF curve, corresponding to ZOF/HPBCD PM, indicated that the ZOF melting peak was shifted to 254.5 °C. The endothermic peak of ZOF melting process from ZOF/HPBCD KP was reduced in comparison with that from the physical mixture and was shifted to a lower temperature of 240.6 °C. Hence, a decrease in the thermal stability of the kneaded product was observed, which was the consequence of ZOF amorphization through the formation of the inclusion complex.[25] Similar results were also reported for the inclusion process of other substances.[26,16]

By corroborating the DTG and HF results, a different thermal pattern of ZOF was observed within the kneaded product, because the melting point of the ZOF guest molecule, which is entrapped within HPBCD cavity, was shifted to a different, lower temperature and therefore the peak intensity was decreased. These results indicate a molecular interaction between ZOF and HPBCD, endorsing the hypothesis of the existence of an inclusion complex between the two components when the kneading method was employed.

Solubility

The water solubility appraisal of the ZOF/HPBCD inclusion complex prepared by kneading was the milestone in our experimental efforts. Hence, the saturation shake-flask method[27] was employed for measuring the water solubility at 25 °C of ZOF in ZOF/HPBCD KP using the standard curve of ZOF in water, at 25 °C (Fig. 6).

The obtained standard curve of ZOF was characterized by the equation $A = 0.02909c + 0.01022$ ($R = 0.9999$), where A stands for absorbance, measured at 248 nm, and c is the concentration in μg ml^{-1}.

The water solubility of the ZOF/HPBCD KP was estimated by preparing a concentrated solution.[28,29] The UV spectrophotometric measurements were achieved after adequate dilution, indicating that the water solubility of the included ZOF was 1.510±0.005 mg mL^{-1} (an average value of five experimental

determinations). This result emphasizes that the water solubility of ZOF was increased five-fold in comparison with the free ZOF (0.3 mg mL^{-1}), due to the solubilizing effect of HPBCD.
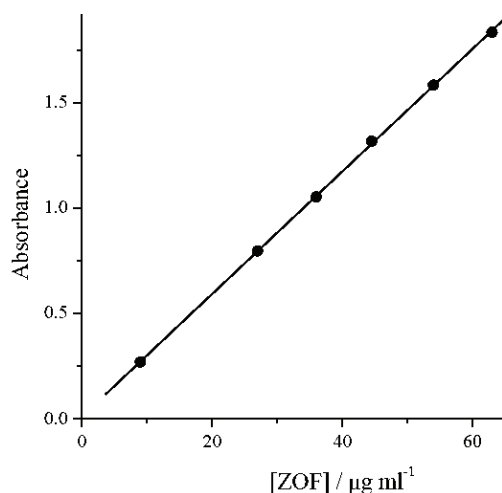
Fig. 6. Standard curve of ZOF (water, 25 °C).

A standard control experiment was further performed by dissolving the ZOF/ /HPBCD kneaded complex (59.2 mg), thus obtaining a clear solution that was equivalent to 1.51 mg of ZOF. This indicates that the solubility of the ZOF/ /HPBCD inclusion complex was adequate for tablet dosage form.[28,29]

CONCLUSIONS

This is the first work to report the physicochemical characterization of an inclusion complex between ZOF and HPBCD. Simultaneously, it brings forth the role of cyclodextrins, and HPBCD in particular, in improving the water solubility of the calcium salt of zofenopril. The formation of the 1:1 inclusion complex between ZOF and HPBCD, prepared by the kneading method, was proven by ATR-FTIR spectroscopy, PXRD and thermal analysis. The ZOF/HPBCD KP exhibited lower crystallinity and enhanced water solubility in comparison with free ZOF.

И З В О Д
ФИЗИЧКОХЕМИЈСКА КАРАКТЕРИЗАЦИЈА ИНКЛУЗИОНОГ КОМПЛЕКСА КОЈИ НАСТАЈЕ ИНТЕРАКЦИЈОМ ИЗМЕЂУ ЗОФЕНОПРИЛА И ХИДРОКСИПРОПИЛ-β-ЦИКЛОДЕКСТРИНА

LUCRETIA UDRESCU[1,2], LAURA SBÂRCEA[1], ADRIANA FULIAS[1], IONUT LEDETI[1], TITUS VLASE[3], PAUL BARVINSCHI[4] И LUDOVIC KURUNCZI[1,2]

[1]Faculty of Pharmacy, University of Medicine and Pharmacy, 300041 Timisoara, Romania, [2]Institute of Chemistry Timisoara of the Romanian Academy, 300223 Timisoara, Romania, [3]Research Center for Thermal Analysis in Environmental Problems, West University of Timisoara, 300115 Timisoara, Romania и [4]Faculty of Physics, West University of Timisoara, 300223 Timisoara, Romania

Калцијум-зофеноприл (ZOF) је један од најновијих инхибитора ангиотензин- кон- вертирајућег ензима (ACE), који је високо липофилан и слабо растворан у води. У циљу

потврде формирања инклузионог комплекса који има већу растворљивост у односу на ZOF, испитивана је интеракција између ZOF и хемијски модификованог β-циклодекс-трина (2-хидроксипропил-β-циклодекстрин, HPBCD). По први пут у овом раду дате су физичкохемијске карактеристике и описана је растворљивост комплекса који настаје инклузијом између ZOF и HPBCD. Формирање инклузионог комплекса ZOF/HPBCD, како у чврстом стању тако и у воденом раствору, потврђено је применом различитих спектроскопских техника (UV апсорпциона спектрофотометрија, дифракција рендген-ских зрака са прахова, IR спектроскопија са Фуријеовом трансформацијом). Добијени резултати ових испитивања су додатно потврђени на основу термалне анализе (TG/DTG/ /HF). На основу добијених резултата потврђено је да су физичкохемијске карактерис-тике бинарног ZOF/HPBCD система различите у односу на полазне супстанце, као и њихову смешу, што недвосмислено указује на формирање инклузионог комплекса. Нађено је да овај инклузиони комплекс има пет пута већу растворљивост у води у односу на полазни ZOF.

REFERENCES

1. A. Subissi, S. Evangelista, A. Giachetti, *Cardiovasc. Drug Rev.* **17** (1999) 115
2. E. Ambrosioni, *Am. J. Cardiovasc. Drugs* **7** (2007) 17
3. C. Borghi, A. F. G. Cicero, E. Ambrosioni, *Vasc. Health Risk Manag.* **4** (2008) 665
4. S. M. Singhvi, J. E. Foley, D. A. Willard, R. A. Morrison, *J. Pharm. Sci.* **79** (1990) 970
5. S. Evangelista, S. Manzini, *J. Int. Med. Res.* **33** (2005) 42
6. A. F. Pasini, U. Garbin, M. C. Nava, C. Stranieri, M. Pellegrini, V. Boccioletti, M. L. Lucheta, P. Fabrizzi, V. Lo Cascio, L. Cominacini, *Am. J. Hypertens.* **20** (2007) 443
7. R. Lozano, J. M. Joseph, B. J. Kline, *J. Pharm. Biomed. Anal.* **12** (1994) 173
8. T. Loftsson, *J. Inclusion Phenom. Macrocyclic Chem.* **44** (2002) 63
9. M. S. Ku, *AAPS J.* **10** (2008) 208
10. T. Loftsson, M. E. Brewster, *J. Pharm. Pharmacol.* **62** (2010) 1607
11. T. Loftsson, M. E. Brewster, M. Masson, *Am. J. Drug Deliv.* **2** (2004) 261
12. V. J. Stella, Q. He, *Toxicol. Pathol.* **36** (2008) 30
13. M. Semalty, M. Panchpuri, D. Singh, A. Semalty, *Curr. Drugs Discovery Technol.* **11** (2014) 154
14. L. Sbârcea, L. Udrescu, L. Drăgan, C. Trandafirescu, Z. Szabadai, M. Bojiţă, *Farmacia* **58** (2010) 478
15. P. Job, *Ann. Chim.* **9** (1928) 113
16. J. S. Negi, S. Singh, *Carbohydr. Polym.* **92** (2013) 1835
17. H. A. Benesi, J. H. Hildebrand, *J. Am. Chem. Soc.* **71** (1949) 2703
18. W. Misiuk, M. Zalewska, *Carbohydr. Polym.* **77** (2009) 482
19. A. Barth, C. Zscherp, *Q. Rev. Biophys.* **35** (2002) 369
20. R. Ručman, P. Zupet (Silverstone Pharma), Patent No. WO2013095307 A1 (2013)
21. C. Yuan, Z. Jin, X. Xu, *Carbohydr. Polym.* **89** (2012) 492
22. T. Mihajlovic, K. Kachrimanis, A. Graovac, Z. Djuric, S. Ibric, *AAPS PharmSciTech* **13** (2012) 623
23. K. M. Ahmed, Y. R. Singh, T. N. Rasiklal, L. S. Mahadeo (Glenmark Generics Limited), Patent No WO 2010084515 A2 (2010)
24. D. R. de Araujo, S. S. Tsuneda, C. M. S. Cereda, F. Del G. F. Carvalho, P. S. C. Prete, S. A. Fernandes, F. Yokaichiya, M. K. K. D. Franco, I. Mazzaro, L. F. Fraceto, A. de F. A. Braga, E. de Paula. *Eur. J. Pharm. Sci.* **33** (2008) 60

25. M. M. Doile, K. A. Fortunato, I. C. Schmucker, S. K. Schucko, M. A. S. Silva, P. O. Rodrigues, *AAPS PharmSciTech.* **9** (2008) 314
26. L. Sbârcea, L. Udrescu, L. Drăgan, C. Trandafirescu, Z. Szabadai, M. Bojiţă, *Pharmazie* **66** (2011) 584
27. E. Baka, J. E. A. Comer, K. Takács-Novák, *J. Pharm. Biomed. Anal.* **46** (2008) 335
28. W. Chen, L. J. Yang, S. X. Ma, X. D. Yang, B. M. Fan, J. Lin, *Carbohydr. Polym.* **84** (2011) 1321
29. S. X. Ma, W. Chen, X. D. Yang, N. Zhang, S. J. Wang, L. Liu, L. J. Yang, *J. Pharm. Biomed. Anal.* **67**–**68** (2012) 193.

QSPR study of supercooled liquid vapour pressures of polybrominated diphenyl ethers using the molecular distance–edge vector index

LONG JIAO[1,2]*, XIAOFEI WANG[1], SHAN BING[1], ZHIWEI XUE[3] and HUA LI[2]

[1]*College of Chemistry and Chemical Engineering, Xi'an Shiyou University, Xi'an 710065, P. R. China,* [2]*College of Chemistry and Materials Science, Northwest University, Xi'an 710069, P. R. China and* [3]*No. 203 Research Institute of the Nuclear Industry, Xianyang 712000, P. R. China*

Abstract: The quantitative structure property relationship (QSPR) for supercooled liquid vapour pressures (p_L) of polybrominated diphenyl ethers (PBDEs) was investigated. The molecular distance–edge vector (MDEV) index was used as the structural descriptor. The quantitative relationship between the MDEV index and log p_L was modelled by multivariate linear regression (MLR) and an artificial neural network (ANN). The leave-one-out cross validation and *k*-fold cross validation were performed to assess the prediction ability of the developed models. For the MLR method, the prediction root mean square relative error (*RMSRE*) of the leave-one-out cross validation and the *k*-fold cross validation were 9.95 and 9.05, respectively. For the ANN method, the prediction *RMSRE* of the leave-one-out cross validation and the *k*-fold cross validation were 8.75 and 8.31, respectively. It was demonstrated that the established models were practicable for predicting the log p_L values of PBDEs. The MDEV index was quantitatively related to the log p_L of PBDEs. MLR and linear ANN were practicable for modelling this relationship. Compared with the MLR, the ANN method exhibited slightly higher prediction accuracy. Subsequently, an MLR model, the regression equation of which was log $p_L =$ $= 0.2868M_{11} - 0.8449M_{12} - 0.0605$, and an ANN model, which was a two-input linear network, were developed. The two models could be used to predict the log p_L value of each PBDE.

Keywords: QSPR; PBDEs; supercooled liquid vapour pressures; molecular distance–edge vector index; artificial neural network.

INTRODUCTION

Polybrominated diphenyl ethers (PBDEs) are a group of brominated organic compounds that have been widely used as flame-retardants in many products,

499

such as building materials, electronics, furnishings, coatings, plastics, textiles, *etc*.[1,2] There are 209 PBDE congeners, distinguished by the number and position of bromine atoms. Although the production of some PBDEs has been restricted under the Stockholm Convention since 2010, PBDEs already exist in many environmental compartments, such as water, air, soil, vegetation, animals and humans.[3–6] They have gained increasing attention due to their environmental persistence, tendency to bioaccumulate through the food chain and risk to ecosystems and human health.[1,7,8] Being volatile organic compounds, the volatility of PBDEs may affect their fate and distribution in the environment. The super-cooled liquid vapour pressures at 298.15 K (p_L) is usually used to describe the volatility of non-polar organic pollutants and the equilibrium partitioning of a compound between the vapour phase and the liquid state. Thus, a quantitative study on the p_L of PBDEs is of great importance to understand the distribution, fate and transportation of PBDEs in the environment. A study on the p_L is also necessary for the design of extraction and cleanup techniques and for the environmental modelling of PBDEs.[4,9,10] Many studies focused on the p_L of PBDEs have been reported.[1,4–14] However, the determination of p_L is still a hard difficult due to the complexity of the analytical methods, high cost of experiments, and lack of chemical standards of some PBDEs.[4,9,10] To overcome this problem, much attention has been given to the quantitative structure property relationship (QSPR) method for a preliminarily estimate the p_L of PBDEs. Several QSPR models for the p_L of PBDEs were proposed.[9–14] These studies demonstrated that it is practicable to predict the p_L of PBDEs by using QSPR methods. However, some of the proposed QSPR models were not global models for the P_L of PBDEs and the used structural descriptors were not satisfactory. There are many limitations in the use of such models.[4] In addition, the development of some QSPR models was not easy because quantum chemical descriptors were used.[9,10] Actually, the generation and selection of quantum chemical descriptors are always time-consuming and complicated in QSPR studies. The need to develop more easy-to-use QSPR models for the p_L of PBDEs still exists. Therefore, the QSPR model for the p_L of PBDEs was investigated in this work. The molecular distance–edge vector (MDEV) index[15–19] was used as the structural descriptor of PBDEs. Multivariate linear regression (MLR) and linear artificial neural network (L-ANN) were employed to model the quantitative relationship between the p_L and the MDEV index of PBDEs.

CALCULATION METHODS

Data set

The MDEV index was calculated according to the approach presented in the following section. The calculated MDEV indexes are listed in Table S-I of the Supplementary material to this paper. The experimental p_L values of the 22 PBDEs given in Table S-II of the

Supplementary material are the super-cooled liquid vapour pressures at 298 K. The values of the p_L were taken from the literature.[9]

Root mean square relative error (*RMSRE*) was used to indicate the prediction performance of the obtained QSPR models. The *RMSRE* is defined as:

$$RMSRE = \sqrt{\frac{\sum (RE_i)^2}{n}} \tag{1}$$

where RE_i is the relative error of the ith sample, and n is the number of samples.

MDEV index

When calculating the MDEV index of a PBDE molecule, each non-hydrogen atom is regarded as a point and each chemical bond is considered as an edge. The whole molecule is regarded as a topological graph. The relative electronegativity of each bromine atom and benzene ring is defined as 1. Correspondingly, the MDEV index is defined as:

$$M_{kl} = \sum_{j \geq i} \frac{1}{d_{ik,jl}^2} , k, l = 1,2 \text{ and } l \geq k \tag{2}$$

In Eq. (2), k and l are the type of atoms ($k = 1$ or $l = 1$ denotes the bromine atom, and $k = 2$ or $l = 2$ denotes the benzene ring); items i and j are the coding number of a bromine atom or benzene ring. Additionally, i and j belongs to the kth and l^{th} type, respectively. The $d_{ik,jl}$ value represents the nearest relative distance between the ith and j^{th} atom. For example, $d_{i1,j1}$ means the shortest relative distance between the ith and j^{th} bromine atom. The relative distance between the two adjacent non-hydrogen atoms is defined as $d = 1$. According to Eq. (2), there are three elements, M_{11}, M_{12} and M_{22}, in the MDEV index for a PBDE molecule. For instance, the MDEV index of 2,2′,4,4′-PBDE should be calculated as follows:

$$M_{11} = \left(\frac{1}{4}\right)^2 + \left(\frac{1}{6}\right)^2 + \left(\frac{1}{8}\right)^2 + \left(\frac{1}{8}\right)^2 + \left(\frac{1}{10}\right)^2 + \left(\frac{1}{4}\right)^2 = 0.1940$$

$$M_{12} = \left(\frac{1}{1}\right)^2 + \left(\frac{1}{4}\right)^2 + \left(\frac{1}{1}\right)^2 + \left(\frac{1}{6}\right)^2 + \left(\frac{1}{1}\right)^2 + \left(\frac{1}{4}\right)^2 + \left(\frac{1}{1}\right)^2 + \left(\frac{1}{6}\right)^2 = 4.1806$$

$$M_{22} = \left(\frac{1}{2}\right)^2 = 0.25 \tag{3}$$

Obviously, the M_{22} value of each PBDE is equal to 0.25. Thus, M_{11} and M_{12} were used to quantitatively describe the structure of the PBDEs.

Artificial neural network

ANN[20-30] is a multivariate calibration method capable of modelling complex functions. Its basic processing unit is the neuron (node). An ANN comprises a number of neurons organized in different layers. A linear artificial neural network,[26-30] is a kind of neural network having no hidden layers, but an output layer with fully linear neurons (*i.e.*, linear neurons with a linear activation function). It is the simplest ANN and is usually used to develop a linear model, In a L-ANN, the neurons between the input and output layers fully connect, while the neurons in the same layer do not. The basic architecture of a L-ANN is shown in Fig. 1.
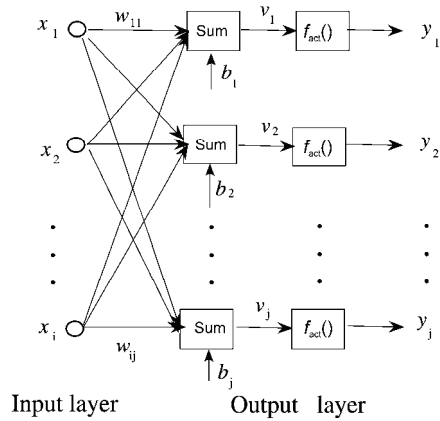
Fig. 1. The architecture of the employed linear artificial neural network.

Input layer   Output layer

In Fig. 1, x_i (i = 1, 2,…, n), y_j (j =1, 2,…, m) and w_{ij} are the input variables, output variables and the element of connection weight matrix **W**, respectively, and b_j is the bias vector, which corresponds to the thresholds. The symbol $f_{act}()$ denotes the activation function. Prior to a training procedure, the input and output variables require normalization. When the network is executed, it effectively multiplies the input variables by the weights matrix, and then adds the bias vector. Hence, the post synaptic potential (PSP) function of a neuron can be described as follows:

$$v_j = \sum_{i=1}^{n} x_i w_{ij} + b_j \tag{4}$$

Routinely, the activation function used in a L-ANN is a linear function described by:

$$y_j = v_j \tag{5}$$

As there are no non-linear functions or hidden neurons in the network, a L-ANN is ideal for dealing with linear problems. Actually, the training of a linear network means finding the optimal setting for the weight matrix **W** to minimize the root-mean-squared-error of the calibration set. In order to achieve this aim, known samples are generally divided into two sets: a training set and a verification set. The network is trained using the training set, but is also tested after each epoch using the verification set. The training should be stopped once a deterioration in the verification error is observed. Overfitting and overlearning can be effectively avoided in this way. Although the verification set is used to identify the best network, actually, training algorithms do not use the verification set to adjust the weights of the network. A standard pseudo-inverse linear optimization algorithm[26] is usually employed to train the network. This algorithm uses the singular value decomposition technique to calculate the pseudo-inverse of the matrix needed to set the weights in a linear output layer, so as to find the least mean squared solution. Essentially, it guarantees finding the optimal setting for the weights in a linear layer.

The main difference between a MLR and a L-ANN is the optimization algorithm. In a MLR, the aim of the least square algorithm is to minimize the sum of the squared residuals of the training set. As for L-ANN, the aim of the training algorithm is to minimize the root mean squared error of the verification set.[26] Thus, the prediction ability of a L-ANN is usually superior to that of a MLR.

Leave-one-out cross validation

The leave-one-out cross validation[18-20,27,31] is a conventional algorithm for estimating the predictive performance of a multivariable calibration model. Usually, practical calibration experiments have to be based on a limited set of available samples. The idea behind the leave-one-out cross validation algorithm is to predict the property value of each sample in turn with the calibration model developed with the remaining samples. When applying the algorithm to a dataset with N samples, the calibration modelling is performed N times, each time using $N–1$ samples for the modelling and one sample for testing. Thus, the procedure of leave-one-out cross validation can be divided into N segment. In each segment i ($i = 1,…, N$), there are three steps: 1) taking sample i out as temporary 'test set', which is not used to develop the calibration model, 2) developing a calibration model with the remaining $N–1$ samples, 3) testing the developed model with sample i, calculating and storing the prediction error of the sample. The advantage of leave-one-out cross validation over random sub-sampling is that each sample is used for both training and validation, and each sample is used for validation exactly once.

k-*Fold cross validation*

In k-fold cross validation,[32,33] the original N samples are randomly partitioned into k equal size subgroups, called folds (if $k = N$, this is equivalent to the leave-one-out cross validation). Of the k subgroups, a single subgroup is retained as the test set for testing the model, and the remaining $k−1$ subgroups are used as the training set for generating the model. The cross validation process is then repeated k times, with each of the k subgroups used exactly once as the test set. The k results from the folds can then be averaged (or otherwise combined) to produce a single estimation.

Software

All data processing was realized with subroutines developed under Matlab (ver. 7.0). The computation was performed on a personal computer equipped with Core2 T9400 processor.

RESULTS AND DISCUSSION

The MDEV index of the investigated 22 PBDEs was calculated. The obtained MDEV indexes are listed in Table S-I of the Supplementary material. Clearly, the MDEV indexes of different PBDE molecules are quite different. It was demonstrated that MDEV index can describe the structural differences among these PBDE molecules. Thus, it is reasonable to use the MDEV index as the structural descriptor for developing a QSPR model of PBDEs.

MLR model

Generally, a simple model should always be chosen in preference to a complex model unless the latter fits the data better. Thus, first, it was investigated whether MLR is practicable to model the quantitative relationship between the MDEV index and log p_L value of these PBDEs. The MDEV index was used as the independent variable and log p_L as the dependent variable to develop the regression model. In order to assess the predictive ability of the developed model, two validation methods, leave-one-out cross validation and k-fold cross validation, were performed. The results of the leave-one-out cross validation are presented in Table S-II of the Supplementary material, from which it could be seen

that the predicted log p_L values were in agreement with the experimental values of log p_L. For the 22 compounds, the *RMSRE* of prediction was 9.95. Moreover, the predicted log p_L values were plotted *versus* the experimental values (shown in Fig. 2a) and the plot showed a linear relationship ($y = 0.9470x - 0.1433$ with $R = 0.9853$) between the predicted and experimental log p_L values. Subsequently, *k*-fold cross validation was performed to assess further the predictive ability of the MLR model. In this procedure, the 22 samples were partitioned into 7 folds. There were 4 samples in each fold. The prediction results of the *k*-fold cross validation are given in Table S-III of the Supplementary material. As shown in this table, the predicted log p_L values were still in agreement with the experimental values. For the 7 folds, the total prediction *RMSRE* was 9.05. A plot of the predicted log p_L values *versus* the experimental values (presented in Fig. 2b) shows a linear relationship ($y = 0.9591x - 0.0722$ with $R = 0.9818$). The results of the leave-one-out and *k*-fold cross validation demonstrate that the MDEV index is quantitatively related to the log p_L of these PBDEs. MLR was shown to be practicable for modelling the quantitative relationship between the MDEV index and log p_L. Obviously, a linear QSPR model based on the MDEV index could be used to predict the log p_L values of PBDEs. Hence, an MLR model was developed using the 22 PBDEs listed in Table S-I of the Supplementary material. The obtained regression equation was log $p_L = 0.2868M_{11} - 0.8449M_{12} - 0.0605$. The R^2, standard error of the estimate and the F value of the regression model were 0.9800, 0.2007 and 466.5, respectively. Thus, this model could be used to predict the log p_L value of all the PBDEs.

Fig. 2. Experimental log p_L values *vs.* the log p_L values predicted by the MLR model: a) results of the leave-one-out cross validation and b) results of the *k*-fold cross validation.

L-ANN model

Besides MLR, L-ANN, which is the simplest artificial neural network, is a commonly used linear calibration method in QSPR studies. Thus, it was investigated whether a better model could be established using a L-ANN. A 2–1 L-ANN (*i.e.*, 2 input variables and 1 output variable in the network) was used to establish the calibration model. The used activation function is presented as Eq. (5). The MDEV index and log p_L were used as input and output variables, respectively. Prior to the training procedure, the input and output variables were normalized. In each run of the ANN, the verification set comprised four randomly selected samples.

The leave-one-out cross validation and *k*-fold cross validation were still performed to assess the prediction performance of the developed model. The results of the leave-one-out cross validation are listed in Table S-II of the Supplementary material. As shown in Table S-II, the predicted log p_L values were in good agreement with the experimental log p_L values. For all 22 compounds, the *RMSRE* of the prediction was 8.75. Moreover, the predicted log p_L value were plotted *versus* the experimental ones (presented in Fig. 3a) and the plot showed a linear relationship ($y = 0.9515x – 0.1309$ with $R = 0.9873$) between the predicted and experimental log p_L values. The results of the *k*-fold cross validation are given in Table S-III. As shown in the table, the predicted log p_L values were also in good agreement with the experimental log p_L values. For the 7 folds, the total prediction *RMSRE* was 8.31. The plot of the predicted log p_L *versus* the experimental log p_L values (presented in Fig. 3b) showed a linear relationship ($y = 0.9643x – 0.0557$ with $R = 0.9826$). Obviously, the prediction accuracy of the L-ANN model was slightly better than that of the MLR model. Using the L-ANN was slightly better than using the MLR for the prediction of the log p_L values of
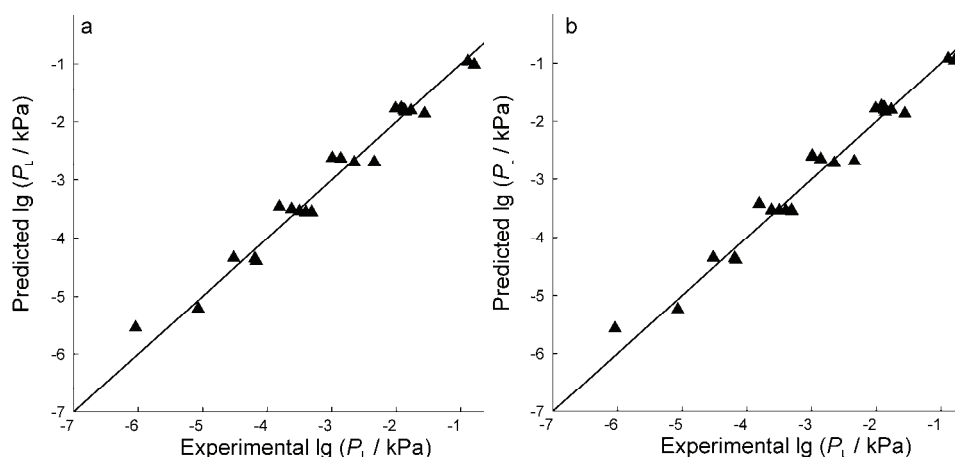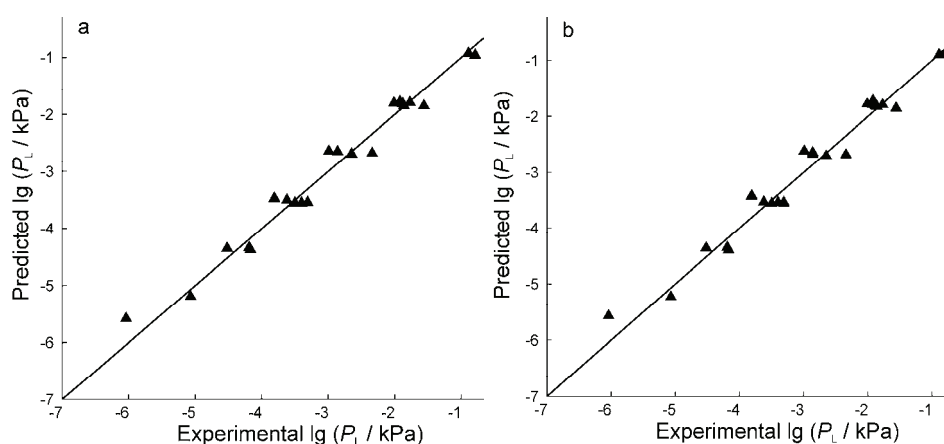

Fig. 3. Experimental log p_L values *vs.* the log p_L values predicted by the L-ANN model: a) results of the leave-one-out cross validation and b) the results of the *k*-fold cross validation.

the PBDEs. It was demonstrated that L-ANN is a practicable and promising method for modelling the quantitative relationship between the MDEV index and log p_L of PBDEs. Thus, a 2–1 L-ANN model was developed by using the 22 PBDEs listed in Table S-1 of the Supplementary material as the calibration set. The verification set for training the model comprises 4 randomly selected samples. The input and output variables were normalized in the training procedure. This model could be used to predict the log p_L values of all PBDEs.

CONCLUSIONS

A method for developing a QSPR model of the supercooled liquid vapour pressures of PBDEs was investigated. The MDEV index, which can be generated easier than quantum chemical descriptors, was used as the structural descriptor of the PBDEs. Accordingly, the use of the MDEV index as structural descriptor was more convenient than using quantum chemical descriptor when developing a QSPR model for the p_L of PBDEs. Calibration models between the MDEV index and log p_L were established using MLR and ANN methods. The predictive ability of the developed models was assessed using leave-one-out cross validation and k-fold cross validation. The validation result demonstrated that the MDEV indexes of the PBDEs were quantitatively related to the log p_L values of the PBDEs. Thus, it was reasonable to establish the QSPR model for the log p_L values of the PBDEs based on the MDEV index. In addition, the result indicated that both MLR and L-ANN are practicable for modelling the quantitative relationship between the MDEV index and log p_L value of PBDEs. In summary, the proposed method should be easy-to-use and practicable for predicting the log p_L values of PBDEs. Therefore, an MLR model and an ANN model, which could be used to predict the log p_L values of all PBDEs, were developed. The regression equation of the MLR model was log $p_L = 0.2868M_{11} - 0.8449M_{12} - 0.0605$. The ANN model was a 2–1 L-ANN that was trained using the 22 known PBDEs as a calibration set.

SUPPLEMENTARY MATERIAL

MDEV indexes of the investigated PBDEs and results of the leave-one-out cross validation and k-fold cross validation, Tables S-I–S-III. respectively, are available electronically from http://www.shd.org.rs/JSCS/, or from the corresponding author on request.

И З В О Д

QSPR СТУДИЈА НАПОНА ПАРЕ СУПЕРОХЛАЂЕНИХ ПОЛИБРОМОВАНИХ ДИФЕНИЛ ЕТАРА ПРИМЕНОМ МОЛЕКУЛСКОГ ВЕКТОРСКОГ ИНДЕКСА

LING JIAO[1,2], XIAOFEI WANG[2], SHAN BING[1], ZHIWEI XUE[3] и HUA LI[2]

[1]Xi'an Shiyou University, Xi'an, P. R. China, [2]Northwest University, Xi'an, P. R. China и [3]Research Institute of Nuclear Industry, Xianyang, P. R. China

Испитивана је квантитативна релација између структуре и својства (QSPR) за напон паре суперохлађених полибромованих дифенил етара (PBDE). Као структурни дескриптор, примењен је молекулски векторски индекс MDEV. Корелација између напона паре и MDEV анализирана је мултиваријантном линеарном регресијом (MLR) помоћу вештачких неуронских мрежа (ANN). Показано је да добијени модели омогућују квантитативно предвиђање напона паре за PBDE. Методом ANN се постижу нешто тачнији резултати него са MLR.

(Примљено 17. јула, ревидирано 30. августа, прихваћено 1. септембра 2014)

REFERENCES

1. H. A. Anderson, P. Imma, L. Knobeloch, M. Turyk, J. Mathew, C. Buelow, V. Persky, *Chemosphere* **73** (2008) 187
2. EPA, http://www.epa.gov/ace/pdfs/Biomonitoring-PBDEs.pdf (accessed in Jan, 2014)
3. Stockholm Convention, http://chm.pops.int/TheConvention/ThePOPs/ListingofPOPs/ /tabid/2509/Default.aspx (accessed on 10th July, 2014)
4. C. Y. Yue, L. Y. Li, *Environ. Pollut.* **180** (2013) 312
5. M. Alaee, R. J. Wenning. *Chemosphere* **46** (2002) 579
6. F. M. Jaward, N. J. Farrar, T. Harner, A. J. Sweetman, K. C. Jones, *Environ. Sci. Technol.* **38** (2004) 34
7. Y. W. Wang, C. Y. Zhao, W. P. Ma, H. X. Liu, T. Wang, G. B. Jiang, *Chemosphere* **64** (2006) 515
8. D. J. Watkins, M. D. McClean, A. J. Fraser, J. Weinberg, H. M. Stapleton, T. F. Webster, *Environ. Int.* **59** (2013) 124
9. H. Y. Xu, J. W. Zou, Q. S. Yu, Y. H. Wang, J. Y. Zhang, H. X. Jin, *Chemosphere* **66** (2007) 1998
10. Z. Y. Wang, X. L. Zeng, Z. C. Zhai, *Sci. Total Environ.* **389** (2008) 296
11. E. Papa, S. Kovarich, P. Gramatica, *QSAR Comb. Sci.* **28** (2009) 790
12. A. Wong, Y. D. Lei, M. Alaee, F. Wania, *J. Chem. Eng. Data* **46** (2001) 239
13. S. A. Tittlemier, G. T. Tomy, *Environ. Toxicol. Chem.* **20**(2001) 146
14. S. A. Tittlemier, T. Halldorson, G. A. Stern, G. T. Tomy, *Environ. Toxicol. Chem.* **21** (2002) 1804
15. S. S. Liu, H. L. Liu, Z. N. Xia, C. Z. Cao, Z. L. Li, *J. Chem. Inf. Comput. Sci.* **39** (1999) 951
16. C. S. Yin, W. M. Guo, T. Lin, S. S. Liu, R. Q. Fu, Z. X. Pan, L. S. Wang, *J. Chin. Chem. Soc.* **48** (2001) 739
17. H. H. Liu, X. Xiao, J. Qin, Y. M. Liu, *J. Chongqing Inst. Tech.* **19** (2005) 67 (In Chinese)
18. L. Jiao, X. Wang, H. Li, Y. Wang, *J. Serb. Chem. Soc.* **79** (2014) 965
19. L. Jiao, Z. W. Xue, G. F. Wang, X. F. Wang, H. Li, *Chemometr. Intell. Lab. Syst.* **137** (2014) 91
20. L. Jiao, *Chemosphere* **80** (2010) 671

21. M. Jalali-Heravi, M. Asadollahi-Baboli, P. Shahbazikhah, *Euro. J. Med. Chem.* **43** (2008) 548
22. M. H. Fatemi, Z. G. Chahi, *SAR QSAR Environ. Res.* **23** (2012) 155
23. R. Smiljanic, D. Lazic, M. Gligoric, M. Jotanovic, Z. Zivkovic, I. Mihajlovic, *J. Serb. Chem. Soc.* **76** (2011) 1163
24. X. J. Yao, A. Panaye, J. P. Doucet, H. F. Chen, R. S. Zhang, B. T. Fan, M. C. Liu, Z. D. Hu, *Anal. Chim. Acta* **535** (2005) 259
25. M. Fatemi, Z. Ghorbannezhad, *J. Serb. Chem. Soc.* **76** (2011) 1003
26. Statsoft, http://www.statsoft.com/textbook/neural-networks (accessed on 10th July, 2014)
27. L. Jiao, H. Li, Chemometr. *Intell. Lab. Syst.* **103** (2010) 90
28. Y. X. Zhang, H. Li, A. X. Hou, J. Havel, *Chemometr. Intell. Lab. Syst.* **82** (2006) 165
29. C. S. Yin, Y. Shen, S. S. Liu, Q. S. Yin, W. M. Guo, Z. X. Pan, *Comput. Chem.* **25** (2001) 239
30. W. J. Zhang, X. Q. Zhong, G. H. Liu, *Stoch. Environ. Res. Risk, A* **22** (2008) 207
31. H. A. Martens, P. Dardenne, *Chemometr. Intell. Lab. Syst.* **44** (1998) 99
32. M. Zounemat-Kermani, O. Kisi, T. Rajaee, *Appl. Soft Comput.* **13** (2013) 4633
33. Wikipedia, http://en.wikipedia.org/wiki/Cross-validation(statistics) (accessed on 10th July 2014).

QSPR study of supercooled liquid vapour pressures of polybrominated diphenyl ethers using the molecular distance–edge vector index

LONG JIAO[1,2]*, XIAOFEI WANG[1], SHAN BING[1], ZHIWEI XUE[3] and HUA LI[2]

[1]College of Chemistry and Chemical Engineering, Xi'an Shiyou University, Xi'an 710065, P. R. China, [2]College of Chemistry and Materials Science, Northwest University, Xi'an 710069, P. R. China and [3]No. 203 Research Institute of the Nuclear Industry, Xianyang 712000, P. R. China

TABLE S-I. MDEV indexes of the investigated PBDEs

No.	PBDE	M_{11}	M_{12}
1	2-BDE	0	1.0625
2	3-BDE	0	1.04
3	2,4-BDE	0.0625	2.0903
4	2,4′-BDE	0.0156	2.0903
5	2,6-BDE	0.0625	2.125
6	3,4-BDE	0.1111	2.0678
7	3,4′-BDE	0.0123	2.0678
8	4,4′-BDE	0.01	2.0556
9	2,4,6-BDE	0.1875	3.1528
10	2,4′,6-BDE	0.0938	3.1528
11	3,3′,4-BDE	0.1391	3.1078
12	3,4,4′-BDE	0.1335	3.0956
13	2,2′,4,4′-BDE	0.194	4.1806
14	2,3′,4,4′-BDE	0.232	4.1581
15	2,3′,4,6-BDE	0.2407	4.1928
16	2,4,4′,6-BDE	0.2288	4.1806
17	3,3′,4,4′-BDE	0.2725	4.1356
18	2,2′,3,3′,4-BDE	0.508	5.2328
19	2,2′,4,4′,5-BDE	0.3779	5.2206
20	2,3′,4,4′,6-BDE	0.393	5.2206
21	2,2′,4,4′,5,5′-BDE	0.5774	6.2606
22	2,3,3′,4,4′,5,6-BDE	1.0359	7.3006

---

* Corresponding author. E-mail: mop@xsyu.edu.cn

JIAO *et al*

TABLE S-II. Results of the leave-one-out cross validation

No.	PBDE	Experimental log p_L	Predicted log p_L		Relative error, %	
			MLR	ANN	MLR	ANN
1	2-BDE	–0.79	–1.01	–0.96	27.85	21.52
2	3-BDE	–0.89	–0.95	–0.93	6.74	4.49
3	2,4-BDE	–1.77	–1.81	–1.79	2.26	1.13
4	2,4′-BDE	–1.86	–1.82	–1.85	–2.15	–0.54
5	2,6-BDE	–1.56	–1.86	–1.85	19.23	18.59
6	3,4-BDE	–1.92	–1.76	–1.78	–8.33	–7.29
7	3,4′-BDE	–1.88	–1.80	–1.81	–4.26	–3.72
8	4,4′-BDE	–2.01	–1.77	–1.80	–11.94	–10.45
9	2,4,6-BDE	–2.34	–2.69	–2.68	14.96	14.53
10	2,4′,6-BDE	–2.65	–2.70	–2.69	1.89	1.51
11	3,3′,4-BDE	–2.86	–2.63	–2.65	–8.04	–7.34
12	3,4,4′-BDE	–2.99	–2.62	–2.64	–12.37	–11.71
13	2,2′,4,4′-BDE	–3.5	–3.54	–3.55	1.14	1.43
14	2,3′,4,4′-BDE	–3.62	–3.50	–3.50	–3.31	–3.31
15	2,3′,4,6-BDE	–3.4	–3.55	–3.55	4.41	4.41
16	2,4,4′,6-BDE	–3.31	–3.55	–3.54	7.25	6.95
17	3,3′,4,4′-BDE	–3.81	–3.46	–3.47	–9.19	–8.92
18	2,2′,3,3′,4-BDE	–4.19	–4.35	–4.34	3.82	3.58
19	2,2′,4,4′,5-BDE	–4.17	–4.39	–4.37	5.28	4.80
20	2,3′,4,4′,6-BDE	–4.52	–4.34	–4.35	–3.98	–3.76
21	2,2′,4,4′,5,5′-BDE	–5.07	–5.21	–5.19	2.76	2.37
22	2,3,3′,4,4′,5,6-BDE	–6.04	–5.54	–5.58	–8.28	–7.62

TABLE S-III. Results of the *k*-fold cross validation

Fold	PBDE	Experimental log p_L	Predicted log p_L		Relative error, %	
			MLR	ANN	MLR	ANN
1	2-BDE	–0.79	–0.95	–0.89	20.25	12.66
	3,4-BDE	–1.92	–1.77	–1.72	–7.81	–10.42
	3,3′,4-BDE	–2.86	–2.65	–2.64	–7.34	–7.69
	2,4,4′,6-BDE	–3.31	–3.53	–3.54	6.65	6.95
2	3-BDE	–0.89	–0.92	–0.90	3.37	1.12
	3,4′-BDE	–1.88	–1.76	–1.79	–6.38	–4.79
	3,4,4′-BDE	–2.99	–2.59	–2.61	–13.38	–12.71
	3,3,4,4′-BDE	–3.81	–3.43	–3.43	–9.97	–9.97
3	2,4-BDE	–1.77	–1.80	–1.79	1.69	1.13
	4,4′-BDE	–2.01	–1.78	–1.78	–11.44	–11.44
	2,2′,4,4′-BDE	–3.50	–3.54	–3.56	1.14	1.71
	2,2′,3,3′,4-BDE	–4.19	–4.36	–4.35	4.06	3.82
4	2,4′-BDE	–1.86	–1.84	–1.82	–1.08	–2.15
	2,4,6-BDE	–2.34	–2.69	–2.68	14.96	14.53
	2,3′,4,4′-BDE	–3.62	–3.53	–3.53	–2.49	–2.49
	2,2′,4,4′,5-BDE	–4.17	–4.39	–4.40	5.28	5.52

TABLE S-III. Continued

Fold	PBDE	Experimental log p_L	Predicted log p_L		Relative error, %	
			MLR	ANN	MLR	ANN
5	2,6-BDE	−1.56	−1.87	−1.85	19.87	18.59
	2,4′,6-BDE	−2.65	−2.72	−2.70	2.64	1.89
	2,3′,4,6-BDE	−3.40	−3.54	−3.54	4.12	4.12
	2,3′,4,4′,6-BDE	−4.52	−4.35	−4.36	−3.76	−3.54
6	3,4-BDE	−1.92	−1.74	−1.79	−9.38	−6.77
	3,3′,4-BDE	−2.86	−2.65	−2.67	−7.34	−6.64
	2,4,4′,6-BDE	−3.31	−3.55	−3.56	7.25	7.55
	2,2′,4,4′,5,5′-BDE	−5.07	−5.24	−5.23	3.35	3.16
7	3,4′-BDE	−1.88	−1.80	−1.81	−4.26	−3.72
	3,4,4′-BDE	−2.99	−2.61	−2.62	−12.71	−12.37
	3,3,4,4′-BDE	−3.81	−3.42	−3.42	−10.24	−10.24
	2,3,3′,4,4′,5,6-BDE	−6.04	−5.57	−5.57	−7.78	−7.78

Thermodynamic solubility of piroxicam in propylene glycol + water mixtures at 298.2–323.2 K – data report and modeling

SHAHLA SOLTANPOUR* and ZAHRA BASTAMI

Faculty of Pharmacy, Zanjan University of Medical Sciences, Zanjan 45139, Iran

Abstract: The solubility of piroxicam (66 data points) in binary mixtures of propylene glycol (PG) + water at six different temperatures ranging from 298.2 to 323.2 K are reported. Three different cosolvency models, *i.e.*, the Yalkowsky, the Jouyban–Acree and a combined version of the Jouyban–Acree model with the van't Hoff approach, were used for correlating the reported data. All the results of the analyses showed an acceptable range of the error percentages.

Keywords: thermodynamic; solubility; piroxicam; propylene glycol.

INTRODUCTION

The solubility of drugs is an important field in the pharmaceutical area, because it permits the scientist to choose the best solvent or solvent mixture for dissolving a drug or a combination of drugs. Solutions of drugs could be used to measure the purity of the bulk drug, prepare a liquid formulation and/or extract an ingredient from a synthetic mixture or a natural source. Hence, it is important to determine systematically the solubility of pharmaceutical compounds. The dependence of the solubility enhancement at higher temperatures to the molecular mechanisms enables respective thermodynamic analyses.

Piroxicam is a nonsteroidal anti-inflammatory drug, which is used for pain relieving and anti-inflammatory effects. The anhydrate form of piroxicam can be hydrated to dihydrate species by crystallization with water or exposure to a relative humidity over 43 %. The drug is described as a poorly water soluble and highly permeable drug (class II of the Biopharmaceutics Classification System (BCS)).[1,2]

To achieve an optimized solvent composition of a mixture for dissolving a certain amount of a drug in a given volume of the solvent, the trial and error approach is employed in practice, which is time consuming and expensive.

509

Therefore, using cosolvency models could be an appropriate solution. Numerous models have been presented for correlation/prediction of the solubility of drugs in mixed solvents.[3] The final goal of developing cosolvency equations is to predict the solute solubility in mixed solvents using a minimum number of experimental data points or even without them.

COMPUTATIONAL METHOD END EXPERIMENTAL

One of the main cosolvency models is the log–linear model of Yalkowsky, which has a linear relationship between the solute solubility and the solvent fraction and is very simple and suitable for mixtures. It can be written as:[4]

$$\log X_m^{Sat} = w_1 \log X_1^{Sat} + w_2 \log X_2^{Sat} \tag{1}$$

where X_m^{Sat} is the solubility of the solute in the solvent mixture; X_1^{Sat} and X_2^{Sat} denote the solubility in neat solvents 1 and 2, respectively; and w_1 and w_2 represent the mass fraction of solvents 1 (cosolvent) and 2 (water) in the absence of the solute. Equation (1) can be rearranged as Eq. (2) by considering $w_2 = 1 - w_1$:

$$\log X_m^{Sat} = \log X_2^{Sat} + K_1 w_1 \tag{2}$$

or

$$\log X_m^{Sat} = K_0 + K_1 w_1 \tag{3}$$

By further investigations, $K_1 = A + B \log P$ was obtained in which $\log P$ is the partition coefficient of the drug:[5]

$$\log X_m^{Sat} = \log X_2^{Sat} + (A + B \log P)w_1 \tag{4}$$

where A and B are model constants and w_1 is the mass fraction of the cosolvent.

If there is no interaction between solvent–solvent or solvent–solute, the model of Yalkowsky can predict the solubility well. However, most solvent mixtures are not ideal and interactions occur; therefore, other terms need to be added to the basic log–linear model in order to illustrate the roles of these interactions in the solute solubility.

For showing the variation of the solubility with both temperature and solvent composition, the Jouyban–Acree model, which can compute the mathematical descriptors for the probable interactions in the mixture, can be used. The general form of the model for the solubility in binary solvent mixture at various temperatures can be written as:[3]

$$\log X_{m,T}^{Sat} = w_1 \log X_{1,T}^{Sat} + w_2 \log X_{2,T}^{Sat} + \frac{w_1 w_2}{T} \sum_{i=0}^{2} J_i (w_1 - w_2)^i \tag{5}$$

in which $X_{m,T}^{Sat}$ is the molar solubility of the solute in the solvent mixture at temperature T, w_1 and w_2 are the mass fractions of solvents 1 and 2, respectively. $X_{1,T}^{Sat}$ and $X_{2,T}^{Sat}$ are the solubility of the solute in the neat solvents 1 and 2, respectively, and J_i are the constants of the model computed by regression analysis. A limitation for the Jouyban–Acree model is computing the model constants that require a number of experimental solubility data of the solute in the binary solvent mixtures.

Solubility of the drugs in mono-solvents at different temperatures can be predicted using the van't Hoff approach (Eq. (6)).[6] The required experimental data are the solubilities in the solvents mixture ($\log X_T^{Sat}$).

$$\log X_T^{\text{Sat}} = A + \frac{B}{T} \tag{6}$$

where *A* and *B* are the model constants calculated by regression method.

A combination of the Jouyban–Acree and van't Hoff models enables the prediction of drug solubility in mixed solvents at different temperatures after a training process using solubility data points; e.g. at the lowest and highest temperatures.[7,8] The combined version could be represented as:

$$\log X_{\text{m},T}^{\text{Sat}} = w_1\left(A_1 + \frac{B_1}{T}\right) + w_2\left(A_2 + \frac{B_2}{T}\right) + \frac{w_1 w_2}{T}\sum_{i=0}^{2} J_i (w_1 - w_2)^i \tag{7}$$

where A_1, B_1, A_2, B_2 and J_i terms are the model constants. With this combination, the experimental solubility data are replaced with the calculated ones, which in this case, Eq. (7) is a valuable model for fitting the solubility data because the input includes no experimental data.

In a previous study,[9] a generally trained version of the Jouyban–Acree model was reported for propylene glycol (PG)–water binary mixtures:

$$\log X_{\text{m},T}^{\text{Sat}} = w_1 \log X_{1,T}^{\text{Sat}} + w_2 \log X_{2,T}^{\text{Sat}} + \frac{w_1 w_2}{T}\left[37.030 + 319.490(w_1 - w_2)\right] \tag{8}$$

In this step, this equation was used for predicting the solubilities of piroxicam at 6 different temperatures.

To evaluate the accuracy of the computational parts, the mean relative deviation (*MRD*) between the calculated and observed solubilities was used. The *MRD* value is calculated using:

$$MRD = \frac{100}{N}\left(\frac{\left|X_{\text{m},T}^{\text{Calculated}} - X_{m,T}^{\text{Observed}}\right|}{X_{\text{m},T}^{\text{Observed}}}\right) \tag{9}$$

where *N* is the number of data points in each set.

Materials

Piroxicam (0.999 mass fraction) was purchased from Alborz–Daru (Qazvin, Iran). The purity of piroxicam was checked by measuring the melting point range (471–473 K) and by comparing the measured solubilities in monosolvents with the corresponding data from the literature.[10] PG (0.995 mass fraction) was purchased from Merck (Germany). Double distilled water was used for the preparation of the solutions.

Drug solution preparation

All binary mixtures were prepared with an accuracy of 0.001 mass fractions.

Solubility determination

The solubility of piroxicam was determined by equilibrating an excess amount of the solid in the prepared binary solvent mixtures using a shaker (Behdad, Tehran, Iran) placed in an incubator equipped with a temperature-controlling system at different temperatures with an uncertainty of 0.2 K (Hoorteb, Tehran, Iran) for 3 days to reach the equilibrium at 298.2 K. After solubility determination and density measurement at 298.2 K, the remaining solutions containing the excess solid were placed at 303.2 K for 2 day and the measurements were performed. The same procedure was repeated for the other temperatures. The solutions were

filtered using hydrophilic Durapore filters (0.45 μm, Millipore, Ireland) and after diluting with methanol, the absorbance of these solutions were recorded at 360 nm using a UV–Vis spectrophotometer (Beckman DU-650, Fullerton, USA). The reported concentrations of the dilute solutions are an average of at least three experimental measurements, and the mean relative standard deviation (*RSD*) of three repetitive experiments was 2.6 %. The densities of the saturated solutions were determined using a 5 mL pycnometer.

RESULTS AND DISCUSSION

The minimum solubility of piroxicam was observed in aqueous solution (2.8×10^{-5} M or 1.3×10^{-7} mole fraction), which is in agreement with the literature value,[11] and the maximum solubility of piroxicam was observed in neat PG at 323.2 K (1.95×10^{-4} M). As a clear result for the experimental solubility data, the addition of the cosolvent to the aqueous solutions and increasing the temperature led to solubility enhancement. Table S-I of the Supplementary material to this paper presents the mass fractions of the binary solvent mixtures, the densities of the saturated solutions, the experimental and calculated solubilities of piroxicam at different temperatures using three analyses, which are described as follow.

Numerical analysis I includes fitting the binary solubility data to Eq. (4) (Yalkowsky). The highest and lowest *MRD*s belong to the solubility set at 298.2 and 318.2 K with 16.6 and 1.4 %, respectively, and the overall mean relative deviation (*OMRD*) was 9.6 %. As it is clear from the equation, the aqueous solubility is the only input data that was used for the fitting process, and the purpose of the modeling was to use a model with less input data and the simplest view. Thus, the *OMRD* value of 9.6 % for Eq. (4) is very good and acceptable.

In numerical analysis II, the solubility data were fitted to the Eq. (5) (the Jouyban–Acree model) and the highest *MRD* was 6.6 % for the solubilities at 323.2 K, and the lowest one was 0.7 % for the solubilities at 318.2 K. In this model, the solubilities of piroxicam in the neat solvents were the input data, and some terms were also added to the model to cover the interactions between solvent–solvent and solvent–solute molecules. Overall, these additions in this model resulted in a very low *OMRD* (2.5 %) for fitting process, which was completely good and acceptable. The produced model is:

$$\log X_{m,T}^{Sat} = f_1 \log X_{1,T}^{Sat} + f_2 \log X_{2,T}^{Sat} +$$
$$+ \frac{f_1 f_2}{T}\left(1.244 - 20.174\left(f_1 - f\right) - 39.030\left(f_1 - f\right)^2\right) \tag{10}$$

In numerical analysis III, the reported solubility data were fitted to Eq. (7), the Jouyban–Acree model combined with the van't Hoff equation. The highest and lowest *MRD*s were for the solubilities at 298.2 and 318.2 K with 29.9 and 4.5 %, respectively. In this analysis, the input data contained no experimental values, and the solubilities in the neat solvents were replaced by the constants from the van't Hoff approach. Hence, despite its complicated view compared with that of

the Yalkowsky model, this model is very valuable for cases for which there is no experimental data available. The *OMRD* for the fitting process was 13.8 %, which is acceptable.

The back-calculated *MRD* values of piroxicam solubility calculated by the different numerical analyses at different temperatures are presented in Table I. The results show that the highest and lowest *OMRD* values were achieved in analysis III and II, with 13.8 and 2.5 %, respectively.

TABLE I. *MRD*s and *OMRD*s of the three fitting analyses of piroxicam solubility in binary aqueous mixtures of PG at six different temperatures

T / K	Analysis		
	I, Eq. (4)	II, Eq. (5)	III, Eq. (7)
298.2	16.6	2.1	29.9
303.2	15.8	2.0	19.1
308.2	9.7	1.8	12.3
313.2	6.0	1.9	5.1
318.2	1.4	0.7	4.5
323.2	8.1	6.6	12.2
OMRD	9.6	2.5	13.8

In numerical analysis IV, Eq. (8) was used for predicting the solubility of piroxicam in the reported mixtures at 6 different temperatures. The highest and lowest prediction *MRD*s were for the solubility sets at 323.2 and 318.2 K with 19.1 and 14.2 %, respectively, and the *OMRD* value was 15.4 % for all 66 data points. The predicted solubilities and the *MRD* values are listed in Table II.

TABLE II. Predicted solubilities ($X_m^{predicted} \times 10^5$) of piroxicam in PG (1) + water (2) mixtures at different temperatures (*T*), prediction *MRD*s and *OMRD* obtained by the trained version (Eq. (9))

w_1	T / K					
	298.2	303.2	308.2	313.2	318.2	323.2
0.00	2.8	7.6	8.1	8.7	9.1	9.7
0.10	2.7	6.9	7.4	7.9	8.3	9.0
0.20	3.0	6.9	7.4	7.9	8.4	9.3
0.30	3.5	7.6	8.1	8.6	9.2	10.4
0.40	4.4	8.7	9.4	9.9	10.6	12.2
0.50	5.6	10.3	11.0	11.5	12.5	14.7
0.60	7.2	12.1	12.9	13.5	14.6	17.5
0.70	8.9	13.7	14.6	15.2	16.6	20.3
0.80	10.2	14.5	15.6	16.1	17.7	22.0
0.90	10.7	14.1	15.1	15.6	17.2	22.0
1.00	9.9	12.1	13.0	13.4	15.0	19.5
MRD	15.4	14.9	14.6	14.3	14.2	19.1
OMRD						15.4

CONCLUSIONS

Experimental solubilities of piroxicam are reported in aqueous binary mixtures of PG at six different temperatures ranging from 298.2 to 323.2 K, which extended the available solubility database of pharmaceuticals in mixed solvents.[12]

The main goal of this research was to improve the aqueous solubility of piroxicam by adding a cosolvent and increasing the temperature. The additions of PG and temperature enhancement increased the solubility of piroxicam dramatically. PG is a safe pharmaceutical cosolvent and could be used for formulating piroxicam in liquid forms (oral or parenteral) after performance of the appropriate toxicity tests.

The linear model of Yalkowsky, the Jouyban−Acree model and the version of the Jouyban–Acree model combined with the van't Hoff approach fitted the experimental solubility data for piroxicam well at almost all compositions of the solvent mixtures. These findings were supported by the acceptable *MRD* values of the back-calculated and experimental solubility data.

In modeling, the simplest model is the best unless its error percentage is high. The results of this study showed that the Jouyban–Acree model has the lowest fitting *MRD* values in comparison with the other two models. The noticeable point is that in the Jouyban–Acree model, the solubilities of piroxicam in the neat solvents at each temperature were added to the model; hence, for modeling the solubility data, these experimental values were required. Also in the Yalkowsky linear model, one must know the aqueous solubility of the drug at each temperature. However, when the van't Hoff approach was used in conjunction with the Jouyban–Acree model, in fact, the experimental data were replaced with calculated values.

SUPPLEMENTARY MATERIAL

Mass fractions of PG, experimental molar solubility of piroxicam in PG (1) + water (2) mixtures at various temperatures, the predicted solubilities by numerical analyses I, II and III, the densities of the saturated solutions and the fitting *OMRD*s are available electronically from http://www.shd.org.rs/JSCS/, or from the corresponding author on request.

И З В О Д
РАСТВОРЉИВОСТ ПИРОКСИКАМА У СМЕШИ ПРОПИЛЕН-ГЛИКОЛ (1,2-ПРОПАНДИОЛ)–ВОДА НА ТЕМПЕРАТУРАМА ОД 298,2 ДО 323,2 К

SHAHLA SOLTANPOUR и ZAHRA BASTAMI

Faculty of Pharmacy, Zanjan University of Medical Sciences, Zanjan 45139, Iran

Одређена је растворљивост пироксикама у бинарним смешама 1,2-пропандиол––вода на шест температура у интервалу од 298,2 до 323,2 К (66 експерименталних

тачака). Коришћена су три модела за корелацију експерименталних резултата: модел Yalkowsky, Jouyban–Acree модел и облик последњег модела модификован приступом van't Hoff-а. Анализа резултата обраде моделима је показала прихватљив опсег грешке.

(Примљено 10. новембра 2013, ревидирано 23. марта, прихваћено 24. марта 2014)

REFERENCES

1. P. Zakeri-Milani, M. Barzegar-Jalali, M. Azimi, H. Valizadeh, *Eur. J. Pharm. Biopharm.* **73** (2009) 102
2. K. J. Box, J. E. Comer, *Curr. Drug Metab.* **9** (2008) 869
3. A. Jouyban, *J. Pharm. Pharm. Sci.* **11** (2008) 32
4. J. W. Millard, F. A. Alvarez-Nunez, S. H. Yalkowsky, *Int. J. Pharm.* **245** (2002) 153
5. A. Yurquina, M. E. Manzur, M. A. A. Molina, R. Manzo, *Acta Farm. Bonaer.* **19** (2000) 49
6. D. J. W. Grant, M. Mehdizadeh, *Int. J. Pharm.* **18** (1984) 25
7. A. Jouyban, M. A. Fakhree, in *Toxicity and Drug Testing*, B. Acree, Ed., Intech, Rijeka, 2012, Ch. 9
8. F. Sardari, A. Jouyban, *Ind. Eng. Chem. Res.* **52** (2013) 14353
9. A. Jouyban, *Pharmazie* **62** (2007) 365
10. A. C. Moffat, *Clarke's Analysis of Drugs and Poisons*, Pharmaceutical Press, London, 2004
11. R. G. Stomayor, A. R. Andres, A. Romdhani, F. Martinez, A. Jouyban, *J. Solution Chem.* **42** (2013) 358
12. A. Jouyban, *Handbook of solubility data for pharmaceuticals*, CRC Press Inc., Boca Raton, FL, 2009.

SUPPLEMENTARY MATERIAL TO

Thermodynamic solubility of piroxicam in propylene glycol + water mixtures at 298.2–323.2 K – data report and modeling

SHAHLA SOLTANPOUR* and ZAHRA BASTAMI

Faculty of Pharmacy, Zanjan University of Medical Sciences, Zanjan 45139, Iran

TABLE S-I. Mass fractions (w_1) of PG, experimental molar solubility (X_m^{sat}) of piroxicam in PG (1) + water (2) mixtures at various temperatures, the predicted solubilities by numerical analyses I, II and III, the densities (ρ_m^{sat}) of the saturated solutions and the fitting *OMRD*s

w_1	ρ_m^{sat}	X_m^{sat}	Analysis		
			I, Eq. (4)	II, Eq. (5)	III, Eq. (7)
			298.2 K		
0.00	1.006	0.000028	0.000028	0.000028	0.000044
0.10	1.016	0.000031	0.000030	0.000031	0.000047
0.20	1.020	0.000035	0.000033	0.000036	0.000052
0.30	1.027	0.000041	0.000036	0.000041	0.000057
0.40	1.035	0.000045	0.000039	0.000047	0.000062
0.50	1.039	0.000050	0.000043	0.000053	0.000067
0.60	1.043	0.000062	0.000047	0.000059	0.000073
0.70	1.046	0.000068	0.000051	0.000066	0.000078
0.80	1.048	0.000075	0.000056	0.000075	0.000085
0.90	1.050	0.000082	0.000061	0.000085	0.000093
1.00	1.054	0.000099	0.000066	0.000099	0.000104
			303.2 K		
0.00	1.008	0.000076	0.000076	0.000076	0.000054
0.10	1.018	0.000081	0.000082	0.000079	0.000058
0.20	1.023	0.000084	0.000089	0.000083	0.000062
0.30	1.027	0.000089	0.000096	0.000088	0.000068
0.40	1.037	0.000096	0.000104	0.000092	0.000073
0.50	1.043	0.000100	0.000112	0.000096	0.000079
0.60	1.046	0.000103	0.000121	0.000100	0.000084
0.70	1.048	0.000106	0.000130	0.000103	0.000090
0.80	1.050	0.000109	0.000141	0.000107	0.000096
0.90	1.052	0.000113	0.000152	0.000112	0.000104
1.00	1.058	0.000121	0.000164	0.000121	0.000116

* Corresponding author. E-mail: shahla.soltanpour@gmail.com

S132

TABLE S-I. Continued

w_1	ρ_m^{sat}	X_m^{sat}	Analysis		
			I, Eq. (4)	II, Eq. (5)	III, Eq. (7)
			308.2 K		
0.00	1.010	0.000081	0.000082	0.000081	0.000065
0.10	1.020	0.000086	0.000087	0.000085	0.000070
0.20	1.027	0.000091	0.000093	0.000089	0.000075
0.30	1.029	0.000095	0.000100	0.000094	0.000080
0.40	1.039	0.000102	0.000107	0.000099	0.000086
0.50	1.046	0.000107	0.000114	0.000103	0.000092
0.60	1.048	0.000110	0.000122	0.000107	0.000097
0.70	1.050	0.000113	0.000130	0.000111	0.000103
0.80	1.052	0.000117	0.000139	0.000115	0.000109
0.90	1.056	0.000124	0.000148	0.000121	0.000117
1.00	1.060	0.000130	0.000158	0.000130	0.000129
			313.2 K		
0.00	1.012	0.000087	0.000087	0.000087	0.000079
0.10	1.023	0.000092	0.000092	0.000090	0.000084
0.20	1.029	0.000097	0.000098	0.000095	0.000089
0.30	1.033	0.000101	0.000103	0.000099	0.000095
0.40	1.041	0.000107	0.000109	0.000104	0.000101
0.50	1.050	0.000111	0.000116	0.000108	0.000107
0.60	1.052	0.000115	0.000122	0.000112	0.000112
0.70	1.056	0.000119	0.000130	0.000115	0.000117
0.80	1.058	0.000125	0.000137	0.000119	0.000123
0.90	1.060	0.000126	0.000145	0.000125	0.000131
1.00	1.062	0.000134	0.000153	0.000134	0.000143
			318.2 K		
0.00	1.016	0.000091	0.000091	0.000091	0.000095
0.10	1.027	0.000095	0.000095	0.000095	0.000100
0.20	1.031	0.000101	0.000100	0.000100	0.000105
0.30	1.037	0.000106	0.000105	0.000106	0.000111
0.40	1.044	0.000112	0.000110	0.000112	0.000117
0.50	1.052	0.000118	0.000115	0.000117	0.000123
0.60	1.056	0.000123	0.000121	0.000122	0.000128
0.70	1.060	0.000129	0.000126	0.000126	0.000133
0.80	1.064	0.000134	0.000133	0.000132	0.000139
0.90	1.066	0.000140	0.000139	0.000139	0.000146
1.00	1.068	0.000150	0.000146	0.000150	0.000158
			323.2 K		
0.00	1.020	0.000097	0.000097	0.000097	0.000114
0.10	1.029	0.000101	0.000101	0.000103	0.000119
0.20	1.035	0.000107	0.000105	0.000111	0.000124
0.30	1.039	0.000112	0.000109	0.000120	0.000130
0.40	1.046	0.000120	0.000113	0.000129	0.000136
0.50	1.054	0.000126	0.000118	0.000138	0.000141
0.60	1.058	0.000132	0.000122	0.000146	0.000146

SOLTANPOUR and BASTAMI

TABLE S-I. Continued

w_1	ρ_m^{sat}	X_m^{sat}	Analysis		
			I, Eq. (4)	II, Eq. (5)	III, Eq. (7)
			323.2 K		
0.70	1.062	0.000135	0.000127	0.000155	0.000150
0.80	1.068	0.000149	0.000132	0.000165	0.000155
0.90	1.071	0.000168	0.000137	0.000177	0.000162
1.00	1.077	0.000195	0.000142	0.000195	0.000174
		OMRD	9.6	2.5	13.8

Journal of the Serbian Chemical Society

3-Hydroxyflavone–bovine serum albumin interaction in dextran medium

MARIANA VOICESCU[1]* and SORANA IONESCU[2]

[1]*Romanian Academy, Institute of Physical Chemistry "Ilie Murgulescu", Splaiul Independentei 202, 060021 Bucharest, Romania and [2]Department of Physical Chemistry, University of Bucharest, Bd Regina Elisabeta 4–12, Bucharest 030018, Romania*

Abstract: A bioactive flavonol, 3-hydroxyflavone (3-HF), in systems based on dextran 70 (Dx70, an important bio-relevant polysaccharide) and bovine serum albumin (BSA, a carrier protein) was studied by fluorescence and circular dichroism. Changes produced by different concentrations of Dx70 on the fluorescent characteristics of 3-HF and on the excited-state intramolecular proton transfer (ESIPT) process were studied. The influences of 3-HF binding and of Dx70 on the secondary structure of BSA were investigated by circular dichroism spectroscopy. The influence of temperature (30–80 °C range) on the intrinsic tryptophan fluorescence in 3-HF/BSA/Dx70 systems was investigated. The results are discussed with relevance to 3-HF as a sensitive fluorescence probe for exploring flavone–protein interactions in plasma expander media and for its biological evaluation.

Keywords: flavones; proteins; dextran 70; fluorescence spectroscopy; ESIPT.

INTRODUCTION

Flavones and related compounds of the flavonoid group in plant polyphenolic compounds have various therapeutic properties, such as: antioxidant, antiradical, angioprotective, making them effective agents against cancers, tumors, cardiac problems, inflammations, allergies and acquired immune deficiency syndrome.[1–6] Other remarkable types of activity of flavones are based on their dual fluorescence behavior, known as systems exhibiting excited state intramolecular proton transfer, ESIPT, which is useful for exploring the structure, function, dynamics, interactions and microenvironment in biological systems, *e.g.*, proteins.[7–12]

The interaction between flavonoid compounds and serum albumins were reported.[9,13–22] Bovine serum albumin (BSA) represents the major globular protein of bovine blood plasma. BSA is structurally a polypeptide chain containing

---

* Corresponding author. E-mail: voicescu@icf.ro

582 amino acids residues, which, due to its relatively high aqueous solubility, binds to several types of biological molecules and thus determines physiological function.[23,24] The two tryptophan (Trp) residues in the BSA structure are responsible for its intrinsic fluorescence: Trp212 that belongs to subdomain IIA within a hydrophobic binding pocket and Trp134 that belongs to the first subdomain IB, located on the surface of the albumin molecule. Based on this, fluorescence spectroscopy is a suitable tool to monitor changes in the intrinsic fluorescence of BSA on binding of various ligands.[25]

Dextran is a family of microbial 1→6−α–D−glucans derived from *Leuconostoc mesenteroides* with varying proportions of other types of linkages, (1→2)--α-, (1→3)-α- and (1→4)-α-branch linkages, which is used as plasma expander.[26] Due to its solubility in water and organic solvents, dextran is a versatile biomacromolecule for preparing nanofibrous electro-spun membranes for biomedical applications.[27] In line with this, it was found that BSA and lysozyme were directly incorporated into an electro-spun dextran membrane without compromising its morphology.[27] According to Jung *et al.*, depending on the ratio of dextran to BSA used, about 0.5–1 mol of dextran could be bound to 1 mol of native BSA, indicating that the BSA surface in the conjugates was covered with dextran without disruption of its native conformation.[28]

This study deals with an analysis of the bioactive flavonol, 3-hydroxyflavone (3-HF) in systems based on dextran 70 (Dx70) and bovine serum albumin (BSA) (a carrier protein), by fluorescence and circular dichroism spectroscopy.

EXPERIMENTAL

Materials

A stock solution of 3-hydroxyflavone (3-HF, Sigma) was prepared in methanol (spectrophotometric grade, Sigma). Aliquots from stock solution were used to prepare the working solutions of concentration 6×10^{-5} M. A stock solution of dextran 70 (Dx70) was prepared in distilled water, with working concentrations in the range 0.33–1.66 µM. The molecular structure of 3-HF and Dx70 are shown in Scheme 1. Bovine serum albumin (BSA) was purchased from Merck, Darmstadt. Phosphate buffer used was 0.1 M, pH 7.4. A phosphate buffer was purchased from Sigma–Aldrich, Steinheim, Germany.

3-Hydroxyflavone (3-HF)   Dextran
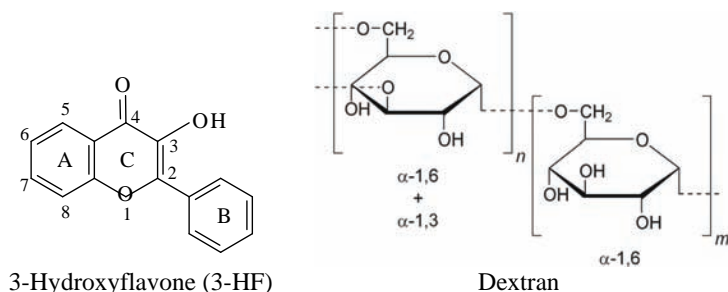
Scheme 1. Molecular structure of 3-hydroxyflavone (3-HF) and dextran.

Methods and apparatus

The fluorescence emission and excitation spectra were recorded with a Jasco FP-6500 spectrofluorometer, using 3 nm bandpasses for the excitation and the emission monochromators, a detector response of 1 sec, data pitch of 1 nm, a scanning speed of 100 nm min^{-1}. The excitation wavelengths were 365 nm (for hydroxyflavone emission) and 280 nm (for Trp emission of the BSA protein).

The fluorescence lifetime decays were recorded in a time-correlated, single photon counting FLS920 system from Edinburgh Instruments, with laser excitation at 375 nm, a lifetime scale of 100 ns and 2048 channels. The laser had a width of 1.5±0.5 nm, and a pulse duration of 50 ps. The data were fitted with a multi-exponential decay (reconvolution) and the accuracy of the fit was checked on grounds of χ^2, which was less than 1.2. Intensity-averaged lifetimes were calculated according to the equation:[29]

$$\langle \tau \rangle = \frac{\sum_i \alpha_i \tau_i^2}{\sum_i \alpha_i \tau_i} \; ; \; f_i = \frac{\alpha_i \tau_i}{\sum_i \alpha_i \tau_i} \; ; \; a_i = \frac{\alpha_i}{\sum_i \alpha_i}$$

The circular dichroism spectra were measured on a Jasco J-815 spectropolarimeter in the wavelength range of 200–300 nm. The experimental data was fitted with DichroWeb[30] in order to obtain the secondary structure with the K2D neural network algorithm.[31]

RESULTS AND DISCUSSION

Steady-state fluorescence analysis

The fluorescence emission spectra of 6×10^{-5} M, 3-HF in the presence of Dx70, for an excitation wavelength, $\lambda_{ex} = 365$ nm, is shown in Fig. 1A. Two fluorescence emission bands were observed: a broad band at 470 nm, which corresponds to the normal (N*) form (S$_1$ (π–π*) → S$_0$, where no proton transfer process occurs) and at 528 nm, attributed to the tautomer (T*) form, which is generated from an excited-state intramolecular proton transfer (ESIPT) process of the internal H-bond, C(4)=O···HO–C(3).[7] No significant changes in emission wavelengths for the N* and T* forms were observed with increasing concentration of DX70, but the fluorescence intensity of the bands increased slightly. In the fluorescence excitation spectra of 3-HF, monitored at 530 nm, of 3-HF in the presence of Dx70 and in direct comparison with 3-HF at pH 7.4 (Fig. 5B), two bands at λ_{ex} around 304 and 350 nm were observed, which are attributed to the absorption of 3-HF. According to Schipfer *et al*., the UV-absorption spectra of flavones are characterized by two absorption bands (π–π*), Band I (300–380 nm) attributed to the absorption by the cinnamoylic portion (B+C rings) and band II (240–285 nm), by the benzoyl portion (A+C rings) of flavornoid molecules.[32]

Addition of BSA (Fig. 1C) leads to a 5-nm red-shifted fluorescence emission of the N* form, $\lambda_{em} = 475$ nm, and a 4-nm red-shifted fluorescence emission of the T* form, $\lambda_{em} = 532$ nm. As could be observed, the fluorescence intensity of both forms increased with increasing concentration of BSA. It could be noticed that the T* emission was higher than the N* emission, indicating an efficient

excited-state proton transfer process. In addition, with increasing BSA concentration, the intensity ratio of N*:T* fluorescence (I_{N*}/I_{T*}) decreased from $I_{N*}/I_{T*} = 0.625$ for a concentration of 0.33 μM BSA to $I_{N*}/I_{T*} = 0.406$ for 1.66 μM BSA. This feature was attributed to the more hydrophobic environment of 3-HF in the presence of BSA. Moreover, a high affinity binding of 3-HF on BSA in the presence of Dx70 was considered. The fluorescence excitation spectra of 3-HF, monitored at 530 nm, in the presence of Dx70 with varying BSA concentrations is presented in Fig. 1D. Comparing the spectra in Fig. 1D with those in Fig. 1B, the bands with λ_{ex} in the region 285–293 nm are attributed to π–π* transitions of the aromatic amino acid residues, Tyr and Trp.[33,34] The broad band at $\lambda_{ex} \approx 312$ nm may be due to 3-HF binding to the BSA structure, while the band in the region 353–372 nm corresponds to the absorption of 3-HF. The band with $\lambda_{ex} \approx 419$ nm, attributed to the anion form 3-HF,[12] was 3 nm red-shifted ($\lambda_{ex} \approx 422$ nm) with increasing BSA concentration. These features are due to specific interactions of 3-HF anion form with the environment of amino acid residues in the BSA structure.
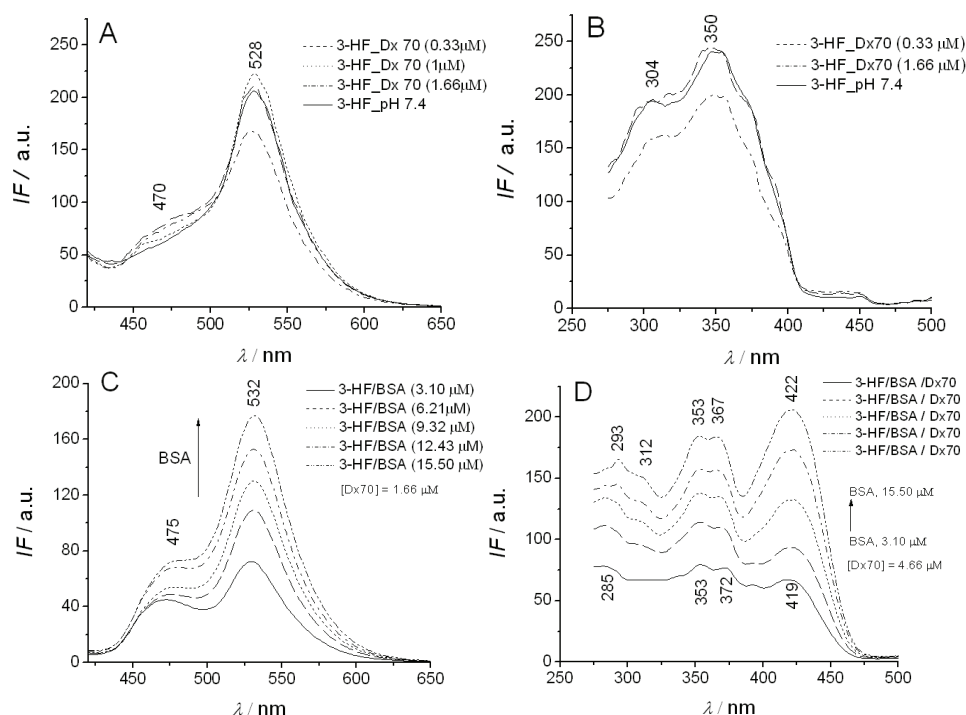

Fig. 1. Fluorescence emission spectra of 6×10^{-5} M 3-HF in Dx70 medium without (A) and with BSA(C), $\lambda_{ex} = 365$ nm, and their corresponding excitation spectra (B and D); $\lambda_{em} = 530$ nm.

The influence of temperature on intramolecular ESPT

The influence of temperature in the range of 30–80 °C on the excited-state intramolecular proton transfer (ESIPT) tautomer emission of 3-HF in the presence of BSA and Dx70 at pH 7.4 for an excitation wavelength of 365 nm, is shown in Fig. 2A. No changes in the fluorescence emission wavelengths of the N* (λ_{em} = 475 nm) and T* (λ_{em} = 532nm) forms were observed but their intensities decreased with increasing temperature. With gradual increase in temperature, the intensity ratio I_{N*}/I_{T*} decreased, Table I, providing a less hydrophobic environment of 3-HF, in that the internal H-bonds at the binding sites in BSA are weak. Without Dx70, it was found that the intensity ratio I_{N*}/I_{T*} of 3-HF increased, a fact corresponding to the more hydrophobic environment of 3-HF, Table I. The intramolecular ESPT tautomer emission of 3-HF in the presence of BSA and Dx70 was notably even when the temperature increased. From the excitation spectra in Fig. 2B, it could be seen that with increasing temperature, the bands at $\lambda_{ex} \approx 293$ nm, characteristic for Tyr and Trp absorption, strongly decrease at 80 °C and a broad absorption band appeared around 306 nm. The broad band around 357 nm corresponds to 3-HF absorption. This is indi-
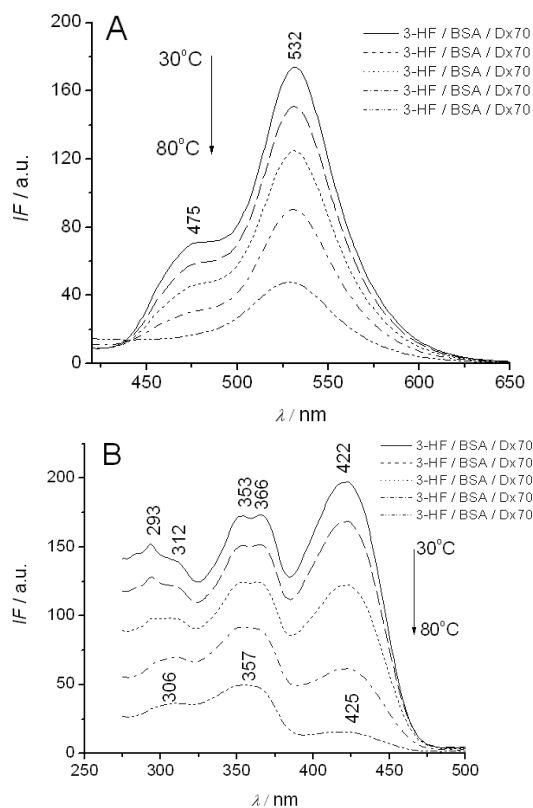

Fig. 2. A) Fluorescence emission and B) excitation spectra of 3-HF/ /BSA interaction in the presence of Dx70 at pH 7.4 *vs.* temperature: Dx70:BSA = 1:1 (*V/V*); [3-HF] = 6×10^{-5} M; λ_{ex} = 365 nm, λ_{em} = 530 nm.

cative of 3-HF binding to BSA, especially at the site in the proximity of the Trp 212 residue. The band at λ_{ex} = 422 nm was attributed to the absorption of the anion form of 3-HF[12] and as the temperature increased, a slight bathochromic shift to 425 nm was registered at 80 °C. A slight denaturation of BSA at this temperature should also be taken into consideration.

TABLE I. Fluorescence characteristics of the 3-HF/BSA interaction with and without Dx70, in phosphate buffer pH 7.4 (PBS). λ_{N*} and λ_{T*}, position of the fluorescence emission maxima of the normal (N*) and tautomer (T*) forms; λ_{ex} = 365 nm

System	t / °C	λ_{N*} / nm	λ_{T*} /nm	I_{N*} / I_{T*}
3-HF / BSA / PBS	25	471	530	0.460
	30	475	530	0.469
	40	475	530	0.477
	50	475	530	0.495
	60	475	529	0.525
	80	475	528	0.545
3-HF / BSA / Dx70 / PBS	25	476	532	0.406
	30	476	532	0.402
	40	476	531	0.381
	50	476	531	0.368
	60	474	531	0.333
	80	–	528	0

The influence of temperature on the intrinsic fluorescence emission of BSA

It is known that BSA has two Trp residues involved in its intrinsic fluorescence emission: Trp212, in a hydrophobic binding pocket of the subdomain IIA, and Trp134, belonging to the first subdomain IB, on the surface, more exposed to hydrophilic environment.[35] The fluorescence emission of the native BSA at an excitation wavelength of 279 nm, is 340 nm,[28] and changes in the intrinsic fluorescence of BSA may occur in dependence on the environment of the Trp residues.

Intrinsic tryptophan fluorescence emission spectra of 3-HF binding and Dx70 on the BSA structure at pH 7.4 for an excitation wavelength λ_{ex} = 280 nm are shown in Fig. 3A. It was registered that with increasing BSA concentration, the fluorescence intensity of Trp gradually increased, but with no significant emission shifts λ_{em} to 334–336 nm. Thus, 3-HF in the presence of Dx70 does not cause conformational changes in the secondary structure of BSA.

The secondary structure of the BSA undergoes conformational changes under thermal treatment. The helicity of the protein (66 %) decreased with rising temperature; half of the original helicity was lost at 80 °C, while a helicity of 16 % was still maintained even at 130 °C.[36] As the temperature increases, Fig. 3B, an 8-nm blue-shift in the fluorescence emission was observed, λ_{em} = 327 nm,

and the feature corresponds to a more hydrophobic environment of the Trp 212 residue when 3-HF binds to BSA.
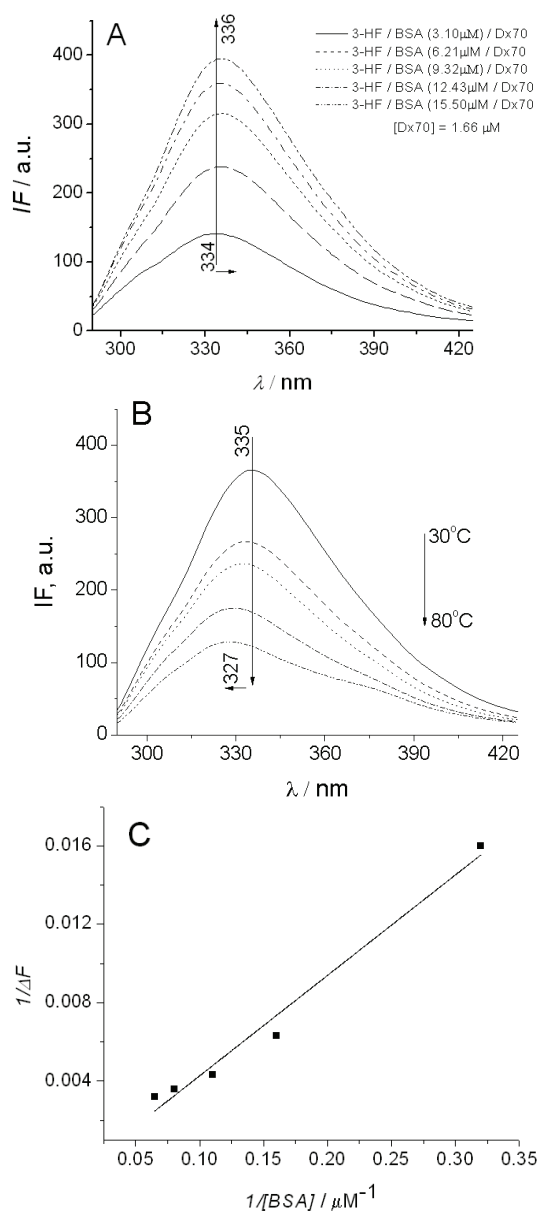
Fig. 3. Tryptophan intrinsic fluorescence emission spectra of 3-HF binding and Dx70 on the BSA structure, A) at different BSA concentrations and B) at different temperatures at Dx70: BSA = 1:1 (*V/V*), pH 7.4 and λ_{ex} = 280 nm. C) The variation *1/ΔF* of Trp fluorescence emission as a function of the molar concentration of BSA.

The binding constant between 3-HF and BSA in Dx70 medium could be estimated from the fluorescence emission data using a modified Benesi–Hildebrand equation, as follows:[37]

$$\frac{1}{\Delta F} = \frac{1}{\Delta F_{\max} K [\text{BSA}]} + \frac{1}{\Delta F_{\max}}$$

where $\Delta F = F_{\text{x}} - F_0$, whereby F_{x} and F_0 represent the Trp fluorescence intensities in the presence of Dx70 at pH 7.4 and in the absence of Dx70, respectively. $\Delta F_{\max}$ is the maximum change in the Trp fluorescence intensity and K is the binding constant. The variation $1/\Delta F$ for the intrinsic Trp fluorescence emission intensity for various molar concentrations of BSA is presented in Fig. 3C, from which the K value was estimated to be 5.13×10^4 M^{-1} ($SE = 7.17 \times 10^{-4}$, $r^2 = 0.975$). Thus, a high binding affinity of 3-HF to BSA in the presence of Dx70 was registered. For human serum albumin (HSA), Sytnik and Litvinyuk[12] reported that the higher affinity site of HSA has an association constant of $K = 7.2 \times 10^5$ M^{-1} and predominantly hosts the 3-HF anion, while the normal tautomer has a lower affinity, $K = 2.5 \times 10^5$ M^{-1}.

Time-resolved fluorescence analysis

Lifetime measurements on the 3-HF band were performed in order to see the effect that the presence of Dx70 has on the species present in solution. The results are presented in Table II and the decay profiles in Fig. 4. When bound with BSA, 3-HF had three lifetime components, as was found in pH 7.4 phosphate buffer solution (PBS) as well. In order of increasing lifetime, the three components were attributed to the tautomer, T* (0.18 ns), anion, A* (1.46 ns) and normal, N* (5.39 ns), species of 3-HF.[38] Lifetime measurements can also yield information on the relative population of these species and the changes that occur upon interaction with BSA.

TABLE II. Lifetimes (τ / ns), fractional intensities (f / %) and relative populations (a / %) of 3-HF excited species under different experimental conditions

System	τ_1	τ_2	τ_3	f_1	f_2	f_3	a_1	a_2	a_3	$<\tau>$
PBS	0.18	1.46	5.39	44.39	31.60	24.02	90.20	8.16	1.63	1.82
BSA	1.03	4.11	8.08	13.92	47.74	38.34	45.13	38.94	15.93	5.21
BSA/Dx70	1.07	3.75	7.94	20.34	47.55	32.11	53.08	35.38	11.54	4.58

In the presence of BSA, all the lifetimes increased to 1.03, 4.11, 8.08 ns, respectively, and the average lifetime increased as well from 1.82 to 5.21 ns. The relative population of the T* form decreased two-fold, from 90.20 to 45.13, while both the anion and the normal species increased, which determined a similar trend for the fractional intensities. As both T* and N* are tautomers of the neutral molecule, the anion increased from 8.16 to 38.94 % in BSA, at the expense of neutral 3-HF, which decreased from 91.84 to 61.96 %. This means that deprotonated 3-HF is favored as the binding species. A third effect of binding to BSA was perturbation of the excited state processes, as the T*/N* popul-

ation ratio dramatically decreased from 55.34 to 2.83 and the intensity ratio from 1.85 to 0.36.
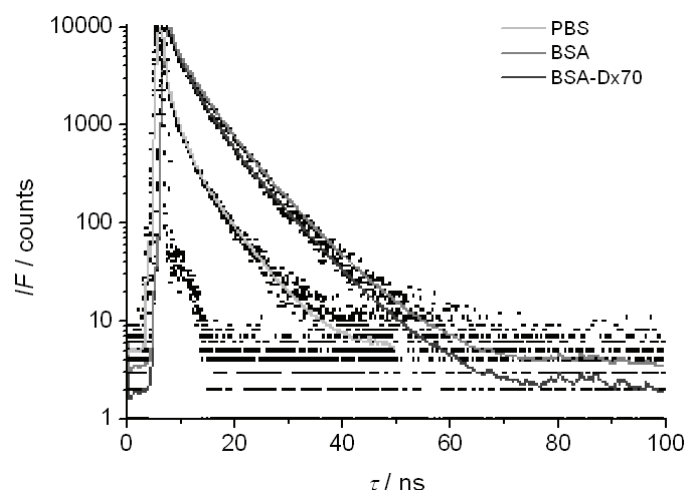

Fig. 4. Decay profiles for 3-HF in PBS, BSA and BSA in the presence of Dx70:
(○) – instrument response; (●) – experimental data; lines – fitted data.

The addition of Dx70 had a slight tendency of reverting the effect that BSA had on 3-HF, *i.e.*, a slight decrease in the lifetimes to 1.07, 3.75 and 7.94 ns, respectively, and of the average lifetime to 4.58 ns, on one hand, and on the other a slight decrease of the deprotonated 3-HF to 35.38 %, while the neutral mole-cule percentage rises to 64.62 %. The reverting tendency is valid also for the excited state processes, as the population ratio becomes 4.60 and the intensity ratio 0.63.

Circular dichroism analysis

A circular dichroism spectrum of a protein can be considered the sum of the characteristic individual spectra of each type of secondary structure present in the protein. Thus, by deconvolution, the contents of each of the secondary structures of proteins can be determined. The data in Table III show that binding of 3HF decreased the α-helix percentage by 6 %, from 59 to 53 %, increasing thereby the content of the random coil structure the most, as is the case with most ligands. On the other hand, Dx70 increased the α-helix percentage by 3–5 % at the exp-ense of both the β-sheet and random coil structures, both in the absence and in the presence of the ligand. It can be seen that bound BSA in the presence of Dx70 reverts to a structure very similar to the native one, 58, 8 and 34 % for the content α-helix, β-sheet and random coil, respectively, compared to 59, 8 and 33 %, respectively, for the native protein. Thus, Dx70 had the effect of renaturation on the serum albumin.

TABLE III. The effect of 3HF binding and Dx70 on the secondary structure of BSA; *NRSMD*: normalized root mean square deviation

System	α-helix, %	β-sheet, %	Random coil, %	*NRMSD**
BSA	59	8	33	0.109
BSA /Dx70	62	6	31	0.185
3-HF /BSA	53	10	37	0.187
3-HF /BSA /Dx70	58	8	34	0.202

The reverting effect of Dx70 on both BSA in the presence of the ligand and on 3-HF bound to BSA may be due to both a competitive interaction of the 3-HF to BSA and Dx70 and to slight structural modifications that the presence of Dx70 induced on the protein that increased the percentage of the α-helix structure.

CONCLUSIONS

In Dx70 medium and with gradual increase in the temperature, the intensity ratio of N* and T* fluorescence (I_{N*}/I_{T*}) in the 3-HF / BSA systems decreased, leading to a less hydrophobic environment of 3-HF, because the internal H-bonds at the binding sites in BSA are weak.

In Dx70 medium, 3-HF binds to BSA especially at the site in the proximity of Trp 212 residue. The value of binding constant, 3-HF to BSA in the presence of Dx70 was $K = 5.13 \times 10^4$ M^{-1}.

Dx70 increased the α-helix percentage by 3–5 % at the expense of both the β-sheet and random coil structures, both in the absence and in the presence of 3-HF. It was observed that the bound BSA in the presence of Dx70 reverted to a structure very similar to the native one, 58, 8 and 34 % for α-helix, β-sheet and random coil, respectively, compared to 59, 8 and 33 %, for the native protein. Thus, Dx70 had an effect of renaturation on the serum albumin.

The data have relevance in future studies concerning flavone–protein interaction with 3-HF as a sensitive fluorescence probe in plasma expanders media, as well as in the future studies concerning its biological evaluation.

ABBREVIATION LIST

3-HF – 3-Hydroxyflavone
Dx70 – Dextran 70
BSA – Bovine serum albumin
Trp – Tryptophan
ESIPT – Excited-state Intramolecular Proton Transfer
N* and T* – Normal and tautomer forms
I_{N*}/I_{T*} – The intensity ratio of N*:T* fluorescence

И З В О Д

ИНТЕРАКЦИЈА 3-ХИДРОКСИФЛАВОН–ГОВЕЂИ СЕРУМСКИ АЛБУМИН У МЕДИЈУМУ ДЕКСТРАНА

MARIANA VOICESCU[1] и SORANA IONESCU[2]

[1]*Romanian Academy, Institute of Physical Chemistry "Ilie Murgulescu", Splaiul Independentei 202, 060021 Bucharest, Romania и* [2]*Department of Physical Chemistry, University of Bucharest, Blvd. Regina Elisabeta 4–12, Bucharest 030018, Romania*

Спектроскопска анализа биоактивног флавонола, 3-хидроксифлавона (3-HF), у систему базираном на декстрану 70 (Dx70, важан био-релевантан полисахарид) и говеђег серумског албумина (BSA, протеин носач), изведена је применом флуоресценције и циркуларног дихроизма. Студиране су промене настале применом различитих концентрација Dx70 на флуоресцентне карактеристике 3-HF, као и побуђено стање – процеси интрамолекуларних трансфера протона (ESIPT). Утицај везивања 3-HF и Dx70 на секундарну структуру BSA испитиван је преко циркуларног дихроизма. Испитиван је такође утицај темеператутре (30–80 °C) на својствену флуоресценцију триптофана у систему 3-HF/BSA/Dx70. Резултати су дискутовани у односу на релевантност 3-HF, као осетљиве флуоресцентне пробе за испитивање интеракција флавон–протеин у плазми, као медијуму, као и у смислу биолошке евалуације.

(Примљено 25. априла, ревидирано 18. јуна, прихваћено 15. јула 2014)

REFERENCES

1. St. Rusznyak, A. Szent-Gyorgi, *Nature* **138** (1936) 27
2. U. J. Takahama, *Photochem. Photobiol.* **38** (1983) 363
3. J. B. Harborne, in *Plant flavonoids in Biology and Medicine II: Biochemical, Cellular, and Medicinal Properties*, V. Cody, E. Middleton, J. B. Harborne, A. Beretz, Eds., Alan R. Liss, New York, 1988, p. 17
4. S. W. Lamson, M. S. Brignall, *Altern. Med. Rev.* **5** (2000)196
5. R. J. William, J. P. E. Spenger, C. Rice-Evans, *Free Radical Biol. Med.* **36** (2004) 838
6. O. M. Anderson, K. R. Markham, *Flavonoids: Chemistry, Biochemistry and Applications*, CRC Press, Boca Raton, FL, 2006
7. P. K. Sengupta, M. Kasha, *Chem. Phys. Lett.* **68** (1979) 382
8. O. S. Wolfbeis, in *Molecular Luminescence Spectroscopy: methods and applications*, Part I, S. G. Schulman, Ed., Wiley, New York, 1985
9. J. Guharay, B. Sengupta, P. K. Sengupta, *Proteins* **43** (2001) 75
10. A. P. Demchenko, S. Ercelen, A. D. Roshal, A. S. Klymchenko, *Pol. J. Chem.* **76** (2002) 1287
11. A. Sytnik, D. Gormin, M. Kasha, *Proc. Natl. Acad. Sci. USA* **91** (1994) 11968
12. A. Sytnik, I. Litvinyuk, *Proc. Natl. Acad. Sci. USA* **93** (1996) 12959
13. B. Sengupta, P. K. Sengupta, *Biochem. Biophys. Res. Commun.* **299** (2002) 400
14. F. Zsila, Z. Bikadi, M. Simonyi, *Biochem. Pharmacol.* **65** (2003) 447
15. J. Tian, J. Liu, J. Xie, X. Yao, Z. Hu, X. J. Chen, *J. Photochem. Photobiol., B* **74** (2004) 39
16. C. Dufour, O. Dangles, *Biochim. Biophys. Acta* **1721** (2005) 164
17. V. V. Sentchouk, E. V. Bondaryuk, *J. Appl. Spectrosc.* **74** (2007) 731
18. A. Banerjee, K. Basu, P. K. Sengupta, *J. Photochem. Photobiol., B* **90** (2008) 33
19. X. Hu, S. Cui, J. Qin Liu, *Spectrochim. Acta, A* **77** (2010) 548
20. P. K. Sengupta, S. Chaudhuri, *J. Indian Chem. Soc.* **87** (2010) 213

21. S. Naveenraj, S. Anandan, *J. Photochem. Photobiol., C* **14** (2013) 53
22. A. Abo Mareb, N. Abo El-Maali, *Talanta* **119** (2014) 417
23. A. Tobitani, S. B. Ross-Murphy, *Macromolecules* **30** (1997) 4845
24. S. A. Gani, D. C. Mukherjee, D. K. Chattoraj, *Langmuir* **15** (1999) 7139
25. M. R. Eftink, C. A. Ghiron, *Anal. Biochem.* **144** (1981) 199
26. J. F. Robyt, *Essentials of carbohydrate chemistry*, Springer, New York, 1998
27. H. Jiang, D. Fang, B. S. Hsiao, B. Chu, W. Chen, *Biomacromolecules* **5** (2004) 326
28. S. H. Jung, S. J. Choi, H. J. Kim, T. W. Moon, *Biosci. Biotechnol. Biochem.* **70** (2006) 2064
29. J. R. Lakowicz, *Principles of Fluorescence Spectroscopy*, 3rd ed., Springer, Berlin, 2006, pp. 141–143
30. L. Whitmore, B. A. Wallace, *Nucleic Acids Res.* **32** (2004) W668
31. M. A. Andrade, P. Chacón, J. J. Merelo, F. Morán, *Protein Eng.* **6** (1993) 383
32. R. Schipfer, O. S. Wolfbeis, A. Kneirzinger, *J. Chem. Soc., Perkin Trans.* **2** (1989) 1443
33. M. Voicescu, M. Heinrich, P. Hellwig*, J. Fluoresc*. **19** (2009) 257
34. M. Voicescu, Y. El Khoury, D. Martel, M. Heinrich, P. Hellwig, *J. Phys. Chem., B* **113** (2009) 13429
35. G. Sudlow, D. J. Birkett, D. N. Wade, *Mol. Pharmacol*. **12** (1976) 1052
36. Y. Moriyama, E. Watanabe, K. Kobayashi, H. I Harano, E. Inui, K. Takeda, *J. Phys. Chem., B* **112** (2008) 16585
37. H. A. Benesi, J. H. Hildebrand, *J. Am. Chem. Soc*. **71** (1949) 2703
38. M. Voicescu, S. Ionescu, F. Gatea, *Spectrochim. Acta, A* **123** (2014) 303.

Influence of clay organic modifier on the morphology and performance of poly(ℰ-caprolactone)/clay nanocomposites

MARIJA S. NIKOLIĆ*#, NATAŠA ĐORĐEVIĆ, JELENA ROGAN#
and JASNA ĐONLAGIĆ#

Faculty of Technology and Metallurgy, University of Belgrade, Karnegijeva 4, 11000 Belgrade, Serbia

Abstract: Two series of poly(ℰ-caprolactone) poly(oxepan-2-one) nanocomposites with different organo-modified clays (1 to 8 wt. %) were prepared by the solution casting method. Organoclays with polar (Cloisite® C30B) and nonpolar (Cloisite® C15A) organic modifiers and with different miscibility with the poly(ℰ-caprolactone) matrix were chosen. Exfoliated and/or intercalated structures of the nanocomposite were obtained using high dilution and ultrasonic treatment for the preparation of the composite. The effects of the surface modification and clay content on the morphology, and mechanical and thermal properties of the nanocomposites were studied. Scanning electron microscopy excluded the formation of microcomposites. The wide-angle X-ray diffraction analysis revealed that the tendency toward exfoliated structures was higher with Cloisite® C30B, which had better miscibility with poly(ℰ-caprolactone) matrix, than with Cloisite® C15A. Differences in the sizes of the spherulites and morphology between two series of the nanocomposites were observed by optical microscopy performed on as-cast films. The enthalpies of fusion and degrees of crystallinity were higher for the nanocomposites than for the neat poly(ℰ-caprolactone) and increased with clay loading in both series, because of the nucleating effect of the clay. The decreased thermal stability of the nanocomposites was ascribed to the thermal instability of the organic modifiers of the clays. The Halpin–Tsai model was used to compare the theoretically predicted values of the Young's modulus with the ones experimentally obtained in tensile tests.

Keywords: biodegradable; aliphatic polyester; layered silicate; solution casting.

INTRODUCTION

Polymer nanocomposites are already established as materials with remarkably enhanced and improved properties compared to the pure polymers and con-

ventional microcomposites. If a very low amount of nanometer filler is successfully dispersed in a polymer matrix, the interface between the filler and the matrix dramatically increases, allowing a full contribution of the filler to the improvement of the properties. Among polymer/inorganic filler composites, polymer/layered silicate nanocomposites have induced a great interest in industry, as well as in academia.[1–4] Layered silicates found such a prominent place among other nanofillers due to their natural abundance, high mechanical strength, chemical resistance and well-investigated intercalation chemistry. Different polymers, such as polyamides, polypropylene, polyurethane, aliphatic polyesters, aimed at diverse applications, were investigated as matrices in polymer/layer silicate nanocomposites. The resulting nanocomposites often exhibit higher stiffness, lower permeability, reduced coefficient of thermal expansion and reduced flammability than the corresponding neat polymer.[4–7]

A layered silicate with a layer thickens of 1 nm and high aspect ratio (10––1000) is organized in stacks with regular gaps between them, called interlayers or galleries. The clay layers are negatively charged with this charge being counterbalanced by alkali or alkaline earth cations that reside in the galleries. In a preparation of polymer/layered silicate nanocomposite, the tendency is to obtain a full, nanometer dispersion of clay layers, *i.e.* exfoliation, in order to achieve the best performance. It was also shown that the intercalation of polymer chains into the interlayer space, resulting in a well-ordered multilayer morphology with a few clay layers in dispersed stacks, can also result in a substantial improvement of material properties.[8,9] The particular structure that is obtained is influenced by the elaboration route and the favorable polymer–clay interactions. Clay is usually modified by exchanging the interlayer inorganic cations with organic ions, which enables more favorable interactions with the desired, usually hydrophobic, matrix. At the same time, the tethering of long alkyl chains to the surface of the layer increases the interlayer spacing, allowing an easier approach of a polymer chain. A range of commercial organoclays is available, intercalated with different organic cations, usually quaternary ammonium ions.

Poly(ε-caprolactone), PCL (poly(oxepan-2-one)) belongs to an important class of biodegradable polymers – aliphatic polyesters. It is a semi-crystalline polymer with low melting and glass transition temperatures. PCL degrades by hydrolytic cleavage of the ester bonds along the polymer chain, yet with a much slower rate compared to those of other aliphatic polyesters, such as poly(L,D--lactic acid). Therefore, when medical applications are in question, this polyester has been investigated for some long-term applications, such as in some prolonged controlled release systems or for different scaffolds, where physical and mechanical properties should be maintained for at least 6 months.[10] In the case of scaffolds in bone tissue engineering, the mechanical properties of PCL might not be adequate for such high-load-bearing applications and therefore need some

improvements. PCL is also considered as a suitable, environmentally friendly replacement for some non-biodegradable commodity polymers that are currently in use, *e.g.*, for packaging or in agriculture. It is, therefore, of considerable interest to investigate and develop improvements of PCL-based materials in terms of mechanical, barrier and thermal properties. Judging from the literature citations, a nanocomposite approach has been especially investigated.[11–15] Nanoclays which provide a range of aforementioned improvements of materials seems to be a particularly promising filler for materials based on a PCL-matrix.[16]

The main elaboration routes to PCL/clay nanocomposites are *in situ* polymerization of the ε-caprolactone monomer intercalated in the clay galleries, melt processing and casting from solution. By *in situ* intercalative polymerization, well-defined exfoliated nanocomposites could be obtained, though high molecular weights of the matrix are not easy to attain.[17–23] A process was also developed in which an exfoliated master batch, prepared by *in situ* polymerization, was dispersed in the desired matrix by melt processing.[24] Melt processing was not so efficient as *in situ* polymerization in achieving exfoliated state, even though it is the simplest and industrially most acceptable route to nanocomposites.[25–30] An important point in melt processing when used for organically modified clay is the thermal stability of the organic modifiers. A number of papers dealing with commercial organoclays presented the influence of the thermal instability of the organic modifier on the final performance of melt processed nanocomposites.[31,32] Early work on the preparation of PCL/clay nanocomposites by solution casting resulted in only slightly intercalated nanocomposites.[33] Unlike poly(lactic acid)/clay nanocomposites, for which solution casting was proved to be a good method for obtaining exfoliated/intercalated and intercalated structures of nanocomposites,[34,35] in the preparation of PCL/clay nanocomposites, this route was not that successful. However, recent reports on PCL/clay composites claimed that an intercalated/exfoliated structure could be achieved by the proper choice of solvent in respect to the clay and PCL and a highly dilute starting suspension.[36] By applying the solution casting method, the danger of thermal degradation of the organic modifier is eliminated. This allows the investigation and better understanding of the impact of interactions between an organic modifier and the PCL matrix on clay dispersion and the final performance of the nanocomposites.[37]

In this report, an attempt to obtain PCL/clay nanocomposites *via* the film casting technique is described. The aim was to explore the influence of organic modifiers on clay dispersion within a PCL matrix. Two organoclays (Cloisite® 30B and Cloisite® 15A), which differ in respect to their affinity toward the used solvent and the PCL matrix, were investigated. The organo-modifier in the case of Cloisite® 30B was the methyl bis-2-hydroxyethyl tallow quaternary ammonium cation and in the case of Cloisite® 15A, the dimethyl dehydrogenated

tallow quaternary ammonium cation (Fig. 1). In addition, the thermal and mechanical properties of the as-prepared samples were investigated and the results interpreted in terms of the achieved clay dispersion and interactions between the clay organic modifier and the matrix.
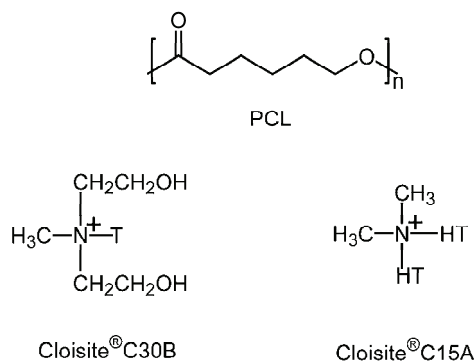
PCL

Fig. 1. Chemical structures of PCL and organic modifier of the clays: for Cloisite® 30B methyl bis-2-hydroxyethyl tallow (T) quaternary ammonium cation and for Cloisite® 15A dimethyl dehydrogenated tallow (HT) quaternary ammonium cation (T is tallow (≈65 % C18, ≈30 % C16, ≈5 % C14).

EXPERIMENTAL

Materials

Poly(ε-caprolactone) was synthesized by ring-opening polymerization of ε-caprolactone in the presence of stannous octoate catalyst.[38] The stannous octoate was purchased from Aldrich and used as received. The number average molecular weight of the synthesized PCL was 43300 g mol^{-1} with a polydispersity of 1.95, as obtained from size exclusion chromatography measurements performed in chloroform (solution concentration 10 mg mL^{-1}; mobile phase flow rate 1 mL min^{-1}) with polystyrene calibration. The two organo-modified clays were supplied by Southern Clay Products, Inc. (Texas, USA) under the trade name Cloisite® 30B and Cloisite® 15A (hereafter denoted as C30B and C15A, respectively). The cation exchange capacity (*CEC*) was 90 mmol M$^+$ 100 g^{-1} for C30B and 125 mmol M$^+$ 100 g^{-1} for C15A. The organic content of the organo-modified clay was determined by thermogravimetric analysis TGA, *i.e.*, 30 wt. % for C30B and 43 wt% for C15A. All solvents were purchased from Merck and used as received.

Preparation of PCL/organoclay nanocomposites

PCL/organoclay nanocomposites were prepared by a solvent casting method. The compositions of the nanocomposites with used designation of the samples are presented in Table I. Dispersion of clay and a solution of PCL in chloroform were prepared separately. For the clay dispersion (10 mg ml^{-1}), intensive mixing with a magnetic stirrer (1000 s^{-1}) and ultrasonic treatment in two 10 min cycles were applied. A predetermined amount of clay dispersion was added dropwise in the PCL solution and final dispersion was treated in an ultrasonic bath for 15 min, followed by intensive mixing at 1000 s^{-1} on a magnetic stirrer for one hour. The resultant dispersion was poured into Petri dishes and chloroform was allowed to evaporate under atmospheric conditions. The films of around 200 μm thickness were peeled from the dishes and subjected to further analysis.

X-Ray diffraction

Wide-angle X-ray diffraction (WAXD) patterns were recorded on an ItalStructure APD2000 powder diffractometer in a Bragg–Brentano geometry using CuK$_\alpha$ radiation (λ =

= 0.15418 nm) and step–scan mode (range: 3–10° 2θ, step-time: 4 s, step-width: 0.02°). The organoclays were in the form of powder and the nanocomposites were analyzed as obtained in a form of thin flat films. The interlayer mean *d*-spacing of the clays was calculated by means of Bragg's law.

Optical microscopy

The surface of nanocomposite films was observed by an optical microscope Leica DM ILM in reflected light. The spherulites' diameters were measured from obtained microphotographs and given as a mean value calculated from 200 independent measurements.

Scanning electron microscopy

Scanning electron microscopy (SEM) measurements were carried out on a JEOL JSM--6610LV microscope operating at 30 kV acceleration voltage. The surfaces of the as-cast films as well as fractured surfaces of the nanocomposite films were observed. The samples were cryo-fractured in liquid nitrogen and coated with a thin layer of gold prior to the measurements.

Differential scanning calorimetry

Differential scanning calorimetry (DSC) tests were performed on an SDT Q600 (TA instruments, USA) instrument. The samples (around 5 mg) were scanned from 30 to 200 °C at a rate of 10 °C min^{-1} in a nitrogen atmosphere.

Thermogravimetric analysis

Thermogravimetric analysis (TGA) was carried out with an SDT Q600 (TA instruments, USA) instrument by recording the weight loss during the heating of the samples of around 5 mg to 800 °C with a 10 °C min^{-1} heating rate under a nitrogen flow of 0.1 dm^3 min^{-1}.

Tensile properties

The mechanical properties were studied using an AG-Xplus Testing machine (Shimadzu, Japan) at a crosshead speed of 1 mm min^{-1}. The tests were performed on as-obtained samples after solution casting, which were shaped in rectangular form with the dimensions 40 mm×10 mm and thickness of around 200 μm. An average of five measurements was taken for each sample. The samples were conditioned prior to the measurements at 25 °C and 65 % relative humidity for 24 h.

RESULTS AND DISCUSSION

Structural and morphological characterization

The clay dispersion in the nanocomposites was analyzed by wide-angle X-ray diffraction. The WAXD patterns for the pure clays and the corresponding nanocomposites are presented in Fig. 2. The pattern of the PCL matrix is also presented as a baseline to compare the difference between the matrix and the nanocomposites. The mean interlayer spacing in C30B clay, elucidated from (001) plane diffraction at 2θ 4.7° was about 1.88 nm. The absence of a (001) reflection in investigated 2θ region in the diffractograms of the nanocomposites with C30B (Fig. 2a) is a strong indication that the clay was dispersed at a level of a single platelet, or that an intercalated structure with an interlayer spacing greater than 2.94 nm was obtained (as indicated with the asterisk in Fig. 2a). If an intercalated structure is assumed, the increase in the interlayer spacing obtained

for the C30B clay was thus greater than 1.06 nm. The WAXD pattern for the C15A clay, presented in the Fig. 2b exhibits reflections at around 2θ 3.0, 4.2 and 6.9°. As stated by the supplier, the interlayer spacing of the (001) plane (d_{001}) for this type of organically modified clay is 3.15 nm; thus, the corresponding reflection in the WAXD pattern should appear at 3.10° 2θ, just within the measurable range of the instrument, as indicated with the arrow in Fig. 2b. As in the case of the nanocomposites with the C30B clay, the absence of reflections in the WAXD patterns of the nanocomposites implies that the dispersion of the clay in the nanocomposites was either intercalated, with a *d*-spacing greater than 3.15 nm, or exfoliated. Only in the case of nanocomposite PCL/C15A-8, could an intercalated structure be confirmed from the observed shift in the diffraction peak at 2θ 6.9° (1.28 nm) in pristine clay to 2θ 4.5° (1.96 nm) in the nanocomposite. The well pronounced broad diffraction peak at 2θ 4.5° could imply that the clay created a dispersion of stacks with very well defined interlayer distances.[34]
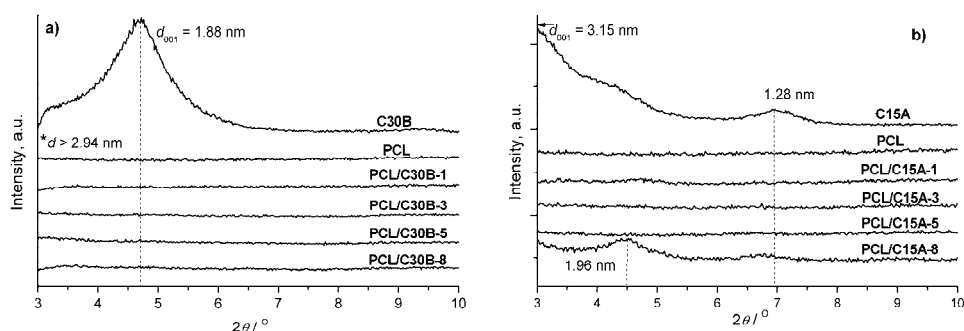
Fig. 2. WAXD patterns for pristine organoclays and the corresponding nanocomposites with a) C30B and b) C15A organoclay.

The nanocomposites reported in the literature prepared by solution casting usually possessed an intercalated structure. Using dichloromethane as a dispersion medium, Ahmed *et al.*[39] obtained an intercalated structure of PCL/C30B nanocomposites unaffected by the clay amount, with a reported interlayer distance increase of 1.14 nm compared to pristine C30B clay, even with the lowest amount of clay (2.5 wt. %). The authors applied the same experimental procedure using the C15A clay; however, no intercalation of PCL into the galleries of this clay was obtained. Ludũena with coworkers reported a mixed exfoliated/intercalated structure of PCL/C30B nanocomposites obtained from dichloromethane and a mixture of dichloromethane/dimethylformamide, judging from the broadening of the diffraction peak in comparison to the clay alone.[40] Neppali reported an intercalated structure for a PCL/C15A nanocomposite prepared from chloroform solution, with an achieved increase in interlayer distance of 0.8 nm.[41] The experimental protocol for the preparation of nanocomposites applied in the pre-

sent study included high dilution of the clay dispersion prior to the addition of this dispersion to the PCL solution. The applied ultrasonic treatment, although not optimized in the term of duration, seems to be well chosen for promoting PCL inclusion into the clay galleries. A similar experimental protocol in terms of high dilution was recently successfully applied for the preparation of exfoliated PCL/clay nanocomposites, even from unmodified clay.[36]

In the elaboration of a solvent casting route, the first thing that must be considered for the achievement of good clay dispersion is the interaction of the solvent with the clay and the polymer. In this study, chloroform was chosen as the dispersion medium being a good solvent for PCL. Moreover, the interaction of chloroform with the two types of clays and its ability to macroscopically swell the clay as well as to increase the interlayer spacing of the clay platelets was thoroughly investigated.[42] Both these parameters, the degree of swelling of the clay in the chloroform (with free swelling factor of 0.5 for C15A and 0.25 for C30B) and the increase in the interlayer spacing in the presence of the solvent, are in favor of C15A, due to the better interactions of the dispersive type of organic modifier of the C15A clay with chloroform. The polarity of the organic modifier of C30B did not provide for good interaction with chloroform. At the same time, the initial basal spacing of C15A (3.15 nm), caused by the tethering of organic ammonium ions on the platelet surface, is higher compared to C30B (1.88 nm). This fact also supports the expectation of better clay dispersion in the polymer matrix in the former case.

However, besides these initial requirements of compatibility of the dispersion medium and blend components, a factor that also influences the final clay dispersion is a good enthalpic interaction between the matrix and the organic modifiers of the clay. The interaction between the organic modifiers and the polymer chain serves to promote the inclusion of the polymer chains in between the clay platelets and to promote exfoliation. As a rough estimation of the interaction of the chosen organic modifiers and PCL, the solubility parameters (δ), calculated by the Hoftyzer–Van Krevelen group contribution method, of the organic modifiers and PCL were compared.[34,43] The δ values: 16.74 for the organic modifier of C15A and 18.73 for organic modifier of C30B in comparison to δ value of 19.44 calculated for the PCL show the better compatibility of PCL and the organic modifier of C30B clay. Thus, from the presented results, it could be concluded that good compatibility between the polymer matrix and the organic modifier of the clay plays the main role in achieving a good clay dispersion, although the process for clay dispersion in the polymer has to be carefully designed.

The surface and cryo-fractured surface morphology of nanocomposite films was observed *via* SEM analysis. Some representative micrographs are presented in Fig. S-1 of the Supplementary material to this paper. The surface of the

as-prepared films was smooth (the micrographs are not presented) without any observable holes, which could be created through fast chloroform evaporation, as previously reported for nanocomposites prepared from low-boiling solvents.[40] However, in the cryo-fractured surfaces, some holes in the sample bulk were registered, which could have an impact on the mechanical properties of the nanocomposites as weak places in the structures. No observable aggregates of the inorganic part of the nanocomposites could be detected by SEM, which is in agreement with the exfoliated/intercalated structure claimed from the WAXD analysis. However, there was a difference in the cryo-fractured surface morphology, which followed the trend of the observed differences in the nanocomposite morphology deduced from WAXD. The fractured surface of PCL was relatively smooth with observable plastic deformations typical for a ductile polymer. With the addition of C30B clay, no change in the cryo-fractured surface morphology was observed. In the case of nanocomposites with higher amount of the C15A clay, large voids and cavities were observable in the cryo-fractured surface. This was especially pronounced for the nanocomposite PCL/C15A-8 with the proven presence of an intercalated morphology. Presumably, the clay stacks present in the PCL/C15A-8 nanocomposite acted as microvoid nucleation sites in this case. The microvoids further grow through debonding between clay and PCL matrix. The smaller interaction between C15A and PCL could possibly favor this process, leading to the formation of many voids. As a result, the coalescence of microvoids leads to the formation of large voids and cavities protruding through the matrix bulk. Fibrillation of the polymer observed for some samples is highly atypical for cryo-fractured surfaces. Some earlier reports on nanocomposites with organically modified clays found that the organic modifier could have a plasticizing effect.[20,44] The possible plasticizing effect of the organic modifier present in the highest amount in PCL/C15A-8 (Table I) could be a reason for the observed fibrillation of the polymer matrix.

TABLE I. Composition of PCL/clay nanocomposites

Sample	Type of clay	PCL content wt. %	Organoclay content[a] wt. %	ϕ_{clay}[b] vol. %
PCL/C30B-1	Cloisite® 30B	99.0	1.0 (0.7)	0.6
PCL/C30B-3		97.0	3.0 (2.2)	1.8
PCL/C30B-5		95.0	5.0 (3.6)	2.9
PCL/C30B-8		92.0	8.0 (5.8)	4.6
PCL/C15A-1	Cloisite® 15A	99.0	1.0 (0.6)	0.7
PCL/C15A-3		97.0	3.0 (1.8)	2.1
PCL/C15A-5		95.0	5.0 (2.9)	3.5
PCL/C15A-8		92.0	8.0 (4.6)	5.5

[a]Values in the brackets refer to inorganic part; [b]the volume fraction of the clay calculated using the following values of the densities of the composite constituents: ρ_{PCL} = 1.2 g cm^{-3}, ρ_{C30B} = 1.98 g cm^{-3}, ρ_{C15A} = 1.66 g cm^{-3}

Thermal properties and crystallization

Melting temperatures and heats of fusion of PCL/clay nanocomposites were probed by DSC analysis. The results of the analysis of the DSC thermograms are summarized in Table II, from which it could be seen that there were no differences (within experimental error) in melting temperatures of the nanocomposites compared to that of the neat matrix. This means that the crystalline lamellae structure was not affected by the presence of the clay. However, marked differences were observed for the heat of fusion of the nanocomposites compared to that of neat PCL. The heats of fusion were determined by integration of the endothermic peak on the DSC thermograms. The values of the enthalpies of fusion of the nanocomposites exhibited differences that follow a similar, increasing trend with the increasing clay content in both series. The degree of crystallinity of the PCL matrix (X_c) in the samples was obtained from the values of enthalpies of fusion, by normalizing them to the PCL content and comparing to the heat of fusion of 100 % crystalline PCL (136.1 J g^{-1}).[19] Judging from obtained values for the degree of crystallinity of the nanocomposites, the amount of the crystalline PCL fraction was increased in the presence of the clay and this enhancement was influenced by the clay content.

TABLE II. Melting temperatures, heats of fusion, degree of crystallinity and spherulite diameters measured for neat PCL and PCL/clay nanocomposites

Sample	T_m[a] / °C	ΔH_m / J g^{-1}	X_c / %	$d_{spherulite}$ / μm
PCL	66	85.2	63	84 ± 12
PCL/C30B-1	66	90.5	67	79 ± 14
PCL/C30B-3	68	98.9	75	–
PCL/C30B-5	66	88.5	69	–
PCL/C30B-8	67	105.4	84	–
PCL/C15A-1	67	85.8	64	73 ± 15
PCL/C15A-3	66	97.0	73	94 ± 20
PCL/C15A-5	67	81.9	63	90 ± 20
PCL/C15A-8	66	95.9	77	92 ± 19

[a]Determined as the temperature of the maximum of the endothermic peak in DSC thermograms

The diameters of spherulites, observed by optical microscopy, are also given in Table II. In the images obtained using optical microscopy (Fig. S-2 of the Supplementary material), no holes or voids could be detected at the surface, as also shown by SEM. In the images of the surface of the nanocomposites formed in contact with a flat glass surface, a developed spherulite structure could be nicely observed. The spherulites structure and their border in neat PCL could be very well captured.

With the addition of the clay, the spherulite structure was severely destroyed with their borders fusing together. The effect was more pronounced in the case of the PCL/C30B nanocomposites, where the spherulite borders were observable

only for the nanocomposite with the lowest amount of clay. The diameter of spherulites decreased from around 84 μm for neat PCL to 79 μm for PCL/C30B-1 and 73 μm for PCL/C15A-1. The decrease in the diameter of the spherulites with increasing clay content, which is very often observed, is a consequence of the nucleating effect of the clay. As a result, the nanocomposites contained a higher number of smaller spherulites with increasing clay content. This trend was obviously continued in the case of the nanocomposites with C30B clay, for which, with increasing clay content, no clear spherulite borders could be distinguished. The change in the morphology of the spherulites can be explained if it is assumed that C30B clay, besides acting as a nucleating agent, disturbs the spherulite radial growth by a network of finely dispersed platelets/tactoids (clay stacks). Simultaneously, samples in PCL/C30B series had higher degrees of crystallinity compared to neat PCL and the nanocomposites containing C15A clay. An increased degree of crystallinity of nanocomposites compared to the matrix polymer is rarely observed in the literature and is explained with the nucleating effect of the clay.[20]

Interestingly, in the case of nanocomposites with C15A clay, an increase in spherulite diameter compared to neat PCL, for clay loadings higher than 1 wt. % was observed. The increase of spherulites in the presence of the clay was reported for poly(L-lactic acid)/clay nanocomposites,[35] albeit in nanocomposites where exfoliation of the clay was achieved, which is quite contrary to the present situation. The highest value of spherulite diameters for presented series of nanocomposites were observed in the case of an intercalated structure. The observed higher diameters of spherulites in the as-cast films might be a consequence of more effective heterogeneous nucleation in the PCL/C15A series, which accelerates the overall process of crystallization from the solution. Thus, the crystallization process was not restricted by the evaporation of the solvent and was accompanied with no disturbances by the silicate layer network. Since a larger portion of the silicate layers is present as tactoids rather than as single platelets, the possibility of network formation was lower or a less dense network was formed. In the case of PCL/C30B nanocomposites, which have a better dispersion of the clay platelets silicates layer network, formed from the single clay platelets, the radial growth of spherulites was disturbed, resulting in a quite different morphology of nanocomposites. In the PCL/C15A series, the degree of crystallinity was higher for nanocomposites in comparison to that of neat PCL, and followed a similar trend to that observed in the PCL/C30B series.

Thermal stability of nanocomposites

Thermal degradation of nanocomposites was investigated in non-isothermal TG experiments under a nitrogen atmosphere at a heating rate of 10 °C min^{-1}. The TG thermograms of PCL and PCL/clay nanocomposites of different compositions are presented in Fig. 3a and b.
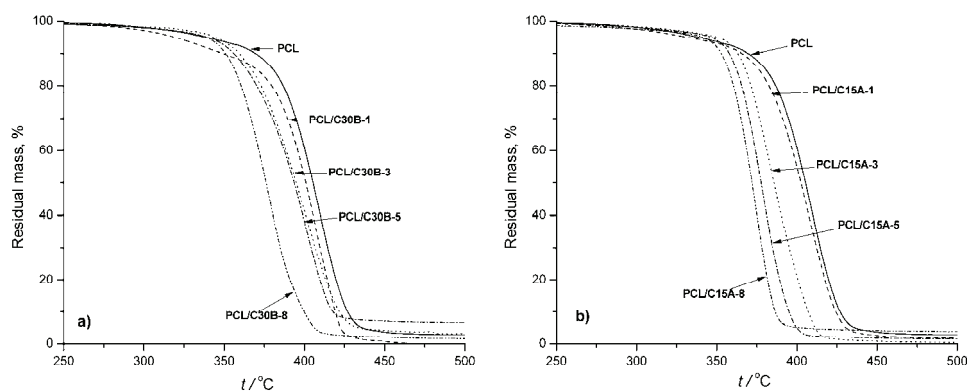
Fig. 3. TG curves obtained in a nitrogen atmosphere at a heating rate of 10 °C min^{-1} for nanocomposites with a) C30B clay and b) C15A clay.

The characteristic temperatures for a mass loss of 3 wt. %, taken as an indication of the beginning of the degradation, and for a mass loss of 50 wt. % are summarized in Table III. The onset temperature of thermal degradation is slightly higher for almost all nanocomposites in comparison to the neat PCL, with the exceptions of the nanocomposites with the lowest amount of both types of the clay. However, after this initial stage, a pronounced decomposition of the nanocomposites occurred with all TG curves shifted to lower temperature values relative to the curve for the matrix polymer. The temperatures of the maximum rate of weight loss, obtained from the corresponding DTG curves (not presented) were shifted to lower temperatures, in a trend that followed the increase in the amount of clay in the nanocomposites. Thus, the nanocomposites were less thermally stable, which was unexpected in comparison to some previous findings where an improvement in thermal stability was observed with the inclusion of clay in a polymer matrix.[18,25,36] On the other hand, there are reports of worsened thermal stability of nanocomposites containing clay.[20,45–47] According to the literature, the observed enhancement in thermal stability of polymer/clay nano-composites is usually ascribed to the shielding effect of clay layers, which act as a barrier to the gasses and volatile degradation products. Moreover, the clay platelets are considered as heat barriers and obstacles for polymer chain motion, leading to further stabilization.[48] However, the organically modified clays possess organic ions, in an amount of 30 to 40 wt. %, which are more prone to thermal degradation compared to the matrix and could affect the overall degradation process. The thermal degradation of the organoclays occurred between 220 and 450 °C (TG curves not presented) under the applied experimental conditions and was connected with the degradation of the organic modifiers. It could be assumed that the degradation of the organic ions had an accelerating effect on the degradation of the polymer. This was further supported by the trend of thermal

stability decrease with increasing amount of organic modifier present in the nanocomposite. Nanocomposites with the C30B clay had lower thermal stability than the corresponding nanocomposites with the C15A clay, even though the content of organic modifier was higher in the latter case. This could be connected to the different thermal stabilities of the corresponding organic modifiers of C30B and C15A[31] and/or the state of the clay dispersion,[49] which could override the influence of the amount of thermally labile organic ions. The results are consistent with previously reported ones, *i.e*., that a lower thermal stability was noticed for PCL/C30B due to PCL hydrolysis caused by the presence of hydroxyl groups in the modifier compared to nanocomposites with organoclays whose modifier contained only nonpolar groups.[23]

TABLE III. Characteristic temperatures obtained from the TG and DTG curves of PCL and the PCL/clay nanocomposites

Sample	$T_{3\%}$ / °C	$T_{50\%}$ / °C	T_{maxDTG} / °C
PCL	319	405	410
PCL/C30B-1	303	401	410
PCL/C30B-3	329	395	403
PCL/C30B-5	320	394	401
PCL/C30B-8	322	376	385
PCL/C15A-1	310	402	407
PCL/C15A-3	330	385	383
PCL/C15A-5	326	377	378
PCL/C15A-8	319	371	374

Mechanical properties of the nanocomposites

The characteristic properties of the as-prepared nanocomposite films were determined from tensile tests.

The results of these experiments, *i.e.,* Young's modulus, stress at break and strain at break are summarized in Table IV.

TABLE IV. Tensile properties of PCL and its nanocomposites; E and E_m refer to Young's modulus of the nanocomposite and matrix, respectively

Sample	Young's Modus, MPa	E/E_m[a]	Stress at break, MPa	Strain at break, %
PCL	327±21	1	15.0 ±1.1	9.8±0.9
PCL/C30B-1	313±26	0.96	14.4±0.7	9.0±1.0
PCL/C30B-3	339±23	1.04	14.1±0.5	9.3±0.9
PCL/C30B-5	289± 11	0.89	11.7±1.4	7.1±1.2
PCL/C30B-8	332±9	1.02	11.9±0.3	6.2±0.4
PCL/C15A-1	331±13	1.01	13.2±0.6	7.3±0.3
PCL/C15A-3	318±14	0.97	10.3±0.4	4.9±1.1
PCL/C15A-5	352±18	1.08	9.6±0.5	4.3±0.5
PCL/C15A-8	417±12	1.28	9.0±0.3	3.2±0.6

PCL is ductile polymer with moderate values of elastic modulus and high values of strain at break. The usually observed effect of the addition of a filler to a polymer matrix is increased stiffness accompanied with embrittlement. The embrittlement is usually ascribed to the formation of agglomerates, particularly at higher clay loadings, which induce weak places in the nanocomposite structure. A lowering of the strain at break from 700 to 7 % was reported for a PCL nanocomposite with 10 wt. % of organo-modified clay, which was ascribed to agglomerate formation.[25] In the present case, the reason for the measured low absolute values of the strain at break, even at very low clay contents and also for the neat PCL, accompanied with the absence of yielding, probably lies in the structure of the specimens. The specimens used in the tensile tests were as-prepared solution cast films with holes and voids as weak places. However, the addition of clay also contributes to the embrittlement of the material. A trend of decreasing strain at break with increasing clay loading was observed, similar to the usually found embrittlement effect of clay. A distinction could be made between the different clays used; at all compositions, the nanocomposite containing C30B exhibited higher values of the strain at break in comparison to the nanocomposite containing C15A, as a consequence of better clay dispersion, better interaction of organic modifier of C30B with PCL and, consequently, less weak places for the initiation of the cracks.

The values of stress at break were typical for PCL and its nanocomposites reported in the literature. The stress at break followed a similar trend to that of the strain at break, with higher values for the nanocomposites with C30B clay. Analogous argumentation proposed for the trends in the strain at break values probably holds for the observed change in the stress at break values.

The value of the elastic modulus obtained for the PCL matrix was comparable to those hitherto reported for this polyester. Some of the nanocomposites, especially those containing the C30B clay, exhibited lower values of the modulus compared to the PCL matrix. Such unexpected behavior is very rarely reported or explained in the literature. Pentoustier *et al.* reported a decrease in the modulus of a nanocomposite with unmodified clay prepared by *in situ* intercalative polymerization.[18] Ludũena *et al.* observed a reduced modulus relative to the PCL matrix for some nanocomposites prepared by solution casting from dichloromethane or dichloromethane/dimethylformamide.[40] PCL nanocomposites with C15A clay and varying molecular weights of the matrix, studied by Causin *et al.*, showed a reduced modulus in comparison to the neat PCL, in the whole investigated range of clay loadings for nanocomposites prepared by solution casting from tetrahydrofuran.[41,50]

It was interesting to compare the obtained experimental data with theoretical predictions for elastic modulus of nanocomposites with plate-like fillers. The most frequently used Halpin–Tsai Equation was applied to calculate the theo-

retical values for elastic moduli.[50–52] The longitudinal, $E_\parallel$, and transverse, $E_\perp$, modulus of Halpin–Tsai model can be expressed by the following equation:

$$\frac{E}{E_m} = \frac{1+\zeta\eta\phi_{filler}}{1-\eta\phi_{filler}} \tag{1}$$

where E and E_m are the Young's modulus of the composite and matrix, respectively, ϕ_{filler} is the volume fraction of the filler in the nanocomposite and ζ is a shape parameter: $\zeta = 2(l/t)_{filler}$ for the longitudinal modulus ($E_\parallel$) and $\zeta = 2$ for perpendicular modulus ($E_\perp$), where l and t are the length and thickness of the dispersed phase, *i.e.*, clay. The parameter η is defined as:

$$\eta = \frac{(E_{filler}/E_m)-1}{(E_{filler}/E_m)+\zeta} \tag{2}$$

In the case of randomly oriented clay platelets, the equation for the calculation of the modulus is:

$$E = 0.49\,E_\parallel + 0.51\,E_\perp \tag{3}$$

In the calculations of the elastic modulus, when good exfoliation could be assumed, single platelets are treated as filler particles or, in the case of intercalated structure, a filler particle is a stack of clay platelets with gallery material. In the case of composites with C30B clay, good exfoliation was assumed and the parameters used for the calculation were $E_{filler} = E_{clay} = 178$ GPa[50] and $\phi_{filler} = \phi_{clay}$ (Table I). E_m was assumed equal to the modulus of the PCL matrix, 327 MPa (Table IV). The calculations were performed for two different aspect ratios of the clay platelets, $l/t = 80$ and 10, and compared to the experimentally observed modulus of the nanocomposite (Fig. 4a). It could be observed that the values predicted by the Halpin–Tsai Model were higher than those experimentally determined and that, even on decreasing the aspect ratio to 10, these corresponding modulus values could not fit to those experimentally determined. It was previously observed that the model cannot accurately predict the E values for particles less than 100 nm in size.[53] Namely, the Halpin–Tsai method does not take into account interfacial molecular structure, which probably played the dominant role for the nanocomposites with particle sizes less than 100 nm.

The second approach, *i.e.*, the intercalated case, was applied for the calculation of the theoretical modulus for the series of nanocomposites with C15A clay. The effective modulus of the filler (a stack of clay platelets in this case) could be approximated by using the rule of mixtures:

$$E_{filler} = \phi_{platelet}E_{clay} + \phi_{gallery}E_{gallery} \tag{4}$$

where $\phi_{platelet}$ and $\phi_{gallery}$ are the volume fractions of clay platelets and gallery space in the stack, respectively, while E_{clay} and $E_{gallery}$ are the modulus of silicate platelets and the intercalated material in the gallery, respectively. The

volume fraction of clay platelets in the lamellar stacks, $\phi_{platelet}$, was calculated as the ratio of the total thickness of the clay platelet (obtained by multiplying the thickness of a single platelet, $t_{platelet}$, by the number of the platelets per stuck, $n_{platelet}$) and the thickness of the entire lamellar stack (t_{stack}) and could be expressed as follows:

$$\phi_{platelet} = \frac{n_{platelet} t_{platelet}}{t_{stack}} = \frac{t_{platelet}}{d_{001}} \tag{5}$$

Thus, the volume fraction of clay platelets can be calculated by using the thickness of a single platelet (1 nm)[51] and the number of platelets in the stack (which is usually determined from TEM measurements), or by using the d-spacing of the nanocomposite determined by WAXD. Here, the literature value of d_{001}=3.63 nm from a similar pattern as in the present case was used.[39] The value of 27.5 vol. % for the volume fraction of silicate platelets, $\phi_{platelet}$, was obtained. A value of 178 GPa was used for the modulus of the silicate platelets. The modulus of the organic interlayer material (organic modifier of C15A and PCL chains) was expected to be significantly smaller than the modulus of the clay platelets. Thus, the contribution of $E_{gallery}$ to the E_{filler} could be neglected. Hence, the calculated modulus of the filler decreased form 178 GPa to 49 GPa, because of the intercalation. In this way, the calculated modulus of the filler was reduced by 72 %. However, there are some reports that the so-obtained modulus is still an overestimation of the real filler modulus.[54]

The intercalation of the clay by PCL will increase the effective volume fraction of the filler. Under the assumption that the effective volume is proportional to the interlayer spacing,[53] the increase in the volume fraction was taken to be equal to the increase in the d_{001}-spacing, which was 1.15 times. Although intercalation was not proven for the nanocomposites with less than 8 wt. % of C15A, all theoretical predictions were also performed for these nanocomposites for the sake of comparison (Fig. 4b).

Based on a comparison of theoretical and experimental nanocomposite modulus, it is clear that the theoretical Halpin–Tasai modulus could approach the experimentally observed values if the aspect ratio of the filler was lowered, in the case of nanocomposites with C15A clay even to a value of $(l/t)_{filler}$= 4. For the nanocomposite PCL/C15A-8, with proven intercalated structure and with $d_{001} = 3.63$ nm, which was used for the calculations, the number of platelets per filler stack is greater than 7, if the value of l is assumed to be 100 nm. However, as shown in the case of nanocomposites of C30B clay, the value of l is possibly lower than 100 nm, which would decrease the number of platelets in the clay stack.

In summary, the Halpin–Tsai Model can better predict the modulus in the case of intercalated nanocomposites obtained with the C15A clay, while for the

exfoliated structure, this model overestimates the modulus as was shown previously for PLA nanocomposites.[53]
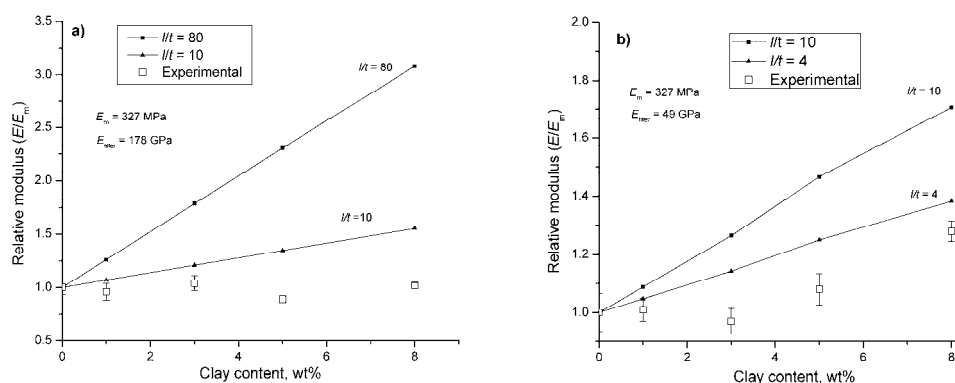

Fig. 4. Comparison of the experimental relative modulus and predictions by the Halpin–Tsai Model for the nanocomposites with a) C30B and b) C15A clay.

CONCLUSIONS

Two series of PCL nanocomposites with organoclays possessing different organic modifiers were prepared from chloroform solution. The conditions of experimental protocol for composite preparation were optimal from the aspect of achieving the best clay dispersion. WAXD and SEM confirmed that exfoliated or exfoliated/intercalated nanocomposite morphology was obtained. The favorable interaction between organic modifier of the clay and PCL is the most important factor that must be optimized in order to achieve the best clay dispersion. The differences in nanocomposite morphology and degree of crystallinity are ascribed to the differences in the dispersion of the clay. The nanocomposites are less thermally stable than the neat PCL. The decreased thermal stability of the nanocomposites is the consequence of the presence of thermally less stable organic ammonium ions, which accelerate the degradation of the matrix. In terms of mechanical properties, despite the good clay dispersion, almost all nanocomposites have reduced values of the characteristic parameters obtained in tensile tests performed on as-prepared films. The strain at break is reduced with the increasing clay loading. The highest modulus was obtained for the nanocomposite with the intercalated structure. For the composites with exfoliated structure, the Halpin–Tsai Model was found to be inappropriate, while for the intercalated composite, the model was able to capture modulus increase with a very low value of the clay "stuck" aspect ratio.

SUPPLEMENTARY MATERIAL

SEM micrographs of the fractured surface of the nanocomposites and images of PCL and PCL/clay nanocomposite films obtained by optical microscopy are available electronically from http://www.shd.org.rs/JSCS/, or from the corresponding author on request.

И З В О Д

УТИЦАЈ ОРГАНСКОГ МОДИФИКАТОРА ГЛИНА НА МОРФОЛОГИЈУ И ПЕРФОРМАНСЕ PCL/ГЛИНА НАНОКОМПОЗИТА

МАРИЈА С. НИКОЛИЋ, НАТАША ЂОРЂЕВИЋ, ЈЕЛЕНА РОГАН и ЈАСНА ЂОНЛАГИЋ

Технолошко–металуршки факултет, Универзитет у Београду, Карнегијева 4, 11000 Београд

Припремљене су две серије нанокомпозита на бази поли(ε-капролактона) и две врсте органомодификованих глина, различитих састава (1 до 8 мас. %), методом из раствора. Одабране органомодификоване глине поседују поларни (Cloisite® C30B) и неполарни (Cloisite® C15A) органски модификатор и разликују се по мешљивости са полимерном матрицом. Велико разблажење и третман ултразвуком, коришћени у поступку припреме омогућили су добијање нанокомпозита са ексфолираном и ексфолираном/интеркаларном структуром. Испитиван је утицај модификације и садржаја глина на морфологију, механичка и термичка својства нанокомпозита. Скенирајућом електронском микроскопијом је утврђено да нису добијени микрокомпозити. Дифракцијом рендгенских зрака на великим угловима је утврђено да се боља дисперзија постиже код нанокомпозита са оном глином (Cloisite® C30B) чији органски модификатори имају бољу интеракцију са полимерном матрицом. Оптичком микроскопијом је уочено да филмови добијених нанокомпозита имају сферулите различите величине и морфологије. Промене енталпије топљења и степени кристалиничности су већи код нанокомпозита у односу на чисту матрицу и имају растући тренд са повећањем удела глине у обе серије, што је последица дејства наноглина као центара за нуклеацију. Мања термичка стабилност нанокомпозита у односу на чисту матрицу је приписана термичкој нестабилности самих органских модификатора. Вредности модула еластичности, добијене у тестовима истезања, су упоређене са теоријски прорачунатим према Halpin– Tsai моделу.

(Примљено 24. септембра, ревидирано 19. новембра, прихваћено 20. новембра 2014)

REFERENCES

1. D. R. Paul, L. M. Robeson, *Polymer* **49** (2008) 3187
2. S. Sinha Ray, M. Okamoto, *Prog. Polym. Sci.* **28** (2003) 1539
3. M. Alexandre, P. Dubois, *Mater. Sci. Eng. R* **28** (2000) 1
4. S. Pavlidou, C. D. Papaspyrides, *Prog. Polym. Sci.* **33** (2008) 1119
5. M. A. Tasdelen, *Eur. Polym. J.* **47** (2011) 937
6. B. Chen, J. R. G. Evans, *Macromolecules* **39** (2005) 747
7. G. Gorrasi, M. Tortora, V. Vittoria, E. Pollet, B. Lepoittevin, M. Alexandre, P. Dubois, *Polymer* **44** (2003) 2271
8. E. Manias, A. Touny, L. Wu, K. Strawhecker, B. Lu, T. C. Chung, *Chem. Mater.* **13** (2001) 3516
9. S. Sinha Ray, K. Okamoto, M. Okamoto, *Macromolecules* **36** (2003) 2355

10. M. A. Woodruff, D. W. Hutmacher, *Prog. Polym. Sci.* **35** (2010) 1217
11. Y. Li, C. Han, J. Bian, X. Zhang, L. Han, L. Dong, *Polym. Compos.* **34** (2013) 131
12. N. Moussaif, S. Irusta, C. Yagüe, M. Arruebo, J. G. Meier, C. Crespo, M. A. Jimenez, J. Santamaría, *Polymer* **51** (2010) 6132
13. K. K. Gupta, A. Kundan, P. K. Mishra, P. Srivastava, S. Mohanty, N. K. Singh, A. Mishra, P. Maiti, *Phys. Chem. Chem. Phys.* **14** (2012) 12844
14. R. Augustine, H. Malik, D. Singhal, A. Mukherjee, D. Malakar, N. Kalarikkal, S. Thomas, *J. Polym. Res.* **21** (2014) 347
15. I. Armentano, M. Dottori, E. Fortunati, S. Mattioli, J. M. Kenny, *Polym. Degrad. Stability* **95** (2010) 2126
16. P. Bordes, E. Pollet, L. Averous, *Prog. Polym. Sci.* **34** (2009) 125
17. B. Lepoittevin, N. Pantoustier, M. Devalckenaere, M. Alexandre, D. Kubies, C. Calberg, R. Jérôme, P. Dubois, *Macromolecules* **35** (2002) 8385
18. N. Pantoustier, B. Lepoittevin, M. Alexandre, P. Dubois, D. Kubies, C. Calberg, R. Jérôme, *Polym. Eng. Sci.* **42** (2002) 1928
19. A. Kiersnowski, J. S. Gutmann, J. Pigłowski, *J. Polym. Sci., Polym. Phys.* **45** (2007) 2350
20. K. Chrissafis, G. Antoniadis, K. M. Paraskevopoulos, A. Vassiliou, D. N. Bikiaris, *Compos. Sci. Technol.* **67** (2007) 2165
21. R. Pucciariello, V. Villani, L. Guadagno, V. Vittoria, *J. Polym. Sci., Polym. Phys.* **44** (2006) 22
22. N. Pantoustier, M. Alexandre, P. Degée, C. Calberg, R. Jérôme, C. Henrist, R. Cloots, A. Rulmont, P. Dubois, *e-Polymers* **1** (2001) 77
23. A. Harrane, M. Belbachir, *Macromol. Symp.* **247** (2007) 379
24. J. Kotek, D. Kubies, J. Baldrian, J. Kovářová, *Eur. Polym. J.* **47** (2011) 2197
25. B. Lepoittevin, M. Devalckenaere, N. Pantoustier, M. Alexandre, D. Kubies, C. Calberg, R. Jérôme, P. Dubois, *Polymer* **43** (2002) 4017
26. Y. Di, S. Iannace, E. Di Maio, L. Nicolais, *J. Polym. Sci., Polym. Phys.* **41** (2003) 670
27. I. Janigová, F. Lednický, D. J. Mošková, I. Chodák, *Macromol. Symp.* **301** (2011) 1
28. S. Labidi, N. Azema, D. Perrin, J.-M. Lopez-Cuesta, *Polym. Degrad. Stab.* **95** (2010) 382
29. D. Homminga, B. Goderis, I. Dolbnya, G. Groeninckx, *Polymer* **47** (2006) 1620
30. L. Ludueña, A. Vázquez, V. Alvarez, *J. Comp. Mat.* **46** (2012) 677
31. L. N. Ludueña, J. M. Kenny, A. Vasquez, V. A. Alvarez, *Mater. Sci. Eng., A* **529** (2011) 215
32. L. N. Ludueña, A. Vázquez, V. A. Alvarez, *J. Appl. Polym. Sci.* **128** (2013) 2648
33. G. Jimenez, N. Ogata, H. Kawai, T. Ogihara, *J. Appl. Polym. Sci.* **64** (1997) 2211
34. V. Krikorian, D. J. Pochan, *Chem. Mater.* **15** (2003) 4317
35. V. Krikorian, D. J. Pochan, *Macromolecules* **37** (2004) 6480
36. T. Wu, T. Xie, G. Yang, *Appl. Clay Sci.* **45** (2009) 105
37. F. Clegg, C. Breen, *Appl. Clay Sci.* **85** (2013) 80
38. S. A. Papadimitriou, G. Z. Papageorgiou, D. N. Bikiaris, *Eur. Polym. J.* **44** (2008) 2356
39. J. Ahmed, R. Auras, T. Kijchavengkul, S. K. Varshney, *J. Food Eng.* **111** (2012) 580
40. L. N. Ludueña, V. A. Alvarez, A. Vazquez, *Mater. Sci. Eng.* **460–461** (2007) 121
41. R. Neppalli, V. Causin, C. Marega, R. Saini, M. Mba, A. Marigo, *Polym. Eng. Sci.* **51** (2011) 1489
42. D. Burgentzle, J. Duchet, J. F. Gerard, A. Jupin, B. Fillon, *J. Colloid Interface Sci.* **278** (2004) 26
43. D. W. Van Krevelen, *Properties of the polymers*, Elsevier, Amsterdam, 1976.

44. W. Xie, J. M. Hwu, G. J. Jiang, T. M. Buthelezi, W.-P. Pan, *Polym. Eng. Sci.* **43** (2003) 214
45. J.-H. Chang, Y. U. An, G. S. Sur, *J. Polym. Sci., Polym. Phys.* **41** (2003) 94
46. D. S. Dlamini, S. B. Mishra, A. K. Mishra, B. B. Mamba, *J. Inorg. Organomet. Polym. Mater.* **21** (2011) 229
47. M. S. S. B. Monteiro, C. L. Rodrigues, R. P. C. Neto, M. I. B. Tavares, *J. Nanosci. Nanotech.* **12** (2012) 7307
48. A. Leszczyńska, J. Njuguna, K. Pielichowski, J. R. Banerjee, *Thermochim. Acta* **453** (2007) 75
49. G.-X. Chen, J.-S. Yoon, *Polym. Degrad. Stability* **88** (2005) 206
50. T. D. Fornes, D. R. Paul, *Polymer* **44** (2003) 4993
51. J. I. Weon, H. J. Sue, *Polymer* **46** (2005) 6325
52. K. C. Yung, J. Wang, T. M. Yue, *J. Reinf. Plast. Compos.* **25** (2006) 847
53. S.-M. Lai, S.-H. Wu, G.-G. Lin, T.-M. Don, *Eur. Polym. J.* **52** (2014) 193
54. M. W. Spencer, L. Cui, Y. Yoo, D. R. Paul, *Polymer* **51** (2010) 1056.

Influence of clay organic modifier on the morphology and performance of poly(ε-caprolactone)/clay nanocomposites

MARIJA S. NIKOLIĆ*#, NATAŠA ĐORĐEVIĆ, JELENA ROGAN#
and JASNA ĐONLAGIĆ#

*Faculty of Technology and Metallurgy, University of Belgrade, Karnegijeva 4,
11000 Belgrade, Serbia*
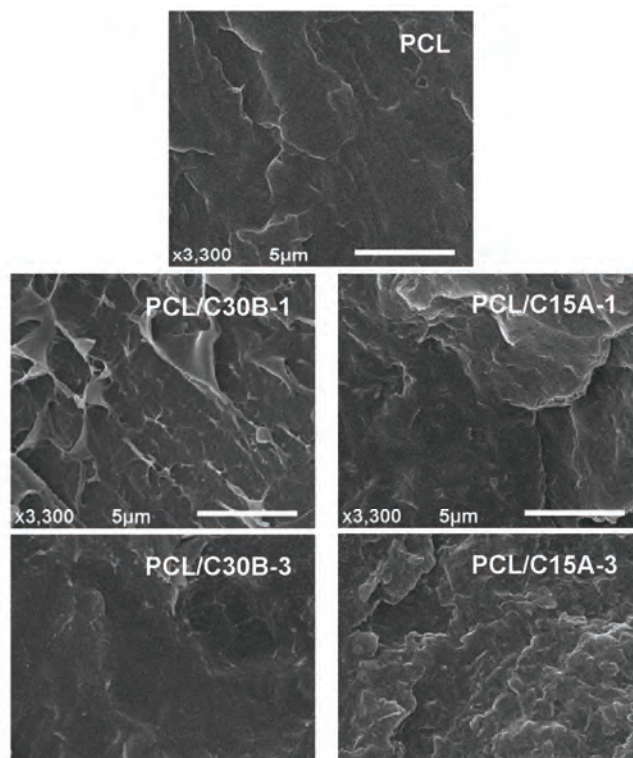
Fig. S-1. SEM micrographs of the fractured surface of the nanocomposites.

* Corresponding author. E-mail: mnikolic@tmf.bg.ac.rs
# Serbian Chemical Society member.
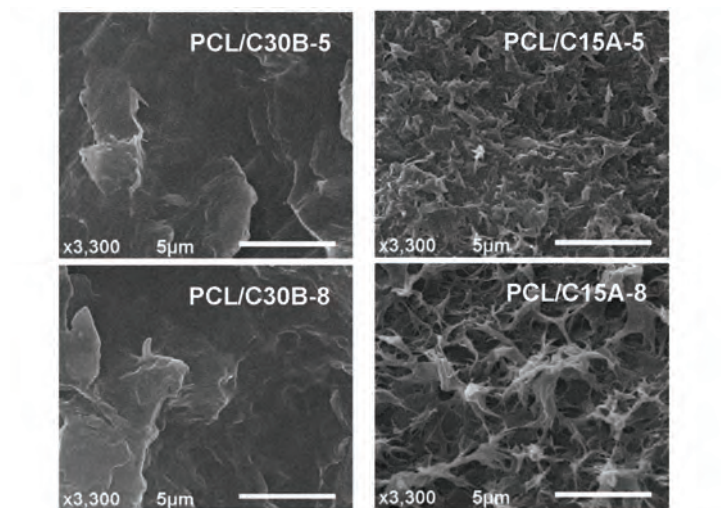
Fig. S-1 (Continued). SEM micrographs of the fractured surface of the nanocomposites.
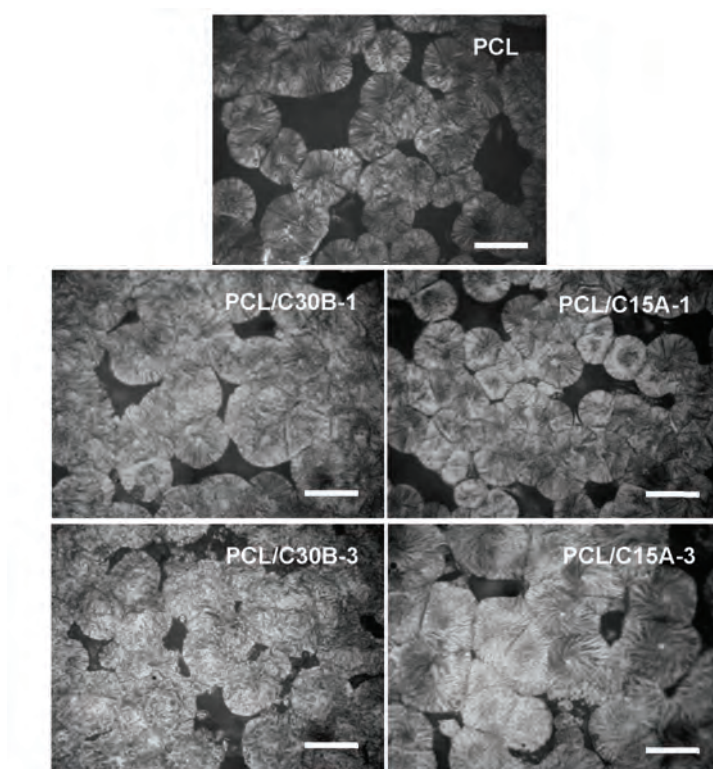
Fig. S-2. Images of PCL and PCL/clay nanocomposite films obtained by optical microscopy (bar 100 μm).
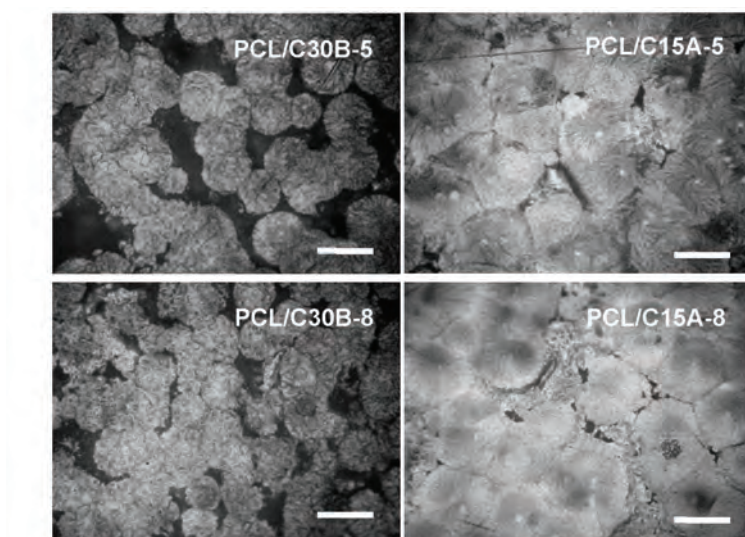
Fig. S-2 (Continued). Images of PCL and PCL/clay nanocomposite films obtained by optical microscopy (bar 100 µm).

Modeling of the reactions of a calcium-based sorbent with sulfur dioxide

IVAN TOMANOVIĆ[1]*, SRĐAN BELOŠEVIĆ[1], ALEKSANDAR MILIĆEVIĆ[1]
and DRAGAN TUCAKOVIĆ[2]

[1]*University of Belgrade, Vinča Institute of Nuclear Sciences, Mike Petrovića Alasa 12–14,
P. O. Box 522, 11001 Belgrade, Serbia and* [2]*University of Belgrade, Faculty of Mechanical
Engineering, Kraljice Marije 16, 11120 Belgrade 35, Serbia*

Abstract: A mathematical model of calcium sorbent reactions for the simulation of sulfur dioxide reduction from pulverized coal combustion flue gasses was developed, implemented within a numerical code and validated against available measurements under controlled conditions. The model attempts to resemble closely the reactions of calcination, sintering and sulfation occurring during the motion of the sorbent particles in the furnace. The sulfation was based on the partially sintered spheres model (PSSM), coupled with simulated particle calcination and sintering. The complex geometry of the particle was taken into account, with the assumption that it consists of spherical grains in contact with each other. Numerical simulations of drop down tube reactors were performed for both $CaCO_3$ and $Ca(OH)_2$ sorbent particles and results were compared with experimental data available from the literature. The model of the sorbent reactions will be further used for simulations of desulfurization reactions in turbulent gas–particle flow under coal combustion conditions.

Keywords: lime; particle; desulfurization; flue gas; model.

INTRODUCTION

In order to investigate in detail the possible reduction of sulfur oxides in flue gas by injection of a pulverized sorbent into coal-fired boiler furnaces, a model of sorbent reactions is required. In the literature, various models are available that can be roughly divided into groups according to the way they treat the sorbent particles. The simplest of them are shrinking unreacted core models, such as the one described by Borgwardt.[1] More complex and computationally demanding models are the partially sintered spheres model (PSSM),[2–5] the pore model,[2,3] the network model[2,3] and their variations. The PSSM and pore models have a certain


549

level of similarity, both observing the particle structure during reactions and highly depending on particle transformation over time.

The Borgwardt model was implemented in previous research in a numerical model and used to simulate reactions of larger particle fractions (around 90 µm and a few larger and smaller fractions) in a fixed bed reactor as a method of validation[6] and in a complex model of the boiler furnace.[7] Implementation showed good agreement with experimental results, however, due to the short particle residence time, effects of sulfur reduction were not sufficient, and sorbent utilization was low. For this reason, the possible use of finely pulverized particle fractions (smaller than, or around 10 µm) had to be analyzed. Due to the lack of data and different reaction mechanism, this model could not be used to describe the reaction of smaller particles at high temperatures. Experimental studies conducted by Borgwardt,[8] Flament,[9] Miline,[10–12] Silcox,[13] Fan[14] and Chen[15] showed the great potential for the use of finely pulverized sorbent particles when the sorbent is injected directly into the boiler furnace. Several models are available in literature.[2–5,8,10–14]

The most used sorbents are calcium-based, *i.e.*, $CaCO_3$ and $Ca(OH)_2$, due to their availability and good reactivity with sulfur oxides under combustion conditions. Reactions of particles consist of calcination, sintering and sulfation. During the calcination process, $CaCO_3$ is converted to CaO whereby the BET surface available for reaction increases greatly.[8,9,13] If the reactant in use is $Ca(OH)_2$, then during a short period, a dehydration reaction occurs[9,14] that is followed by a rapid increase in the BET surface, much faster in comparison with the development of the surface obtained by calcination of calcium carbonate. These reactions are shown in Eq. (1).

At high temperatures together with calcination, sintering of the particles occurs, which leads to rapid loss of BET surface.[8,9,13] The final reaction that occurs together with the two previous ones is sulfation of sorbent in atmospheres containing sulfur oxides:

$$CaCO_3 \rightarrow CaO + CO_2$$
$$Ca(OH)_2 \rightarrow CaO + H_2O \qquad (1)$$
$$CaO + SO_2 + 0.5O_2 \rightarrow CaSO_4$$
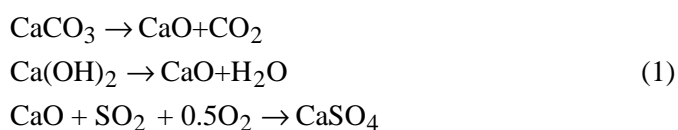
THE SORBENT REACTIONS MODEL, ITS NUMERICAL IMPLEMENTATION AND EXPERIMENTAL

The model is based on the sulfation PSSM approach combined with the calcination model, both presented by Alvfors[5] for a single particle. A brief description of the model is presented, with most significant equations given for reference. Further details on the model for single particle sulfation can be found in the papers by Lindner,[2] Kocafe[3] and Alvfors.[4,5] This model is implemented and used with a complex numerical code for the simulations. The particle calcination model, used to determine the development of the particle surface during

reaction time, was first introduced by Alvfors[5] in combination with the PSSM. Alvfors[5] showed that the expression given by Beruto,[16] together with the German–Munir sintering formula,[17] could give good agreement with the measured[9] particle calcination and surface development.[9]

Expression used for the calcination model given by Beruto[16] describes the extent of calcination at a given time:

$$\ln(1 - X_c(t)) = -k_c M_{M,CaCO_3} S_{CaCO_3} t \tag{2}$$

The extent of calcination was determined by expressing $X_C(t)$ from Eq. (2) used to calculate surface area of the calcium sorbent given later in Eq. (4).

Loss of surface due to sintering of a particle is modeled by the German–Munir formula:[17]

$$\left[\frac{S_0 - S}{S_0} \right]^\gamma = K_s t \tag{3}$$

Equation (3) assumes the particle consists of spherical grains connected by necks between neighboring grains, and when sintering occurs, the necks connecting the grains begin to overlap.

Surface area of calcium sorbent, expressed in $m^2\ cm^{-3}$, at a given time step consists of a $CaCO_3$ part and a CaO part, depending on the extent of calcination $X_c(t)$:

$$S_{0,Ca}^n = \frac{(X_c(t_n) S_{CaO}^n M_{M,CaO} + (1 - X_c(t_n)) S_{CaCO_3} M_{M,CaCO_3})}{X_c(t_n) V_{M,CaO} + (1 - X_c(t_n)) V_{M,CaCO_3}} (1 - \varepsilon_{Ca}) \tag{4}$$

At a given time step, the surface area of the calcium oxide part, derived from Eqs. (2) and (3), is:

$$S_{CaO}^n = \sum_{k=1}^{n} S_{0,CaO} (1 - (K_s(T_k) t_n)^{1/\gamma(T_k)}) (X_c(t_k) - X_c(t_{k-1})) \tag{5}$$

As suggested by Alvfors,[5] the PSSM should take into account the development of the BET surface, obtained by application of the calcination and sintering model, and use it as the basis for the determination of the sulfation rate.

The coefficients for calcination of $CaCO_3$, given by Alvfors,[5] show good agreement with the available experimental data for small particles; however, the development of the BET surface is significantly slower, compared to the experimental one. Due to this, the calcination and sintering coefficients for $CaCO_3$ given by Borgwardt[8,5] are used. For temperatures above 950 °C, the calculated BET surfaces show excellent agreement with the experimental data. The porosity of the particle is considered to be initially small, but afterwards, the porosity of the particle increases during the reaction.

The model for the development of the BET surface of $Ca(OH)_2$ particles given by Fan[14] is more complex compared to the one described above. In order to simplify the calculations, the above model was used and the experimental data given by Fan[14] were fitted with it. The coefficients used for the calculations of k_c, K_S and γ are given in Table I. The initial porosity of $Ca(OH)_2$ was considered to be high, and to decrease with time.

Sulfation model used was the PSS model introduced by Lindner[2] and further described in the literature.[2–5] The model assumes that a sorbent particle consists of small non-porous spherical grains in contact with m other grains (Fig. 1). During the initial time step, all grains

are the same and have radius r_0. When reaction begins, unreacted core reduces in size and its radius changes to r_2 (in dimensionless form $g_2 = r_2/r_0$), while the product layer increases in size and has radius r_1 (in dimensionless form $g_1 = r_1/r_0$). The change of the unreacted core over time, due to conversion, can be given by the differential equation:

$$\frac{\mathrm{d}g_2}{\mathrm{d}t*} = \frac{S_0}{S_2}\bar{r} \tag{6}$$

TABLE I. Coefficients used for the calculations of calcination and sintering of the sorbent particle, and the particle porosity

Coefficient	Sorbent	
	CaCO$_3$ (Borgwardt[18])	Ca(OH)$_2$ (Fan[14])
k_c / mol m^{-2} s^{-1}	$3.405 \times 10^7 e^{\frac{-201}{RT_p}}$	$2.2 \times 10^6 e^{\frac{-141}{RT_p}}$
K_s / s^{-1}	$e^{6.735 - \frac{11660}{T_p}}$	$e^{-1.4 - \frac{2000}{T_p}}$
γ	$e^{0.0018T_p + 0.8154}$	$e^{0.002T_p + 0.89694}$

Conversion is obtained by comparing the initial and sulfated particle geometries, and it can be expressed by:

$$X_s = 1 - \frac{g_2^3 - \frac{m}{4}F(g_2, \lambda)}{1 - \frac{m}{4}(1-\lambda)^2(2+\lambda)} \tag{7}$$

When the values of g_2 and X_s are known, the following volumetric balance can be used to determine value of g_1 if the molar volume ratio (α) between the solid product and solid reactant is known:

$$g_1^3 - g_2^3 - \frac{m}{4}\left((g_1-\lambda)^2(2g_1+\lambda) - F(g_2,\lambda)\right) = \alpha X_s\left(1 - \frac{m}{4}(1-\lambda)^2(2+\lambda)\right) \tag{8}$$

The reaction rate on the particle surface can be given by $r_A = -k\, c_{A,s}S_2$, while the diffusion through product layer is $r_A = -D_s(c_A - c_{A,s})S_{avg}/L$. From these two equations, an expression for local reaction rate is derived:

$$-\bar{r} = \frac{-r_A}{kc_{A0}S_0} = \frac{C}{\frac{S_0}{S_2} + \frac{DaLS_0}{l_0 S_{avg}}} \tag{9}$$

The interaction between the local kinetics and pore diffusion is obtained by differential mass balance for the gaseous reactant, assuming pseudo steady state conditions:

$$\frac{1}{z^2}\frac{\mathrm{d}}{\mathrm{d}z}\left(z^2\delta\frac{\mathrm{d}C}{\mathrm{d}z}\right) = -\Phi_{Th}^2\frac{C}{S_0/S_2 + DaLS_0/l_0 S_{avg}} \tag{10}$$

From Eq. (9), the average reaction rate in the particle, which depends on pore diffusion, is obtained. Furthermore, it is used to determine the rate of sulfur oxide depletion from the surrounding gas.
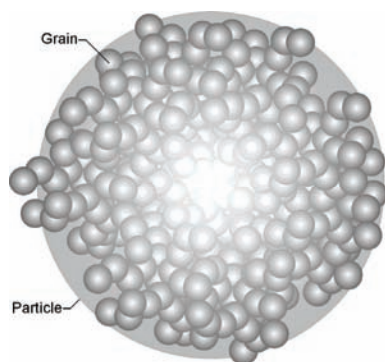
Fig. 1. Model of a sorbent particle.

A particle is considered to consist entirely of calcium. The initial particle parameters used are the ones given for the experimental data described in the literature:[5,8,9] BET = 0.9 m^2 g^{-1}, ε_0 = 3 %, $S_{0,CaO}$ = 104 m^2 g^{-1} and λ = 80 %. Sulfation rate coefficients, and diffusion coefficients are the ones given by Alvfors[4], as follows: k = 20exp($-25/RT_p$), m s^{-1}; D_0 = = 1.5×10^{-4}(T_p/1123)$^{1.7}$, m^2 s^{-1}, and D_s = 1.913×10^{-5}exp($-125/RT_p$), m^2 s^{-1}.

Two drop down tube reactors were modeled in a 2D model with a grid of 600 cells×30 cells in size (estimated to provide stable numerical solutions). The system of gas phase transport equations of momentum, continuity and energy in an Eulerian field were solved by using the control volume numerical method. The fluid flow equations were coupled with the chemical reactions equations. The general form of the conservation equations used in the model could be written in index notation as:

$$\frac{\partial}{\partial x_j}\left(\rho U_j \Phi\right) = \frac{\partial}{\partial x_j}\left(\Gamma_\Phi \frac{\partial \Phi}{\partial x_j}\right) + S_\Phi + S_p^\Phi \qquad (11)$$

Φ represents a general variable, such as U, V, W, x_{O_2}, x_{N_2}, x_{CO_2}, x_{H_2O}, x_{SO_2}, *etc.* Terms in Eq. (11) from left to right are convection, diffusion, source term for variable Φ, and additional source term due to particles.

The tubes considered in the simulations had the same dimensions and gas phase flow conditions as in the experiments conducted by Flament[9] with $CaCO_3$ and Fan[14] with $Ca(OH)_2$. Gas mixture components and their concentrations used in the simulations correspond to those found in experiments[9,14]. The conditions are also similar to the flue gas composition that can be found during the pulverized coal combustion, providing useful data in simulations of large boiler furnaces.

Sorbent particles are injected at the beginning of a reactor tube. Their velocity is determined from gas velocity field in the reactor, and interphase slipping is considered to have no influence on particle velocity. Particles are tracked in Lagrangian system.

Conservation equation for every gaseous component in fluid mixture can be written in a form derived from the general Eq. (11). In this form, Γ_A is a transport coefficient for variable "A":

$$\frac{\partial}{\partial x_j}\left(\rho U_j \chi_A\right) = \frac{\partial}{\partial x_j}\left(\Gamma_A \frac{\partial \chi_A}{\partial x_j}\right) + S_{p,A}^m \qquad (12)$$

Here the "A" represents O_2, N_2, CO_2, H_2O, SO_2 and other components if needed. The source term for these gaseous components represents their generation or depletion in a two-phase

flow due to particle reactions. The conservation equation for the SO_2 component of a gas mixture has two source terms due to the particles; one is from combustion of coal particles, while the other is due to absorption of SO_2 by the CaO particle:

$$\frac{\partial}{\partial x_j}\left(\rho U_j \chi_{SO_2}\right) = \frac{\partial}{\partial x_j}\left(\Gamma_{j,SO_2}\frac{\partial \chi_{SO_2}}{\partial x_j}\right) + S_{p,SO_2} + S_{p,SO_2}^{CaO} \tag{13}$$

For each time step, the particle obtains information about the temperature and gas concentration in the cell corresponding to the particle position at the given time.

After obtaining these values as input for the particle reactions model, the BET surface is calculated. The most important influential factor in determining the BET surface is the particle temperature. For this temperature, the calcination rate, and sintering parameter and exponent are determined for each time step. After this, for the current time step, the surface of the calcium oxide part is determined using Eq. (5), with respect to the thermal history of the particle from previous time steps. With knowledge of extent of calcination, we can estimate the particle porosity can be estimated. After this, a specific particle surface is determined using Eq. (4). Knowing this particle surface, the sulfation reaction is calculated for the same time step.

The sulfation model considers the reactions of a single grain in the particle with an averaged reaction rate over the entire particle. Particle temperature is considered the same as the temperature of surrounding gas;[14] this approximation is valid due to the rapid heating rate of the particle. The particle velocity in the reactor tube is considered to be the same as gas velocity.[14] Particle position in the axial direction at each time step is determined from the previous position and time of the particle. Reaction rate constant and diffusion coefficients are determined for the current temperature of the particle and surrounding gas. The concentration of sulfur dioxide at the surface is calculated based on the numerical grid cell in which the particle currently is. The dimensionless time step is calculated using the particle parameters: grain radius, sulfur dioxide and calcium oxide concentration. Specific surfaces are determined using expressions given in the literature;[2,3] these expressions are derived from the assumed particle geometry. Dimensionless unreacted core radius, g_2, is determined from dimensionless rate and dimensionless time using Eq. (6). This is employed to determine further the extent of sulfation, X_s (Eq. (7)). When the dimensionless unreacted core radius and extent of sulfation are known, the dimensionless radius of reaction products, g_1, can be estimated using Eq. (8). From this radius, the current porosity can be determined, and from it the effective diffusion. With this data, the differential Eq. (10) is used to determine concentration profile within the particle, from which the overall reaction rate is obtained, Eq. (9). This reaction rate is used to estimate the sulfur reduction for given trajectory, in a given cell during the residence time of the particle in the reactor.

RESULTS AND DISCUSSION

Comparison of calculated particle calcination showed that the Alvfors[5] calcination rate constant provided better agreement with the experimental data than the ones given by Borgwardt;[8,5] however, the results for the simulation of BET surface development, shown in Fig. 2A, suggest that use of the combined calcination and sintering models with the Borgwardt coefficients gave a faster surface development and better agreement with the experimental data. The results suggest that simulated surface for temperatures below 950 °C would give poor

agreement with experimental data. Due to relatively high local temperatures in pulverized coal-fired boiler, this will probably not be a problem but it could be overcome by switching between the use of Alvfors and Borgwardt coefficients, depending on whether the current temperature is below or above 950 °C.
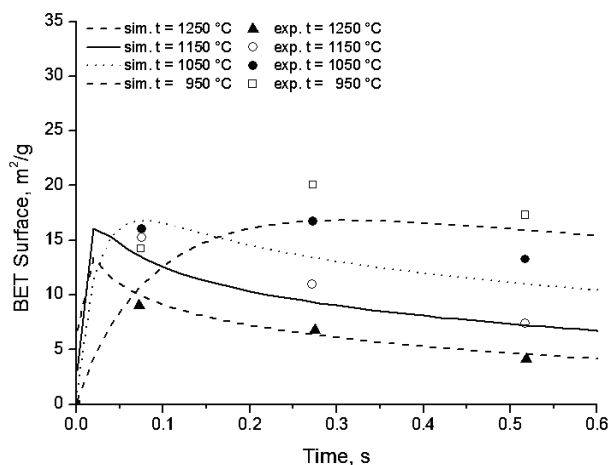
(A)
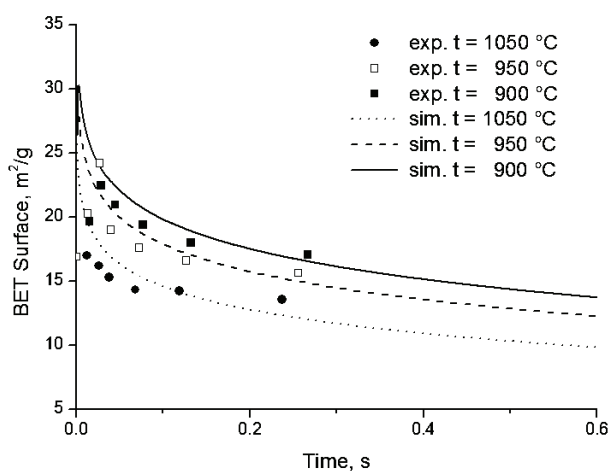
(B)

Fig. 2. Development of the BET surface – simulated with coefficients calculated by Borgwardt for $CaCO_3$, compared to experimental data of Flament and with fitted coefficients for $Ca(OH)_2$ sorbent, based on experimental data by Fan.[14]

The calculated calcination rates for calcium hydroxide are higher, compared to the ones obtained in the experiments by Fan,[14] but the calculated BET surface development agrees well with the experimental data. The fitted data for BET

surfaces when calcium hydroxide was used as the sorbent for the simulations of the reactor used by Fan are shown in Fig. 2B.[14] For the entire temperature range considered, the calculated data is in good agreement with the experimental data, especially when the residence time of the sorbent particle was longer than 0.1 s. It should be stressed that the typical residence time of a sorbent particle within a pulverized coal-fired furnace is around 2 to 5 s, or longer, depending on the sorbent injection location and aerodynamic conditions in the furnace. As expected, the BET surface was lower for higher temperatures, due to more intensive sintering reactions.

The sulfur dioxide concentration field along the simulated experimental IFRF reactor tube is shown in Fig. 3. It is noticeable that fastest reduction is achieved near the center of the reactor, while it is slower near the walls, but as the fluid flow develops, concentration level evens out over the tube cross-section.
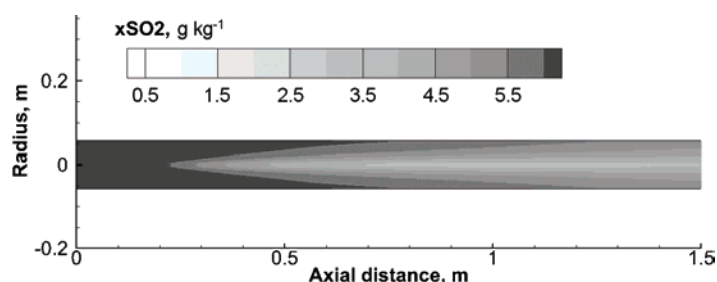
Fig. 3. Axial SO_2 concentration profile over the simulated IFRF reactor (total simulated length 3 m, sorbent $CaCO_3$).

Extent of calcination, shown in Fig. 4A, follows well the trend of experimental data in the case of $CaCO_3$ sorbent, giving better agreement when reaction temperatures were higher, while in the case of $Ca(OH)_2$ sorbent, the predicted calcination (Fig. 4B) was lower than the experimentally one obtained in the experiments by Fan,[14] suggesting that corresponding reaction model used for $Ca(OH)_2$ needs to be improved – an initial surface development model is required to provide higher initial BET surfaces in order to properly simulate the more intensive initial sulfur capture.

The simulation results obtained for sulfur capture with $CaCO_3$ using the diffusion rates and reaction rate constant suggested by Alvfors,[5] are compared with the experimental results of Flament[9] in Fig. 5A for a range of Ca/S mole ratios. Figure 5B shows the results for simulated sulfur capture when $Ca(OH)_2$ was used as sorbent are presented in Fig. 5B for a range of temperatures with a fixed Ca/S mole ratio = 2.0. From Fig. 5, it is clear that reactivity of $Ca(OH)_2$ was significantly higher during the initial period compared to the reactivity of $CaCO_3$ for the same Ca/S mole ratios. This could be attributed to the faster development of the BET surface of $Ca(OH)_2$ in this initial period. However, at

higher temperatures, $Ca(OH)_2$ lost its reactivity more rapidly due to the rapid loss of internal surface. The calcination and sintering surface area development were simulated using the data of Borgwardt data for the calcination and sintering rate coefficients in the case of $CaCO_3$ and with the use of fitted data based on the experimental data of Fan[14] in the case of the $Ca(OH)_2$ reactor. Using these data in the model, good agreement was obtained between the experimental and simulated reduction of sulfur oxides, but it is expected that with further improvements, the calculated sulfation of $Ca(OH)_2$ would be more accurate.

(A)

(B)
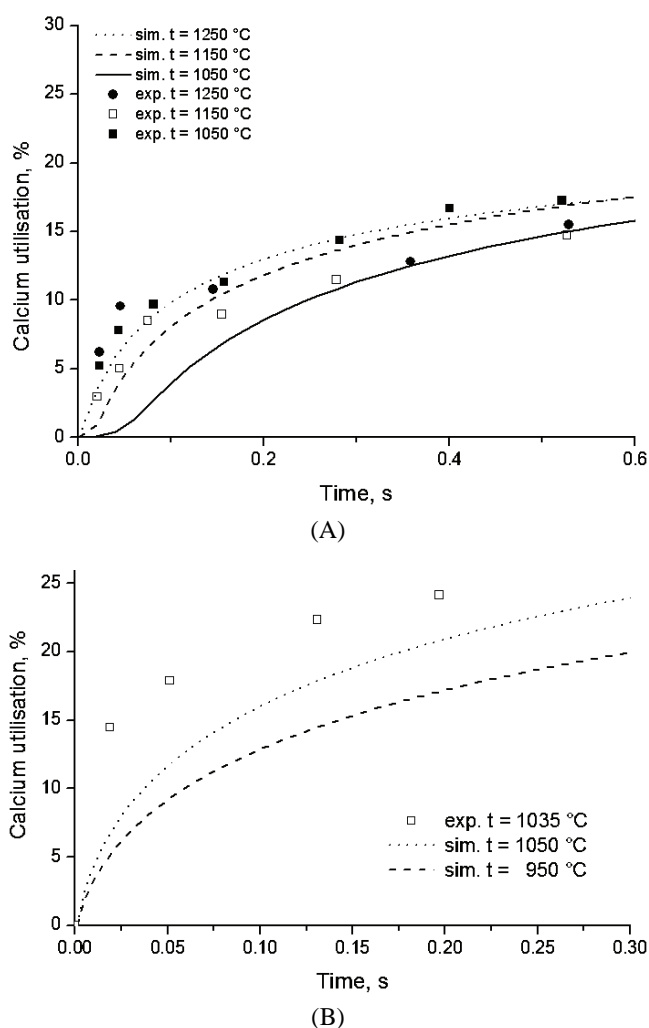
Fig. 4. Simulated extent of calcination of sorbent compared to experimental results by Flament ($CaCO_3$ sorbent)[9] and experimental results by Fan ($Ca(OH)_2$ sorbent).[14]
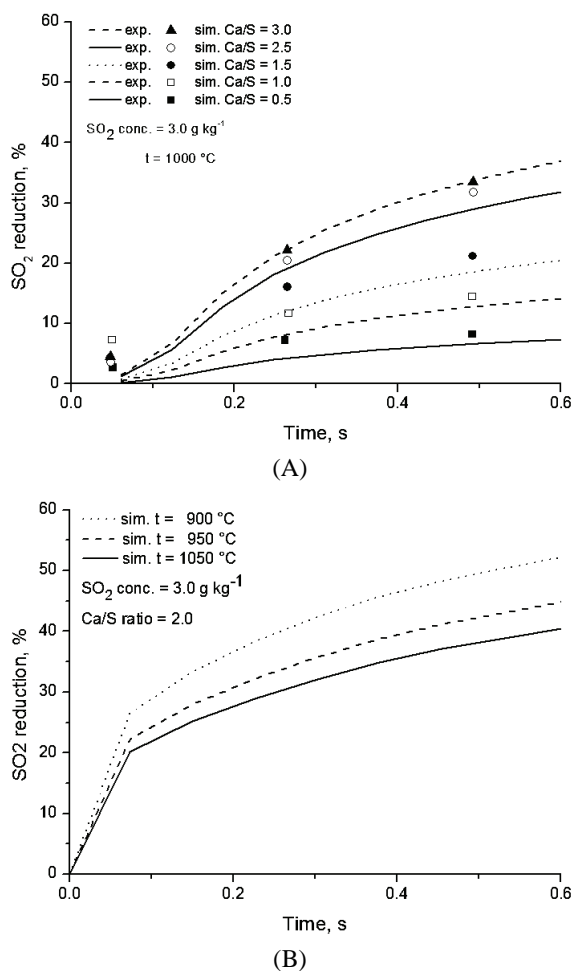
Fig. 5. Simulated data compared to experimental data from Flament for SO$_2$ reduction (CaCO$_3$ sorbent)[9] and simulated data for SO$_2$ reduction (Ca(OH)$_2$ sorbent).

CONCLUSIONS

Simulations with selected models particle calcination, sintering and sulfation reactions of Ca-based sorbents, coupled with particle tracking in the gas phase of a referent drop down tube reactors, provided the basis for the validation of the model and showed a considerable reduction in sulfur oxides. In the case of CaCO$_3$, experimental and simulation data showed good agreement, while the simulation with Ca(OH)$_2$ underestimated calcium utilization at lower temperatures. This could probably be attributed to the BET surface development model not capturing the narrow time interval with extremely high BET surfaces. With high Ca/S mole ratios, the reduction was estimated to be up to 35 % during first

0.5 s of reaction for an initial sulfur concentration of 3.0 g kg^{-1}. With Ca/S molar ratios around 2.0, the simulated reduction at the reactor exit was over 25 % (when sorbent was $CaCO_3$), and over 30 % (for $Ca(OH)_2$ as the sorbent), with respect to the given temperature ranges in the simulations. Considering the obtained agreement with experimental results, the model will be further improved and adapted to be used in conjunction with a complex flow, heat transfer and combustion model of a pulverized coal-fired boiler furnace. Due to higher particle residence times, ranging from 2 to about 5 seconds in the boiler furnace, it is expected that with a proper distribution of particles over the furnace cross-section, sorbent injection would achieve good results in emission reduction of sulfur oxides.

The model for prediction of calcium sorbent particles reaction with sulfur dioxide, together with numerical code for fluid flow simulation could be used to obtain insight into the complex processes in boiler furnaces. The simulation results depend highly on the prediction of the development of the reactive (BET) surface. The model underestimates to some extent $Ca(OH)_2$ surface development, thus underestimating utilization of CaO obtained during calcination of $Ca(OH)_2$. Consequently, this results in an underestimation of the final amount of reduced SO_2 with this sorbent. For $CaCO_3$, the surface development estimation was in good agreement with experimental results, which influence the final results, giving good agreement with measured utilization of Ca and reduction of SO_2. The model is intended to be used in the simulation of sorbent particles injection into utility boiler furnaces with pulverized coal combustion. For simulations of $CaCO_3$, the model is usable in the temperature range from 950 °C to 1250 °C, and results are in good agreement with the measured values, while for $Ca(OH)_2$ a sorbent, compared with available experimental results, the usable temperature range is from 950 to 1100 °C, but it must be kept in mind that the predictions underestimated SO_2 reduction to a certain extent. With these limitations, the model could be used to simulate $CaCO_3$ sorbent injection into a boiler furnace, giving good qualitative and quantitative predictions, and in the case of $Ca(OH)_2$ sorbent, it could be used for qualitative analysis, but it should be further improved to provide better agreement, and to be able to give better quantitative predictions.

NOMENCLATURE

BET = initial particle surface (measured), m^2 g^{-1}
c_{A0}, c_{B0} − concentrations of reactants (SO_2 and CaO), mol m^{-3}
C − local reactant concentration at position z

Da − Damköhler number , $Da = kl_0/D_s$

D_{eff} − effective diffusion coefficient in the particle, $m^2\ s^{-1}$

D_0 − diffusion coefficient in the bulk gas phase, $m^2\ s^{-1}$

D_s − diffusion coefficient of the solid product layer, $m^2\ s^{-1}$

$F(g_2, \lambda)$ − structural function that depends on the extent of particle sulfation

g_0, g_1, g_2 − dimensionless grain radius

k − sulfation reaction rate constant, $m\ s^{-1}$

k_c − calcination rate constant, $mol\ m^{-2}\ s^{-1}$

K_s − sintering rate kinetic factor, s^{-1}

l_0 − characteristic distance, m

L − product layer thickness, m

$M_{M,CaCO_3}$ − molar mass of calcium carbonate, $g\ mol^{-1}$

$M_{M,CaO}$ − molar mass of calcium oxide, $g\ mol^{-1}$

m − number of particles in contact

r_0, r_1, r_2 − grain radius for initial time step, unreacted core and product layer, respectively, m

S_{avg} − average specific surface area, $S_{avg}^2 = S_1 S_2$

S − the surface after sintering, $m^2\ g^{-1}$

S_{CaCO_3} − surface of calcium carbonate part, $m^2\ g^{-1}$

S_{CaO}^n − surface area of calcium oxide part at a given time, $m^2\ g^{-1}$

S_0 − the initial specific surface of particle, $m^2\ m^{-3}$

$S_{0,CaO}$ − nascent calcium surface area, Borgwardt,[18] $m^2\ g^{-1}$

S_1 − specific surface of product layer, $m^2\ m^{-3}$

S_2 − specific surface of unreacted core, $m^2\ m^{-3}$

S_{p,SO_2} − source term for SO_2 due to particles

t − reaction time, s

t^* − dimensionless time, $t^* = (kc_{A0}t)/(r_0 c_{B0})$

U_j − velocity component, $m\ s^{-1}$

$V_{M,CaCO_3}$ − molar volume of calcium carbonate

$V_{M,CaO}$ − molar volumes of calcium oxide

$X_c(t)$ − extent of calcination at a given time step, -

$X_s(t)$ − extent of sulfation at a given time step, -

χ_{SO_2} − concentration of component in gas phase, $kg\ kg^{-1}$

z − dimensionless position inside the particle, -

α − molar volume ratio

γ − exponent

Γ_A − Effective diffusion (transport coefficient for variable Φ)

δ − relation between effective diffusivity at the beginning and at the current time step

ε_{Ca} − particle porosity, influenced by sintering of particle

λ − structural parameter, and depends on connected grains neck overlapping

ρ − gas mixture density, $kg\ m^{-3}$

Φ_{Th} − Thiele modulus, $\Phi_{Th}^2 = R_0^2 k S_0 / D_{eff,0}$

Φ − general scalar variable

Subscript

n − a current time step at which the surfaces are calculated.

И З В О Д

МОДЕЛОВАЊЕ РЕАКЦИЈА СОРБЕНТА НА БАЗИ КАЛЦИЈУМА СА СУМПОР-ДИОКСИДОМ

ИВАН ТОМАНОВИЋ[1], СРЂАН БЕЛОШЕВИЋ[1], АЛЕКСАНДАР МИЛИЋЕВИЋ[1] и ДРАГАН ТУЦАКОВИЋ[2]

[1]*Универзитет у Београду, Институт за нуклеарне науке „Винча", Мике Петровића Аласа 12–14, п. пр. 522, 11001 Београд и* [2]*Универзитет у Београду, Машински факултет, Краљице Марије 16, 11120 Београд*

Математички модел реакција сорбента на бази калцијума ради симулације смањења емисије сумпор-диоксида из димних гасова при сагоревању спрашеног угља је развијен, уграђен у нумерички код и проверен поређењем са доступним мерењима под контролисаним условима. Модел би требало да детаљно опише реакције калцинације, синтеровања и сулфатизације, које се одвијају током кретања честица сорбента кроз ложиште. Модел сулфатизације је заснован на тзв. моделу делимично синтерованих сфера, повезаног са изабраним моделима калцинације и синтеровања. Модел узима у обзир сложену геометрију честице, под претпоставком да се састоји од сферичних зрна у додиру. Нумеричке симулације реактора са вертикалном цеви су изведене за честице $CaCO_3$ и $Ca(OH)_2$ као сорбента и резултати су упоређени са доступним експерименталним подацима из литературе. Модел реакција сорбента ће бити даље коришћен за симулацију реакција одсумпоравања у турбулентном двофазном току гаса и честица у условима који владају при сагоревању угља.

REFERENCES

1. R. H. Borgwardt, *Environ. Sci. Technol.* **4** (1970) 59
2. B. Lindner, D. Simonsson, *Chem. Eng. Sci.* **36** (1981) 1519
3. D. Kocafe, D. Karman, F. R. Steward, *AIChE J.* **33** (1987) 1835
4. P. Alvfors, G. Svedberg, *Chem. Eng. Sci.* **43** (1988) 1183
5. P. Alvfors, G. Svedberg, *Chem. Eng. Sci.* **47** (1992) 1903
6. V. B. Beljanski, I. D. Tomanović, S. V. Belošević, M. A. Sijerčić, B. D. Stanković, N. Đ. Crnomarković, A. D. Stojanović, in *Proceedings of International Conference on Power Plants*, 2012, Zlatibor, Serbia, 2012, p. 1001
7. I. D. Tomanović, V. B. Beljanski, S. V. Belošević, M. A. Sijerčić, B. D. Stanković, N. Đ. Crnomarković, A. D. Stojanović, in *Proceedings of International Conference on Power Plants*, 2012, Zlatibor, Serbia, 2012, p. 1013
8. R. H. Borgwardt, *AIChE J.* **31** (1985) 103
9. F. Flament, M. Morgan, *Fundamental and technical aspects of SO₂ capture by Ca based sorbents in pulverized coal combustion*, Report on the S 2–4 study, IFRF, Ijmuiden, December, 1987.
10. C. R. Miline, G. D. Silcox, D. W. Pershing, D. A. Kirchgessner, *Ind. Eng. Chem. Res.* **29** (1990) 139
11. C. R. Miline, G. D. Silcox, D. W. Pershing, D. A. Kirchgessner, *Ind. Eng. Chem. Res.* **29** (1990) 2192
12. C. R. Miline, G. D. Silcox, D. W. Pershing, D. A. Kirchgessner, *Ind. Eng. Chem. Res.* **29** (1990) 2201
13. G. D. Silcox, J. C. Kramlich, D. W. Pershing, *Ind. Eng. Chem. Res.* **28** (1989) 155

14. L. S. Fan, A. Ghosh-Dastidar, S. Mahuli, R. Agnihotri, in *Dry scrubbing technologies for flue gas desulfurization*, B. Toole-O'Neil, Ed., Kluwer Academic Publishers, Norwell, MA, USA, 1998, p. 421
15. C. Chen, C. Zhao, *Ind. Eng. Chem. Res.* **45** (2006) 5078
16. D. Beruto, A. W. Searcy, *J. Chem. Soc., Faraday Trans.* **12** (1974) 2145
17. R. M. German, Z. A. Munir, *J. Am. Ceram. Soc.* **59** (1976) 379
18. R. H. Borgwardt, *Chem. Eng. Sci.* **44** (1989) 53.

Microwave and acid-modified talc for the adsorption of Methylene Blue in aqueous solution

SI-FAN LI, SHUANG-CHUN YANG*, SHAN-LIN ZHAO, PING LI and JIN-HUI ZHANG

College of Chemistry, Chemical Engineering and Environmental Engineering, Liaoning Shihua University, FuShun 113001, China

Abstract: Batch adsorption experiments for the removal of Methylene Blue from aqueous solutions onto talcum powder were investigated using microwave-assisted and acetic acid-modified talcum powder. In batch adsorption experiments for the removal of Methylene Blue by the new sorbents, the influences of particle size of the talcum powder, the acid concentration, acidification time and temperature, and radiation time and power were investigated. The results showed that the efficiency for the removal of Methylene Blue was up to 83.03 % under the optimum conditions, namely, talcum powder of 10 μm treated with 1.0 M acetic acid at 313 K for 9 h under 600 W microwave radiation for 5 min. The modified talcum powder was characterized by Fourier transform infrared spectroscopy, X-ray diffraction and scanning electron microscopy. The adsorptive capability of the adsorbent was greatly enhanced because of the active groups OH$^-$ and broken Si–O$^-$ and the cracks produced in the face of talcum powder on modification.

Keywords: talcum powder; microwave; acidification; adsorption; Methylene Blue.

INTRODUCTION

Talc, $Mg_3(Si_4O_{10})(OH)_2$, is a major hydrous magnesium silicate with the chemical composition MgO 31.72, SiO_2 63.52 and H_2O 4.76 %. The crystal structure of talc is a monoclinic system consisting of layers of brucite octahedral, sandwiched between silica tetrahedron sheets.[1] Such successive layers of talc, resulting in the breaking of sheets during grinding, are bonded together by weak van der Waals forces and have no other cation is present. A successive network of silica tetrahedron is formed through bridging oxygen atoms and the reactive oxygens are all toward one side in the crystalline lattice, as shown in Fig. 1. The difference in the surface energy between face surfaces and edge surfaces is relatively large in talc. In addition, some intrinsic properties of talc, such as

563

chemical inertness, high thermal stability, good lubricity, low electrical conductivity, unique pore structure, high specific surface area, low cost and abundant resources, are beneficial for some applications.
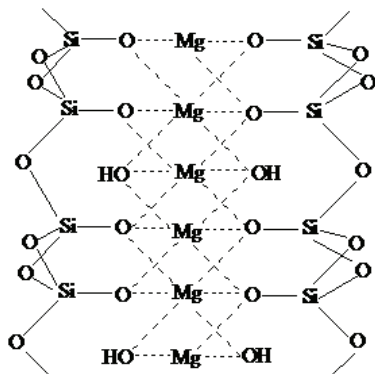
Fig. 1. Schematic diagram of the crystal structure of talc.

The proven talc reserves in China are 250 million tons, which are the second largest in the world. China is the largest exporter of talc in the world, with an estimated annual output accounting for 40 % of the total World exports.[2] Talc is used extensively in industry, such as, in the automotive, ceramics and coating industries.[3] It is also used as an adsorbent in sewage treatment. In addition, talcum powder was employed as a filter aid for the treatment of papermaking wastewater in a membrane bioreactor. The results showed that there was a decrease both in membrane resistance and filter cake resistance when 1.2 g L^{-1} of talcum powder was added to the membrane bioreactor.[4] In other studies, talcum powder was used as a coagulant aid in the treatment of papermaking wastewater, and the effects were remarkable.[5–7] In addition, the adsorption of heavy metal ions was studied, and it was found that talcum powder showed fairly good adsorption for lead ions and the data conformed to the Langmuir model.[8] Moreover, benzene and toluene removal from aromatic organic wastewater was reported to be much better using talcum powder than when mesoporous silica materials were employed.[9] Furthermore, the adsorption of a cationic dye using talcum powder was also studied and favorable adsorption of the dye on the adsorbent was evidenced.[10,11] In conclusion, talc is a promising adsorbent for wastewater treatment, but with some shortcomings. For example, the scope and adsorption amounts of pollutants on talc are limited. In addition, the selectivity of talc for pollutants is low. Therefore, it seemed especially important to study methods of talc modification to improve further its performance in wastewater treatment.

Hitherto, very little work has been performed on the modification of talc using the microwave radiation technology. Modification by microwave heating is more rapid and more uniform, and thus could greatly reduce the heating time and

energy consumption, and the heating quality could also be improved.[12] Meanwhile, minerals treated by acid are more pure. Research showed that associated minerals in talc were dissolved away by monocarboxylic organic acids, with the result that the talc as more pure and particle size of the talc was smaller.[13] Simultaneously, it was found that the adsorptive ability of talcum powder modified by nitric acid was increased compared to that of unmodified talcum powder, and that the acid could dissolve inorganic salts, which open the internal pores of the talcum powder.[10] Taken together, acid treatments could improve the adsorptive ability of minerals. Furthermore, the adsorption capacity of diatomite treated with vitriol and microwave irradiation was greatly increased, the removal efficiency of sulfide was up to 87 %.[14]

Talc has a structure similar to diatomite and they are both porous materials. Therefore, the work presented herein represents a first attempt to modify talcum powder with microwave and acetic acid. The modified adsorbents were applied to Methylene Blue in aqueous solution. The optimum conditions are determined for batch adsorption and a modified mechanism determined by characterization of unmodified and modified talcum powder is discussed.

EXPERIMENTAL

Material

Talcum powder (1250 mesh) samples from Liaoning Haicheng Talcum Powder Company (Haicheng, China), acetic acid 99.5 % purity and Methylene Blue (MB, C.I: 52015, chemical formula: $C_{16}H_{18}ClN_3S\cdot3H_2O$, molecular weight: 373.90 g mol^{-1}, maximum absorption: 664 nm) from Sinopharm Chemical Reagent Co., Ltd. (Shanghai, China) were used in this study.

Modification methods

Pretreatment of talcum powder. The talcum powder samples were treated before use in the experiments as follows. Different mesh sizes of talcum powder were mixed with 300 mL distilled water, and the mixtures were stirred for 1 h. After stirring, all mixtures were stood for 1 h and the small impurities suspended in the supernatant were removed with a pipette. This process was repeated until the supernatant was clear. The resulting products were then dried at 105 °C.

Acid modified. Talcum powder (10 g) of different mesh sizes was mixed with different concentrations of acetic acid solutions 100 mL at different temperatures for different times. The mixtures were then filtered, washed with distilled water to neutral, and dried at 105 °C.

Microwave-assisted acid modified. The acid modified talcum powder suspensions were placed in flasks and then transferred to the MAS-I microwave synthesis system (Shanghai Sineo Microwave Chemical Technology Co., Ltd.) for different times at 40 °C. The treated products were then dried at 120 °C. The samples were designated M-A-T.

Batch adsorption experiments

To 50 mL of MB solution (20 mg L^{-1}), 0.25 g of unmodified or modified talcum powder were added. The suspension was placed in a water bath shaker at 293 K for 1 h. After the adsorption of MB, the mixtures were centrifuged, and the absorbance of the supernatant was

measured at a wavelength of 664 nm using a 752-B UV–visible spectrophotometer. The efficiency of MB removal, q, was calculated using the following formula:

$$q = 100 \frac{A_0 - A_i}{A_0} \tag{1}$$

where A_0 and A_i are the absorbance of Methylene Blue before and after adsorption.

Characterization

Chemical bonds of in the unmodified and modified talcum powder were determined by Fourier Transform Infrared Spectroscopy (FTIR) using a Perkin Elmer Spectrum Two instrument (USA). The spectra were obtained in the wavenumber range from 400 to 4000 cm^{-1}. X-Ray diffraction (XRD) was used to identify the phase constitution of the original talcum powder and modified talcum powder. The diffraction patterns were obtained in a Rigaku D/max RB diffractometer (Japan) at 40 kV and 30 mA in the 2θ range from 5 to 70°. The particle sizes of the modified and unmodified talcum powders were calculated using the Scherrer Equation:

$$D = \frac{K\lambda}{\beta \cos\theta} \tag{2}$$

where D is the particle size (nm), K is the Scherrer constant ($K = 0.89$), λ is the X-ray wavelength ($\lambda = 0.15418$ nm), β is the half-high width of the diffraction peak and θ is diffraction angle ($2\theta = 5.12°$).

The morphologies of the powders were examined by scanning electron microscopy (SEM) using a VEGA3 instrument (Tescan, Czech Republic).

RESULTS AND DISCUSSION

Effect of the particle size of the talcum powder on adsorption

Talcum powder of different particle sizes (33, 15, 10, 6.5 μm) were modified with 1 mol L^{-1} acetic acid at 313 K for 3 h. The effect on the removal efficiency of MB on the particle size of the talcum powder is shown in Fig. 2, from which it is clear that the efficiency of MB removal increased with increasing particle size of the talcum powder, but then decreased when the particle size exceeded 10 μm. This might be because more surface bonds were exposed in the larger particles size during grinding.[15] Thus the surface structures tended to be more active, and
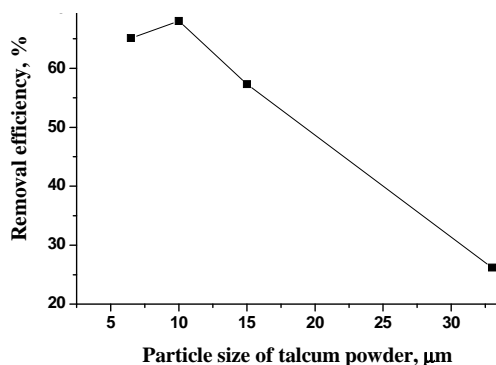
Fig. 2. Effect of the particle size of talcum powder acid-modified with 1 mol L^{-1} acetic acid at 313 K for 3 h on the adsorption of MB.

the surface activity increased. However, the talcum powder with the largest particle size (*i.e*., 33 μm) removed less MB in the adsorption process, which might be caused by deformation of the lattice and a weakening of the forces between successive layers during grinding. Thus, for remaining adsorption studies, the particle size talcum powder was kept at 10 μm.

Effect of acid concentration on adsorption of talcum powder

In order to study the effect of the acetic acid concentration on the modification of talcum powder, 10 μm powder was modified in 0.1, 1, 2, 3, 4 and 5 mol L^{-1} acetic acid solutions at 313 K for 3 h. The efficiency of MB removal by the modified talcum powders was found to increase from 64 % to 68 % on increasing the acetic acid concentration employed in the modification from 0.1 to 1 mol L^{-1}. When the acetic acid concentrations were higher than 1 mol L^{-1}, the removal efficiencies of the modified talcum powders decreased; the value decreased by 17.4 % when the acetic acid concentration was increased to 5 mol L^{-1}. Thus, a high acetic acid concentration had no positive effects on the adsorption of MB by the acidified talcum powder. This might be because the acetic acid blocked the active sites and more acetic acid was bonded with the groups on talc surface with increasing acetic acid concentration. On the other hand, the particles of talcum powder modified with 1 mol L^{-1} acetic acid were more homogeneous in size, which made the adsorption of MB easier. The best adsorptive capability of talcum powder was then shown.

Effect of acidification time on the adsorption of talcum powder

Talcum powder of 10 μm were mixed with 1 mol L^{-1} acetic acid at 313 K for different times (3, 6, 9, 12, 15 and 18 h). The effect of different acidification time on the adsorption of MB by the modified talcum powder is illustrated in Fig. 3, curve 2. It can be seen that the efficiency of MB removal increased with the acidification time and reached its highest value (73.4 %) at 9 h. Thereafter, it tended to decrease gradually. The above results were probably because the
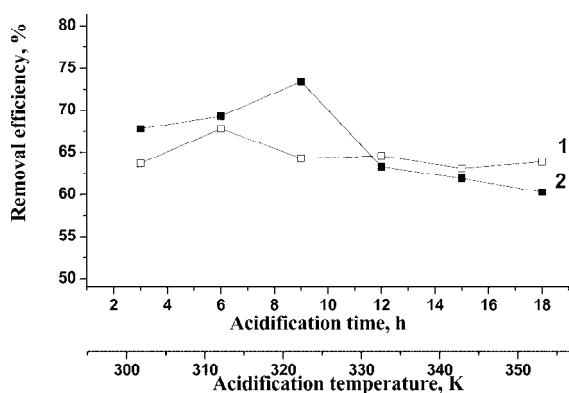
Fig. 3. The effect of the acidification time at 313 K (curve 2) and acidification temperature for 3 h (curve 1) for the modification of talcum powder on the adsorption of MB. The powder size was 10 μm and the acetic acid concentration was 1 mol L^{-1}.

reaction between talcum powder and acetic acid was not sufficient at shorter time for the internal pores to be opened completely. While at longer times, unreacted acetic acid would enter into the holes of the talcum powder, which might reduce the amount of adsorbed MB. Therefore, the best modification time was 9 h.

Effect of acidification temperature on the adsorption by talcum powder

Talcum powder of 10 μm was mixed with 1 mol L^{-1} acetic acid at the desired temperatures, namely 303, 313, 323, 333, 343 and 353 K, for 3 h. The effect of the modification temperature on the adsorption of MB by the resulting talcum powder is shown in Fig. 3, curve 1. It could be seen that the removal efficiency were all above 63.1 % and differed by only 4.7 % from the highest to the lowest removal efficiency. Thus, it could be considered that there was no apparent effect of acidification temperature on the adsorption efficiencies of the talcum powder over the studied temperature range. The reason might be that more acetic acid would volatilize with increasing temperature and then the talcum powder would become insoluble in the small amounts of remaining acetic acid solution.

Effect of microwave radiation time on the adsorption by talcum powder

Talcum powder of 10 μm and acetic acid (1 mol L^{-1}) were placed in a flask and then transferred to the microwave synthesis system for different times (5, 10, 15, 20, 25 min) at 400 W working power. The effect of M-A-T on the removal of MB for different radiation times is presented in Fig. 4, curve 2. It was observed that as the time of microwave radiation increased, the efficiency of MB removal by the treated talcum powder decreased. The highest MB removal efficiency (80.1 %) was attained at 5 min radiation time, which was about 6.7 % higher than the removal efficiency of MB onto talcum powder modified only by acid. Meanwhile, the two sets of data were equivalent between 10 min and 20min. Thus, microwave radiation for 5 min was the best.
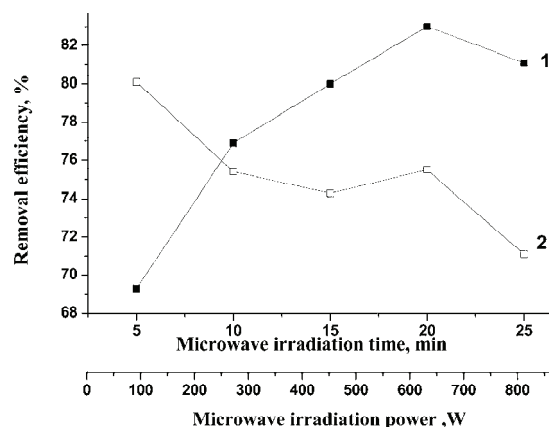
Fig. 4. The effect of microwave radiation time at a power of 400 W (curve 2) and microwave radiation power for 5 min (curve 1) on the adsorption of MB by the modified talcum powders.

Effect of microwave radiation power on the adsorption by talcum powder

Talcum powder of 10 μm and acetic acid (1 mol L^{-1}) were placed in a flask and then transferred to the microwave synthesis system for 5 min at different working powers (100, 200, 400, 600 and 800 W). The effect of M-A-T and microwave radiation of different powers on the adsorption of MB is shown in Fig. 4, curve 1. It was noted that the removal efficiency increased at first but then decreased with increasing power of the microwave radiation. The highest removal efficiency was 83.03 % when the microwave radiation power was 600W. Moreover, the efficiencies of MB removal under microwave irradiation were higher than on the acetic acid modified talcum powder when the power of the microwave radiation exceeded 400 W.

The observations that a suitable power of microwave radiation for a short period was beneficial in improving the adsorption capability of M-A-T might result from two reasons. On the one hand, the unique thermal effect from microwave radiation provided heat from the interior to external in the acidification process, making reactive bonds tend to break into negatively charged groups in the reaction between talcum powder and acetic acid. Then the adsorptive capability of talcum powder was improved. On the other hand, more impurities and water in M-A-T were eliminated by microwave radiation. This led to more pores within the talc. However, as the microwave radiation time and power increased, the structure of M-A-T would be destroyed, then the internal pores would collapse, which would be unfavorable for the adsorption of MB.

Characterization of talcum powder and its mechanism

FTIR spectra. The FTIR spectra of the unmodified and modified talcum powder are presented in Fig. 5. An analysis of the unmodified talcum powder was realized in Fig. 5.[13,16,17]

The peak areas of Mg–O bonds (463 cm^{-1}) and Si–O–Mg bonds (539 cm^{-1}) were both decreased in the spectrum of M-A-T. This showed that the ordering and bonding effects were influenced in the layer structure of M-A-T, because some of the Mg–O bonds were broken with radiant energy from the microwave synthesis system, making the binding force weaken in the interlayer, then the Si–O$^-$ and Mg$^+$ were exposed. The active Si–O$^-$ and OH$^-$ groups that were unchanged after modification from edge surface could adsorb MB cations. Hence, the efficiency of MB removal was improved. Moreover, the absorption peak of carbonate minerals decreased, or even disappeared. This also indicated that the purity of M-A-T samples were increased, which might be because impurities in the pores of talcum powder were removed by acetic acid.[13]

X-Ray diffraction. The results of characterization by XRD of unmodified talcum powder and M-A-T are presented in Fig. 6. The diffraction angles that indicated typical diffraction peaks of the unmodified talcum powder were 9.451°,
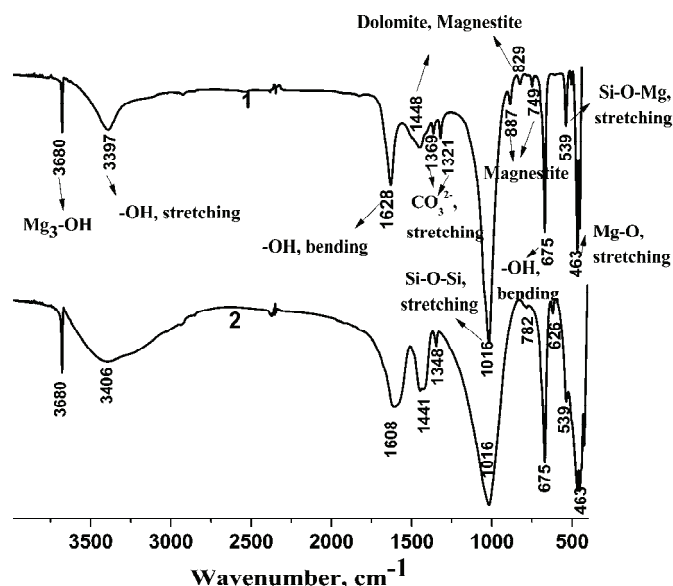
Fig.5. FTIR spectra of the unmodified talcum powder (spectrum 1) and M-A-T (spectrum 2).
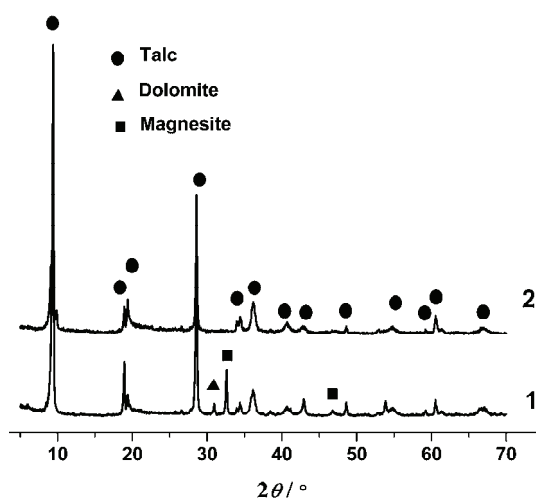
Fig. 6. XRD patterns of unmodified talcum powder (pattern 1) (max. intensity = 16593 counts) and M-A-T (pattern 2) (max. intensity = 7580 counts).

18.988 and 28.586°. The values of the interplane spacing, d, corresponding to $d_{(002)}$, $d_{(004)}$ and $d_{(006)}$, were 9.35, 4.67 and 3.12 Å, respectively. The intensities of the typical M-A-T diffraction peaks were significantly decreased compared with those of the unmodified talcum powder. The interlayer and constituent water were lost and then the layer structure was slightly damaged under the short microwave radiation. Meanwhile, more pores were exposed on the surface of M-A-T. This contributed more MB being adsorbed from the aqueous solution. Accord-

ing to the Scherrer formula, the particle size of talcum powder decreased from 31.5 nm to 22.9 nm after modification. The specific surface area and the activity of the particles could be increased with decreasing particle size This contributed to the increasing rate of adsorption of MB.

Moreover, as can be seen from Fig. 6, the diffraction peaks for dolomite ($2\theta = 30.962°$) and magnesite ($2\theta = 32.629°$) had both disappeared completely, which corresponded to the results of the FTIR analysis.

SEM micrographs. The SEM micrographs from the unmodified talcum powder and M-A-T at 2000-times magnification are given in Fig. 7a and b, respectively. A large number of attachments, such as fine fragments, could be seen on the unmodified talcum powder surface (Fig. 7a), and these attachments were decreased greatly after microwave radiation and acidification (Fig. 7b). In case of

(a)   (b)

(a)   (b)
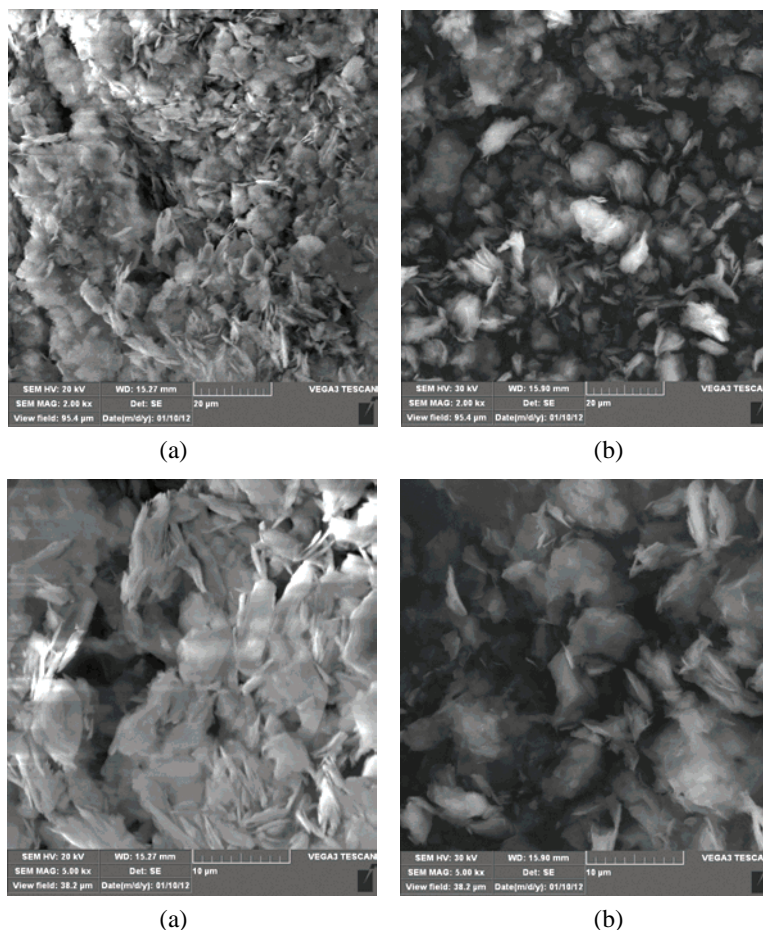
Fig.7. SEM micrographs of: a) unmodified talcum powder and b) M-A-T at 2000× magnification; c) unmodified talcum powder and d) M-A-T at 5000× magnification.

LI *et al.*

talc, which has a wetting angle a 64°, a lower roughness of the surface hinders wetting.[18] In Fig. 7b, The surface of M-A-T was more clear and orderly, the roughness was lower and the particles were in loose accumulation. Therefore, the hydrophobic character of M-A-T was enhanced compared to that of the unmodified talcum powder.

The SEM micrographs of the unmodified talcum powder and M-A-T at 5000-times magnification are shown in Fig. 7c and d, respectively. The boundary layers were significant in Fig. 7d. Many cracks occurred in the interparticles on the face surface, which might increase the specific surface area of the pores. Furthermore, these cracks could also produce small fissures, and thus most of the MB adsorption occurred inside the fissures. Overall, the breakage of some of the Mg–O bonds and Si–O–Mg bonds produced cracks on the surface of the M-A-T particles. This corresponded with the results of the FTIR and XRD analyses.

It could be inferred that acetic acid as a polar molecule could absorb the microwave energy strongly.[19] Then a rapid and intensive internal mixing process between acetic acid and the talcum powder occurred in a short period. This enabled the impurities to be removed more completely; hence, the channels of talcum powder could be further enlarged. Likewise, most fine attachments dissolved through the reaction of talcum powder and acetic acid, forming charged states around the interface. These fine attachments then rapidly broke away from the surface of the talcum powder in an instant because of electrostatic repulsion of the interparticles.[20] As the fine attachments remaining were removed, most surface groups and pores were exposed. Therefore, the adsorptive capability of M-A-T was greatly enhanced.

CONCLUSIONS

In this work, talcum powder modified by microwave and acetic acid was utilized for the removal of MB from aqueous solution. The chemical bonds, phase constitution and morphology of the unmodified and modified talcum powder were also studied by FTIR, XRD and SEM, respectively. It was found that the particle size of talcum powder, acid concentration, acidification time, and radiation time and radiation power had important influences on the removal process of MB in aqueous solution. The optimum conditions for the microwave-assisted acidification talcum powder were treatment of talcum powder of 10 μm with acetic acid at 313 K for 9 h. The optimal microwave radiation power and time were found to be 600 W and 5 min, respectively. The efficiency of MB removal reached 83.03 % for the microwave-assisted modified and 73.4 % for the acetic acid-modified talcum powder, while the unmodified talcum powder had the lowest removal efficiency of 29.0 %.

The Si–O–Mg bonds from edge surface of talcum powder that were modified by microwave and acid were broken into Si–O⁻ groups, providing more

adsorption sites of higher activity. Moreover, the impurities dolomite and magnesite were completely removed. In addition, the talcum powder surface was more pure. Its roughness was greatly decreased, while many cracks were produced on the face surface by microwave-assisted acidification. Consequently, the adsorption capability of the talcum powder was greatly enhanced. The amount of MB cations adsorbed was increased due to more exposed pores and small cracks and the active Si–O⁻ and OH⁻ groups formed.

Besides, the M-A-T adsorbent shows potential for the treatment of anionic dye wastewater because of the possible adsorption of anionic pollutants between Mg⁺ ions.

И З В О Д
ТАЛК МОДИФИКОВАН МИКРОТАЛАСИМА И КИСЕЛИНОМ КАО АДСОРБЕНС МЕТИЛЕНСКОГ ПЛАВОГ У ВОДЕНОМ РАСТВОРУ

SI-FAN LI, SHUANG-CHUN YANG*, SHAN-LIN ZHAO, PING LI и JIN-HUI ZHANG

College of Chemistry Chemical Engineering and Environment Engineering, Liaoning Shihua University, FuShun 113001, China

Изведени су шаржне експерименти адсорпције за уклањање метиленског плавог из воденог раствора на талку који је био модификован микроталасима или киселином. Испитивани су утицаји величине зрна праха талка, концентрације киселине, времена ацидификације, температуре ацидификације, времена озрачивања и снаге озрачивања. Резултати су показали да је ефикасност уклањања метиленског плавог до 83,03 % у оптималним условима, тј. талк величине зрна од 10 μm је третиран са 1,0 M сирћетном киселином на 313 K током 9 h, а снага и време озрачивања микроталасима били су 600 W и 5 min, редом. Модификовани талк је карактерисан помоћу FTIR, дифраксије X-зрака и SEM. Због активних OH⁻ група и раскинутих Si–O⁻ веза, као и пукотина које су произведене на површини зрна талка, значајно је увећана његова адсорпциона моћ.

(Примљено 18. јула, ревидирано 19. новембра, прихваћено 21. новембра 2014)

REFERENCES

1. A. Mierczynska-Vasilev, D. A. Beattie, *Int. J. Miner. Process.* **118** (2013) 34
2. L. S. Chen, C. Y. Peng, *Industrial Minerals and Processing* (ISSN: 1008-7524) **7** (2008) 33 (in Chinese)
3. P. Li, W. L. Liu, S. C. Yang, S. Cui, W. Zhang, *Bull. Chin. Ceram. Soc.* (ISSN: 1001--1625) **32** (2013) 668 (in Chinese)
4. X. D. Liu, Z. L. Wang, *J. Shenyang Jianzhu Univ.* (Nat. Sci.) (ISSN: 2095-1922) **22** (2006) 821 (in Chinese)
5. Y. L. Gao, L. T. Wang, W. F. Wang, X. W. Song, *J. West Anhui Univ.* (ISSN: 1009--9735) **25** (2009) 73 (in Chinese)
6. Y. R. Wang, W. Y. Hu, G. M. Liao, *Industrial Safety and Environmental Protection* (ISSN: 1001-425X) **34** (2008) 6 (in Chinese)
7. C. H. Yang, R. Y. Zhou, J. Zhang, *China Pulp and Paper* (ISSN: 0254-508X) **6** (2006) 28 (in Chinese)

8. N. Chandra, N. Agnihotri, P. Sharma, S. Bhasin, S. S. Amritphale, *J. Sci. Ind. Res.* **64** (2005) 674
9. H. Hshizume, *Appl. Clay. Sci.* **14** (2009) 61
10. W. L. Liu, S. L Zhao, S. Cui, S. C. Yang, L. Y Shang, *Adv. Mater. Res.* **610**–**613** (2013) 1443
11. Y. S. Feng, P. Li, S. Cui, L. Y. Shang, *Industrial Water & Wastewater* (ISSN: 1009--2455) **42** (2011) 25 (in Chinese)
12. C. A. Crane, M. L. Pantoya, B. L. Weeks, M. Saed, *Powder. Technol.* **256** (2014) 113
13. L. A. Castillo, S. E. Barbosa, P. Maiza, N. J. Capiati, *J. Mater. Sci.* **46** (2011) 2578
14. J. H. Liu, X. L. Lv, L. D. Wei, Z. Q. Cheng, N. L. Zhang, X. Dou, *Non-Metallic Mines* (ISSN: 1000-8098) **29** (2006) 36 (in Chinese)
15. H. M. Yang, G. Z. Qiu, D. Z. Wang, *J. Chin. Ceram. Soc.* (ISSN: 0454-5648) **27** (1999) 580 (in Chinese)
16. C. Nkoumbou, F. Villieras, D. Njopwouo, C. Y. Ngoune, O. Barres, M. Pelletier, A. Razafitianamaharavo, J. Yvon, *Appl. Clay Sci.* **41** (2008) 113
17. S. Petit, F. Martin, A. Wiewora, P. De Parseval, A. Decarreau, *Am. Mineral.* **89** (2004) 319
18. Y. D. Yao, S. G. Wang, *Multipurpose Utilization of Mineral Resources* (ISSN: 1000-6532) **4** (1998) 35 (in Chinese)
19. J. C. Gu, Y. X. Zhang, Y. C. Liu, *J. Sichuan Univ.* (ISSN: 1009-3087) **36** (2004) 43 (in Chinese)
20. K. R. Paton, A. H. Windle, *Carbon* **46** (2008) 1935.

Preliminary organic geochemical study of lignite from the Smederevsko Pomoravlje field (Kostolac Basin, Serbia) – Reconstruction of geological evolution and potential for rational utilization

NATAŠA ĐOKOVIĆ[1], DANICA MITROVIĆ[1], DRAGANA ŽIVOTIĆ[2], DARKO ŠPANIĆ[3], TAMARA TROSKOT-ČORBIĆ[3], OLGA CVETKOVIĆ[4] and KSENIJA STOJANOVIĆ[5]**

[1]*University of Belgrade, Innovation Center of the Faculty of Chemistry, Studentski trg 12–16, 11000 Belgrade, Serbia,* [2]*University of Belgrade, Faculty of Mining and Geology, Đušina 7, 11000 Belgrade, Serbia,* [3]*INA-Industrija nafte d.d., Exploration & Production BD, Exploration Sector, E&P Laboratory Department, Lovinčićeva 4, 10002 Zagreb, Croatia,* [4]*University of Belgrade, Institute of Chemistry, Technology and Metallurgy, Center of Chemistry, Njegoševa 12, 11000 Belgrade, Serbia and* [5]*University of Belgrade, Faculty of Chemistry, Studentski trg 12–16, 11000 Belgrade, Serbia*

Abstract: The study was aimed at determining the origin and geological evolution of lignites from the Smederevsko Pomoravlje field (Kostolac Basin, Serbia). The possibility of a rational utilization of the coal was also considered. For this purpose, numerous organic geochemical analyses were applied to representative lignite samples. The obtained results showed that the coal from the Smederevsko Pomoravlje field is a typical humic coal. The peat-forming vegetation was dominated by gymnosperm plants. The coal-forming plants belonged to the gymnosperm families *Taxodiaceae*, *Cupressaceae*, *Phyllocladaceae* and *Pinaceae*. Other precursors of organic matter (OM) were microbial biomass, ferns and angiosperms. It was established that peatification occurred in a neutral to slightly acidic, fresh water environment under anoxic to suboxic redox conditions. The maturity of the OM is low, in the phase of intense diagenetic processes. The biomarker compositions and values of the corresponding parameters revealed that the Smederevsko Pomoravlje field, the Drmno field (Kostolac Basin) and the "A" field (Kovin deposit) represent a part of a unique lignite basin. The results of this study suggest possible rational utilization of the Smederevsko Pomoravlje lignites in thermal power plants. This is particularly related to samples from coal seam I. A significant amount of gas could be generated from lignites at higher maturities. Eight samples met the basic assumptions for effective gasification.

575

INTRODUCTION

Concerning the significance of the various fossil fuel resources of Serbia, brown coals, particularly lignites, are of great economic importance as they represent the main source for energy production.[1] A significant number of coal bearing basins with huge coal reserves were formed during the Miocene in the territory of Serbia, as a result of favourable peat-forming conditions. The economically most important Upper Miocene coal basins – the Kolubara, Kostolac and Kovin deposits were formed within the Pannonian Basin System in shallow lacustrine, delta plain and fluvial environments.[2] During the early Late Miocene, the Pannonian Basin evolved into the Pannon Lake.[3] The coal deposits have large reserves and resources, and relatively simple exploitation conditions. Annually, the Kolubara Basin produces about 30 Mt of lignite,[4] while the Kostolac Basin produces about 7 Mt.[5] Most of lignite produced (90 %) is used for electricity generation in the thermal power plants (TPP) in Obrenovac and Veliki Crljeni (Kolubara Basin), as well as in Kostolac (Kostolac Basin).

In the past few decades, organic geochemical analysis of coal organic matter has been proved to be a promising tool for an assessment of the possibility of rational utilization of coal,[6–9] as well as for the reconstruction of the vegetation assemblage and palaeoenvironmental conditions in peatlands during the formation of coal-bearing strata.[10–12] For this purpose, proximate and ultimate analyses, Rock–Eval pyrolysis and biomarker analysis were most often used.

In recent years, a new lignite field in the west part of the Kostlac Basin (Serbia), namely Smederevsko Pomoravlje has been investigated. The field is under detailed exploration. In this paper, the organic geochemical features of the Smederevsko Pomoravlje lignite field are presented in detail. Based on comprehensive biomarker analyses, the origin of the organic matter (OM) and the characteristics of the depositional environment of lignites from the Smederevsko Pomoravlje field were reconstructed. The results are compared with lignites from the Drmno field (Kostolac Basin) and the "A" field (Kovin deposit) in order to examine whether the three fields represent a unique productive basin. Moreover, the possibility of rational utilization of coal in order to supply the next generation of Serbian coal-fired power plants or to use lignite as a good raw-material for gasification was also considered.

The lignite samples investigated in this study were of Upper Pontian age (*ca.* 6 Ma) and originated from the boreholes A-339, A2I-414 and A1J-369 of the Smederevsko Pomoravlje field (Fig. S-1 of the Supplementary material to this paper). Samples were collected from the two coal seams, I at a depth interval 23.30 to 67.25 m, and II at a depth interval 56.30 to 85.20 m (Table I). The

thickness of each sample interval was determined as per the changes in the macroscopic lithology of the coal.

EXPERIMENTAL

Elemental analysis was applied to determine the contents of sulphur, nitrogen and organic carbon (C_{org}). The organic carbon content was determined after removal of carbonates with diluted hydrochloric acid (1:3, *V/V*). The measurements were performed using a Vario EL III, CHNS/O Elemental Analyser, Elementar Analysensysteme GmbH. The ash content measurements followed the standard procedure ISO 1171 (1997).[13] Analytical moisture determination followed the SRPS B.H8.390/1987 standard (1987).[14] The calorific value measurements were performed on IKA-Calorimeter adiabatic C400, following the standard procedure SRPS B.H8.318/1972 (1972).[15]

TABLE I. A list of the investigated samples

Borehole	Coal seam	Sample	Depth interval, m	Lithology
A-339	I	1	23.30–26.00	Xylite-rich coal
	I	2	26.00–28.00	Mixture of matrix and mineral-rich coal
	I	3	34.30–37.00	Xylite-rich coal
	I	4	40.50–42.70	Mixture of matrix and mineral-rich coal
	I	5	43.20–46.90	Xylite-rich coal
	II	6	56.30–58.20	Matrix coal
A2I-414	I	7	27.40–30.40	Xylite-rich coal
	I	8	30.40–33.30	Mixture of xylite-rich and matrix coal
	I	9	34.90–38.00	Xylite-rich coal
	I	10	41.00–44.00	Mixture of mineral-rich and matrix coal
	I	11	44.00–46.20	Mineral-rich coal
	I	12	65.45–67.25	Mixture of xylite-rich and matrix coal
	II	13	67.95–69.50	Mixture of matrix and mineral-rich coal
A1J-369	I	14	43.85–48.35	Xylite-rich coal
	I	15	48.35–50.70	Mineral-rich coal
	I	16	51.80–54.80	Mixture of xylite-rich and matrix coal
	I	17	54.80–56.35	Xylite-rich coal
	I	18	57.10–60.00	Mineral-rich coal
	I	19	60.00–63.05	Mixture of matrix and mineral-rich coal
	II	20	80.25–83.20	Mixture of matrix and mineral-rich coal
	II	21	83.20–85.20	Mineral-rich coal

Rock–Eval pyrolysis was performed using a TOC/Rock–Eval-6 apparatus.[16] The sample aliquot was 12–14 mg. The IFP 160000 standard (≈60 mg) was used for calibration.

Bitumens were extracted (42 h) using a Soxhlet apparatus with an azeotropic mixture of dichloromethane and methanol. The asphaltenes were precipitated with *n*-heptane and the remainder (maltenes) was separated into three fractions using column chromatography over silica gel. The saturated hydrocarbons fraction was eluted with *n*-hexane, the aromatic hydrocarbons with a mixture of *n*-hexane and dichloromethane (3:1, *V/V*) and the NSO fractions (polar fraction, which contains nitrogen, sulphur, and oxygen compounds) with a mixture of chloroform and methanol (1: 1, *V/V*).

The saturated fractions isolated from the bitumen were analyzed by gas chromatography-mass spectrometry (GC-MS). A gas chromatograph Agilent 7890A GC (HP5-MS capillary column, 30 m×0.25 mm, He carrier gas 1.5 cm^3 min^{-1}) coupled to an Agilent 5975C mass selective detector (70 eV) was used. The column was heated from 80 °C to 310 °C at a rate of 2 °C min^{-1}, and the final temperature of 310 °C was maintained for an additional 25 min. The individual peaks were identified by comparison with the literature data[17-20] and based on the mass spectra (library: NIST5a). Quantification of the compounds for calculating the biomarker parameters was performed by integration of peak areas (software GCMS Data Analysis) in the appropriate mass chromatograms (*m/z* 71 for *n*-alkanes, *m/z* 215 for sterenes and *m/z* 191 for hopanoids), with the exception of the diterpenoids and non-hopanoid triterpenoids that were integrated from the total ion currents (*TICs*) of the saturated fraction.

RESULTS AND DISCUSSION

Group organic geochemical parameters

The organic carbon contents (C_{org}) are within the limits typical for lignite[21–23] and vary between 29.7 and 55.3 % (Table S-I of the Supplementary material to this paper). The gross and net calorific value (dry basis) of the lignite samples ranges from 9.0 to 25.3 MJ kg^{-1} and from 8.5 to 24.5 MJ kg^{-1}, respectively, which is in range for rational utilization of lignite in thermal power plants (TPPs) recommended by the American Lignite Council.[23] Moreover, all samples (with exception of sample 20) have higher net calorific values than recommended for SFR Yugoslavia (8.89 MJ kg^{-1}).[24] A significant positive correlation between the calorific value and C_{org} was observed (correlation coefficient, r = 0.92), as expected. Therefore, organic carbon contents and calorific values represent the first criteria that indicate possible rational utilization of Smederevsko Pomoravlje lignites in TPPs. This is particularly related to samples from coal seam I at a depth down to 50 m, which generally have higher C_{org} and calorific value (Table S-I). The significant negative correlation between C_{org} and ash content (r = = –0.97) indicates that the differences in the C_{org} contents of the lignites are mainly controlled by the varying amounts of mineral matter.

One of the basic assumptions ensuring efficiency of fluidized bed gasification is the optimal maximum ash content recalculated to a dry basis at 20 %.[25] Data from Table S-I show that 8 samples, particularly those from the upper part of coal seam I meet this basic criteria. Concerning the utilization of this deposit for power production, it is evident that the high proportion of ash, attaining more

than 40 % in some samples (Table S-I), should be taken into consideration in order to optimize the burnout behaviour.

The content of sulphur (dry basis) does not exceed 1.5 %, with the exception of samples 13 and 16 (Table S-I). This result implies a relatively low content of sulphate in the waters within the peat (peatification in a fresh water environment).[26,27] On the other hand, the content of sulphur is an important quality parameter of lignite, due to its corrosive influence on the furnace and is the main cause of "acid rains" after combustion. The sulphur content of Smederevsko Pomoravlje lignites is in range as for other Serbian lignites (Drmno filed, Kostolac Basin, "A" field, Kovin deposit, "D" field, Kolubara Basin, Table S-I),[28,21,22] Achlada and Mavropigi Basins in Greece[6] and even lower than in lignites from Bulgarian deposits (Staniantsi and Beli Breg),[11] which have been extensively utilized for electric energy production. This indicates that the content of this element is not a limiting factor for usage of Smederevsko Pomoravlje lignites in TPPs.

The values of the C/N mole ratio exceed 60 in all the studied samples (Table S-I), which is typical for terrestrial flora.[29,30] This result indicates that Smederevsko Pomoravlje lignites are typical humic coals. This observation is important, because recent investigations showed that coal should contain at least 80 % huminite (mineral-matter free basis) to be useful for fluidized bed gasification.[25] However, the possibility of gasification of Smederevsko Pomoravlje lignites should be further investigated in more detail by petrographic analysis. On the other hand, recent investigations showed that extremely high values of C/N mole ratio (>100), which indicate terrestrial plants with a domination of lignin tissue,[31] may hinder the grindability properties of lignite, also important parameter for coal utilization. According to data from Table S-I, only two samples (3 and 15) have unfavourable C/N ratios.

Taking into account all aforementioned data, it could be assumed that lignite from coal seam I of borehole A-339 shows the best quality.

The yield of the soluble organic matter (bitumen) varies in a wide range 12754–36409 ppm. The soluble organic matter is mainly represented by asphaltenes (40.1–53.2 %) and polar, NSO compounds (36.7–47.1 %). The relative contents of saturated and aromatic hydrocarbons are low, which is as expected for immature terrestrial organic material (Table S-I).

Rock–Eval pyrolysis

Rock Eval analysis revealed a high amount of free (S_1) and pyrolysable hydrocarbons (S_2), consistent with the high content of biogenic and diagenetic compounds. The S_3 peak, which is proportional to the content of oxygen in kerogen, is also relatively high in accordance with immature terrestrial OM rich in lignin and cellulose (Table S-II of the Supplementary material). As expected, a

significant positive correlation was observed between the content of organic carbon and values of S_1, S_2 and S_3 (correlation coefficients > 0.80).

The production index (*PI*) and maximal temperature (T_{max}) imply low OM maturity (phase of intense diagenesis, Table S-II).[32]

The values of the S_2/S_3 ratio and the hydrogen index (*HI*), in the ranges 2.08–3.39 and 157–200, respectively, indicate sufficient gas potential of lignite at higher maturity.[32] The modified van Krevelen hydrogen index *vs.* oxygen index diagram (Fig. 2) indicates kerogen type III, with a certain contribution of kerogen type II/III, confirming the respectable gas potential. Moreover, the contribution of kerogen type II/III suggests some liquid hydrocarbon potential. The presence of kerogen type II/III is consistent with the presence of short chain *n*-alkanes (see Section n-*Alkanes and isoprenoids* later on) and C_{27}–C_{28} sterene homologues (Section *Steroids and hopanoids* later on).
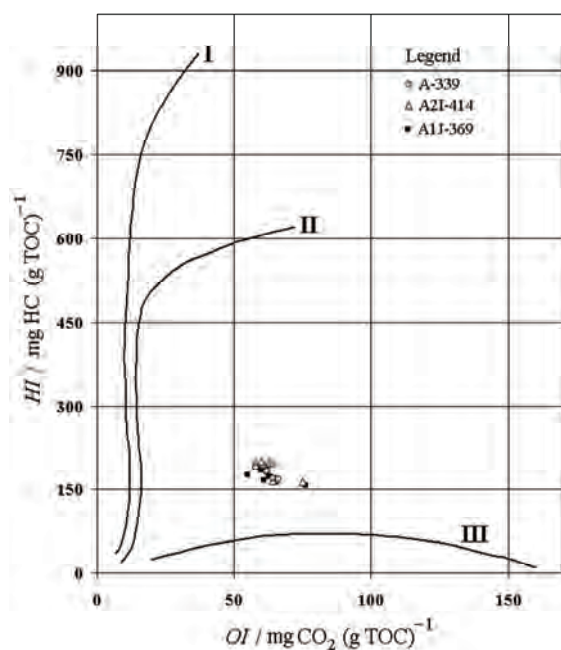
Fig. 2. Modified van Krevelen diagram – hydrogen index (*HI*) *vs.* oxygen index (*OI*).

Molecular composition of the organic matter

General characteristics. The main constituents of the saturated fraction of the coals are diterpenoids, followed by *n*-alkanes and hopanoids. Steroids and non-hopanoid triterpenoids were identified in low amounts (Fig. S-2 of the Supplementary material).

Domination of diterpenoids shows that the main sources of organic matter were gymnosperms (conifers), which confirms that the investigate lignites are

typical humic coals. The presence of hopanoid biomarkers indicates a contribution of prokaryotic organisms, such as bacteria and fungi, whereas the identification of non-hopanoid triterpenoids implies a contribution of angiosperms to the lignite OM (Fig. S-2).

n-*Alkanes and isoprenoids.* Considering the low OM maturity, *n*-alkanes were abundant in the total ion current (*TIC*) of the saturated fraction of the lignites (Fig. S-2). Based on the *m/z* 71 mass chromatogram of the saturated fraction (Fig. S-3a of the Supplementary material), *n*-alkanes were identified in the range C_{15}–C_{35}, or C_{16}–C_{35} (Table S-III). The *n*-alkane patterns were dominated by long-chain homologues (C_{27}–C_{31}), maximizing at *n*-C_{29} (Fig. S-3a; Table S-III) and an expressed odd over even predominance, indicating a significant contribution of epicuticular waxes. The values of carbon preference index (*CPI*)[33] for the full range of *n*-alkanes C_{16}–C_{34} and an odd–even predominance[34] (*OEP*) 2 value higher than 3, *i.e.*, 2, respectively (Table S-III) are in accordance with the low rank of the lignites. Mid-chain *n*-alkanes (*n*-C_{21}–*n*-C_{25}), originating from vascular plants, microalgae, cyanobacteria, sphagnum and submerged aquatic macrophytes,[35–38] are present in lower amount in comparison with the long-chain odd homologues (Fig. S-3a). The predominance of odd over even carbon-number *n*-alkanes in the mid-range *n*-alkanes (parameter *OEP* 1; Table S-III), suggests a microbial input, consistent with presence of hopanoids (Fig. S-3c). Moreover, the dominance of C_{23} and C_{25} *n*-alkane homologues in mid chain range (Fig. S-3a) implies an input of submerged aquatic macrophytes. Variations of *OEP* 1 ratio (Table S-III) suggest variations in bacterial input/communities and the contribution of submerged aquatic macrophytes to the precursor OM. These variations most probably could be attributed to changes in the depositional environment (water column level), due to the pronounced seasonality during the Upper Miocene (hot and humid summers and dry and relatively cold winters).[39,40]

In all the investigated samples, short chain *n*-alkanes ($\leq C_{20}$) were present in low quantities (Fig. S-3a), consistent with typical humic OM. The main precursors of the short chain *n*-alkanes are algae, and photosynthetic and non-photosynthetic bacteria.[41,42] The low values of the sterane to hopane ratio (see Section *Steroids and hopanoids* later on and Table S-V) indicate a greater contribution of prokaryotic organisms than eukaryotic algae to the OM. Therefore, it could be assumed that the short chain *n*-alkanes mainly originated from bacteria. The significant variations of the *CPI* values for the short chain *n*-alkanes (*CPI*$_{16–20}$; Table S-III) confirmed changes in bacterial communities during diagenesis, consistent with above discussed OEP 1 ratio.

Isoprenoids pristane (Pr) and phytane (Ph) were present in low amounts in the lignite extracts (Figs. S-2 and S-3a). Low concentrations of pristane and phytane were often reported in immature organic matter.[43–45] The Pr/Ph ratio is

widely used as an indicator for the redox (*Eh*) conditions of the depositional environment.[46] However, this parameter is also known to be affected by maturation[41] and by differences in the precursors for acyclic isoprenoids, *i.e.*, bacterial origin,[47,48] and the formation of pristane from tocopherols or chromanes.[49] For this lignite sample set, an influence of maturity on the pristane/ /phytane ratio could be ruled out. In addition, the low maturity of the lignite probably argues against the formation of pristane from tocopherols.[49] Therefore, the Pr/Ph ratio, varying between 0.66–1.65 (Table S-III), may be considered as an indicator of the changing of the *Eh* settings from anoxic to slightly oxic during peat deposition. This change was also related to a change in the water level, *i.e.*, pronounced seasonality. Namely, an increase in *Eh* of the environment is often associated with a decrease in water level and in some cases drainage of peat bogs.

Values of aforementioned *n*-alkane parameters and Pr/Ph ratio are in range for those parameters observed for lignite extracts from the Drmno field (Kostolac Basin) and "A" field (Kovin deposit) (Table S-III), suggesting very similar origin and palaeoenvironment of the precursor OM.[21,28]

Diterpenoids and triterpenoids with a non-hopanoid skeleton. Diterpenoids were the main constituents of lignite extracts, indicating a significant contribution of gymnosperms to the precursor OM. Pimarane and particularly 16*α*(*H*)- -phyllocladane were dominant by far in the saturated fractions (Fig. S-2). A high amount of 16*α*(*H*)-phyllocladane indicates that the coal-forming plants belonged to the conifer families *Taxodiaceae*, *Podocarpaceae*, *Cupressaceae*, *Araucariaceae* and *Phyllocladaceae*, while a high abundance of pimarane suggests *Pinaceae*, *Taxodiaceae* and *Cupressaceae*.[50–53] Other diterpenoid type constituents of the saturated fraction were *α*-labdane, *β*-labdane, isopimaradienes, norisopimarane, pimaradiene, atisene, norpimarane, beyerane, isophyllocladene, isopimarane, fichtelite, 16*β*(*H*)-phyllocladane and 16*α*(*H*)-kaurane (Fig. S-2). In all samples, tetracyclic terpenoids predominated over tricyclic terpenoids (with exception of sample 18), whereas bicyclic diterpenoids were present in low amounts (Table S- -IV of the Supplementary material).

The pimarane/16*α*(*H*)-phyllocladane ratio and the ratio of tricyclic to tetracyclic diterpenoids are higher in the upper part of coal seam I in all three boreholes (Table S-IV), which may imply a greater contribution of *Pinacea* to the precursor OM. These samples also contained higher amount of C_{org} (Table S-I). The mentioned results indicate peatification of lignite from the upper part of coal seam I under a higher water level, which contributed to better preservation of OM and growth of *Pinacea*.

The non-hopanoid triterpenoids were present in low amount in the saturated fraction of Smederevsko Pomoravlje lignites and consisted exclusively of des-A- -degraded triterpenoids: des-A-olean-enes, des-A-urs-enes, des-A-oleanadiene,

des-A-oleanane and des-A-lupane (Fig. S-2). The presence of des-A-degraded triterpenoids implies microbial activity, consistent with relatively abundant hopanoids (Figs. S-2 and S-3c). The small amount of non-hopanoid triterpenoids indicates a small contribution of angiosperms to the precursor OM. This result is also important for lignite utilization, because recent studies* showed that elevated amounts of angiosperm organic matter may lower the grindability properties of lignite.

Very similar distributions of diterpenoids and non-hopanoid triterpenoids were observed during investigations of lignites from the Drmno field (Kostolac Basin) and the "A" field (Kovin deposit),[21,28] Table S-IV, indicating that these two fields along with the Smederevsko Pomoravlje field represent parts of a unique basin.

Steroids and hopanoids. Steroid biomarkers of Smederevsko Pomoravlje lignites (based on the *m/z* 215 mass chromatogram of the saturated fraction; Fig. S-3b) consisted predominantly of C_{29} Δ^4-, Δ^2- and Δ^5-sterenes. The C_{27}- and C_{28}-homologues were identified in notably lower amounts (Table S-V). The marked predominance of C_{29} sterenes (Fig. S-3b; Table S-V) clearly indicates peat formation from terrigenous plants.

Hopanoids were more abundant than steroid biomarkers in the coal extracts (Σsteroids/Σhopanoids ratio < 0.26; Table S-V). These results indicate a bacteria-influenced facies and argue for the role of microorganisms in the degradation of the plant tissue.

Based on the *m/z* 191 mass chromatogram of the saturated fraction, the hopane composition was characterized by the presence of $17\alpha(H)21\beta(H)$, $17\beta(H)21\alpha(H)$ and $17\beta(H)21\beta(H)$ compounds with 27 and 29–32 carbon atoms (Fig. S-3c). Other hopanoid-type constituents of the saturated fraction were C_{27} hop-13(18)-ene, C_{27} hop-17(21)-ene and C_{30} hop-17(21)-ene. Moreover, several samples contained hopanoid ketones, C_{27} hop-21-one and C_{30} hop-17(21)-en-20-one (Fig. S-3c). C_{27} Hop-21-one was also observed in lignite extracts from the Drmno field, Serbia,[28] and it was reported in microbial mats and the black sandstone from the Be'eri deposit, Israel.[54] C_{30} hop-17(21)-en-20-one could have been formed by oxidation of the highly sensitive allylic position of hop-17(21)-ene present in the herein studied samples (Fig. S-3c) and resulting either from elimination of an alcohol group on hydroxyhopanoids followed by migration of the double-bond (favoured in acidic conditions),[55] or by bacterial dehydrogenation of saturated hopane skeletons.[56] Therefore, the presence of C_{30} hop-17(21)-en-20-one could indicate slightly acidic suboxic conditions in the mire, which is consistent with the relatively low sulphur content.

In the majority of the samples, the hopane distribution was dominated by $C_{27}17\beta(H)$-hopane; however, in several samples, the most abundant hopanoid

---

* A. Bechtel, personal communication, 2013.

biomarker was C_{31} $17\alpha(H)21\beta(H)22(R)$-hopane (Table S-V). The prominent $C_{27}17\beta(H)$-hopane in distribution of total hopanoids, followed by sharp domination of lower homologues, $C_{27}17\beta(H)$ and $C_{29}17\beta(H)21\beta(H)$ in the distribution of C_{27}–C_{31} $\beta\beta$-hopanes in all samples (Fig. S-3c; Table S-V) could signify that the precursor hopanoid lipids partly originated from methanotrophic bacteria (*e.g.*, *Methylococcus capsulatus* or *Methylomonas methanica*).[57] On the other hand, prominent $C_{31}\alpha\beta(R)$-hopane was often reported in low rank coals.[45,52,53] Killops *et al.*[58] suggested that the decarboxylation of 31,32-bishomohopanoic acid, which is generally abundant in peats and soils,[59,60] could result in the formation of $C_{31}17\alpha(H)21\beta(H)$-hopane in immature coals. The presence of 22(R)-bishomohopanoic acid in the ''geological" $17\alpha(H)21\beta(H)$ configuration in living microbial mats,[61] supports the assumption that the C_{31} $\alpha\beta$-hopane could be derived directly from microorganisms by decarboxylation. According to van Dorselaer *et al.*,[62] a high amount of $C_{31}\alpha\beta(R)$-hopane implies complex reactions in acidic environments under oxic conditions. The observed distributions of hopanes in the Smederevsko Pomoravlje lignites indicate changes in the microbial population, which is consistent with changes in palaeoenvironment, from anoxic to suboxic.

The ratio of $17\beta(H)21\beta(H)$ to ($17\beta(H)21\beta(H)$ + $17\alpha(H)21\beta(H)$) C_{30}-hopanes is within the limits established for lignite (0.5–0.7; Table S-V),[63] in accordance with low thermal maturity of the OM.

Based on the *m/z* 191 mass chromatogram, compounds with the fernene skeleton, fern-9(11)-ene and fern-8-ene, were also identified (Fig. S-3c). Fernenes mainly originate from ferns, which are often typical members of herbaceous precursor vegetation.[39,64] It was shown that ferns could also be the source of hopanes with fewer than 30 carbon atoms. Therefore, it could be speculate that the predominance of C_{27} and C_{29} hopanoids with the $\beta\beta$-configuration in the studied lignites could be attributed, at least to some extent, to sources other than bacteria, probably ferns.

CONCLUSIONS

Smederevsko Pomoravlje lignites are typical humic coals. The main sources of the organic matter were gymnosperms (conifers). Other precursors of OM were microbial biomass, ferns and angiosperms. Based on the composition of diterpenoids, it was established that the coal-forming plants belonged to the gymnosperm families *Taxodiaceae, Podocarpaceae, Cupressaceae, Araucariaceae, Phyllocladaceae* and *Pinaceae*.

Peatification was realized in a neutral to slightly acidic, fresh water environment. Pronounced seasonality caused changes in the water table, which resulted in changes in the redox potential (*Eh*) during peatification, as well as microbial and to lesser extent, vegetation differentiations in the palaeo-communities.

The obtained results indicated low OM maturity (phase of intense diagenetic processes).

Based on the very similar distributions of molecular "fingerprints" and the values of biomarker ratios in Smederevsko Pomoravlje lignites and lignites from the Drmno field (Kostolac Basin) and the "A" field (Kovin deposit), it was established that these three fields represent part of a unique productive basin.

Concerning potential rational utilization of Smederevsko Pomoravlje lignites, the following conclusions were drawn. The group organic geochemical data and net calorific value signified possible usage of the lignites in thermal power plants. This was particularly related to samples from coal seam I (depth down to 50 m). The investigated lignites demonstrated sufficient gas potential and some liquid hydrocarbons potential at higher maturities. Eight samples meet the basic conditions to ensure efficiency of fluidized bed gasification of the lignite.

SUPPLEMENTARY MATERIAL

Geological settings, group organic geochemical parameters, results of the Rock Eval pyrolysis, abundance data for of *n*-alkanes, isoprenoids, diterpenoids, non-hopanoid triterpenoids, steroids and hopanoids, as well as figures sowing total ionic currents and GC–MS diagrams are available electronically from http://www.shd.org.rs/JSCS/, or from the corresponding author on request.

И З В О Д

ПРЕЛИМИНАРНА ОРГАНСКО–ГЕОХЕМИЈСКА СТУДИЈА ЛИГНИТНОГ ПОЉА СМЕДЕРЕВСКО ПОМОРАВЉЕ (БАСЕН КОСТОЛАЦ) – РЕКОНСТРУКЦИЈА ГЕОЛОШКЕ ЕВОЛУЦИЈЕ И МОГУЋНОСТ РАЦИОНАЛНЕ УПОТРЕБЕ УГЉА

НАТАША ЂОКОВИЋ[1], ДАНИЦА МИТРОВИЋ[1], ДРАГАНА ЖИВОТИЋ[2], ДАРКО ШПАНИЋ[3], ТАМАРА ТРОСКОТ – ЧОРБИЋ[3], ОЛГА ЦВЕТКОВИЋ[4] и КСЕНИЈА СТОЈАНОВИЋ[5]

[1]*Иновациони центар, Хемијски факултет, Универзитет у Београду, Студентски трг 12–16, 11000 Београд,* [2]*Рударско–геолошки факултет, Универзитет у Београду, Ђушина 7, 1100 Београд,* [3]*INA – Industrija nafte d.d., Exploration & Production BD, Exploration Sector, E&P Laboratory Department, Lovinčićeva 4, 10002 Zagreb, Croatia,* [4] *ИХТМ – Центар за хемију, Универзитет у Београду, Његошева 12, 11000 Београд и* [5]*Хемијски факултет, Универзитет у Београду, Студентски трг 12–16, 11000 Београд*

Циљ рада је био да се утврди порекло и геолошка еволуција лигнита из поља Смедеревско Поморавље, басен Костолац. Разматрана је и могућност рационалне употребе угља. Бројне органско–геохемијске анализе су изведене на репрезентативним узорцима лигнита. Добијени резултати показују да су лигнити поља Смедеревско Поморавље типични хумусни угљеви. Гимносперме (голосеменице) су биле главни извор органске супстанце лигнита. Материјал потиче од следећих фамилија гимносперми: *Taxodiaceae, Cupressaceae, Phyllocladaceae* и *Pinaceae*. Остали извори органске супстанце лигнита били су

микробна биомаса, папрати и ангиосперме (скривеносеменице). Утврђено је да се хумификација органске супстанце одвијала у слатководној, неутралној до слабо киселој средини, при аноксичним до благо оксичним условима. Органска супстанца је незрела и налази се на стадијуму дијагенезе. Састав биомаркера и вредности одговарајућих параметара указују на то да поља Смедеревско Поморавље, Дрмно (басен Костолац) и „А" (лежиште Ковин) представљају део јединственог басена. Резултати овог истраживања упућују на могућу рационалну употребу лигнита Смедеревско Поморавље у термоелектранама. То се посебно односи на узорке из првог угљеног слоја. Органска супстанца лигнита може генерисати значајне количине гаса на вишем ступњу зрелости. Осам узорака задовољава основне критеријуме за ефикасну гасификацију.

REFERENCES

1. http://www.smeits.rs/include/data/docs0066.doc (in Serbian, last accessed April 5, 2014)
2. R. Jelenković, A. Kostić, D. Životić, M. Ercegovac, *Geol. Carpath.* **59** (2008) 345
3. I. Magyar, D. H. Geary, P. Müller, *Palaeogeogr. Palaeoclimatol. Palaeoecol.* **147** (1999) 151
4. http://www.rbkolubara.rs/index.php?option=com_content&view=article&id=83&Itemid=189&lang=sr (in Serbian, last accessed April 5, 2014)
5. http://www.te-ko.rs (in Serbian, last accessed April 5, 2014)
6. N. Koukouzas, S. P. Kalaitzidis, C. R. Ward, *Int. J. Coal Geol.* **83** (2010) 387
7. I. Suárez-Ruiz, C. R., Ward, *Coal combustion*, in *Applied Coal Petrology. The Role of Petrology in Coal Utilization*, I. Suarez-Ruiz, J. C. Crelling, Eds., Academic Press, Amsterdam, 2008, p. 85
8. M. D. Ercegovac, B. R. Aleksić, O. G. Cvetković, B. Ž. Marković, B. D. Aleksić, D. K. Vitorović, *Bull. Czech Geol. Surv.* **74** (1999) 175
9. M. Ercegovac, B. R. Aleksić, O. Cvetković, B. Marković, B. D. Aleksić, D. Vitorović, *Ann. Geol. Penins. Balk.* **62** (1998) 375
10. M. Stefanova, D. A. Ivanov, B. R. T. Simoneit, *Int. J. Coal Geol.* **120** (2013) 102
11. A. Zdravkov, A. Bechtel, R. F. Sachsenhofer, J. Kortenski, R. Gratzer, *Org. Geochem.* **42** (2011) 237
12. D. Životić, B. Jovančićević, J. Schwarzbauer, O. Cvetković, I. Gržetić, M. Ercegovac, K. Stojanović, A. Šajnović, *Int. J. Coal Geol.* **81** (2010) 227
13. ISO 1171: Methods for analysis and testing of coal and coke. Determination of ash content, 1997
14. SRPS B.H8.390/1987: Brown coals and lignites – Determination of moisture content – Indirect gravimetric method, 1987 (in Serbian)
15. SRPS B.H8.318/1972: Methods of analysis of coal and coke - Determination of the gross calorific value by the calorimetric bomb method, and calculation of net calorific value, 1972, in Serbian
16. J. Espitalié, G. Deroo, F. Marquis, *Rev. Inst. Fr. Pet.* **40** (1985) 563
17. R. P. Philp, *Fossil Fuel Biomarkers. Applications and Spectra.* Elsevier, Amsterdam, 1985, pp. 140, 165, 181, 183, 192, 203, 236, 244, 249
18. S. Stout, *Org. Geochem.* **18** (1992) 51
19. Y. Huang, M. J. Lockheart, J. W. Collister, G. Eglinton, *Org. Geochem.* **23** (1995) 785
20. J. Jacob, J.-R. Disnar, M. Boussafir, A.-L. Spadano Albuquerque, A. Sifeddine, B. Turcq, *Org. Geochem.* **38** (2007) 180
21. K. Stojanović, D. Životić, *Int. J. Coal Geol.* **107** (2013) 3

22. D. Životić, K. Stojanović, I. Gržetić, B. Jovančićević, O. Cvetković, A. Šajnović, V. Simić, R. Stojaković, G. Scheeder, *Int. J. Coal Geol.* **111** (2013) 5
23. http://energy.about.com/od/Coal/a/Lignite.htm (last accessed April 5, 2014)
24. P. Lj. Stefanović, Z. J. Marković, V. V. Bakić, D. B. Cvetinović, V. D. Spasojević, N. V. Živković, *Therm.* S*ci.* **16** (2012) 805
25. B. Bielowicz, *Int. J. Coal Geol.* **116**–**117** (2013) 236
26. A. Bechtel, M. Markic, B. Jelen, R. F. Sachsenhofer, R. Gratzer, A. Lücke, W. Püttmann, *Int. J. Coal Geol.* **57** (2004) 23
27. D. J. Casagrande, *Sulphur in Peat and Soil*, in *Coal and Coal-Bearing Strata: Recent Advances*, A. C. Scott, Ed., Geol. Soc. Spec. Publ., London, UK, 1987, p. 87
28. P. A. Meyers, R. Ishiwatari, *Org. Geochem.* **20** (1993) 867
29. P. A. Meyers, E. Lallier-Vergés, *J. Paleolimnol.* **21** (1999) 345
30. https://www.yumpu.com/en/document/view/13643187/inside-this-issue-iccp (last accessed 5 April, 2014)
31. K. E. Peters, C. C. Walters, J. M. Moldowan, *The Biomarker Guide, Volume 1: Biomarkers and Isotopes in the Environment and Human History.* Cambridge University Press, Cambridge, 2005, pp.72, 77, 88
32. E. E. Bray, E. D. Evans, *Geochim. Cosmochim. Acta* **22** (1961) 2
33. E. S. Scalan, J. E. Smith, *Geochim. Cosmochim. Acta* **34** (1970) 611
34. G. I. Matsumoto, M. Akiyama, K. Watanuki, T. Torii, *Org. Geochem.* **15** (1990) 403
35. C. J. Nott, S. Xie, L. A. Avsejs, D. Maddy, F. M. Chambers, R. P. Evershed, *Org. Geochem.* **31** (2000) 231
36. K. J. Ficken, B. Li, D. L. Swain, G. Eglinton, *Org. Geochem.* **31** (2000) 745
37. R. A. Andersson, P. Kuhry, P. Meyers, Y. Zebühr, P. Crill, M. Mörth, *Org. Geochem.* **42** (2011) 1065
38. T. Utescher, D. Ivanov, M. Harzhauser, V. Bozukov, A. R. Ashraf, C. Rolf, M. Urbat, V. Mosbrugger*, Palaeogeogr. Palaeoclimatol. Palaeoecol.* **272** (2009) 99
39. D. Ivanov, T. Utescher, V. Mosbrugger, D. Djordjević-Milutinović, S. Molchanoff, *Palaeogeogr. Palaeoclimatol. Palaeoecol.* **304** (2011) 262
40. K. E. Peters, C. C. Walters, J. M. Moldowan, *The Biomarker Guide, Volume 2: Biomarkers and Isotopes in Petroleum Exploration and Earth History.* Cambridge University Press, Cambridge, 2005, pp. 493, 499
41. E. V. D. S. Neto, J. M. Hayes, T. Takaki, *Org. Geochem.* **28** (1998) 361
42. L. I. P. Dzou, R. A. Noble, J. T. Senftle, *Org. Geochem.* **23** (1995) 681
43. W. B. Hughes, A. G. Holba, L. I. P. Dzou, *Geochim. Cosmochim. Acta* **59** (1995) 3581
44. T. T. A. Vu, K. G. Zink, K. Mangelsdorf, R. Sykes, H. Wilkes, B. Horsfield, *Org. Geochem.* **40** (2009) 963
45. B. M. Didyk, B. R. T. Simoneit, S. C. Brassell, G. Eglinton, *Nature* **272** (1978) 216
46. H. L ten Haven,. J. W. de Leeuw, J. Rullkötter, J. S. Sinninghe Damsté, *Nature* **330** (1987) 641
47. J. K. Volkman, J. R. Maxwell, Acyclic isoprenoids as biological markers, in Biological Markers in the Sedimentary Record:, R. B. Johns, Ed., Elsevier, Amsterdam, 1986, p. 1
48. H. Goossens, J. W. de Leeuw, P. A. Schenck, S. C. Brassell, *Nature* **312** (1984) 440
49. A. Otto, H. Walther, W. Püttmann, *Org. Geochem.* **26** (1997) 105
50. A. Otto, V. Wilde, *Bot. Rev.* **67** (2001) 141
51. M. Stefanova, D. R. Oros, A. Otto, B. R. T. Simoneit, *Org. Geochem.* **33** (2002) 1079
52. M. Stefanova, K. Markova, S. Marinov, B. R. T. Simoneit, *Bull. Geosci.* **80** (2005) 93

53. R. Y. P. Burhan, J. M. Trendel, P. Adam, P. Wehrung, P. Albrecht, A. Nissenbaum, *Geochim. Cosmochim. Acta* **66** (2002) 4085
54. A. Nissenbaum, I. R. Kaplan, *Chem. Geol.* **1** (1966) 295
55. J. P. Tritz, D. Herrmann, P. Bisseret J. Connan, M. Rohmer, *Org. Geochem.* **30** (1999) 499
56. S. Neunlist, M. Rohmer, *Biochem. J.* **231** (1985) 635
57. S. D. Killops, R. H. Funnell, R. P. Suggate, R. Sykes, K. E. Peters, C. Walters, A. D. Woolhouse, R. J. Weston, J.-P. Boudou, *Org. Geochem.* **29** (1998) 1
58. M. M. Quirk, A. M. K. Wardroper, R. E. Wheatley, J. R. Maxwell, *Chem. Geol.* **42** (1984) 25
59. M. Ries-Kautt, P. Albert, *Chem. Geol.* **76** (1989) 143
60. V. Thiel, M. Blumenberg, T. Pape, R. Seifert, W. Michaelis, *Org. Geochem.* **34** (2003) 81
61. A. van Dorselaer, P. Albrecht, J. Connan, in *Advances in Organic Geochemistry*, R. Campus, J. Goñi, Eds., Enadimsa, Madrid, 1975, p. 53
62. A. S. Mackenzie, R. L. Patience, J. R. Maxwell, in *Origin and Chemistry of Petroleum*, G. Atkinson, J. J. Zuckermann, Eds., Pergamon Press, Oxford, 1981, p. 1
63. T. Utescher, D. Djordjević-Milutinović, A. Bruch, V. Mosbrugger, *Palaeogeogr. Palaeoclimatol. Palaeoecol.* **253** (2007) 141.

Preliminary organic geochemical study of lignite from the Smederevsko Pomoravlje field (Kostolac Basin, Serbia) – reconstruction of geological evolution and potential for rational utilization

NATAŠA ĐOKOVIĆ[1], DANICA MITROVIĆ[1], DRAGANA ŽIVOTIĆ[2], DARKO ŠPANIĆ[3], TAMARA TROSKOT-ČORBIĆ[3], OLGA CVETKOVIĆ[4] and KSENIJA STOJANOVIĆ[5]**

[1]*University of Belgrade, Innovation Center of the Faculty of Chemistry, Studentski trg 12–16, 11000 Belgrade, Serbia,* [2]*University of Belgrade, Faculty of Mining and Geology, Đušina 7, 11000 Belgrade, Serbia,* [3]*INA-Industrija nafte d.d., Exploration & Production BD, Exploration Sector, E&P Laboratory Department, Lovinčićeva 4, 10002 Zagreb, Croatia,* [4]*University of Belgrade, Institute of Chemistry, Technology and Metallurgy, Center of Chemistry, Njegoševa 12, 11000 Belgrade, Serbia and and* [5]*University of Belgrade, Faculty of Chemistry, Studentski trg 12–16, 11000 Belgrade, Serbia*

GEOLOGICAL SETTINGS

The Kostolac Coal Basin, covering an area of 145 km², is located about 90 km east of Belgrade. It is divided into three coal fields: the Drmno field in the eastern, the Ćirikovac field in the central and the Smederevsko Podunavlje field in the western part of the Basin (Fig. S-1). The Drmno field is exploited, while the Smederevsko Podunavlje field is still under preliminary exploration. Exploitation in the Ćirikovac field was ceased a few years ago.

The basement of the Kostolac Basin is formed of Devonian crystalline rocks overlain by Neogene sediments. The total thickness of the Neogene sediments ranges from 300 to 5000 m in the central part of the depression.[1] The complete Neogene generally dips towards the north–west at a low angle of 5–15° with the coal seams following the same dip. The Neogene complex consists of several units, which were explained in detail in a previous paper.[2]

The Upper Pontian coal-bearing series in the Smederevsko Pomoravlje field were studied in detail by Životić[3] and were found to consist of sand, clayey sand, siltstone, clay, sandy clay, carbonaceous clay and five coal seams, named from bottom to top III, II-a, II, I-a, and I, respectively. Coal seams III, II and I are considered to be important for rational exploitation, whereas coal seams II-a and

---

*Corresponding author. E-mail: ksenija@chem.bg.ac.rs and xenasyu@yahoo.com

S138

I-a are only locally developed. About 100 exploration boreholes were drilled in the Smederevsko Pomoravlje field.
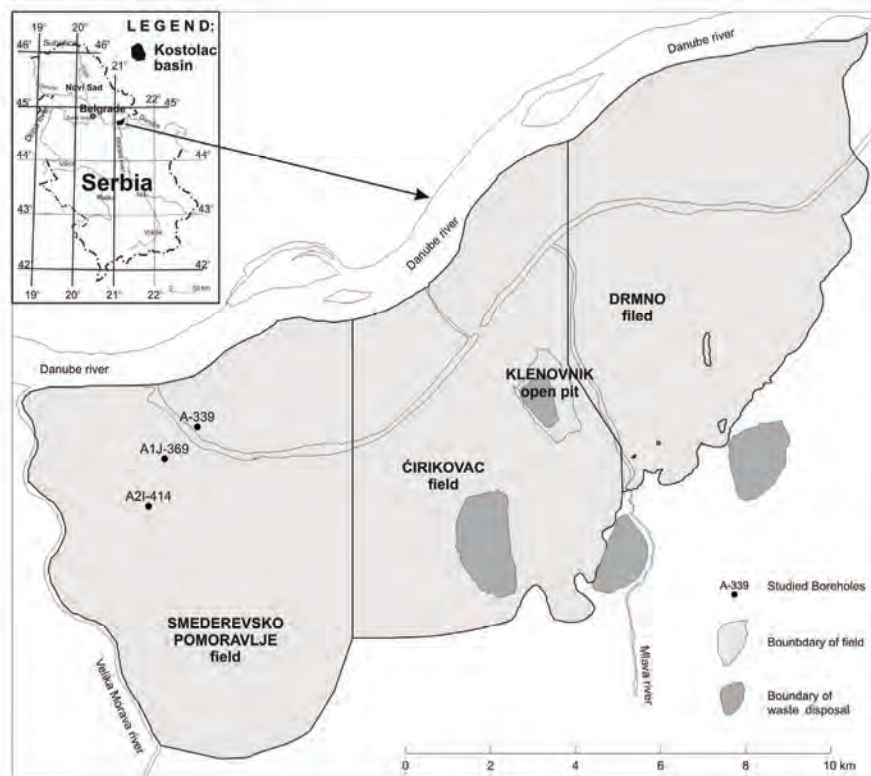
Fig. S-1. Location and coal fields of the Kostolac Basin.

The thickness of coal seam III varies over a wide range due to interbedding, from 18.50 m to 76.00 m (average 38.47 m). Coal seam III splits into three coal layers, the thicknesses of which, from bottom to top, are 0.15–9.00 m (average 2.81 m), 1.00–15.70 m (average 6.93 m) and 0.80–12.40 m (average 4.35 m), respectively. The interbedded waste rocks consist of sand, clay, carbonaceous clay, marly clay, silt and thin coal layers. Their thicknesses between the third and second, and, second and first coal layers vary from a few to 32 m and 36 m, respectively. The coal seam II-a was formed locally in the southern part of the field. The seam thickness varies from 0.15 to 1.00 m. The coal seam II occurs across the entire Smederevsko Pomoravlje field. Typical features of this coal seam are stratification followed by a high content of clayey–sandy sediments. The seam thickness varies from 0.20 to 16.20 m (average 5.69 m). The coal seam I-a is developed in the central, north, north–east, north–west and west parts of the field. The seam thickness varies from 0.10 to 6.00 m (average 2.11 m). The coal seam I

occurs in the central, north, north–east and north–west parts of the field, and it is stratified across the entire area. The thickness of coal seam I varies from 1.40 to 47.50 m (average 28.30 m). Coal seam I splits into two coal layers with thickness from bottom to top of 0.20–12.70 m (average 5.74 m) and 5.65–20.90 m (average 15.70 m), respectively. The interbedded waste sediments between the second and first coal layers comprise sand, carbonaceous-, sandy- and marly-clays, and silt. The thickness of this package varies from 1.72 to 24.50 m (average 8.95 m).

The youngest Upper Pontian sediments, overlying coal seam I, include sand, clayey sand and clays with thin layers of carbonaceous clays, coal and limestone. The thickness of this package varies from 0.80 m to 76.50 m (average 26.92 m).

Quaternary series of Pleistocene age is made of gravel and sand, occasionally with clay and loess. The thickness of the Quaternary sediments varies from 16.70 to 42.40 m (average 22.59 m).

ORGANIC AND OTHER GEOCHEMICAL PARAMETERS

TABLE S-I. Values of group organic geochemical parameters

Bore-hole	Coal seam	Sam-ple	c_{Ash}^{a} %, db[b]	C_{org}^{c} %, db	S %, db	N %, db	C/N^{d}	Q_g^{e} MJ kg^{-1}, db	Q_d^{f} MJ kg^{-1}, db	Bitu-men, ppm, db	c_{Asp}^{g} %	$c_{Sat\,HC}^{h}$ %	$c_{Arom\,HC}^{i}$ %	c_{NSO}^{j} %
A-339	I	1	9.7	55.3	1.5	0.8	80.6	21.5	21.1	29228	53.2	5.2	4.9	36.7
	I	2	12.1	53.2	1.0	0.7	88.7	20.2	19.3	32872	49.1	5.9	4.8	40.3
	I	3	18.3	50.9	1.0	0.6	99.0	18.4	17.6	27302	43.4	5.7	5.6	45.2
	I	4	25.5	44.1	1.4	0.8	64.3	17.1	16.4	34673	40.4	6.0	6.5	47.1
	I	5	28.1	47.3	1.3	0.6	92.0	14.6	14.0	24641	42.8	6.0	5.3	45.9
	II	6	36.2	40.0	1.0	0.7	66.7	13.2	12.6	31312	47.0	5.6	5.4	42.0
A2I-414	I	7	11.2	55.2	1.3	0.9	71.6	21.0	20.1	31034	52.8	5.3	4.3	37.6
	I	8	34.8	44.1	1.2	0.7	73.5	14.2	13.5	27608	48.3	4.7	5.0	42.0
	I	9	16.8	51.0	1.3	0.7	85.0	19.1	18.4	34698	42.6	5.6	5.8	46.0
	I	10	43.5	36.0	0.7	0.6	70.0	9.9	9.4	15662	50.3	4.7	3.8	41.2
	I	11	46.7	29.9	0.8	0.5	69.8	10.0	9.5	20828	47.1	5.4	5.0	42.5
	I	12	31.5	44.3	1.3	0.7	73.8	13.4	12.7	33387	46.2	5.0	5.4	43.3
	II	13	26.8	45.2	1.7	0.6	87.9	15.2	14.4	21443	42.1	5.4	6.2	46.3
A1J-369	I	14	11.3	54.5	0.9	0.9	70.6	25.3	24.5	23841	41.9	5.4	6.6	46.1
	I	15	47.4	30.0	0.6	0.3	116.7	11.6	11.4	29638	47.9	5.4	4.3	42.4
	I	16	15.2	51.5	2.2	0.6	100.1	23.1	22.3	36409	49.3	4.7	4.3	41.8
	I	17	11.1	53.8	1.0	0.8	78.5	22.9	22.1	27510	52.4	3.4	3.7	40.5
	I	18	41.8	40.5	1.0	0.6	78.8	15.1	14.6	19315	52.5	4.0	3.9	39.7
	I	19	30.8	43.5	0.9	0.6	84.6	16.9	16.4	24335	48.5	4.4	4.7	42.4
	II	20	45.7	29.7	1.0	0.5	69.3	9.0	8.5	16870	40.1	6.6	6.3	47.0
	II	21	45.3	33.4	1.4	0.6	64.9	10.2	9.7	12754	43.4	5.3	5.0	46.3
Drmno field[2]	II, III	Range	8.7–47.0	30.7–58.1	0.6–3.4	N.D.[k]	N.D.	N.D.	N.D.	6642–79400	41.4–70.9	2.2–13.2	2.2–5.5	13.7–50.3
"A" field[4]	I, II	Range	12.6–82.6	8.9–60.9	0.2–1.7	0.3–1.2	55.2–97.1	N.D.	N.D.	3326–28145	N.D.	1.2–5.2	2.0–2.8	N.D.

(Table S-I footnote) [a]c_{Ash} – ash content; [b]db – dry basis; [c]C_{org} – organic carbon content; [d]C/N – carbon to nitrogen ratio is given as the molar ratio; [e]Q_g – gross calorific value; [f]Q_d – net calorific value; [g]c_{Asp} – asphaltene content; [h]$c_{Sat\ HC}$ – content of saturated hydrocarbons; [i]$c_{Arom\ HC}$ – content of aromatic hydrocarbons; [j]c_{NSO} – content of NSO fraction (polar fraction, which contains nitrogen-, sulphur- and oxygen--containing compounds); [k]N.D. – not determined

TABLE S-II. Results of the Rock Eval pyrolysis

Bore-hole	Coal seam	Sam-ple	TOC[a] %	S_1[b] mg HC (g sample)$^{-1}$	S_2[d] mg HC (g sample)$^{-1}$	S_3[e] mg CO$_2$ (g sample)$^{-1}$	T_{max}[f] °C	PI[g]	S_2/S_3	HI[h] mg HC (g TOC)$^{-1}$	OI[i] mg CO$_2$ (g TOC)$^{-1}$
A-339	I	1	51.06	4.66	86.89	32.44	349	0.05	2.68	170	64
	I	2	49.51	5.62	93.86	28.79	348	0.06	3.26	190	58
	I	3	43.81	4.86	85.93	27.89	349	0.05	3.08	196	64
	I	4	39.94	4.11	79.57	31.53	350	0.05	2.52	162	64
	I	5	37.42	4.41	67.59	26.21	366	0.06	2.58	169	66
	II	6	33.41	4.65	68.22	23.19	352	0.06	2.94	182	62
A2I-414	I	7	49.15	5.21	83.17	31.72	347	0.06	2.62	169	65
	I	8	35.85	3.59	70.33	21.89	347	0.05	3.21	196	61
	I	9	46.54	6.60	91.97	27.15	347	0.07	3.39	198	58
	I	10	26.55	1.07	43.20	19.86	350	0.02	2.18	163	75
	I	11	26.72	1.88	44.12	17.15	347	0.04	2.57	165	64
	I	12	36.83	4.91	72.59	23.26	371	0.06	3.12	197	63
	II	13	38.11	3.46	76.33	22.89	346	0.04	3.33	200	60
A1J-369	I	14	52.31	5.27	90.73	33.02	346	0.05	2.75	173	63
	I	15	24.12	1.61	44.77	15.05	346	0.03	2.97	186	62
	I	16	47.48	6.66	89.16	27.45	346	0.07	3.25	188	58
	I	17	50.66	4.27	84.75	30.94	346	0.05	2.74	167	61
	I	18	32.61	2.34	53.24	21.17	349	0.04	2.51	163	65
	I	19	37.85	3.23	70.21	22.72	349	0.04	3.09	185	60
	II	20	25.35	1.10	44.69	13.96	354	0.02	3.20	176	55
	II	21	26.93	1.20	42.37	20.34	387	0.03	2.08	157	76

[a]TOC – total organic carbon obtained from Rock–Eval pyrolysis; [b]S_1 – free hydrocarbons; [c]HC – hydrocarbons; [d]S_2 – pyrolysate hydrocarbons; [e]S_3 – amount of CO$_2$ generated from oxygenated functional groups; [f]T_{max} – temperature corresponding to the S_2 peak maximum; [g]PI – production Index = $S_1/(S_1+S_2)$; [h]HI – hydrogen index = $(S_2 \times 100/TOC)$; [i]OI – oxygen index = $(S_3 \times 100/TOC)$; note: Rock–Eval pyrolysis was not performed on samples from the Drmno and "A" fields; therefore, data could not be compared

TABLE S-III. Values of parameters calculated from distributions and abundances of *n*-alkanes and isoprenoids

Borehole	Coal seam	Sample	*n*-Al-kane C range	*n*-Alkane maximum	CPI_{16-34}[a]	CPI_{16-20}[b]	OEP 1[c]	OEP 2[d]	Pristane/ phytane
A-339	I	1	16–35	*n*-C$_{29}$	4.30	1.09	1.24	3.34	0.75
	I	2	16–35	*n*-C$_{29}$	5.12	0.98	1.74	3.65	0.95
	I	3	15–35	*n*-C$_{29}$	4.37	1.33	1.68	3.20	1.14
	I	4	15–35	*n*-C$_{29}$	6.14	2.11	2.53	4.08	1.42
	I	5	15–35	*n*-C$_{29}$	4.31	1.71	2.17	3.19	1.50
	II	6	15–35	*n*-C$_{29}$	4.95	1.60	2.33	3.75	1.27

TABLE S-III. Continued

Borehole	Coal seam	Sample	*n*-Alkane C range	*n*-Alkane maximum	CPI_{16-34}[a]	CPI_{16-20}[b]	OEP 1[c]	OEP 2[d]	Pristane/ phytane
A2I-414	I	7	16–35	n-C_{29}	3.67	0.91	1.46	2.99	1.07
	I	8	16–35	n-C_{29}	4.90	0.75	2.01	3.64	0.72
	I	9	15–35	n-C_{29}	7.91	2.53	1.80	3.12	1.15
	I	10	16–35	n-C_{29}	4.00	1.41	1.58	2.83	1.09
	I	11	16–35	n-C_{29}	3.35	1.71	1.42	3.42	0.67
	I	12	16–35	n-C_{29}	4.15	2.58	1.94	2.77	1.05
	II	13	15–35	n-C_{29}	3.46	2.14	3.25	3.78	1.65
A1J-369	I	14	15–35	n-C_{29}	4.59	0.41	2.80	3.67	1.13
	I	15	15–35	n-C_{29}	4.07	0.81	1.26	3.13	1.06
	I	16	16–35	n-C_{29}	3.85	0.45	1.66	3.39	1.12
	I	17	15–35	n-C_{29}	3.62	0.59	1.33	3.42	1.05
	I	18	15–35	n-C_{29}	3.80	0.63	1.27	3.35	1.40
	I	19	16–35	n-C_{29}	3.01	1.01	1.65	2.96	0.66
	II	20	15–35	n-C_{29}	3.82	1.56	2.00	3.08	1.07
	II	21	15–35	n-C_{29}	3.78	0.64	1.77	3.19	0.97
Drmno field[2]	II, III	Range	16–33	n-C_{29}	2.87–5.30	0.50–2.34	0.92–5.50	3.24–5.13	0.08–1.26
"A" field[4]	I, II	Range	15–33	n-C_{27} or n-C_{29}	1.23–5.94	0.65–1.61	1.14–1.80	1.68–5.14	0.74–1.16

[a]CPI_{16-34} – Carbon Preference Index determined for the full distribution of *n*-alkanes C_{16}–C_{34} (mass chromatogram *m/z* 71), CPI_{16-34} = 1/2 [Σodd(n-C_{17} – n-C_{33})/Σeven(n-C_{16} – n-C_{32}) + Σodd(n-C_{17} – n-C_{33})/Σeven(n-C_{18} – n-C_{34})]; [b]CPI_{16-20} – Carbon Preference Index determined for the distribution of *n*-alkanes C_{16}–C_{20} (mass chromatogram *m/z* 71), CPI_{16-20} = 1/2 [Σodd(n-C_{17} – n-C_{19})/Σeven(n-C_{16} – n-C_{18}) + Σodd(n-C_{17} – n-C_{19})/Σeven(n-C_{18} – n-C_{20})]; [c]OEP 1 = 1/4 [(n-C_{21} + 6 n-C_{23} + n-C_{25})/(n-C_{22} + n-C_{24})], OEP – odd–even predominance; [d]OEP 2 = 1/4 [(n-C_{25} + 6 n-C_{27} + n-C_{29})/(n-C_{26} + n-C_{28})]

TABLE S-IV. Values of parameters calculated from the distributions and abundances of diterpenoids and non-hopanoid triterpenoids

Borehole	Coal seam	Sample	Bicyclic diterpe-noids[a] %	Tricyclic diterpe-noids[b] %	Tetracyclic diter-penoids[c] %	Tricyclic diterpenoids/ tetracyclic diterpenoids	Pimarane/ $16\alpha(H)$--phyllo-cladane	ΣDiterpen oids/(ΣDi-terpe-noids + ΣTriter-penoids)[d]
A-339	I	1	0.07	36.01	63.93	0.56	0.52	0.9983
	I	2	0.04	36.05	63.90	0.56	0.48	0.9990
	I	3	0.39	33.44	66.17	0.51	0.47	0.9958
	I	4	0.29	8.20	91.51	0.09	0.07	0.9765
	I	5	0.47	24.38	75.16	0.32	0.27	0.9879
	II	6	0.90	27.47	71.64	0.38	0.32	0.9746
A2I-414	I	7	0.07	42.74	57.19	0.75	0.65	0.9975
	I	8	0.10	46.94	52.96	0.89	0.84	0.9899
	I	9	0.05	30.50	69.45	0.44	0.25	0.9896
	I	10	0.19	31.58	68.23	0.46	0.44	0.9936
	I	11	0.03	46.87	53.10	0.88	0.89	0.9945

TABLE S-IV. Continued

Borehole	Coal seam	Sample	Bicyclic diterpenoids[a] %	Tricyclic diterpenoids[b] %	Tetracyclic diterpenoids[c] %	Tricyclic diterpenoids/ tetracyclic diterpenoids	Pimarane/ $16\alpha(H)$-phyllocladane	ΣDiterpenoids/(ΣDiterpenoids + ΣTriterpenoids)[d]
A2I-414	I	12	0.13	5.61	94.27	0.06	0.05	0.9915
	II	13	0.25	35.31	64.44	0.55	0.51	0.9933
A1J-369	I	14	0.29	44.75	54.96	0.81	0.79	0.9975
	I	15	0.05	42.25	57.69	0.73	0.69	0.9980
	I	16	0.04	48.90	51.06	0.96	0.90	0.9996
	I	17	0.09	31.66	68.25	0.46	0.43	0.9958
	I	18	0.15	52.92	46.94	1.13	1.11	0.9972
	I	19	0.20	48.28	51.52	0.94	0.93	0.9938
	II	20	0.58	25.89	73.54	0.35	0.31	0.9923
	II	21	0.47	36.09	63.44	0.57	0.41	0.9331
Drmno field[2]	II, III	Range	N.D.[e]	4.39–75.19	24.81–25.60	0.05–3.03	0.03–3.22	0.8096–1.0000
"A" field[4]	I, II	Range	N.D.	12.97–57.37	42.63–87.03	0.15–1.35	0.06–0.69	0.9441–1.0000

[a]Bicyclic diterpenoids = (α-labdane + β-labdane)×100 / ΣDiterpenoids, ΣDiterpenoids = α-labdane + β-labdane + isopimaradienes + norisopimarane + pimaradiene + atisene + norpimarane + beyerane + isophyllocladene + isopimarane + fichtelite + pimarane + $16\beta(H)$-phyllocladane + $16\alpha(H)$-phyllocladane + $16\alpha(H)$-kaurane, calculated from the *TIC* of the saturated fraction; [b]tricyclic diterpenoids = (isopimaradienes + norisopimarane + pimaradiene + norpimarane + isopimarane + fichtelite + pimarane)×100 / ΣDiterpenoids, calculated from the *TIC* of the saturated fraction; [c]tetracyclic diterpenoids = (atisene + beyerane + isophyllocladene + $16\beta(H)$-phyllocladane + $16\alpha(H)$-phyllocladane + $16\alpha(H)$-kaurane)×100 / ΣDiterpenoids, calculated from the *TIC* of the saturated fraction; [d]ΣDiterpenoids = α-labdane + β-labdane + isopimaradienes + norisopimarane + pimaradiene + atisene + norpimarane + beyerane + isophyllocladene + isopimarane + fichtelite + pimarane + $16\beta(H)$-phyllocladane + $16\alpha(H)$-phyllocladane + $16\alpha(H)$-kaurane, ΣTriterpenoids = (des-A-olean-13(18)-ene + des-A-olean-12-ene + des-A-olean-18-ene + des-A-urs-13(18)-ene + des-A-oleanadiene + des-A-urs-12-ene + des-A-lupane + des-A-triterpene + des-A-oleanane), calculated from the *TIC* of the saturated fraction; [e]N.D. – not determined

TABLE S-V. Values of parameters calculated from the distributions and abundances of steroids and hopanoids

Borehole	Coal seam	Sample	C_{27} Sterenes[a] %	C_{28} Sterenes[b] %	C_{29} Sterenes[c] %	ΣSteroids/ ΣHopanoids[d]	Hopane maximum[e]	$C_{27}\beta$-Hopane[f] %	$C_{29}\beta\beta$-Hopane[f] %	$C_{30}\beta\beta$-Hopane[f] %	$C_{31}\beta\beta$-Hopane[f] %	$C_{30}\beta\beta$-Hopane to C_{30} ($\beta\beta+\alpha\beta$)-Hopanes
A-339	I	1	2.02	8.74	89.24	0.15	$C_{27}\beta$	39.81	27.91	20.52	11.76	0.80
	I	2	1.82	6.18	92.01	0.18	$C_{27}\beta$	38.79	28.43	20.28	12.50	0.80
	I	3	1.35	7.47	91.17	0.09	$C_{31}\alpha\beta(R)$	36.15	25.41	20.46	17.98	0.78
	I	4	1.73	6.41	91.86	0.08	$C_{27}\beta$	40.55	26.25	20.83	12.37	0.78
	I	5	1.79	4.89	93.31	0.09	$C_{27}\beta$	44.06	28.39	17.73	9.82	0.77
	II	6	3.54	7.96	88.50	0.06	$C_{27}\beta$	42.87	25.73	20.19	11.21	0.78

TABLE S-V. Continued

Bore-hole	Coal seam	Sample	C_{27} Sterenes[a] %	C_{28} Sterenes[b] %	C_{29} Sterenes[c] %	ΣSteroids/ ΣHopanoids[d]	Hopane maximum[e]	$C_{27}\beta$- Hopane[f] %	$C_{29}\beta\beta$- Hopane[f] %	$C_{30}\beta\beta$- Hopane[f] %	$C_{31}\beta\beta$- Hopane[f] %	$C_{30}\beta\beta$- Hopane to C_{30} $(\beta\beta+\alpha\beta)$ -Hopanes
A2I-414	I	7	2.26	8.49	89.24	0.02	$C_{31}\alpha\beta(R)$	43.20	31.79	9.30	15.71	0.62
	I	8	4.22	10.91	84.86	0.03	$C_{31}\alpha\beta(R)$	48.43	23.34	15.59	12.65	0.57
	I	9	2.17	9.82	88.01	0.04	$C_{31}\alpha\beta(R)$	41.25	27.69	17.15	13.91	0.71
	I	10	3.46	6.57	89.97	0.11	$C_{27}\beta$	43.35	27.12	19.35	10.18	0.74
	I	11	4.02	4.49	91.50	0.24	$C_{31}\alpha\beta(R)$	56.97	24.18	11.64	7.21	0.52
	I	12	3.06	7.11	89.83	0.08	$C_{27}\beta$	51.36	25.33	14.49	8.81	0.65
	II	13	1.11	5.75	93.14	0.26	$C_{27}\beta$	43.85	25.36	19.69	11.10	0.63
A1J-369	I	14	2.53	8.65	88.82	0.12	$C_{27}\beta$	45.47	25.46	18.15	10.93	0.64
	I	15	3.96	10.85	85.20	0.09	$C_{27}\beta$	53.88	24.25	13.99	7.88	0.57
	I	16	1.02	7.25	91.73	0.02	$C_{31}\alpha\beta(R)$	45.54	23.59	18.21	12.67	0.59
	I	17	1.62	9.07	89.31	0.06	$C_{31}\alpha\beta(R)$	45.12	26.19	18.06	10.64	0.67
	I	18	2.13	10.04	87.83	0.03	$C_{27}\beta$	43.59	26.20	18.47	11.74	0.59
	I	19	3.10	7.46	89.43	0.17	$C_{27}\beta$	58.56	25.91	10.44	5.10	0.61
	II	20	3.07	6.14	90.78	0.02	$C_{27}\beta$	51.90	24.04	15.57	8.48	0.58
	II	21	4.45	7.88	87.67	0.04	$C_{27}\beta$	43.57	25.31	19.68	11.44	0.68
Drmno field[4]	II, III	Range	0.00–4.55	0.00–15.94	84.06–100.00	0.07–0.25	$C_{27}\beta$ or $C_{31}\alpha\beta(R)$	26.93–50.24	23.98–36.78	11.52–31.17	8.38–13.93	0.53–0.90
"A" field[5]	I, II	Range	1.20–4.16	2.88–10.64	86.95–95.40	0.04–0.20	$C_{27}\beta$ or $C_{31}\alpha\beta(R)$	24.93–46.13	23.38–39.11	15.16–23.93	8.91–25.35	0.52–0.82

[a]C_{27}-Sterenes = $100 \times C_{27}(\Delta^2 + \Delta^4 + \Delta^5)$-sterenes / $[\Sigma(C_{27}–C_{29})(\Delta^2 + \Delta^4 + \Delta^5)$-sterenes + $C_{29}\Delta^{22}$-sterene + C_{29}-sterene]; [b]C_{28}-Sterenes = $100 \times C_{28}(\Delta^2 + \Delta^4 + \Delta^5)$-sterenes / $[\Sigma(C_{27}–C_{29})(\Delta^2 + \Delta^4 + \Delta^5)$-sterenes + $C_{29}\Delta^{22}$-Sterene + C_{29}-sterenel]; [c]C_{29}-Sterenes = $100 \times [C_{29}(\Delta^2 + \Delta^4 + \Delta^5 + \Delta^{22})$-sterenes + C_{29}-sterenel] / $[\Sigma(C_{27}–C_{29})(\Delta^2 + \Delta^4 + \Delta^5)$-sterenes + $C_{29}\Delta^{22}$-sterene + C_{29}-sterenel]; [d]ΣSteroids / ΣHopanoids = $[\Sigma(C_{27}–C_{29})(\Delta^2 + \Delta^4 + \Delta^5)$-sterenes + $C_{29}\Delta^{22}$-sterene + C_{29}-sterenel] / $[\Sigma(C_{29}–C_{32})17\alpha(H)21\beta(H)$-hopanes + $\Sigma(C_{29}–C_{32})17\beta(H)21\alpha(H)$-hopanes + $\Sigma(C_{29}–C_{32})17\beta(H)21\beta(H)$-hopanes + $C_{27}17\alpha(H)$-Hopane + $C_{27}17\beta(H)$-Hopane + C_{30}-Hop-17(21)-ene + C_{27}-Hop-17(21)-ene + C_{27}-Hop-13(18)-ene]; [e]Hopane maximum – The most abundant hopanoid in the m/z 191 mass chromatogram, $\beta\beta$ and $\alpha\beta$ designate the configurations at C_{17} and C_{21} in hopanes, (R) designates the configuration at C_{22} in the hopanes; Sterenes were quantified from the m/z 215 mass chromatogram, hopenes and hopanes were quantified from the m/z 191 mass chromatogram; [f]against $(C_{27}+\Sigma C_{29}–C_{31})$-$\beta\beta$-hopanes
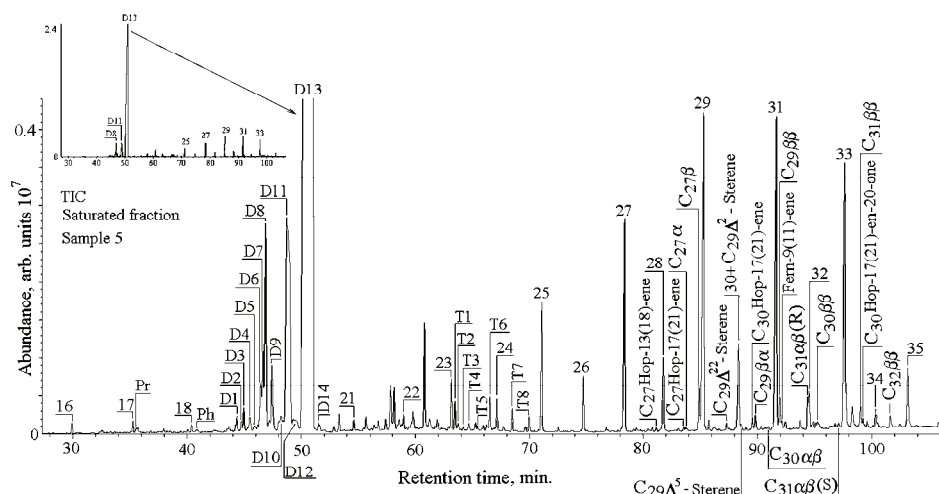
CHROMATOGRAPHIC AND SPECTROMETRY DATA

Fig. S-2. Total ion current (*TIC*) of the saturated fraction typical for the investigated samples. Peak assignments: *n*-alkanes are labelled according to their carbon number; Pr – pristane; Ph – phytane; D1 – isopimaradiene; D2 – 8β(*H*)-Labdane; D3 – isopimaradiene; D4 – nori-sopimarane; D5 – 8α(*H*) – labdane; D6 – atisene; D7 – norpimarane; D8 – beyerane; D9 – isophyllocladene; D10 – fichtelite; D11 – pimarane; D12 – 16β(*H*)-phyllocladane; D13 –16α(*H*)-phyllocladane; D14 – 16α(*H*)-kaurane; T1 – des-A-olean-13(18)-ene; T2 – des-A-olean-12-ene; T3 – des-A-olean-18-ene + Des-A-urs-13(18)-ene; T4 – des-A-oleanadiene; T5 – des-A-urs-12-ene; T6 – des-A-lupane; T7 – des-A-triterpene;[5] T8 – des-A-oleanane;[6] ββ, βα and αβ designate configurations at C_{17} and C_{21} in hopanes; (*S*) and (*R*) designate configuration at C_{22} in hopanes.
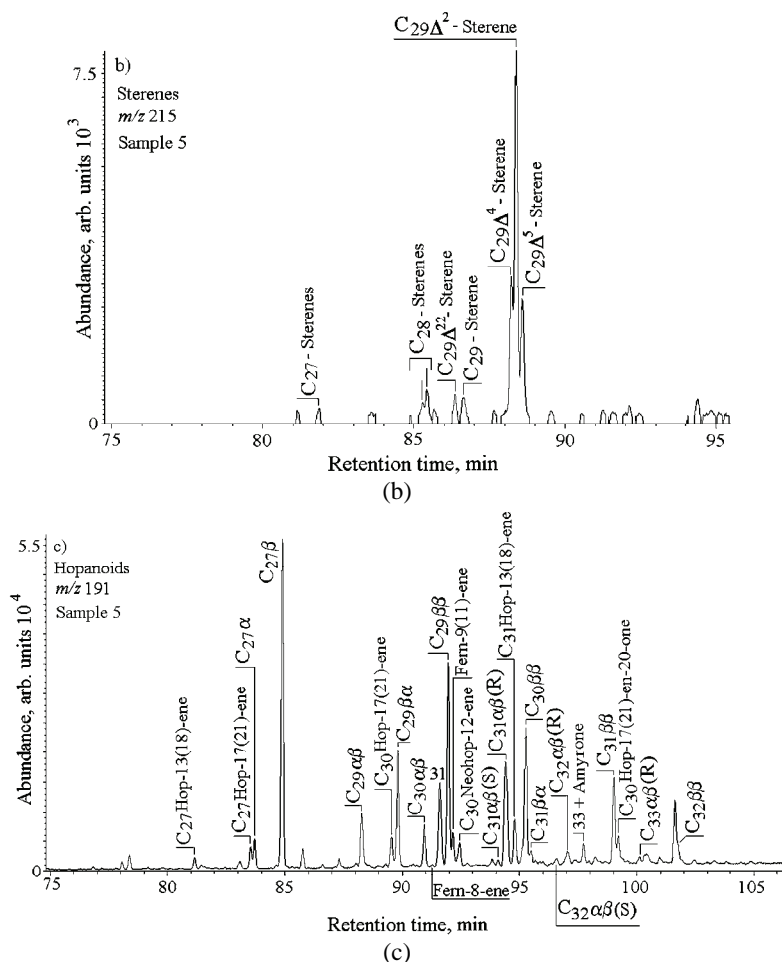

(a)

(b)

(c)
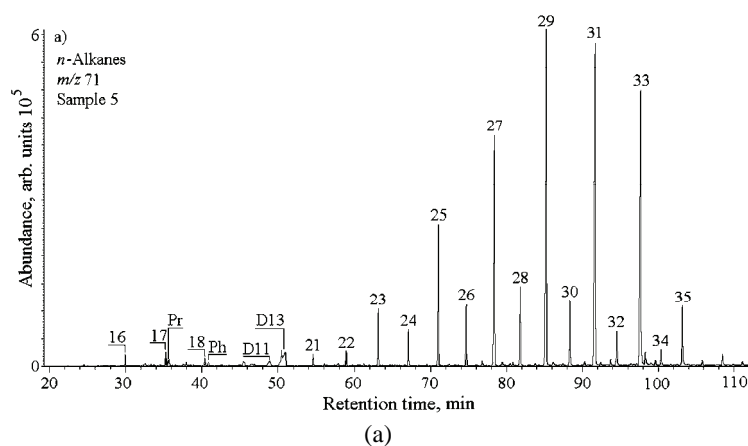
Fig. S-3. GC–MS mass chromatograms of: a) *n*-alkanes, *m/z* 71, b) sterenes, *m/z* 215 and c) hopanoids, *m/z* 191, typical for the investigated samples. For peak assignments, see the legend to Fig. S-2.

REFERENCES

1. A. Kostić, *M.Sc. Thesis*, Faculty of Mining and Geology, University of Belgrade, 1995, p. 160 (in Serbian)
2. K. Stojanović, D. Životić, A. Šajnović, O. Cvetković, H. P. Nytoft, G. Scheeder, *J. Serb. Chem. Soc.* **77** (2012) 1109
3. D. Životić, *M.Sc. Thesis*, Faculty of Mining and Geology, University of Belgrade, 2001, p. 29 (in Serbian)
4. K. Stojanović, D. Životić, *Int. J. Coal Geol.* **107** (2013) 3
5. Y. Huang, M. J. Lockheart, J. W. Collister, G. Eglinton, *Org. Geochem.* **23** (1995) 785
6. J. Jacob, J.-R. Disnar, M. Boussafir, A.-L. Spadano Albuquerque, A. Sifeddine, B. Turcq, *Org. Geochem.* **38** (2007) 180.

DIVISION OF ANALYTICAL CHEMISTRY
EUROPEAN ASSOCIATION FOR CHEMICAL AND
MOLECULAR SCIENCES

EUCHEMS NEWS
European Analytical Column No. 43

IVO LEITO[1], WOLFGANG BUCHBERGER[2] and PAUL WORSFOLD[3]*

[1]University of Tartu, Institute of Chemistry, Ravila 14a, Tartu, 50411, Estonia, ivo.leito@ut.ee, [2]Analytische Chemie, Universität Linz, Altenbergerstrasse 69, A-4040 Linz, Austria, Wolfgang.Buchberger@jku.at and [7]School of Geography, Earth and Environmental Sciences, Plymouth University, Plymouth PL48AA, United Kingdom

INFORMATION FROM THE EUCHEMS DIVISION OF ANALYTICAL CHEMISTRY
(DAC)

The 45th Annual Meeting of the DAC was successfully held on August 31, 2014, in Istanbul prior to the opening of the 5th EuCheMS Chemistry Congress (ECC 5). Paul Worsfold as current Chair of the DAC welcomed Delegates and Observers from 15 countries attending the meeting. The updated DAC strategy for 2015-2017 was approved at the meeting and can be found at http://www.euchems.eu/divisions/analytical-chemistry.html.

In 2015, the prime event within the activities of the DAC will be EUROANALYSIS XVIII, which will be held in Bordeaux, France, at the Congress Center (Bordeaux-Lac), 6-10 September 2015, under the auspices of the Societé Chimique de France. EUROANALYSIS started in 1972 and represents a broad-spectrum conference on Analytical Chemistry organized on a regular basis with its venue rotating between European countries. EUROANALYSIS has established itself as the premier European meeting for discussion and presentation of analytical chemistry in a global sense and constitutes a forum for analytical chemists from academia, governance and industry, allowing the formation of networks between chemical societies and their members working in the diverse fields of analytical sciences. This scientific event returns to France after nearly 40 years and will be a unique chance to gain comprehensive insights into contemporary analytical chemistry. Among the highlights of EUROANALYSIS XVIII will be the Robert Kellner Lecture given by Bernhard Lendl from Vienna, Austria, and the presentation of the newly established DAC-EuCheMS Award to

* Corresponding author. E-mail: pworsfold@plymouth.ac.uk

589

Miguel Valcárcel from Cordoba, Spain. Both the Robert Kellner Lecture and the DAC-EuCheMS Award are sponsored by Springer.

EUROANALYSIS XIX will be organized in Stockholm, Sweden, by the Swedish Chemical Society. The tentative date is August 27-31, 2017.

The next Annual Meeting of the DAC will be held in Bordeaux on September 6, 2015, and a decision about a new Chair of the DAC for the period 2017-2019 will be made. The Steering Committee of the DAC has nominated Slavica Razic to succeed Paul Worsfold. Other nominations are welcome, and an official letter from a member society of the DAC should be sent to the chair or the secretary.

Currently, DAC operates six Study Groups devoted to major topics of particular importance, namely "Education in Analytical Chemistry", "Bioanalytics", "History", "Quality Assurance and Accreditation", "Chemometrics" and "Archeometry and Cultural Heritage in Analytical Chemistry" (see http://www.euchems.eu/divisions/analytical-chemistry/news-current-activities-conferences-and-events/study-groups-and-task-forces.html). These Study Groups are evaluated after a period of three years and may be renewed.

In this European Analytical Column, Ivo Leito provides a personal view on metrology in chemical analysis.

Metrology in Chemical Analysis

Metrology lies at the foundation of any measurement. Metrology in Physics has been a mature science for a long time and metrology of chemical measurements (Metrology in Chemistry, MiC) as a discipline is also approaching maturity. The main concepts have now been firmly established[1] and the tools – certified reference materials (CRMs) and interlaboratory comparisons (ILCs) – are available in increasing diversity. There are guidance materials,[2,3] textbooks,[4–6] training courses[7,8] and even university study programmes[9–11] addressing MiC or some of its sub-topics. Also, when it comes to practical application by laboratories involved in routine analysis, the situation has improved considerably during the last decade. Nevertheless, challenges still remain as evidenced by, for example, discrepancies between participant results in interlaboratory comparisons (ILCs).[12–14] The aim of this contribution is to briefly review why this is so and give some guidance on the most important MiC activities for any laboratory.

The difficulties in applying metrological concepts in chemistry originate largely in the following.

1. In chemical analysis, the analyte is typically determined in the presence of (often numerous) other substances in the sample, many of them at higher (often by orders of magnitude) concentrations than the analyte. Many of them can, in principle, contribute to the analytical signal, leading to higher results (sometimes

they can lead to lower results, *e.g*., matrix effects in LC-ESI-MS[15]). Thus, there is the problem of limited selectivity: the question therefore is often not "How accurately can one measure the analytical signal?" but rather "How can one assure that the signal is wholly due to the analyte and does not include a contribution from some interferent(s)?".[16]

2. In order to achieve sufficient selectivity, most analytical methods involve one or more separation steps (*e.g*., extraction, precipitation, chromatography). Whilst these steps are quite successful in removing interferents, they often (mostly) also remove some of the analyte, leading to lower results.

As can be seen, the main problems (*i.e*., the main uncertainty contributions) in a chemical measurement usually come not from the measurement technique itself but rather from the object under investigation (see, *e.g*.,[17] for examples in spectrophotometry).

In this complex situation, what should a routine laboratory do? The author has attempted to formulate some simple and pragmatic advice below. It is largely based on the author's experience of collaboration with such laboratories. What is described below is by no means "the full story" but rather a "starting point". It assumes that the methods used in a laboratory are, with reasonable probability, fit for purpose (which is usually the case).

3. *Compare your values with reference values*. Comparing your results for a sample with an independent reference value for the same (or identical) sample is useful for confirming that your results have acceptable trueness and that the measurement uncertainty estimate is adequate (or at least suitable for obtaining data for measurement uncertainty evaluation). However, such a comparison gives an additional benefit: good agreement between your result and the reference value also indicates that the selectivity of your analytical method (procedure) is probably adequate and that the robustness is good. The result of such a comparison can, depending on its intended further use, be expressed in different ways, *e.g*., as a zeta or E_n score[18] or as a bias.[19]

There are several ways of "realising" a reference value, all of which have different levels of reliability. The guidance below should therefore be considered in the broadest possible sense.

Perhaps the most obvious approach is analysing certified reference materials (CRMs) using the analytical method established in your laboratory. The reference values carried by CRMs are highly reliable. In order to be useful, the certified analyte(s) of the CRM have to be the same as those required in the target sample(s) and the matrix and concentration range(s) of the analyte(s) in the CRM have to be similar to what is commonly encountered in your laboratory. The main obstacle that frequently emerges is that there is no CRM available for the required analyte-matrix-concentration combination. CRMs can be unavailable

because the analyte-matrix combination is not common or because the analyte (*e.g*., dissolved oxygen, peroxides) and/or the matrix is unstable.

In the case of many analyte-matrix combinations, satisfactory reference values can be achieved by spiking or preparing in-house reference materials (laboratory reference materials, LRM). The main prerequisite is that the matrix has to enable homogenisation of the spiked analyte content.

CRMs can be unavailable for a particular analyte-matrix-concentration combination and the preparation of LRMs can be difficult (*e.g*., if the matrix is solid and highly inhomogeneous). In such cases, nevertheless, ILCs can be available. In contrast to CRMs, ILC samples need not be stable for an extended period, which means that ILCs can also be undertaken with less stable analytes. Most of the ILCs in which commercial laboratories participate are the so-called proficiency tests (PTs) and instead of metrological reference values they use consensus values based on the participant's results, which are generally of lower reliability. However, comparison with PT consensus values is still much better than no comparison at all. Participation in ILCs is, of course, highly recommended (in fact mandatory), even if suitable CRMs exist. When no suitable ILC is available, one can be organized by the participating laboratories themselves. Although it cannot be considered a rigorous ILC, even as few as 2-3 laboratories analysing a few split samples and comparing results is much better than no comparison at all.

Obviously, in order to compare two analytical results obtained for the same sample (or identical samples), the results must refer to the same measurand.

4. *Collect data over long periods*. Repeated measurements are essential when precision or trueness (*e.g*., using a CRM as described above) is evaluated. Replicate measurements performed within a single day enable repeatability, s_r, to be obtained whereas replicate measurements over a longer period can be used to determine intermediate precision, s_{RW} (also known as within-laboratory reproducibility).[19] While both of these characteristics have their uses, intermediate precision is certainly more useful, as it takes into account a (much) larger number of effects influencing the measurement results (uncertainty sources) for one particular parameter. This is because many effects that are systematic within a day (and are thus not accounted for by sr) become random over a longer period and are accounted for by s_{RW}.[20] This also means that if correctly determined, $s_{RW} > sr$. The longer the period, the more effects are included in s_{RW} and consequently the more adequate and useful this characteristic becomes.

When s_{RW} is evaluated then it is often asked, "How many data points do we need for a reliable s_{RW} estimate?". In fact an even more important question is "How long a period should be used?". The answer is the longer the better: sRW found from 8 values collected over 8 months (one per month) more adequately characterises the method than s_{RW} from 16 values collected on 16 consecutive

days. It is of course a necessary prerequisite that the sample that is analyzed is homogenous enough and is stable during the time period used.

When trueness/bias is evaluated using a CRM then again, rather than making four replicate measurements (the amount of CRM in a container is often low and it may be impossible to do many more replicates) in one day, they should be made over a period of several weeks (or a couple of months) and then the obtained average value compared with the reference value or used for bias calculation. It is of course again important to be sure that the CRM is stable over that period.

The determined intermediate precision and bias can be conveniently used by the practical and "safe" within-laboratory validation approach of measurement uncertainty estimation, perhaps best known by the formalisation published by Nordtest.[19] The word "safe" here means that this uncertainty estimation approach tends to lead to somewhat overestimated rather than underestimated measurement uncertainties.

5. *"Do not stop there"*. People from routine laboratories often ask questions similar to the following: "How long should the period be for determining intermediate precision?", "Should I determine parameter X with all my analyte-matrix combinations?", "How many different CRMs should I use for estimating the average bias of my method?". These questions are difficult to answer in an "absolute" way. If rigorous answers are given then the probability is high that the laboratory will find that it should not use the method because so much more needs to be done to meet the ultimate requirements. In the opinion of the author, the best answer is this: when you implement a new method, you can start with a limited objective but you must not stop there and should add new data on a regular basis. So, an s_{RW} value obtained from data collected over four weeks cannot be considered sufficient (preferably data collected over one year should be used [19]) and just one CRM for the evaluation of bias is generally not enough. However, these data can be documented and used as a first approximation and a first measurement uncertainty estimate can already be obtained. As time goes by, s_{RW} can be recalculated based on longer time intervals, bias can be estimated using several reference values and the measurement uncertainty estimate can be recalculated accordingly.

In conclusion: constant improvement is the key to reliable analytical results.

REFERENCES

1. JCGM 200:2008, *International vocabulary of metrology — Basic and general concepts and associated terms (VIM)*, 3rd edition. BIPM, IEC, IFCC, ILAC, ISO, IUPAC, IUPAP and OIML, 2008. Available on-line from http://www.bipm.org/en/publications//guides/vim.html
2. Extensive set of guidance materials on MiC is available from Eurachem at http:////www.eurachem.org/, accessed 31 Oct, 2014

3. Extensive set of guidance materials on MiC is available from Nordtest at http://www.nordtest.info/, Accessed 31 Oct 2014
4. B. W. Wenclawiak, M. Koch, E. Hadjicostas, *Quality Assurance in Analytical Chemistry*, Springer, Berlin, 2004
5. *Practical Examples on Traceability, Measurement Uncertainty and Validation in Chemistry,* N. Majcen, P. Taylor, Eds., Vol. 1, EC-JRC IRMM, Geel, Belgium, 2007
6. *Analytical Measurement: Measurement Uncertainty and Statistics,* N. Majcen, V. Gegevicius, Eds., , EC-JRC IRMM, Geel, Belgium, 2012
7. TrainMiC – Training in Metrology in Chemistry, EC-JRC IRMM, https://ec.europa.eu/jrc/en/trainmic, accessed 31 Oct, 2014
8. *Estimation of measurement uncertainty in chemical analysis*, online course, University of Tartu, 2013, https://sisu.ut.ee/measurement/, accessed 31 Oct, 2014
9. *EACH – Excellence in Analytical Chemistry*, http://www.analyticalchemistry.eu/ accessed 31 Oct, 2014
10. *EMQAL – Erasmus Mundus Master in Quality in Analytical Laboratories*, http://www.emqal.org/, accessed 31, Oct 2014
11. *Measurement Science in Chemistry Euromaster®*, http://www.msc-euromaster.eu/, accessed 31 Oct, 2014
12. Y. Fiamegos, F. Cordeiro, P. Robouch, H. Emteborg, J. Charoud-Gota, L. G. Omberg, I. Rodushkin, B. de la Calle *Food Addit. Contam., A* **31** (2014) 63
13. T. Näykki, L. Jalukse, I. Helm, I. Leito, *Water* **5** (2013) 420
14. *Interlaboratory comparisons organised at UT Testing Centre*, http://www.ut.ee/katsekoda/ILC/, accessed 29 Oct, 2014
15. A. Kruve, I. Leito, *Anal. Methods* **5** (2013) 3035
16. H. Emons, in *Chemical Analysis – Are we ready to deliver?,* presented at the Eurachem Workshop on quality in analytical measurements, Lisbon, 2014
17. L. Sooväli, E.-I. Rõõm, A. Kütt, I. Kaljurand, I. Leito, *Accred. Qual. Assur.* **11** (2006) 246
18. ISO 13528 (2005), *Statistical methods for use in proficiency testing by interlaboratory comparisons*, ISO
19. B. Magnusson, T. Näykki, H. Hovind, M. Krysell, (2012) *Handbook for Calculation of Measurement Uncertainty in Environmental Laboratories*, Nordtest Technical Report 537, ed. 3, Nordtest, available on-line from http://www.nordtest.info/, accessed 01 Nov, 2014
20. I. Leito, *Recovery/bias evaluation*, Presented at the Eurachem Workshop on quality in analytical measurements, Lisbon, 19-21 May, 2014. Available from http://www.ut.ee/EACH/?p=1936, accessed 01 Nov, 2014.